Analysis of Composite Helmet Impact by the Finite Element Method

by

Joseph Edward Callahan

Thesis Submitted to the Faculty of the

Virginia Polytechnic Institute and State University

in partial fulfillment of the requirements for the degree of

Master of Science

in

Aerospace Engineering

Romesh C. Batra, Chair

Craig A. Woolsey

Mayuresh J. Patil

September 5, 2011

Blacksburg, VA

Keywords: Laminated Composite, Helmet, Roma Plastilina #1 Clay, Impact.

Analysis of Composite Helmet Impact by the Finite Element Method

Joseph Edward Callahan

(ABSTRACT)

We analyze by the finite element method transient deformations of a helmet mounted on a Roma Plastilina #1 clay-filled rigid and stationary headform. The helmet is made of a unidirectional fiber reinforced composite that is modeled as a linear elastic orthotropic material. Hashin's criteria are used to simulate the fiber and the matrix failure. The clay (impactor) is modeled as an elastic-plastic (elastic-viscoplastic), isotropic and homogeneous material. The problem is numerically solved by using the commercial software, ABAQUS, with built-in algorithms to simulate contact between distinct materials (e.g., the clay, the helmet, and the penetrator), and to delete elements whose material has failed. We have verified capabilities of the software for analyzing the penetration problems by solving a few impact problems that have been previously studied by others either experimentally or numerically. The effect of the number of layers in the helmet and the crater formed in the clay due to the impact of the projectile on the helmet has been delineated. It is believed that the crater size in the clay will provide useful information regarding the head injury trauma caused by the impact of a projectile on the helmet.

Acknowledgments

I would like to acknowledge the guidance and support Dr. Romesh Batra has provided me during my graduate studies. I also want to thank him for taking a chance, trusting me to succeed and fostering my confidence to handle any challenge.

I would also like to acknowledge the support of Alireza Chadegani and Gautam Gopinath without which this task would have seemed impossible. Alireza's patience, guidance, and wealth of knowledge of ABAQUS have, without a doubt, been a valued contribution to the completion of this project. Gautam's wisdom and insight have saved me from making mistakes that would have derailed this project for many months.

I would like to thank my family and Ms. Rachel Coulter for their continued love and support; this would not have been possible without it.

I would like to acknowledge Chris Fitzgerald for his assistance in providing material properties and experimental data for a selection of Dyneema laminates. Finally I would like to thank Drs. J. Q. Zheng and M. G. Bevan as well as Johns Hopkins Applied Physics Lab for their support.

Contents

1 Introduction 1

2 Formulation of the Problem 8

3 Computation and Discussion of Results 14

3.1 Results for Test Problems 14

3.1.1 Penetration of steel rods into aluminum targets 15

3.1.2 Impact of a composite laminate 15

3.1.3 Impact of composite laminates of different material systems 17

3.1.4 Perforation of circular laminate plates 18

3.1.5 Impact of Dyneema laminates 19

3.2 Impact of Clay Layer 20

3.3 Impact of Composite Plate with Clay Backing 21

3.4 Front Impact of Helmet/Headform 22

4 Conclusions 25

References 26

Appendix A – Material Properties 135

Appendix B – Sample Input File 138

List of Figures

1	Configuration of an ACH (green) mounted on a clay-filled headform (red and tan); (a) isometric view; (b) side view; dimensions are in mm.	30
2	(a) Schematic sketch of the FSP with dimensions in mm; (b) discretization of the 0.22 caliber FSP into finite elements. The FSP's initial velocity is in negative z-direction.	31
3	Three views of a shell model of a helmet with the FE mesh; dimensions are in mm. The bounding surfaces of the helmet are traction free except for the two nodes marked in red which are constrained from moving in all three directions.	32
4	Top view of the helmet showing the hole at the helmet crown.	33
5	The oval headform geometry; (a) rigid frame, and (b) clay with dimensions in mm. The rigid frame is held at rest during the simulations.	34
6	Initial configuration of the impact problem studied by Forrestal et al.; projectile's initial velocity is in –z direction, the target is traction free on all exterior surfaces.	35
7	Comparison of computed and experimental [4] penetration depths for a steel rod impacting at normal incidence a thick aluminum target.	36
8	Contour plots of the equivalent plastic strain obtained using the fine mesh to study Forrestal et al.'s penetration tests for impact speeds of 450 (a), 760 (b), 960 (c), and 1020 m/s (d); dimensions in mm.	37-40
9	(a) Initial configuration of the impact problem studied by Sheikh et al. [2]; edges where boundary conditions are applied are shown in red; the projectile initial velocity is in the negative z-direction. (b) Schematic sketch of the projectile used in Sheikh et al.'s work [2]; all dimensions are in mm.	41
10	Computed time histories of the projectile speed for three types of boundary conditions applied at the edges of the composite laminate and that reported in [2].	42

11	Time histories of the projectile speed for the two FE meshes used to study the impact problem previously analyzed by Sheikh et al. [2].	43
12	Visual comparison of the finite element meshes used to analyze the impact problem studied by Sheikh et al. [2]; the coarse mesh (a) has 2500 elements in the area near impact while the fine mesh (b) has 10000 elements. The rear of the projectile is shown in blue.	44
13	Time histories of the projectile speed for geometrically identical laminates of five material systems.	45
14	Front and side views of the five composite laminates after penetration by the projectile; AS4/3501-6 (a) , E-glass/117-220 (b), Gevetex/LY556 (c), Silenka/MY750 (d), T300/BSL914C (e) ; all dimensions in mm.	46-50
15	For different impact speeds, comparison of the presently computed residual projectile speed with that found by Lee and Sun for laminates I, II, and III.	51-53
16	Time histories of projectile and laminate energies for Dyneema laminate C impacted by a FSP with an initial speed of 750 m/s.	54
17	Fiber tension damage in first (a) and last (b) ply of Dyneema laminate C 200 μs after impact by a FSP with an initial speed of 750 m/s.	55
18	Fiber compression damage in first (a) and last (b) ply of Dyneema laminate C 200 μs after impact by a FSP with an initial speed of 750 m/s.	56
19	Matrix tension damage in first (a) and last (b) ply of Dyneema laminate C 200 μs after impact by a FSP with an initial speed of 750 m/s.	57
20	Matrix compression damage in first (a) and last (b) ply of Dyneema laminate C 200 μs after impact by a FSP with an initial speed of 750 m/s.	58
21	Shear damage in first (a) and last (b) ply of Dyneema laminate C 200 μs after impact by a FSP with an initial speed of 750 m/s.	59

22	Initial configuration of the clay drop test described in the NIJ standard 101.6. Boundary conditions are shown on the side and bottom surfaces. Points on the top surface except those contacting the projectile are traction free and those contacting the projectile conform to the shape of the projectile; projectile moves in the negative z-direction.	60
23	Time histories of energy components in the NIJ clay drop test.	61
24	Contour plot of the equivalent plastic strain in a small region of the clay around the crater at 3 μs (a), 6 μs (b), 9 μs (c), 12 μs (d), 15 μs (e), 21 μs (f), and 27 μs (g).	62-65
25	Contour plot of the von Mises stress in a small region of the clay around the crater at 3 μs (a), 6 μs (b), 9 μs (c), 12 μs (d), 15 μs (e), 21 μs (f), and 27 μs (g); volume of crater ~30 cubic cm; **legend units: Pa**.	66-68
26	Contour plot of pressure in a small region of the clay around the crater at 3 μs (a), 6 μs (b), 9 μs (c), 12 μs (d), 15 μs (e), 21 μs (f), and 27 μs (g); **legend units: Pa**.	70-72
27	Time histories of the transverse displacement of the center of the impacted face of the laminate with and without the clay backing.	73
28	Time histories of the deflection of the center of the bottom surface of the laminate and the corresponding clay particle.	74
29	Time history of projectile and helmet energies for front helmet impact by FSP with an initial speed of 750 m/s.	75
30	Damage modes in helmet for $v_0 = 0.6\, v_{BL}$ at 200 μs.	76
31	Damage modes in helmet for $v_0 = 0.9\, v_{BL}$ at 200 μs.	77
32	Damage modes in helmet for $v_0 = v_{BL}$ at 200 μs.	78

33	Damage modes in helmet for $v_0 = 1.2\ v_{BL}$ at 200 μs.	79
34	Comparison of helmet fiber tension damage for the impact speeds studied at 200 μs.	80
35	Comparison of helmet fiber compression damage for the impact speeds studied at 200 μs.	81
36	Comparison of helmet matrix tension damage for the impact speeds studied at 200 μs.	82
37	Comparison of helmet matrix compression damage for the impact speeds studied at 200 μs.	83
38	Comparison of helmet shear damage for the impact speeds studied at 200 μs.	84
39	Time histories of the pressure at the initial point of contact for impact speeds of 750 m/s and 835 m/s.	85
40	Time histories of the displacement of the initial point of contact for impact speeds of 750 m/s.	86
41	Time history of clay energies for front helmet impact.	87
42	Contour plot of pressure in clay section of headform at 19.5 μs (a), 26 μs (b), 32.5 μs (c), and 39 μs (d) after simulation beginning for $v_0 = 90\%\ v_{BL}$ case; volume of crater ~2100 cubic mm; **legend units: Pa**	88-89
43	Time history of pressure of four elements on the back of the helmet during front helmet impact by FSP with an initial speed of 750 m/s.	90
44	Contour plot of σ_{11}in back ply of helmet at 10 μs (a), 20 μs (b), 30 μs (c), 40 μs (d), 50 μs (e), 60 μs (f), 70 μs (g), 80 μs (h), 90 μs (i), and 100 μs (j) for $v_0 = 0.9\ v_{BL}$; **legend units: Pa**	91-100
45	Contour plot of σ_{22}in back ply of helmet at 10 μs (a), 20 μs (b), 30 μs (c), 40 μs (d), 50 μs (e), 60 μs (f), 70 μs (g), 80 μs (h), 90 μs (i), and 100 μs (j) for	101-110

$v_0 = 0.9\ v_{BL}$; **legend units: Pa**

46 Contour plot of σ_{12}in back ply of helmet at 10 µs (a), 20 µs (b), 30 µs (c), 40 µs (d), 50 µs (e), 60 µs (f), 70 µs (g), 80 µs (h), 90 µs (i), and 100 µs (j) for $v_0 = 0.9\ v_{BL}$; **legend units: Pa** 111-120

47 Normalized kinetic energy time history of the system for $v_0 = 1.2\ v_{BL}$ with times highlighted to note changes in contact behavior. 121

48 Snapshots of projectile/helmet/clay interaction with a projectile initial speed of 1000 m/s at 0 µs (a), 20 µs (b), 40 µs (c), 60 µs (d), 80 µs (e), 100 µs (f), 120 µs (g), 140 µs (h), 160 µs (i), 180 µs (j), 200 µs (k), 300 µs (l), and 400 µs (m) 122-134

List of Tables

1	Residual speed, kinetic energy absorbed, and specific kinetic energy absorbed for five composite laminates	18
2	Experimental V_{50} and computed ballistic limits for four laminates	20
A1	Values of Metal Material Parameters	135
A2	Values of Composite Material Parameters	136
A3	Material Properties of Fibers	137
A4	Values of Material Parameters for Roma Plastilina Clay #1	137

1 Introduction

Composites are being increasingly used to fabricate protective gear for soldiers as well as in numerous other civilian applications (e.g., the Boeing 787 Dreamliner) because of their high specific strength and large specific stiffness. While a wide variety of composites exist, those used for protective gear are usually woven fiber or composite laminates made of unidirectional fiber reinforced plies; a ply is usually referred to as a lamina. A lamina is generally very strong in the fiber direction but weak in directions perpendicular to the fiber; this is overcome by assembling together plies of different fiber orientations. A woven fiber composite, e.g., Kevlar body armor, is similar to a composite laminate except that instead of plies with fibers in different directions a woven fabric of fibers is impregnated with the matrix resin.

The failure of composites under multiaxial states of stress is not well understood and computed results depend upon, among other factors, the failure theory used. Whereas for metals the dominant failure mode is excessive plastic deformations, for composites the failure modes such as fiber breakage, fiber/matrix debonding, matrix cracking and delamination are less well understood and characterized. A fiber usually fails at a small value of the axial strain but can support large axial loads because of the high value of Young's modulus. The matrix can undergo large deformations before failure but cannot support significant normal and shear stresses. The fiber/matrix debonding strongly depends upon the sizing of fibers.

Two commonly used experimental measures to characterize the performance of a ballistic armor are V_0 and V_{50}. V_0 is the maximum speed at which all projectiles of the specified mass and geometry impacting at normal incidence an armor must be stopped, and V_{50} is the speed at which 50% of the projectiles of a given mass and geometry will fully penetrate the armor. A method more commonly used to assess the composite performance in simulations is the reduction of the

kinetic energy of the impacting projectile during its trajectory through the laminate divided by the areal mass density of the laminate. Another measure is the speed at which a specific projectile, impacting at normal incidence, will just penetrate the composite; this speed is referred to as the ballistic limit.

In the ballistics community it is common to find the strength of armor by placing it against a thick layer of clay, impacting the armor at normal incidence with a known projectile moving at a given speed, and finding the clay crater depth. A similar procedure is followed for helmets except that the clay is packed into a headform frame to which the helmet is strapped. Loosely speaking, the crater depth is inversely proportional to armor's strength. The size and the shape of the crater can also be related to the trauma suffered by a person wearing the armor.

The clay layer behind the armor is hereafter referred to as the clay backing. In order to accurately correlate the clay crater depth to damage, standard protocols must be followed before each ballistic test. In the United States these protocols are described in the National Institute of Justice (NIJ) standard-101.06 [6]. This standard requires the clay to be Roma Plastilina #1 that passes a detailed calibration test. The standard requires that the clay be kept at a specified temperature and humidity, and when a sphere of specified mass and radius is dropped onto the clay layer of prescribed thickness from a height of 2 m the crater depth must be within specified limits.

The response of composite materials to ballistic impact has been studied experimentally and numerically by several researchers; e.g., see Abrate [23] for a review of the literature on experimental and analytic approaches. For projectile speeds greater than 1 km/s, the two reports AMMHIS [28] and ADAMMO [27] focus on numerically analyzing the extent of damage caused

by the impact. Lapczyk and Hurtado [24] have used the damage model included in the finite element (FE) software ABAQUS to predict the strength of a fiber metal laminate.

Chan et al. [19] have experimentally and numerically studied the impact of carbon fiber-reinforced polymeric plates and determined their ballistic limits for various stacking sequences. Ganesh and Naik [25] have experimentally analyzed the strength of fiber reinforced plastic laminates and pointed out that important design variables for laminates include the fiber orientation angle, the ply thickness, and the fiber volume fraction [25]. Lee and Sun [5] have experimentally and numerically [5] ascertained the effect of the composite size and thickness on the kinetic energy absorbed during an impact event. Soden et al. [3] have provided material properties for several composite laminates.

Sheikh et al. [2] experimentally and numerically using the finite element method (FEM) evaluated the response of laminated composite plates to impact loads, and concluded the following: (i) the specific energy absorption capacity of thin laminates was more than that of thick laminates; and (ii) multiple thin laminates separated by gaps were significantly weaker than the sum of their specific energy absorption capacities. The drop in the specific energy absorption of the set-up (ii) from that of set-up (i) was attributed to small laminate particles propelled ahead of the projectile and damaging the next plate before it was impacted by the projectile.

Chen et al. [22] have developed a computer code based on the SPH (smooth particle hydrodynamics) method to numerically study the impact and penetration of unidirectional fiber-reinforced composite laminates. Wu and Chang [30] have developed computer software to study 3-dimensional deformations of a laminated composite plate under impact loads using 8-node brick elements and a reduced order integration rule. They computed the contact force between

the impactor and the laminate, time histories of stresses and strains at any point of the composite laminate, and time histories of the displacement and velocity of a point of the impactor. Ahn et al. [14] numerically studied the impact of a Kevlar plate by a fragment simulating projectile (FSP) using LS-DYNA. Schwer [31] has used LS-DYNA to compare results from the erosion, the multi-material ALE (arbitrary Lagrangian Eulerian) formulation, and the SPH methods for the impact of an aluminum projectile onto an aluminum plate. Yen [32] has considered the strain rate dependence of material properties and has analyzed the failure of woven as well as glass/epoxy composites under impact loads.

The analysis of composite helmets has been the focus of recent research as the percentage of head related injuries has been on the rise. van Hoof et al. [16, 17] experimentally and numerically investigated the response of woven composite helmets. Grujicic et al. [13] explored protection from Traumatic Brain Injury (TBI) provided by a helmet when it is subjected to a shock blast load transmitted through air.

Aziz et al. [9] evaluated the ballistic limit and the maximum deflection of a helmet made of woven composite materials, and found that the ballistic limit was highest for carbon reinforced polyester and lowest for Kevlar 29 reinforced phenolic. Although they listed the mass densities, they did not normalize the ballistic limit to find the specific laminate strength.

Aare and Kleiven [8] considered effects of the helmet stiffness and the impact angle on stresses and strains induced in the skull and the brain. Their simulations showed a correlation between the helmet stiffness and strains induced in the brain. Strains increased for a stiff helmet but for a helmet that is compliant enough to allow contact with the skull there is a large increase in stresses induced in the skull. They also found that the maximum stress induced in the skull is

highest for a normal impact but an oblique impact of 45° results in the highest strains in the brain (skull vs. brain).

Yang and Dai [11] used the FE software LSDYNA to compute the Head Injury Criterion Score (HICS) for different values of the impact angle and the impact site by examining large localized deformations of a woven composite helmet and the head. They found that the highest HICS occurred when the helmet was impacted at the back and least when it was hit on the sides. With an increase in the impact angle, the projectile deformed less, transferred less of its kinetic energy to the helmet, and was more likely to skid over the surface of the helmet.

A few attempts have been made to numerically model the clay used in ballistic tests. Bir [21] has studied the blunt ballistic impact of a cadaver's chest and compared the response of cadaver's chest with that of the Roma Plastilina #1 clay and of a ballistic gelatin impacted with the same projectiles. Bir found a good correlation between responses of the clay and those of the cadaver's chest. Munusamy and Barton [7] have experimentally and numerically investigated the blunt impact response of Roma Plastilina #1 clay.

An interesting issue is the delineation of the performance of different composite systems. Accordingly we have analyzed the impact response of five composite systems. Another question that usually comes up is whether or not using high strength fibers such as the Ultra High Molecular Weight Polyethylene (UHMSE-PE) or Dyneema will significantly improve the performance of the composite system. We have studied the impact response of Dyneema fiber reinforced composites but could not compare it with that of other composite systems since the manufacturer limited the distribution of the data. We note that Peijs et al. [29] have described techniques to fabricate UHMW-PE fibers, provided estimates of their strength and stiffness, and

discussed potential applications. Moyre et al. [20] have experimentally investigated the ballistic mechanical properties of gel-spun polyethylene fiber composites fabricated by two different processing schemes, namely, prepeg and hot compaction. However, we have not simulated these.

We have been unable to locate any study investigating the response of unidirectional fiber reinforced composite (UDFRC) helmets to ballistic impact. We note that the H.P. White testing procedure [15] for an Advanced Combat Helmet (ACH) requires analyzing clay deformations induced by impact at 5 locations, namely, the front, the back, the left side, the right side, and the top, of a helmet which is strapped to a headform using only helmet's existing suspension system. In order to complete the thesis in a reasonable time, we study here the front impact of a helmet by a 0.22 caliber FSP with all padding and the suspension system removed from the helmet. As shown in Fig. 1, the helmet is 'attached' to a headform consisting of a rigid support frame filled with clay similar to that described in [15], having an initial gap of at least 3 mm between the headform and the helmet, and the helmet rigidly clamped at two points. We have used functionalities available in the commercial FE software ABAQUS to analyze the impact problem. The version 6.9 of the software does not have the capability to study damage and failure in 3-dimensional deformations of a composite laminate but assumes that the laminate deforms in a state of plane stress. The procedure adopted here can be used to ascertain the effect of different material and geometric parameters on the helmet design and limit the number of physical tests to be conducted for arriving at the final design.

Prior to analyzing the impact of a composite helmet, we have used the software to study three impact and penetration problems for which test results are available in the literature to ensure that we are correctly using the software and algorithms needed to simulate contact and non-

interpenetration conditions give reasonable results. The computed results for these problems have been found to be close to the experimental findings. The first test problem studied is the impact of long steel rods into aluminum targets experimentally studied by Forrestal et al. [4] who compared test results with predictions from the cavity expansion model. Chen and Batra [26] developed software to numerically study this problem and found good agreement between computed and experimental results. Other test problems analyzed include those studied by Sheikh et al. [2] and Lee and Sun [5].

2 Formulation of the Problem

A schematic sketch of the problem studied is depicted in Fig. 1. A composite laminated helmet is supported on clay and a headform. Transient deformations of a continuous body (e.g. the helmet, the clay, the projectile), in rectangular Cartesian coordinate axes (x_1, x_2, x_3), are governed by

$$\rho \ddot{u}_i = \sigma_{ij,j} + \rho b_i, \; i = 1,2,3, \tag{1}$$

where ρ is the mass density, u_i the displacement of a material point along the x_i-axis, $\sigma_{ij,j} = \dfrac{\partial \sigma_{ij}}{\partial x_j}$, σ_{ij} the Cauchy stress tensor, b_i the body force per unit mass, a superimposed dot indicates the material time derivative, and a repeated index implies summation over the range of the index. We assume that initially the helmet, the headform and the clay are at rest, are free of residual stresses, and have null displacements, i.e.,

$$u_i(\boldsymbol{x},0) = 0, \dot{u}_i(\boldsymbol{x},0) = 0. \tag{2}$$

However, the projectile has a non-zero initial velocity but is stress free prior to impacting the helmet. In problems studied herein the body force is assumed to be zero; i.e., the effect of gravity forces on deformations of the body is neglected.

All points on the base of the headform and two points of the helmet are held stationary. Both displacements and surface tractions are taken to be continuous between the contacting bodies. However, when a gap develops between the contacting bodies, surface tractions on the separated surfaces are set equal to zero.

Constitutive relations

In order to complete the problem formulation, we specify constitutive relations for each material. A ply of the helmet is assumed to be linear elastic, homogeneous and orthotropic with the three planes of symmetry aligned along and perpendicular to the fiber direction. Thus

$$\sigma_{ij} = C_{ijkl}\varepsilon_{kl} \tag{3}$$

$$\varepsilon_{ij} = \frac{1}{2}\left(u_{i,j} + u_{j,i}\right) \tag{4}$$

where ε_{ij} is the infinitesimal strain tensor, and C_{ijkl} the tensor of material elasticities. With respect to the material principal axes, an orthotropic material has 9 independent elastic constants.

The projectile material and the clay are modeled as isotropic, homogeneous and elastic-plastic with elastic deformations represented by Hooke's law and plastic deformations by the von Mises yield criterion and the associated flow rule. For an isotropic material, the elasticity tensor C_{ijkl} has only two independent constants. The flow stresses for the clay and the projectile are assumed to be independent of the temperature, and their strain and strain-rate hardening are assumed to be described by the empirical Johnson-Cook relation, namely,

$$\bar{\sigma} = [A + B(\varepsilon^{pl})^n][1 + C\ln(\frac{\dot{\varepsilon}^{pl}}{\dot{\varepsilon}_0})] \tag{5}$$

where $\bar{\sigma}$ is the yield stress, ε^{pl} the equivalent plastic strain, $\dot{\varepsilon}^{pl}$ the equivalent plastic strain rate, $\dot{\varepsilon}_0$ the reference strain rate, and A, B, C and n are material parameters. A equals the yield stress of the material in a quasistatic simple tension/compression test, parameters B and *n* describe strain hardening of the material, and C its strain-rate hardening. We neglect strain-rate hardening of the clay by setting C = 0 for it.

We note that for a rigid body such as the headform the stress tensor is not related to its deformations.

Damage and Failure Criteria

We use Hashin's failure criteria for a state of plane stress already implemented in the software, ABAQUS. When Hashin's failure criterion is satisfied at a material point, it is assumed that damage rather than failure initiates at that point of a composite laminate. In order to use Hashin's failure criteria for deformations in the x_1x_2-plane with the x_1-axis along the fiber, the following four quantities are defined.

$$F_f^t = \left(\frac{\hat{\sigma}_{11}}{X^T}\right)^2 + \left(\frac{\hat{\sigma}_{12}}{S^L}\right)^2 - 1 \tag{6}$$

$$F_f^c = \left(\frac{\hat{\sigma}_{11}}{X^C}\right)^2 - 1 \tag{7}$$

$$F_m^t = \left(\frac{\hat{\sigma}_{22}}{Y^T}\right)^2 + \left(\frac{\hat{\sigma}_{12}}{S^L}\right)^2 - 1 \tag{8}$$

$$F_m^c = \left(\frac{\hat{\sigma}_{22}}{2S^T}\right)^2 + \left[\left(\frac{Y^C}{2S^T}\right)^2 - 1\right]\frac{\hat{\sigma}_{22}}{Y^C} + \left(\frac{\hat{\sigma}_{12}}{S^L}\right)^2 - 1 \tag{9}$$

Here $\hat{\boldsymbol{\sigma}}$ is the effective stress tensor, defined below, for the laminate. The fiber is assumed to fail in tension (compression) when F_f^t (F_f^c) just becomes positive, and the matrix to fail in tension (compression) when F_m^t (F_m^c) just becomes positive. Furthermore, X^T (X^C) equals the longitudinal tensile (compressive) strength of the laminate, Y^T(Y^C) the transverse tensile (compressive) strength, and S^T (S^L) the transverse shear (longitudinal) strength. We note that the failure at the laminate level rather than at the constituent level is being considered.

When any one of F_f^t, F_f^c, F_m^t and F_m^c just becomes non-negative at a material point, damage variables

$$d_f = \begin{cases} F_f^t & if\ \hat{\sigma}_{11} \geq 0 \\ F_f^c & if\ \hat{\sigma}_{11} < 0 \end{cases} \tag{10}$$

$$d_m = \begin{cases} F_m^t & if\ \hat{\sigma}_{22} \geq 0 \\ F_m^c & if\ \hat{\sigma}_{22} < 0 \end{cases} \tag{11}$$

are defined at that point, and the constitutive relation is modified as follows.

$$\boldsymbol{\sigma} = \boldsymbol{C}^d : \boldsymbol{\varepsilon} \tag{12}$$

$$\hat{\boldsymbol{\sigma}} = \boldsymbol{M}\,\boldsymbol{\sigma} \tag{13}$$

$$\boldsymbol{M} = \begin{bmatrix} \frac{1}{1-d_f} & 0 & 0 \\ 0 & \frac{1}{(1-d_m)} & 0 \\ 0 & 0 & \frac{1}{(1-d_s)} \end{bmatrix} \tag{14}$$

$$\boldsymbol{C}^d = \frac{1}{D}\begin{bmatrix} (1-d_f)E_1 & (1-d_f)(1-d_m)\nu_{21}E_1 & 0 \\ (1-d_f)(1-d_m)\nu_{12}E_1 & (1-d_m)E_2 & 0 \\ 0 & 0 & (1-d_s)GD \end{bmatrix} \tag{15}$$

$$d_s = 1 - (1-F_f^t)(1-F_f^c)(1-F_m^t)(1-F_m^c) \tag{16}$$

$$D = (1-d_f)(1-d_m)\nu_{12}\nu_{21} \tag{17}$$

With fibers aligned along the x_1-axis, E_1 and E_2 equal Young's moduli in the x_1 - and the x_2 - directions, respectively, ν_{12} and ν_{21} are Poisson's ratios, $\hat{\boldsymbol{\sigma}}$ the effective stress tensor, $\boldsymbol{C}^d$ the matrix of degraded elastic constants, and $\boldsymbol{M}$ the damage operator. Equation (15) essentially accounts for the reduction in the area supporting the externally applied load subsequent to the damage induced in the material. Thus the induced damage reduces values of elastic constants.

The degradation of the material is accounted for in the failure criteria by enhancing the stresses due to the reduction in the surface areas supporting the externally applied loads. We note that Young's modulus E_1 is reduced by the damage induced in the fiber and Young's modulus E_2 by the damage induced in the matrix. The in-plane shear modulus G is reduced by the damage induced both in the fiber and the matrix.

The delamination between adjoining layers is not simulated in this work.

Elements are deleted from the analysis once the fiber damage has reached 1 at all section points through the thickness.

A clay particle is assumed to fail when the effective plastic strain there equals the critical value, i.e., $\varepsilon^{pl} = \varepsilon_f^{pl}$.

Similarly, a projectile particle is assumed to fail when *d* calculated from Eq. (19) equals 1, and the failed element is deleted by using the NoNodalErosion option in ABAQUS. Deleted elements are not tracked in the analysis even though ABAQUS has the option to track them.

$$\varepsilon_f^{pl} = \left[d_1 + d_2 \exp\left(d_3 \frac{p}{q}\right)\right]\left[1 + d_4 \ln\left(\frac{\dot{\varepsilon}^{pl}}{\dot{\varepsilon}_0}\right)\right], \tag{18}$$

$$\dot{d} = \frac{\dot{u}^{pl}}{u_f^{pl}}, \tag{19}$$

where $p = -\sigma_{kk}/3$ is the hydrostatic pressure, q the von Mises stress, $\dot{u}^{pl} = L\dot{\varepsilon}^{pl}$, L is the characteristic length of an element, u_f^{pl} the effective plastic displacement at failure, d is the damage variable, and d_1, d_2, d_3, and d_4 are material parameters.

We ignore dependence, if any, upon the temperature of material parameters of the clay.

We assume that the FE mesh used to analyze problems provides reasonable 'big picture' results since not much time was spent to get a fully converged solution of a problem. Due to difficulties in duplicating a curved geometry by FEs with flat surfaces, curved sections of different parts may not perfectly match with each other and a small gap may appear between them. The contact is defined between the parts by using the built-in erosion contact algorithm that simulates 'hard' penalty normal behavior and frictionless tangential behavior.

Projectile

A sketch of the 0.22 caliber 4340H steel FSP is shown in Fig. 2a, multiple views of the meshed part are shown in Fig. 2b, and values of material parameters are listed in Table A1. The FSP is made according to military detail specification 46593B [10].

Headform

The headform consists of a rigid oval-like flat base plate, 4 rigid pillars, and the empty space between the pillars filled with the clay. The base plate and structural components are kept stationary during the simulations. The clay fits perfectly within the frame and is unconstrained. The rigid frame is shown without the clay in Fig. 5a, and with the clay in Fig. 5b.

3 Computation and Discussion of Results

Three – dimensional deformations of the FSP and the clay are analyzed by using 8-node C3D8R brick elements with reduced (1-point) integration. The helmet is modeled as a shell with S4R elements deformed in plane state of stress, and we utilized the NoPerimSelf option to limit the thickness reduction checks. The non-interpenetration of the materials is satisfied by using the built-in erosion contact algorithm.

The CAD model of the ACH helmet geometry purchased from www.turbosquid.com was stripped of all interior components, and the outer surface was isolated so that it can be modeled as a shell. The removal of the suspension system resulted in a small hole, as depicted in Figs. 3 and 4, to appear at the crown of the helmet which was kept in our simulations. The two points indicated by red dots are kept fixed during the simulations.

3.1 Results for Test Problems

In order to ensure that we are correctly using different options in ABAQUS, we simulated a few impact problems and compared computed results with either experimental findings or other results available in the literature.

3.1.1 Penetration of steel rods into aluminum targets

The first problem we numerically studied corresponds to the experimental work of Forrestal et al. [4] involving the impact at normal incidence of long hemispherical nosed cylindrical C-300 maraging steel rods on to thick 6061-T651 aluminum cylindrical targets. A schematic sketch of the problem is exhibited in Fig. 6 and values of material parameters, taken from the literature [18], are listed in Table A1 wherein values of material parameters of 1100-H12 aluminum are given since we could not find in the open literature values of material parameters for the 6061-T651 aluminum. From the variation of the penetration depth with the impact speed plotted in

Fig.7, it is clear that the computed penetration depth is higher than that found in experiments possibly due to neglecting friction at the penetrator/target interface, and is mesh dependent being higher for the finer mesh. The coarse FE mesh has 195,588 8-node elements with the smallest element's side equaling 0.743 mm, and the fine FE mesh has 673,920 8-node elements with the smallest element side measuring 0.481 mm. The effect of the FE mesh on the computed penetration depth increases with an increase in the impact speed. The computed diameter of the tunnel mouth (surface at the impacted face of the target) equals about 7.1 mm for each one of the four impact speeds, and is the same for the two FE meshes employed. Fringe plots of the effective plastic strain plotted in Fig. 8 for results computed with the fine mesh indicate that the maximum effective plastic strain is nearly uniform along the tunnel surface and equals almost 1. The peak value of the effective plastic strain on the tunnel surface is higher for the impact speed of 450 m/s than that for the other three impact speeds of 760, 960 and 1020 m/s possibly because more elements failed and were deleted for impact speeds of 760, 960 and 1020 m/s than those for the impact speed of 450 m/s.

3.1.2 Impact of a composite laminate

The second test problem we have simulated is the impact of a composite plate that had been experimentally and numerically studied by Sheikh et al. [2]. With values of material properties taken from Soden et al. [3] and listed in Table A2, we analyze the effect of boundary conditions, and the FE mesh. An 18.8 g rigid projectile moving at 512 m/s impacts at normal incidence either a simply supported or a clamped 300 x 300 x 2.4 mm, $[0^o, 90^o]_5$, E-Glass/117-220 composite laminate with the 0^o ply facing the projectile. The projectile is initially 25.6 mm away

from the laminate and it is assumed that none of its kinetic energy is lost due to interaction with the surrounding air. When analyzing the contact problem it is assumed that the projectile mass is concentrated at its center of gravity. At a clamped edge all three components of displacements are prescribed to be zero. For a simply supported edge results were computed for either boundary condition SS1 or SS2 that are listed below.

SS1: $$f_1 = 0, f_2 = 0, u_3 = 0, \ on\ x_1 = 0, L, x_2 = 0, L \tag{20}$$

SS2: $$f_1 = 0, u_2 = 0, u_3 = 0, \ on\ x_1 = 0, L \quad f_2 = 0, u_1 = 0, u_3 = 0, on\ x_2 = 0, L \tag{21}$$

CL: $$u_i = 0, on\ x_1 = 0, L\ and\ x_2 = 0, L \tag{22}$$

Here f_1 and f_2 equal surface tractions in the x_1 and the x_2 directions, respectively. For the three types of boundary conditions, the computed time histories of the projectile's axial velocity as well as that computed by Sheikh et al. [2] are plotted in Fig. 10. These plots suggest that the three boundary conditions give virtually the same time histories of the projectile axial velocity. At any time the presently computed axial velocity differs from that of Sheikh et al. by about 5%. In Fig. 11 we have exhibited time histories of the projectile speed computed with two different FE meshes. The coarse FE mesh has 2,500 elements in the region surrounding the point directly underneath the impactor and the fine FE mesh has 10,000 elements; e.g. see Fig. 12. Unlike for the previous problem analyzed, the two time histories are very close to each other, and to that computed by Sheikh et al.

3.1.3 Impact of composite laminates of different material systems

We now analyze the impact of a clamped laminate for five different material systems, namely, E-glass/117-220, AS4/3501-6, T300/BSL914C, Gevetex/LY556 and Silenka/MY750 with values of material parameters taken from Soden et al. [3] and listed in Table A2. The laminate geometry including the ply lay-up, the projectile mass and the projectile initial speed are the same as those in the problem studied by Sheikh et al. [2]. Time histories of the projectile speed exhibited in Fig. 13 are close to that reported by Sheikh et al. The AS4/3501-6 and T300/BSL914C composite laminates have nearly the same performance under impact loading as judged from the time histories of the projectile speed. Similarly, the Gevetex/LY556 and Silenka/MY750 composite laminates retard the penetrator equally. The deceleration of the penetrator caused by the E-glass/117-220 laminate is between that of the other two composite systems. The specific energies absorbed, computed from the initial and the final kinetic energies of the projectile and the total mass of the laminate, the hole area, and the approximate length of the ejecta are listed in Table 1. The hole is nearly circular and its diameter is taken to equal the average of that in two orthogonal directions. The ejecta length is taken to equal the maximum height of the contiguous deformed region on the back side of the impacted plate; e.g. see Fig. 14.

Table 1. Residual speed, kinetic energy absorbed, and specific kinetic energy absorbed for five composite laminates

Material system	Residual speed (m/s)	Kinetic energy absorbed (J)	Density (kg/m^3)	Specific kinetic energy absorbed (J/kg)	Hole area (mm^2)	Perforation time (ns)	Ejecta length (mm)
E-glass/117-220	473	360	1850	901	343	464	12.88
AS4/3501-6	460	476	1580	1395	408	283	20.88
T300/BSL914C	460	473	1750	1252	487	213	15.26
Gevetex/LY556	481	294	1585	858	340	286	5.35
Silenka/MY750	479	309	1585	903	302	174	12.45

In terms of the specific kinetic energy absorbed, the material system AS4/3501-6 performs better than the other four material systems.

3.1.4 Perforation of circular laminated plates

We now simulate impact tests performed by Lee and Sun [5] in which a 24 mm long and 14.5 mm diameter hardened 4340 steel cylinder impacts at normal incidence a clamped circular composite plate with (diameter, thickness in mm) equal to (43.5, 2), (87, 2) and (43.5, 4); these are referred to as laminates I, II and III, respectively. The ply layup in each laminate is $([0, 90, 45, -45]_s)_n$ where n = 2 and 4, respectively, for 2 and 4 mm thick laminates. The projectile impact speed is varied and its residual speed is recorded. A comparison of the computed and experimental results for the three laminates is shown in Fig. 15a-c. The presently computed ballistic limit is higher than that found by Lee and Sun [5] who used the commercial software

MARC for numerically solving the problem. It is not clear why the two sets of results differ from each other since the two codes solve the same set of governing equations.

3.1.5 Impact of Dyneema laminates

We now simulate the impact at normal incidence of a 0.22 cal. FSP (see Fig. 2) on a clamped thin 362 mm square Dyneema HB80 plate of four different thicknesses; values of some of the parameters for Dyneema and AS2C carbon fibers are listed in Table A3. The experimental value of V_{50} and the computed ballistic limits are listed in Table 2 for the four laminates. These two speeds cannot be directly correlated since they represent different physical effects. The value of V_{50} implies that 50% of the penetrators moving at 387 m/s fully penetrated the composite laminate. DSM provided material properties including elastic and strength parameters but these are not reported here because of the proprietary nature of data. The fracture energy was determined iteratively adjusting its value until the experimental V_{50} and the calculated ballistic limit for Laminate A were within 1% of each other. Subsequently, the fracture energy was held constant for the other three laminates at 225 kJ/m^3. The time histories of different components of energies for the FSP moving at 750 m/s exhibited in Fig. 16 reveal that nearly 35% of the initial K.E. of 310 J is used to plastically deform the projectile, and about 65% of the initial K.E. of the projectile is used to deform the laminate. The ply that first contacts the projectile is referred to as the first ply. Fringe plots of the damage modes exhibited in Figs. 17-20 show significantly more fiber and matrix compressive damage in the first ply and more fiber and matrix tension damage in the last ply. The shear damage appears to be about the same in the first and last ply, see Fig. 21. Computed values of the ballistic limit listed in Table 2 for laminates B, C and D differ from the corresponding experimental values by less than 5%.

Table 2. Experimental V_{50} and computed ballistic limits for four laminates

Laminate	Experimental V_{50} (m/s)	Numerical ballistic limit (m/s)
A	387	390
B	524	540
C	838	840
D	1150	1155

3.2 Impact of Clay Layer

We have also analyzed deformations of 610 x 610 x 140 mm block of clay caused by a 1.043 kg 63.5 mm diameter steel sphere dropped at normal incidence from a height of 2 m. The clay rests on a rigid platform with particles on the four lateral faces constrained from moving in a direction normal to that face. The steel sphere is regarded as rigid since its deformations are miniscule as compared to those of the clay. The time histories of energy components for the clay and the kinetic energy of the projectile are exhibited in Fig. 23. The impactor contacts the clay at t = ~3 ms, reaches the bottom-most position at t = ~ 12 ms when the K.E. of the weight becomes zero and it rebounds upwards from the clay. Nearly 10 J out of the 20 J of the input K.E. of the drop weight is used to plastically deform the clay. At t = ~30 ms the K.E. of the drop weight equals 4 J, and the strain energy of elastic deformations of the clay is about 1.5 J. Since the effect of gravity has been neglected, the drop weight upon rebounding from the clay will continue moving upwards with a steady speed. The strain and the kinetic energies of the clay will continue interchanging between each other as is the case for a pendulum undergoing a periodic motion till the kinetic energy has been dissipated due to either plastic deformations or frictional/viscous (not considered here) forces in the clay.

We have exhibited in Figs. 24-26 fringe plots of the effective plastic strain, the von-Mises stress, and the pressure in the clay crater at seven different times. One can also deduce from these figures the growth of the crater with the passage of time. The diameter of the crater mouth and the crater depth, respectively, equal 67 and 21.5 mm.

3.3 Impact of Composite Plate with Clay Backing

We study the impact of a 152 x 152 x 2 mm $[(0, 90, 45,-45)_s]_2$ AS4/3501-6 composite plate with and without clay backing and impacted at normal incidence by a rigid cylinder moving at 50 m/s which is just below the computed ballistic limit of the laminate with the laminate properties taken from Lee [5] and Chan [19]. The plate edges are constrained from moving in a direction normal to that edge, and particles on the clay surface furthest from the impact face are held stationary. The computed time histories of the transverse displacement of the center of the laminate surface away from the impacted face with and without the clay backing are exhibited in Fig. 27. These plots suggest that the clay backing reduces the maximum laminate deflection from 7.1 mm to 5 mm. Furthermore, the peak deflection occurs about 5μs earlier with the clay backing as compared to that without the clay backing. The depth and the maximum diameter of the crater formed in the clay equal 30 mm and 85 mm, respectively. In Fig. 28 we have plotted time histories of the deflection of the center of the bottom surface of the laminate and the corresponding clay particle. Because of the initial small gap between the laminate and the clay, the motion of the clay particle is delayed relative to that of the laminate particle. Shifting the red curve to the left by about 5 μs suggests that the laminate center loses contact with the clay at about 30 μs. Because of plastic deformations the clay particle continues to move down but the laminate vibrates about the initial flat configuration.

3.4 Front Impact of Helmet/Headform

Transient deformations of a laminated composite ACH with Dyneema as the reinforcing fibers and sitting on a clay filled headform have been studied for 0.22 cal. FSP impacting the helmet at speeds equal to nearly 0.6, 0.9, 1.0 and 1.2 times the computed ballistic limit, 840 m/s, of Dyneema flat laminate C. The helmet thickness and the lay-up of plies is the same as that of laminate C. The ply on the outside of the helmet that first contacts the projectile is referred to as the first ply and the last ply is closest to the clay with the mid ply being halfway through the thickness.

The time histories of different components of energies for the FSP moving at 750 m/s exhibited in Fig. 29 reveal that nearly 39% of the initial K.E. of 310 J is used to plastically deform the projectile, and about 50% of the initial K.E. of the projectile is used to deform the helmet. These energy components strongly depend upon the projectile and the helmet materials since a projectile will go through a soft material without undergoing significant plastic deformations. For the problem being studied, the remaining 11% or 34J of the initial K.E. of the projectile is used to deform the clay, and increase the strain and the kinetic energies of the helmet. Of these three the energy required to deform the clay is miniscule, totaling a maximum of 0.75 J. The K.E. of the helmet 200 μs after impact equals about 20 J signifying that helmet particles have noticeable speeds.

For the four impact speeds considered, we have displayed in Fig. 34 fringe plots of the damage variables associated with fiber tension in the first, the mid and the last ply. It is evident that the impact speed does not influence much the distribution of the damage due to fiber tension in the three plies except that the size of the damaged area in each ply increases with an increase in the impact speed. In each one of the three plies, the damaged zones are not contiguous. Similar

plots for the fiber compression damage mode reveal that for each one of the four impact speeds studied the damage occurs only in the first ply and is concentrated in a very small area around the point of impact. The qualitative nature of the damage due to matrix tension is unaffected by the impact speed and the damaged area is most in the first ply and least in the last ply. For a given impact speed, the damaged area due to fiber compression is more than that due to fiber tension both in the first and in the last plies.

In order to see how deformations of the helmet correlate with those of a flat laminate, we have plotted in Fig. 39 time histories of the pressure at the initial point of contact for impact speeds of 750 m/s and 835 m/s. For each impact speed, the peak pressure for the plate is higher than that for the helmet, and its occurrence in the plate is delayed by a fraction of a μs. For an increase in the impact speed of 11%, the peak pressures for the laminate and the helmet increase by 23% and 7%, respectively, indicating thereby the effect of the helmet curvature on the contact pressure. For impact at the ballistic limit of 835 m/s the plate experiences 50% larger peak pressure than the helmet. However, at the lower impact speed of 750 m/s, the peak pressure in the flat plate is nearly 25% more than that in the helmet. Because of helmet's curvature, the peak pressures in the helmet and the flat laminate cannot be easily correlated with the peak stresses developed in the two structures. We have also shown a comparison of the penetration depth for the helmet and flat plate in Fig. 39.

To gain an understanding of the injury likely to occur after impact by a 0.22 caliber FSP moving at 750 m/s we study the pressure and energies in the clay as well as stresses developed in the last ply of the helmet. We have displayed in Fig. 41 time histories of energies in the clay. Contour plots of the pressure in the clay region near the impact point, displayed in Fig. 42, show a peak pressure of ~23 MPa and a crater of volume ~2.1 cm^3. Time histories of pressure for four

different elements in the back ply of the helmet as well as the location of these elements are shown in Fig. 43. We have also displayed contour plots of σ_{11}, σ_{22}, and σ_{12} in the last ply of the helmet at 10 different times in Figs. 44-46.

As our study of the helmet and the headform interaction has so far been limited to impact speeds equal to or below the ballistic limit, we conclude our results by considering an impact speed above the ballistic limit. Increasing the impact speed to 1000 m/s we see in Fig. 47 that ~10% of the kinetic energy remains in the system once the projectile ejects out of the helmet. In Fig. 48a-m we have displayed deformed configurations of the helmet and the clay. A scrutiny of these plots suggests that the bullet has penetrated through the helmet in the first 20 μs after impact. Plastic deformations of the FSP result in mushrooming of its head, and the FSP begins to rotate at t = ~ 40 μs. The FSP causes extensive deformations of the clay; however, not much energy is consumed since the clay is very soft.

4. Conclusions

We have used the commercial finite element software, ABAQUS, to analyze transient deformations of a laminated composite helmet supported on a clay filled headform caused by the impact of a 0.22 cal. FSP on the front face of the helmet. The headform is modeled as rigid, the clay as elasto-plastic with strain hardening, the FSP as elasto-viscoplastic and the composite helmet as linear elastic. We have used the software first to analyze several impact problems and compared the computed results with those available in the literature. Subsequently, transient deformations of the helmet have been studied. It is found that the qualitative distribution of the damage due to fiber tension in the first, the mid and the last ply is the same for the four impact speeds which equal 0.6, 0.8, 1.0 and 1.2 times the ballistic limit of the flat composite laminate whose material and the lay-up are the same as that of the helmet. The damage due to fiber compression is essentially concentrated in a small area around the impact point and occurs only in the first ply. The damages due to matrix tension and matrix compression occur at different locations in each ply. For each impact speed, the damaged area in a ply due to the matrix failing in compression is more than that due to the matrix failing in tension. For the composite laminate helmet studied and for the highest impact speed considered, nearly 48 % and 39 % of the initial kinetic energy of the projectile is dissipated due to the composite and the projectile failure, respectively. With an increase in the impact speed of 11%, the peak pressure at the initial point of contact increases by 23% for the flat laminate and by 7% for the helmet. Also the peak pressure in the flat laminate cannot be easily correlated with that in the helmet.

References

1. *ABAQUS version 6.8 Documentation*. SIMULIA. Web.4 Sep 2009. <http://www.esm.vt.edu/v6.8/>.

2. Sheikh, A. H., P. H. Bull, and J. A. Kepler. "Behaviour of Multiple Composite Plates Subjected to Ballistic Impact." *Composite Science and Technology* 69 (2009): 704-710.

3. Soden, P. D., M. J. Hinton, and A. S. Kaddour. "Lamina Properties, Lay-Up Configurations and Loading Conditions for a Range of Fibre-Reinforced Composite Laminates." *Composite Science and Technology* 58.7 (1998): 1011-1022.

4. Forrestal, M. J., K Okajima, and V K Luk. "Penetration of Aluminum Targets with Rigid Long Rods." *Journal of Applied Mechanics* 55 (1988):755.

5. Lee, S., and C. Sun. "Dynamic Penetration of Graphite/Epoxy Laminates Impacted by a Blunt-Ended Projectile."*Composites Science and Technology* 49 (1993): 369-380.

6. http://www.pointblankarmor.com/NewPDFs/NIJ-0101%2006.pdf , page 38.

7. Munusamy, R. and D. Barton. "Behaviour of Roma Plastilina upon Blunt Projectile Impact." *Dymat International Conferences* 1 (2009): 749.

8. Aare, M., and S. Kleiven. "Evaluation of Head Response to Ballistic Helmet Impacts using The Finite Element Method. "*International Journal of Impact Engineering* 34 (2007): 596-608.

9. Aziz, M.R., R. Othman, R. Ahmad, and A.R. Zamri. "Finite Element Analysis of Composite Ballistic Helmet Subjected to High Velocity Impact." (2008)

10. MIL-DTL-46593 B (MR). (11 August 2008).

11. Yang, J., and J. Dai. "Simulation-Based Assessment of Rear Effect to Ballistic Helmet Impact." *Computer-Aided Design and Applications* (2010)

12. "NIJ Standard for Ballistic Helmet." *U.S. Department of Justice-National Institute of Justice* (1981)

13. Grujicic, M., W.C. Bell, B. Pandurangan, and P.S. Glomski. "Fluid/Structure Interaction Computational Investigation of Blast-Wave Mitigation Efficacy of the Advanced Combat Helmet." *ASM International* (2010)

14. Ahn, J., K. Nguyen, Y. Park, J. Kweon, and J. Choi. "A Numerical Study of the High-Velocity Impact Response of a Composite Laminate using LS-DYNA." *International Journal of Aeronautical and Space Science* 11 (2010): 221-226.

15. HPW-TP-0401.01B. (October 1995).

16. J. van Hoof, D.S. Cronin, M.J. Worswick, K.V. Williams, D. Nandlall. "Numerical Head and Composite Helmet Models to Predict Blunt Trauma." *19th International Symposium of Ballistics* (2001): 921-928.

17. J. van Hoof, M.J. van der Jagt-Deutekom, M.J. Worswick, P.V. Straznicky, K.V. Williams. "Experimental and Numerical Analysis of the Ballistic Impact Response of Composite Helmet Materials." *International Symposium of Ballistics* (1999)

18. Li, W. and W. Gao. "Some Aspects on 3D Numerical Modeling of High Velocity Impact of Particles in Cold Spraying by Explicit Finite Element Analysis." *Applied Surface Science* 255 (2009): 7878-7892

19. Chan, S., Z. Fawaz, K. Behdinan, and R. Amid. "Ballistic Limit Prediction using a Numerical Model with Progressive Damage Capability." *Composite Structures* 77 (2007): 466-474

20. Moyre, S., P. Hine, R. Duckett, D. Carr, and I. Ward. "A Comparison of the Properties of Hot Compacted Gel-spun Polyethylene Fibre Composites with Conventional Gel-spun Polyethylene Fibre Composites." *Composites: Part A* 30 (1999): 649-660.

21. Bir, C. "The Evaluation of Blunt Ballistic Impact of the Thorax." *Dissertation: Wayne State University* (2000): 1-163.

22. Chen, J., F. Allahdadi, and T. Carney. " High-Velocity Impact of Graphite/Epoxy Composite Laminates." *Composite Science and Technology* 57 (1997): 1369-1379.

23. Abrate, S. "Impact on Laminated Composite Materials." *Applied Mechanics Reviews* 44 (1991): 155-190.

24. Lapczyk, I. and J. Hurtado. "Progressive Damage Modeling in Fiber-Reinforced Materials." *Composites: Part A* 38 (2007): 2333-2341.

25. Ganesh, V. and N. Naik. "Some Strength Studies on FPR Laminates." *Composite Structures* 24 (1993): 51-58.

26. Batra, R and X. Chen. "Effect of Frictional Force and Nose Shape on Axisymmetric Deformations of a Thick Thermoviscoplastic Target." *Acta Mechanica* 106 (1994): 87-105.

26. Chen, X. and R. Batra. "Deep Penetration of Thick Thermoviscoplastic Targets by Rigid Long Rods." *Computers & Structures* 54 (1995): 655-670.

27. Advanced Material Damage Models for Numerical Simulation Codes; Final Report. *Century Dynamics* (2003).

28. Advanced Material Models for Hypervelocity Impact Simulations; Final Report. *Century Dynamics* (1999).

29. Peijs, T., M. Jacobs, and P. Lemstra. "High Performance Polyethylene Fibers." *Comprehensive Composite Materials* 1 (2000): 263-301.

30. Wu, H. and F. Chang. "Transient Dynamic Analysis of Laminated Composite Plates Subjected to Transverse Impact." *Computers & Structures* 31 (1989): 453-466.

31. Schwer, L. "Aluminum Plate Perforations: A Comparative Case Study using Lagrange with Erosion, Multi-Material ALE, and Smooth Particle Hydrodynamics." *7th European LS-DYNA Conference* (2009)

32. Yen, C. "Ballistic Impact of Composite Materials." *7th International LS-DYNA Users Conference*

33. "Dyneema high-strength, high-modulus polyethylene fiber: Fact Sheet." http://www.dyneema.com/en_US/public/dyneema/downloads/Comprehensive_factsheet_UHMWPE.pdf (2008)

34. "HexTow Continuous Carbon Fiber Products." http://www.hexcel.com/Resources/Cont-Carbon-Fiber-Data-Sheets

6 Figures

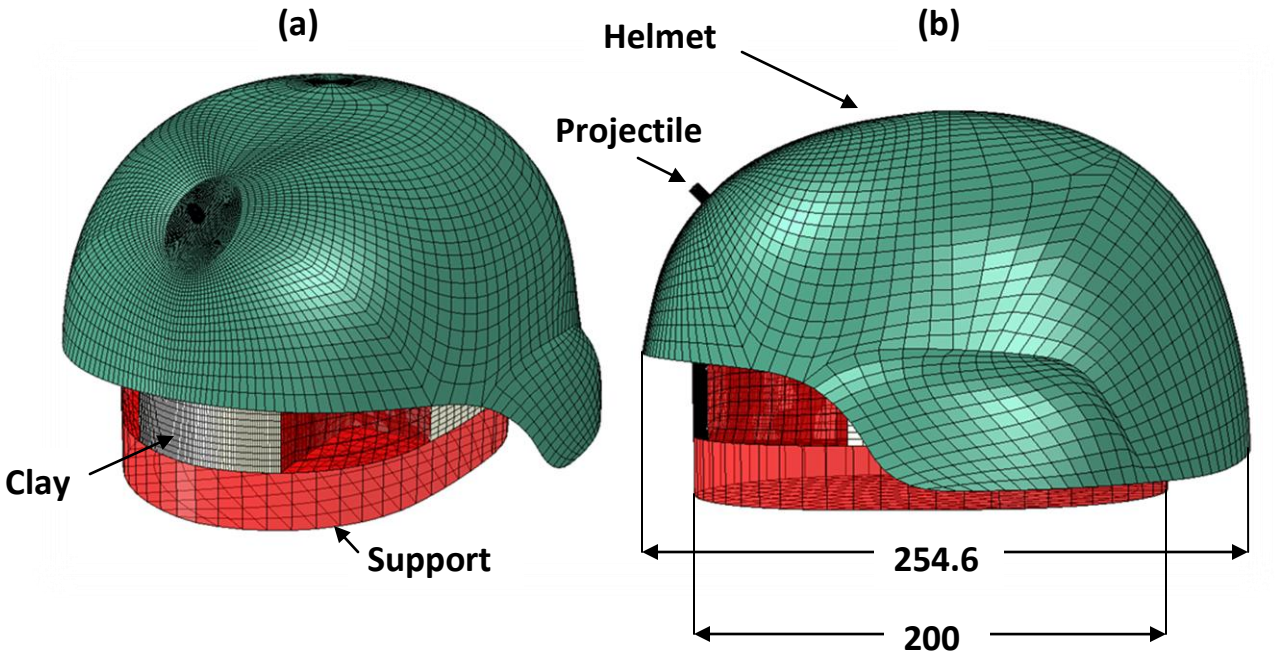

Figure 1. Configuration of an ACH (green) mounted on a clay-filled headform (red and tan); (a) isometric view; (b) side view; dimensions are in mm.

(a)

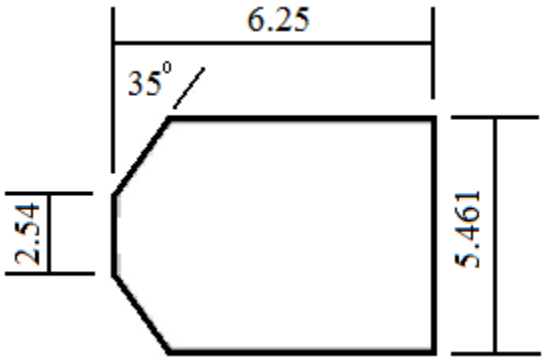

(b)

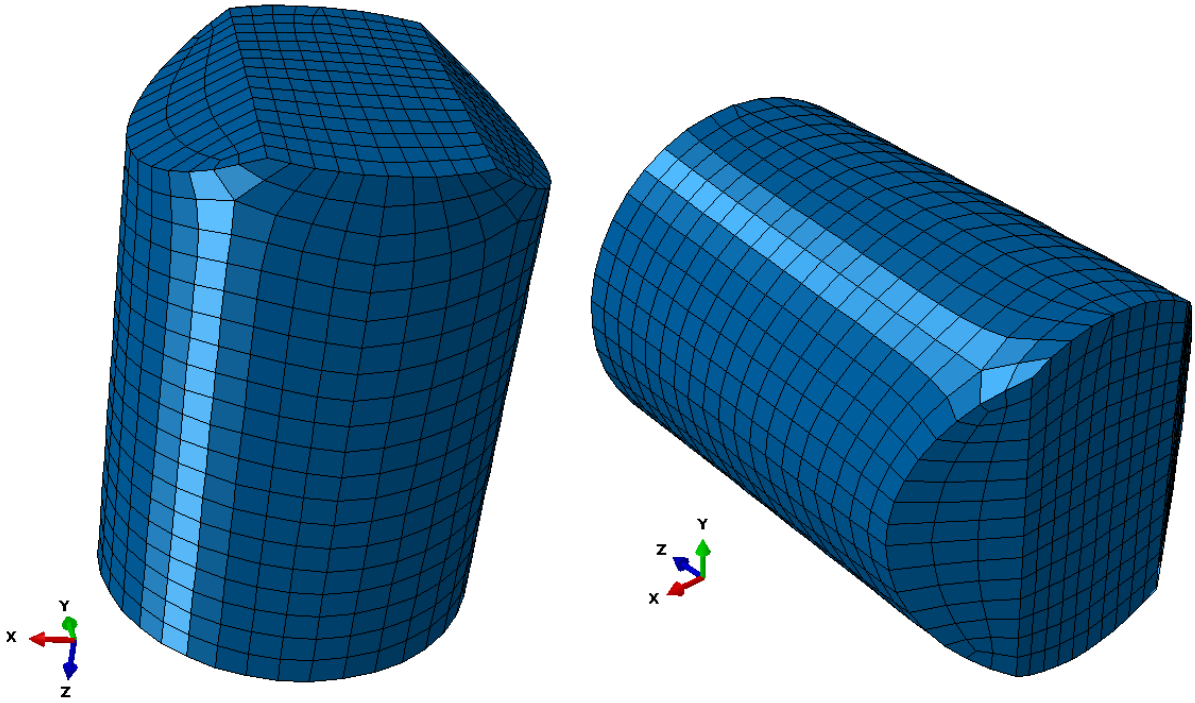

Figure 2. (a) Schematic sketch of the FSP with dimensions in mm; (b) discretization of the 0.22 caliber FSP into finite elements. The FSP's initial velocity is in negative z-direction.

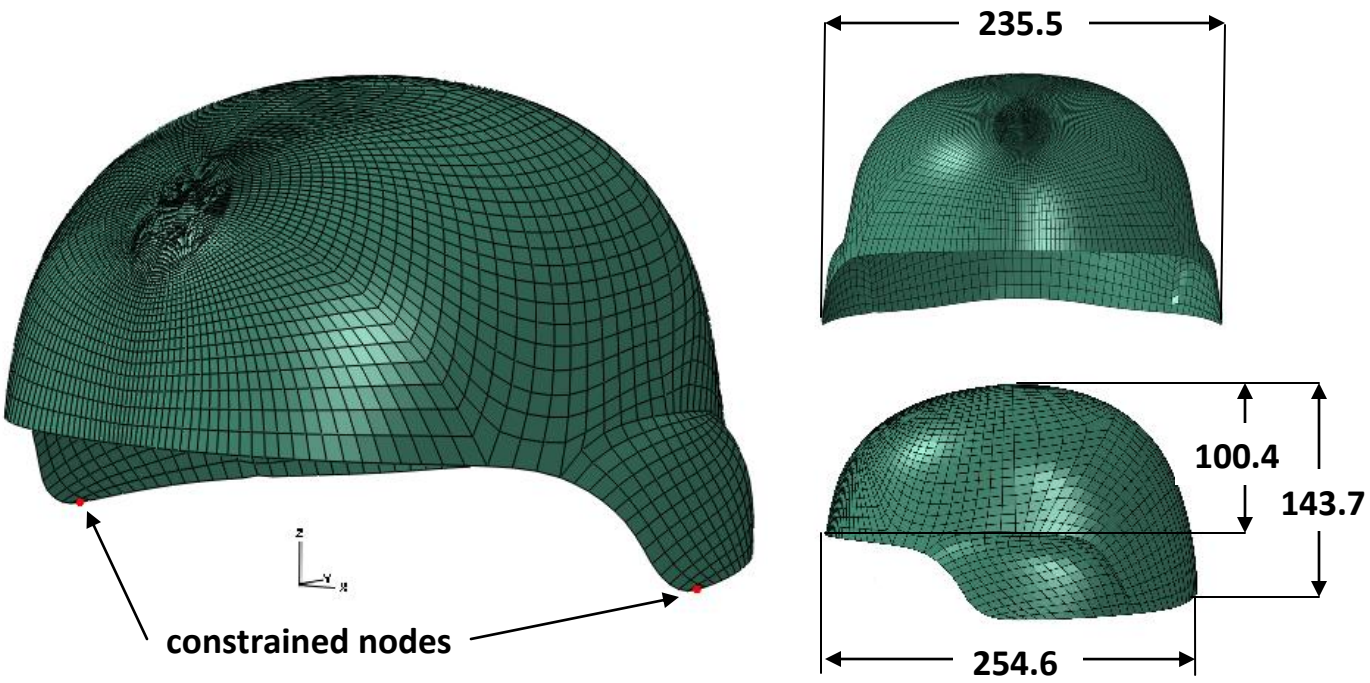

Figure 3. Three views of a shell model of a helmet with the FE mesh; dimensions are in mm. The bounding surfaces of the helmet are traction free except for the two nodes marked in red which are constrained from moving in all three directions.

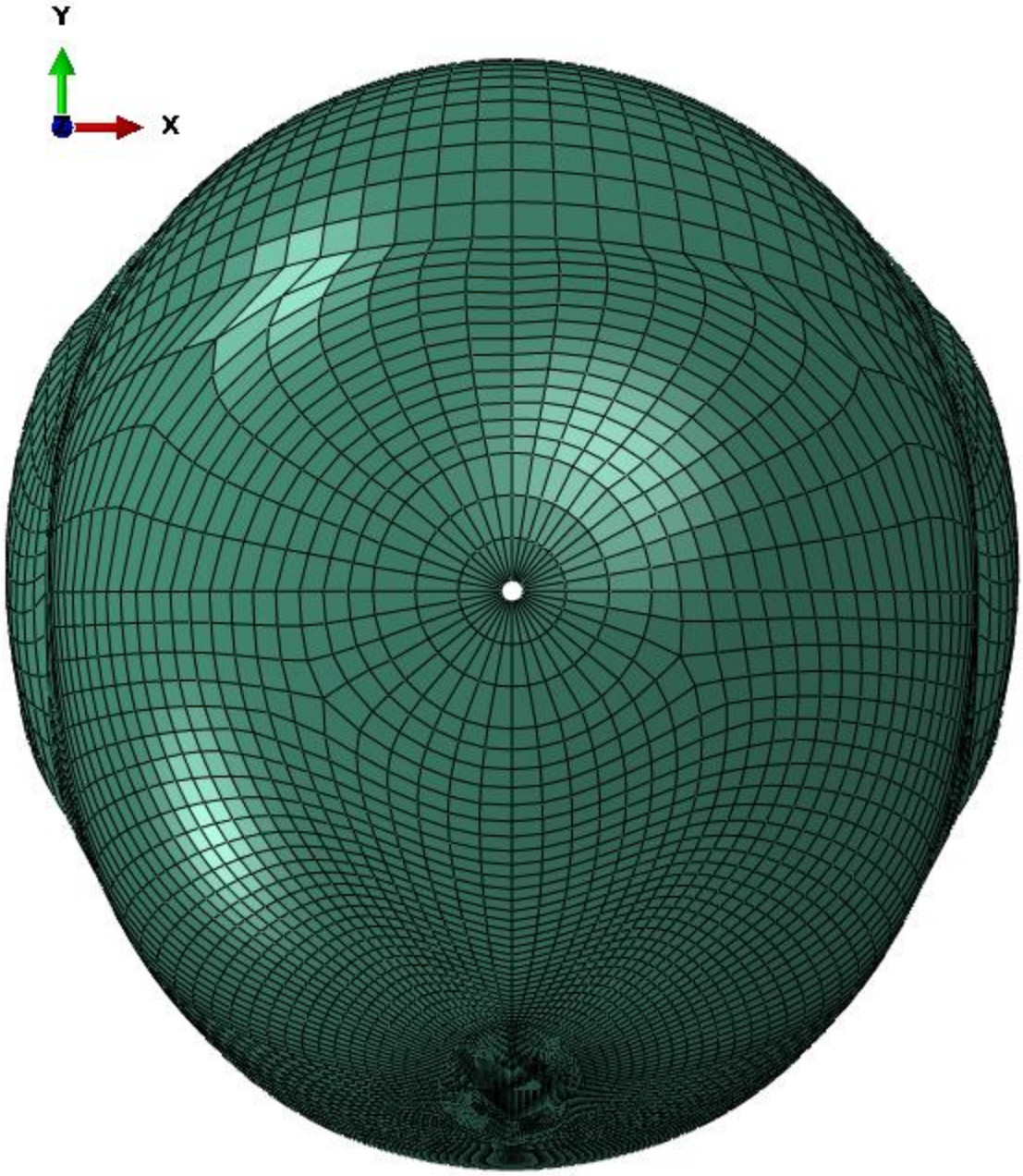

Figure 4. Top view of the helmet showing the hole at the helmet crown.

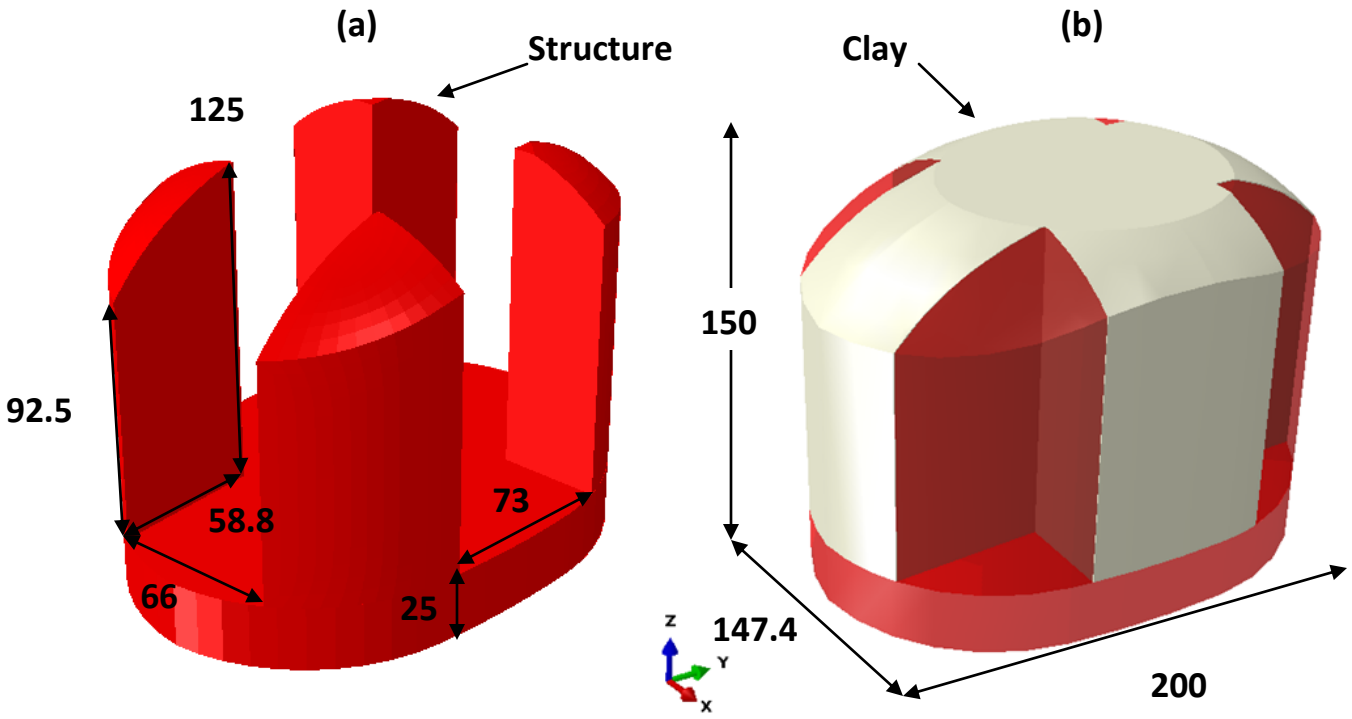

Figure 5. The oval headform geometry; (a) rigid frame, and (b) clay with dimensions in mm. The rigid frame is held at rest during the simulations.

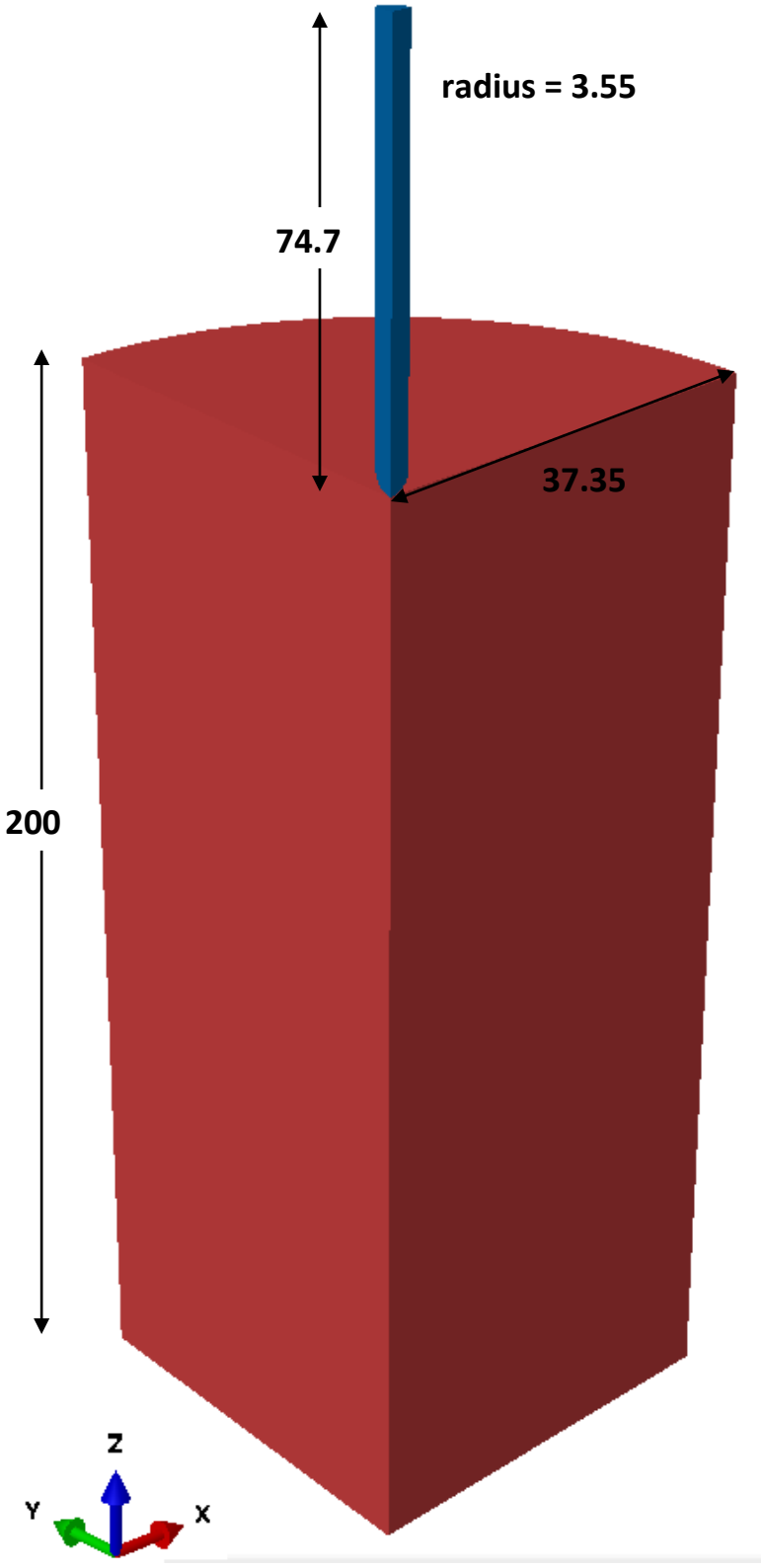

Figure 6. Initial configuration of the impact problem studied by Forrestal et al.; projectile's initial velocity is in –z direction, the target is traction free on all exterior surfaces.

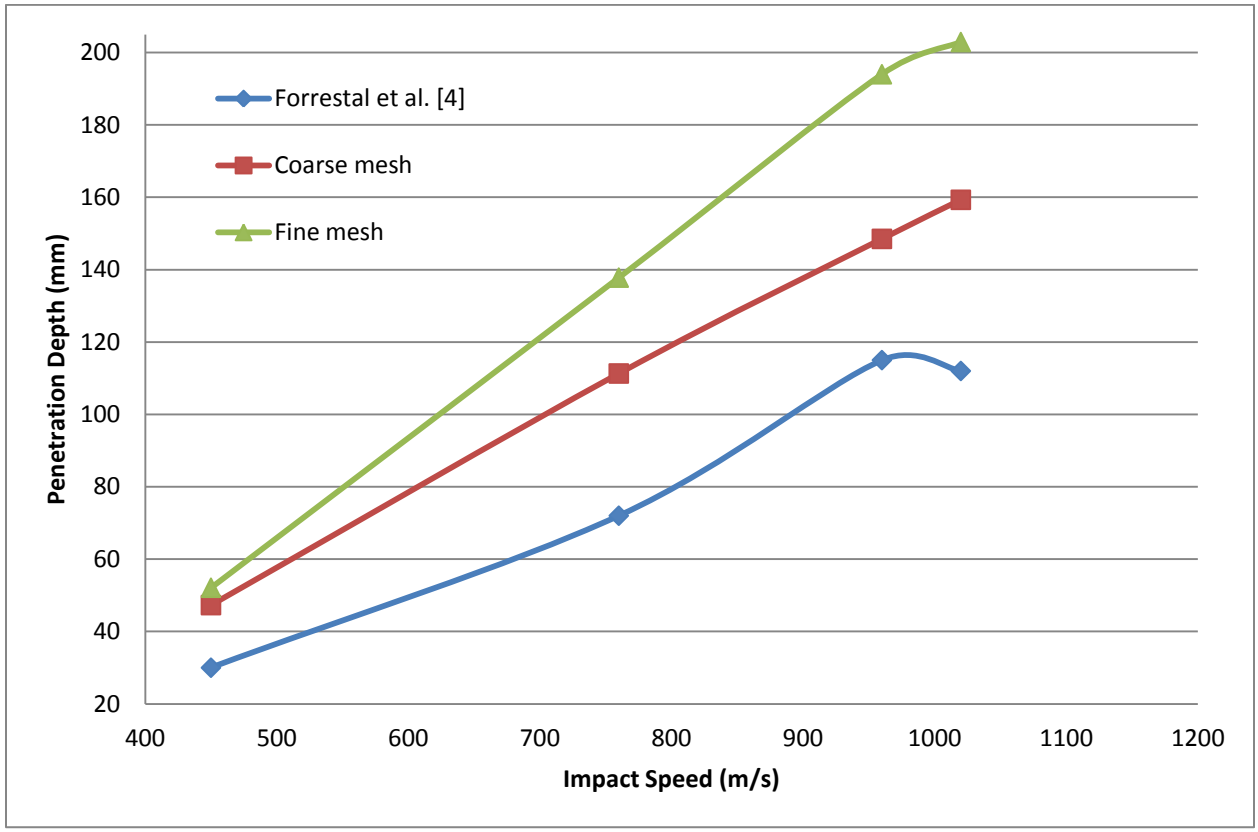

Figure 7. Comparison of computed and experimental [4] penetration depths for a steel rod impacting at normal incidence a thick aluminum target.

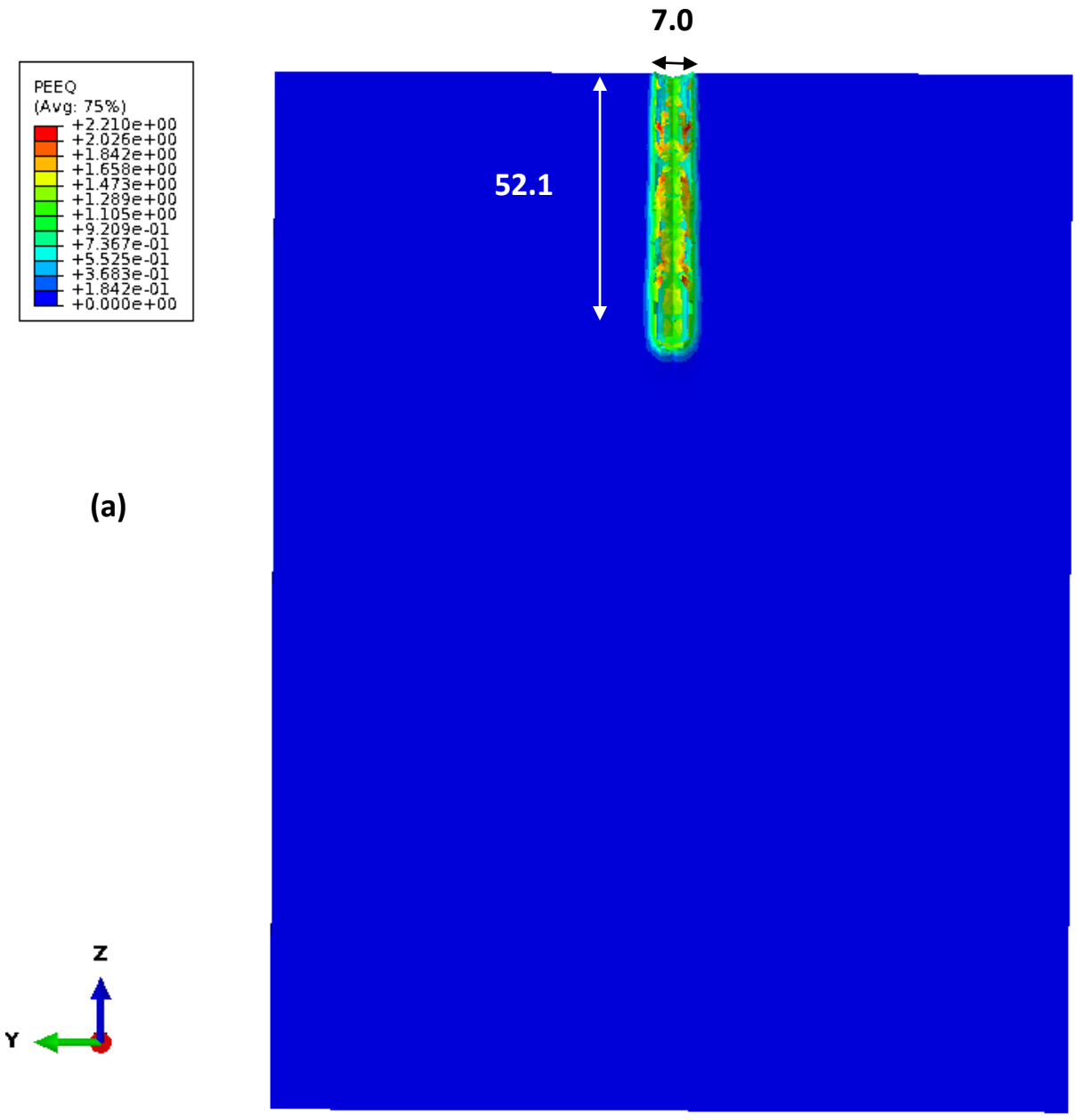
PEEQ
(Avg: 75%)
+2.210e+00
+2.026e+00
+1.842e+00
+1.658e+00
+1.473e+00
+1.289e+00
+1.105e+00
+9.209e-01
+7.367e-01
+5.525e-01
+3.683e-01
+1.842e-01
+0.000e+00
7.0
52.1
Z
Y

(a)

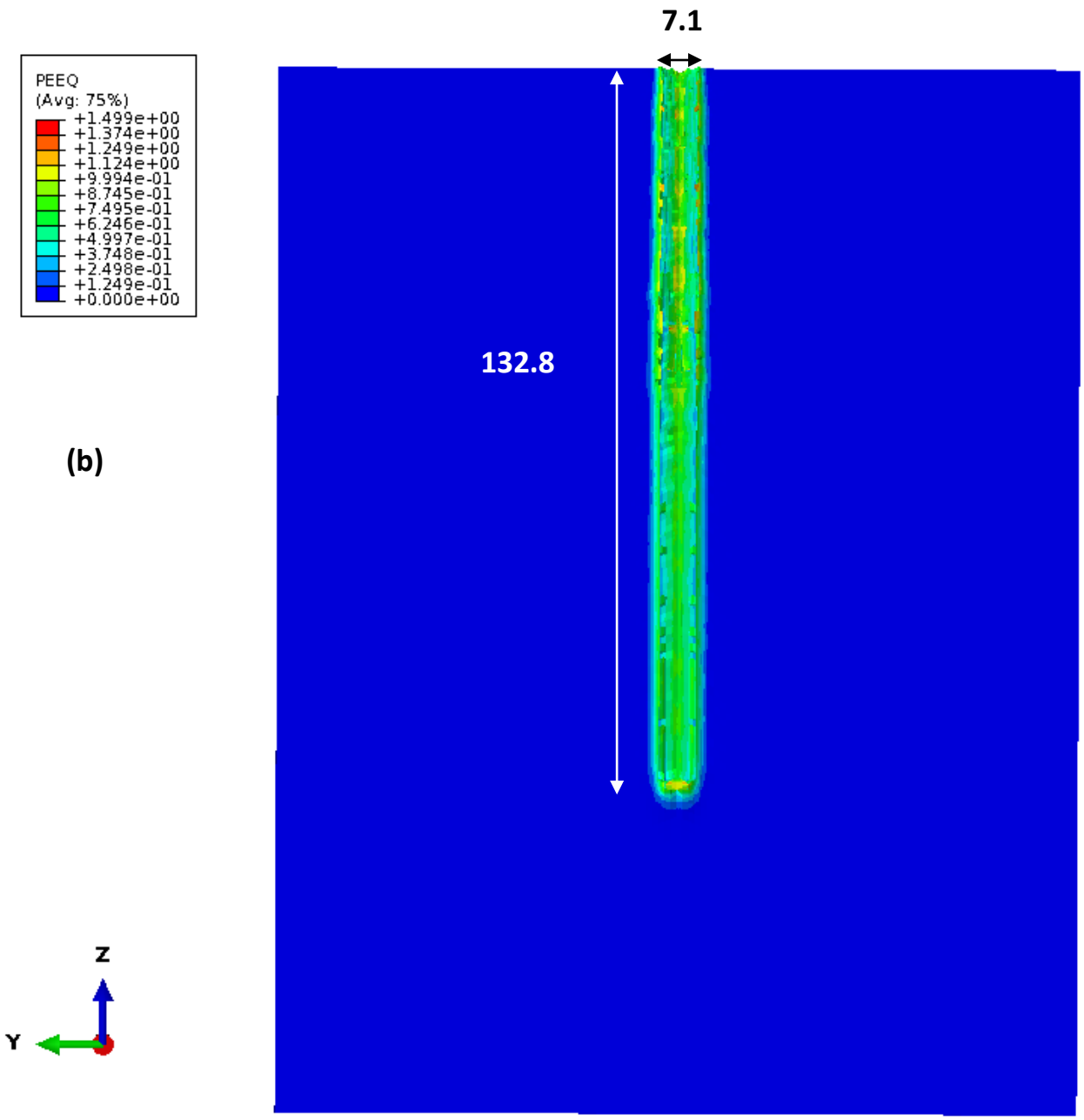
PEEQ
(Avg: 75%)
+1.499e+00
+1.374e+00
+1.249e+00
+1.124e+00
+9.994e-01
+8.745e-01
+7.495e-01
+6.246e-01
+4.997e-01
+3.748e-01
+2.498e-01
+1.249e-01
+0.000e+00
7.1
132.8
(b)
Z
Y

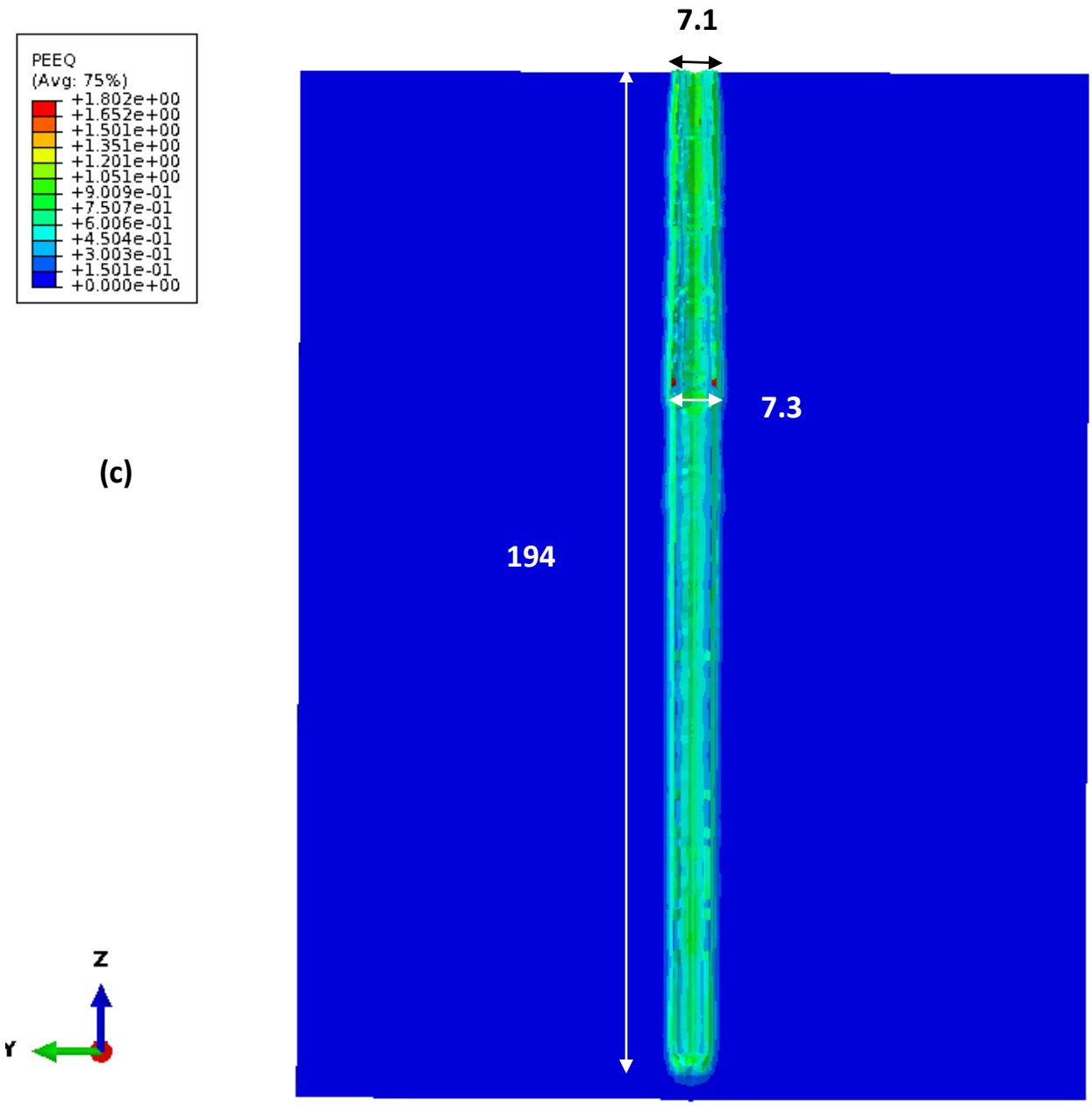
PEEQ
(Avg: 75%)
+1.802e+00
+1.652e+00
+1.501e+00
+1.351e+00
+1.201e+00
+1.051e+00
+9.009e-01
+7.507e-01
+6.006e-01
+4.504e-01
+3.003e-01
+1.501e-01
+0.000e+00
7.1
7.3
194
(c)
Z
Y

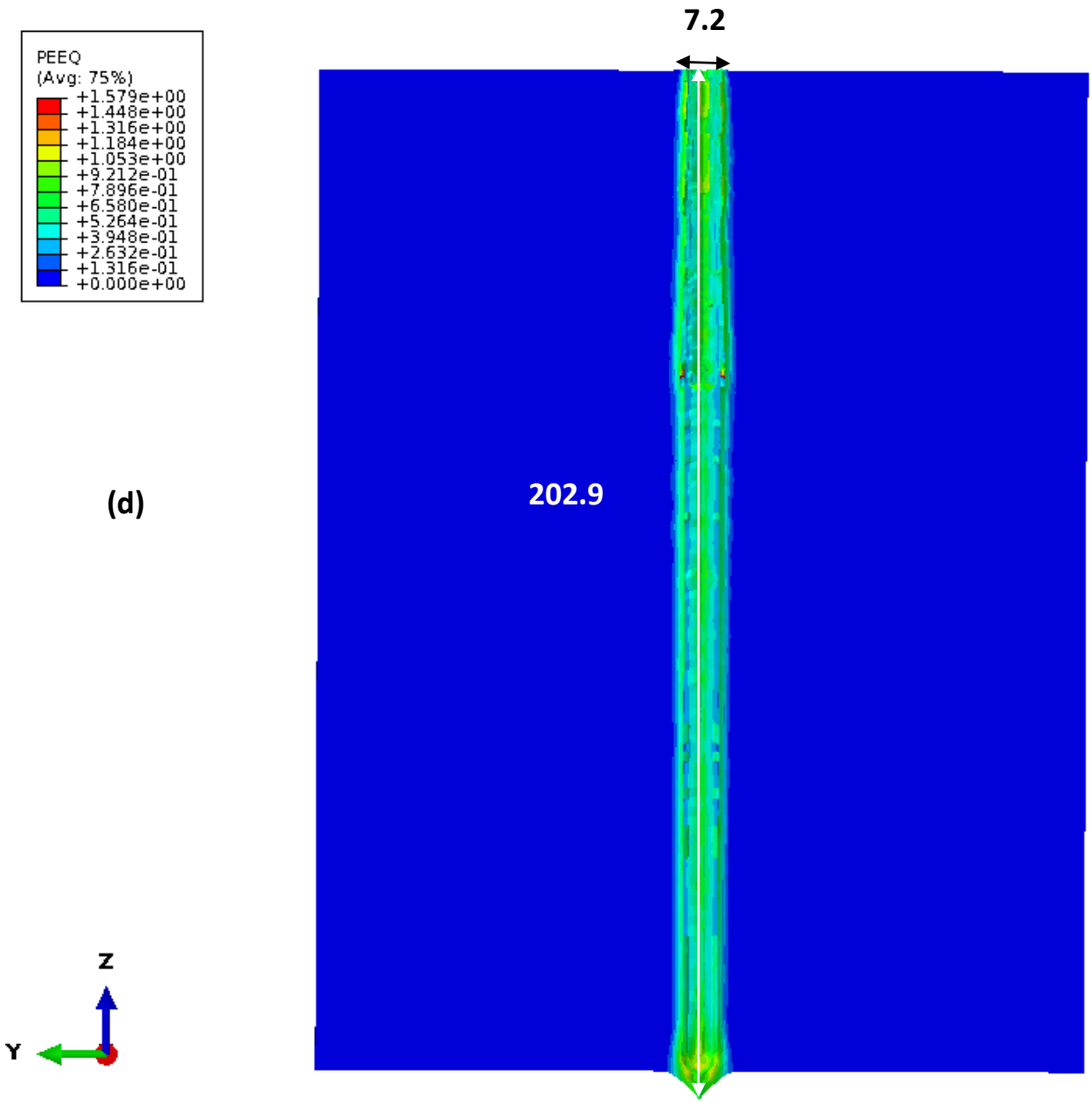

Figure 8. Contour plots of the equivalent plastic strain obtained using the fine mesh to study Forrestal et al.'s penetration tests for impact speeds of 450 (a), 760 (b), 960 (c), and 1020 m/s (d); dimensions in mm.

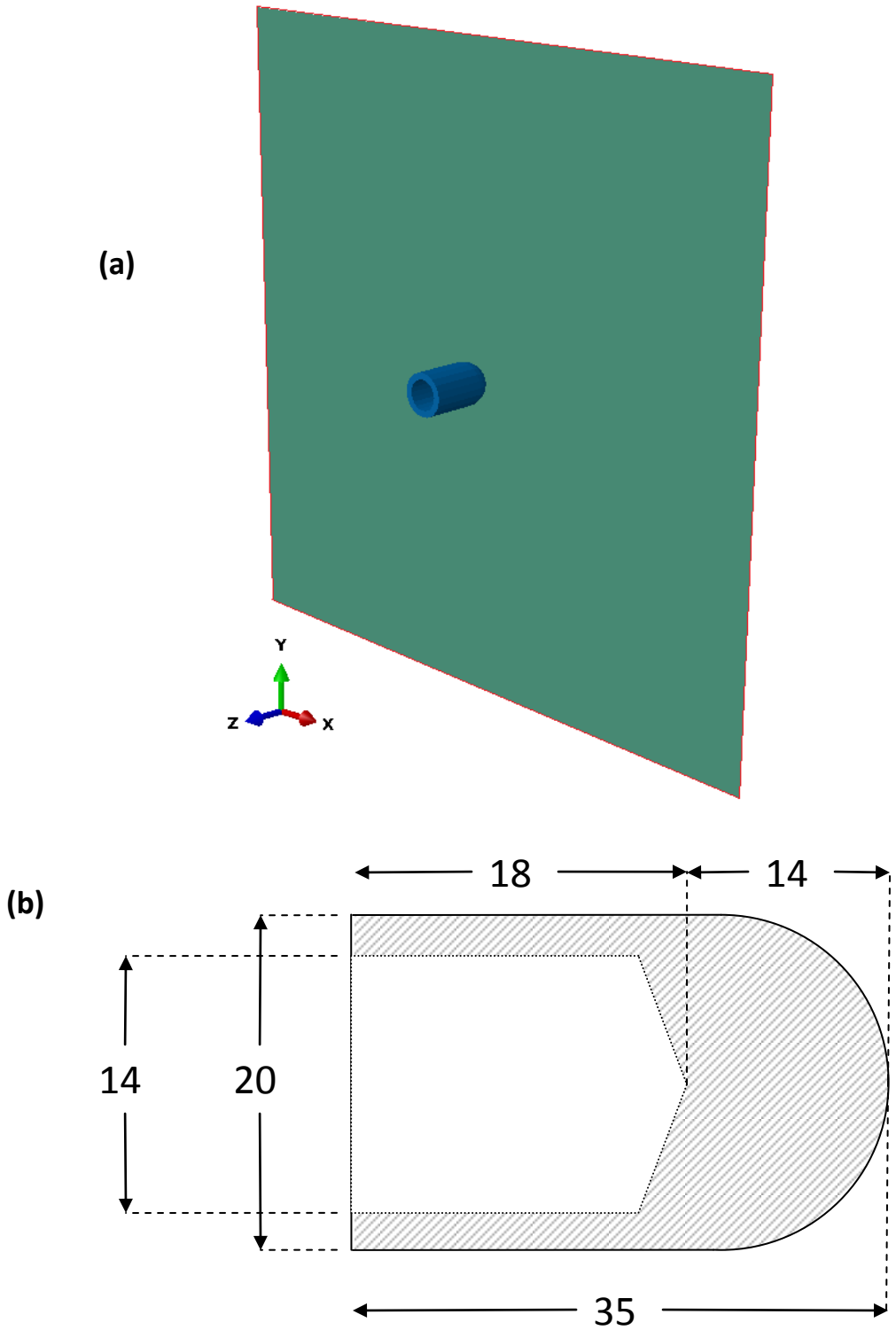

Figure 9. (a) Initial configuration of the impact problem studied by Sheikh et al. [2]; edges where boundary conditions are applied are shown in red; the projectile initial velocity is in the negative z-direction. (b) Schematic sketch of the projectile used in Sheikh et al.'s work [2]; all dimensions are in mm.

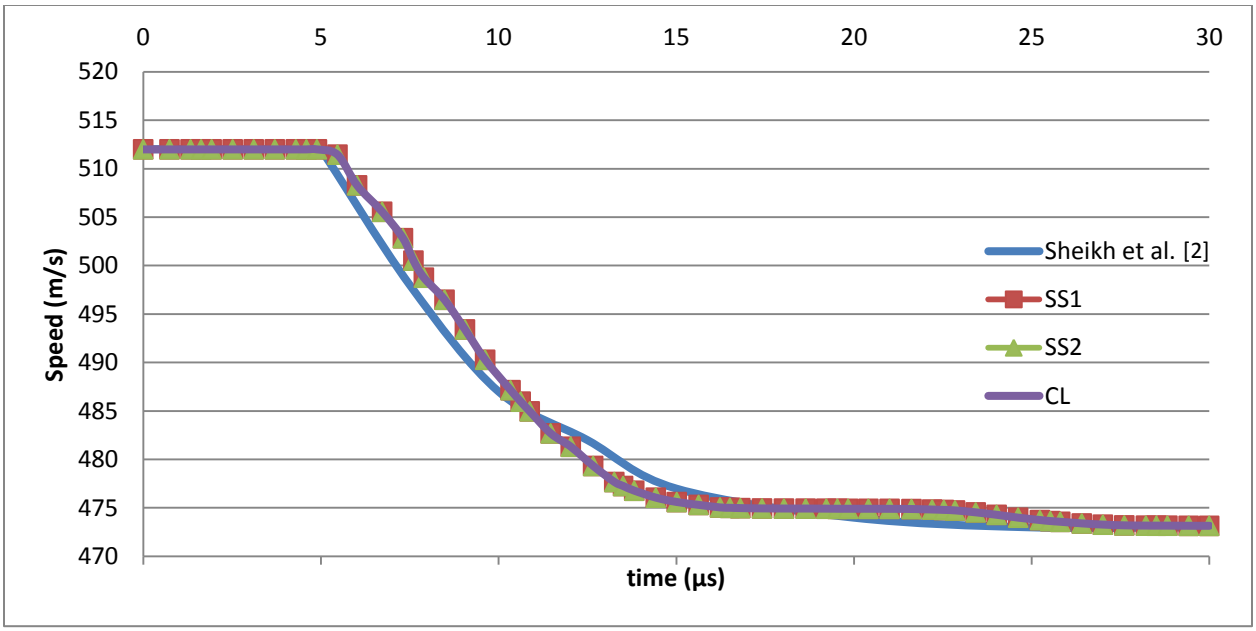

Figure 10. Computed time histories of the projectile speed for three types of boundary conditions applied at the edges of the composite laminate and that reported in [2].

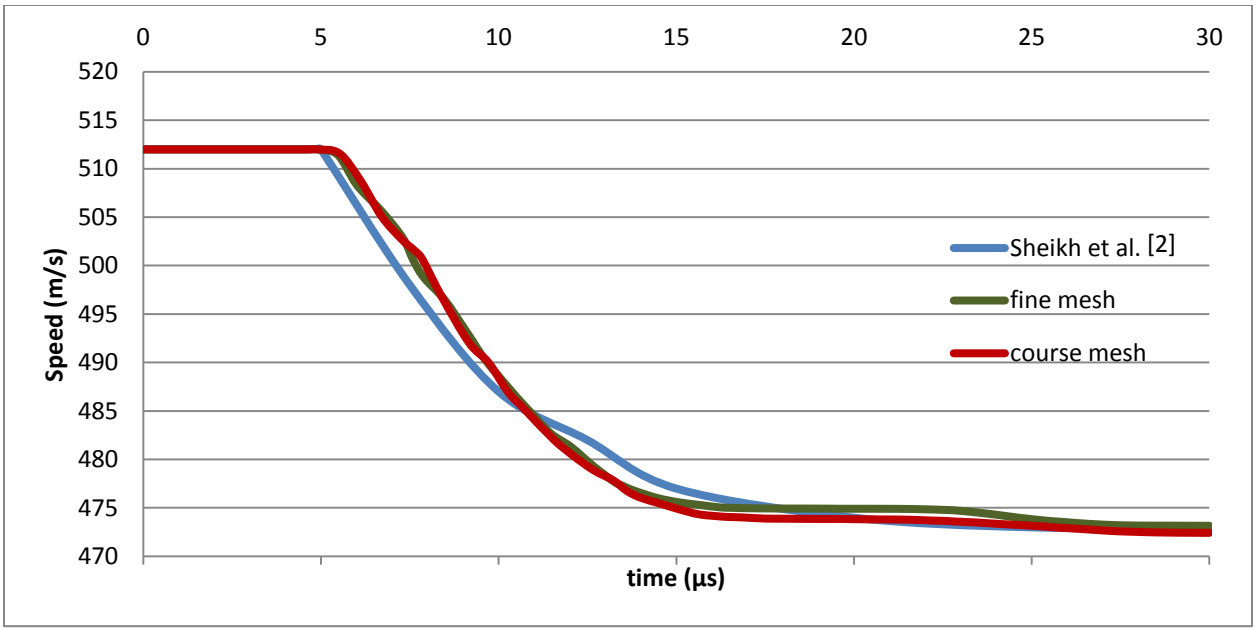

Figure 11. Time histories of the projectile speed for the two FE meshes used to study the impact problem previously analyzed by Sheikh et al. [2].

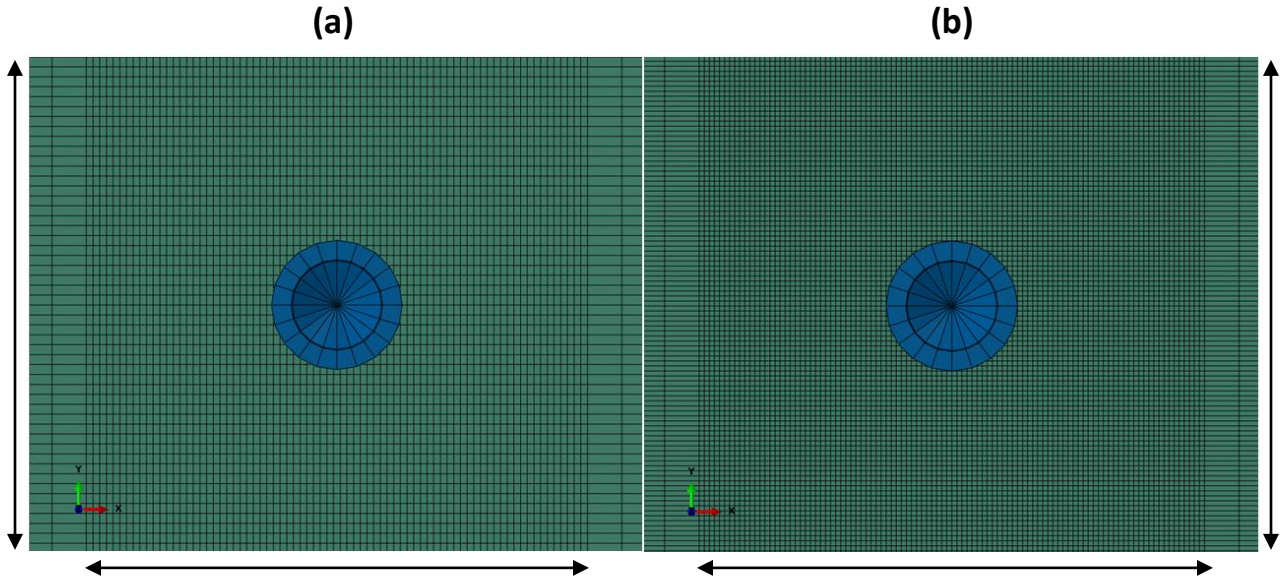

Figure 12. Visual comparison of the finite element meshes used to analyze the impact problem studied by Sheikh et al. [2]; the coarse mesh (a) has 2500 elements in the area near impact while the fine mesh (b) has 10000 elements. The rear of the projectile is shown in blue.

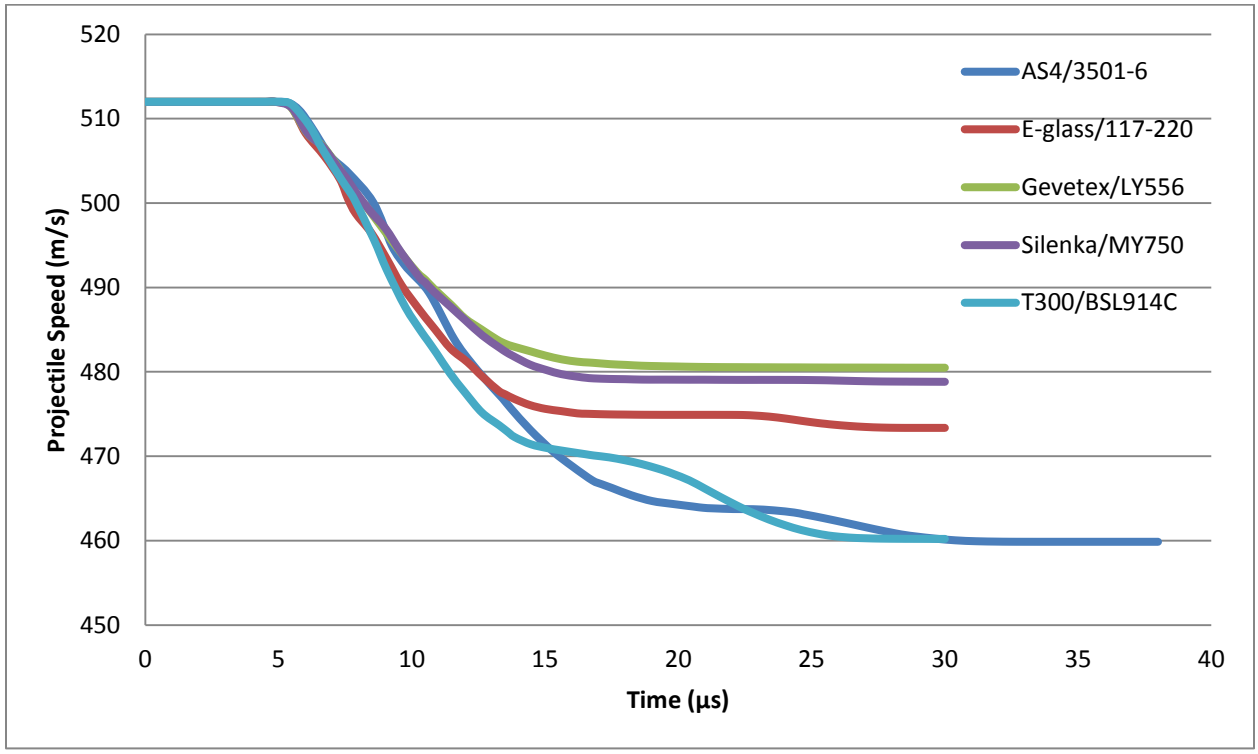

Figure 13. Time histories of the projectile speed for geometrically identical laminates of five material systems.

(a)

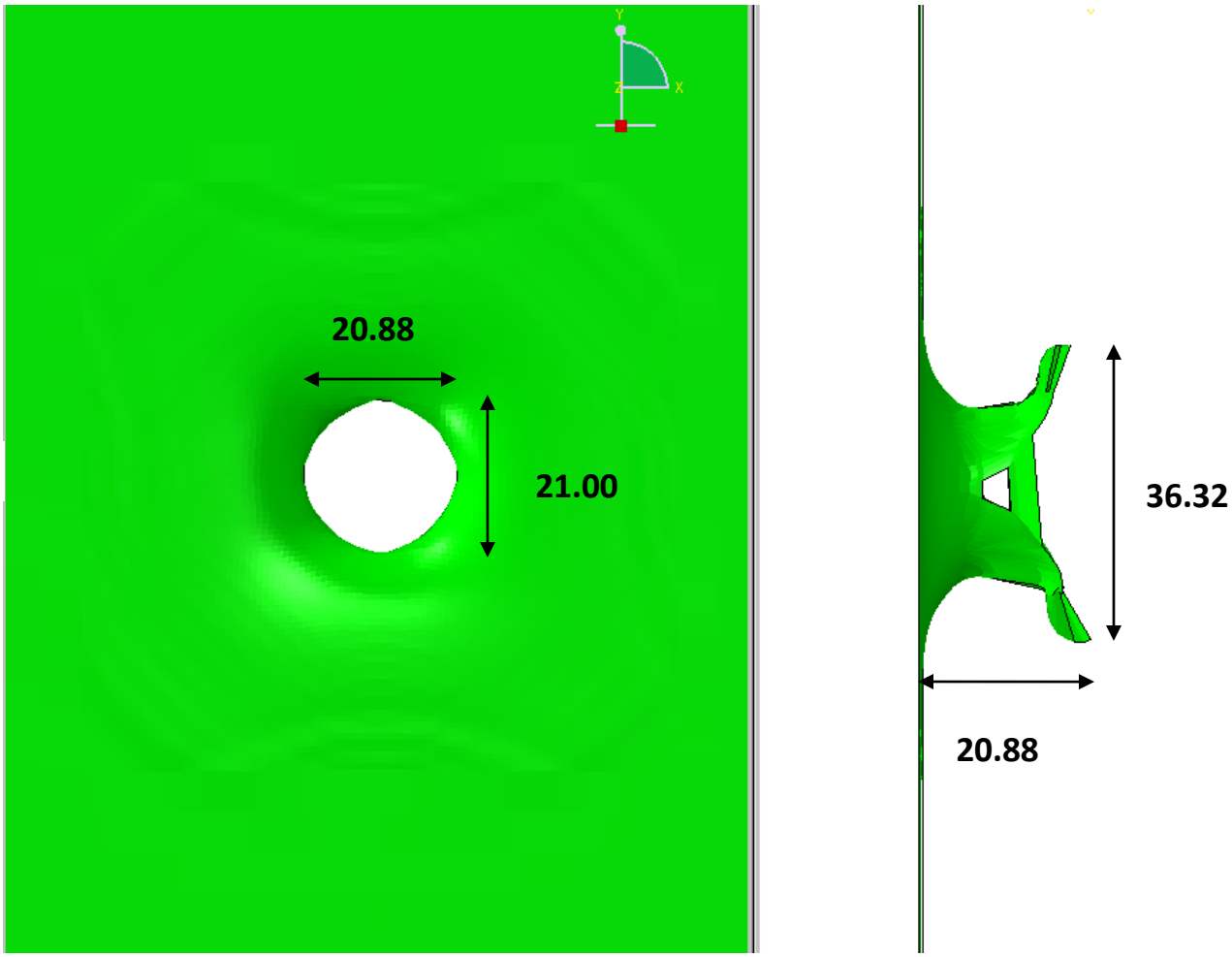

(b)

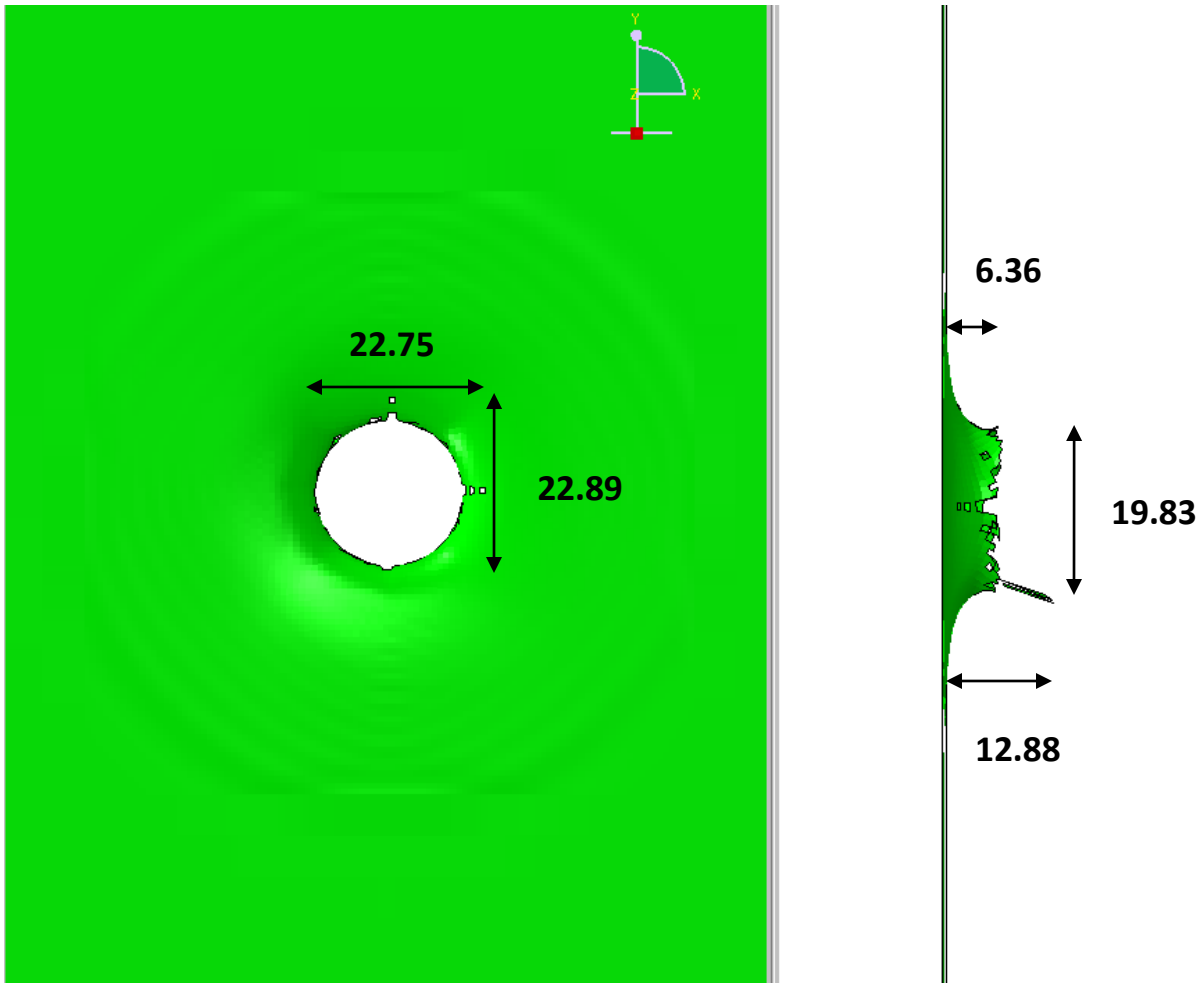

(c)

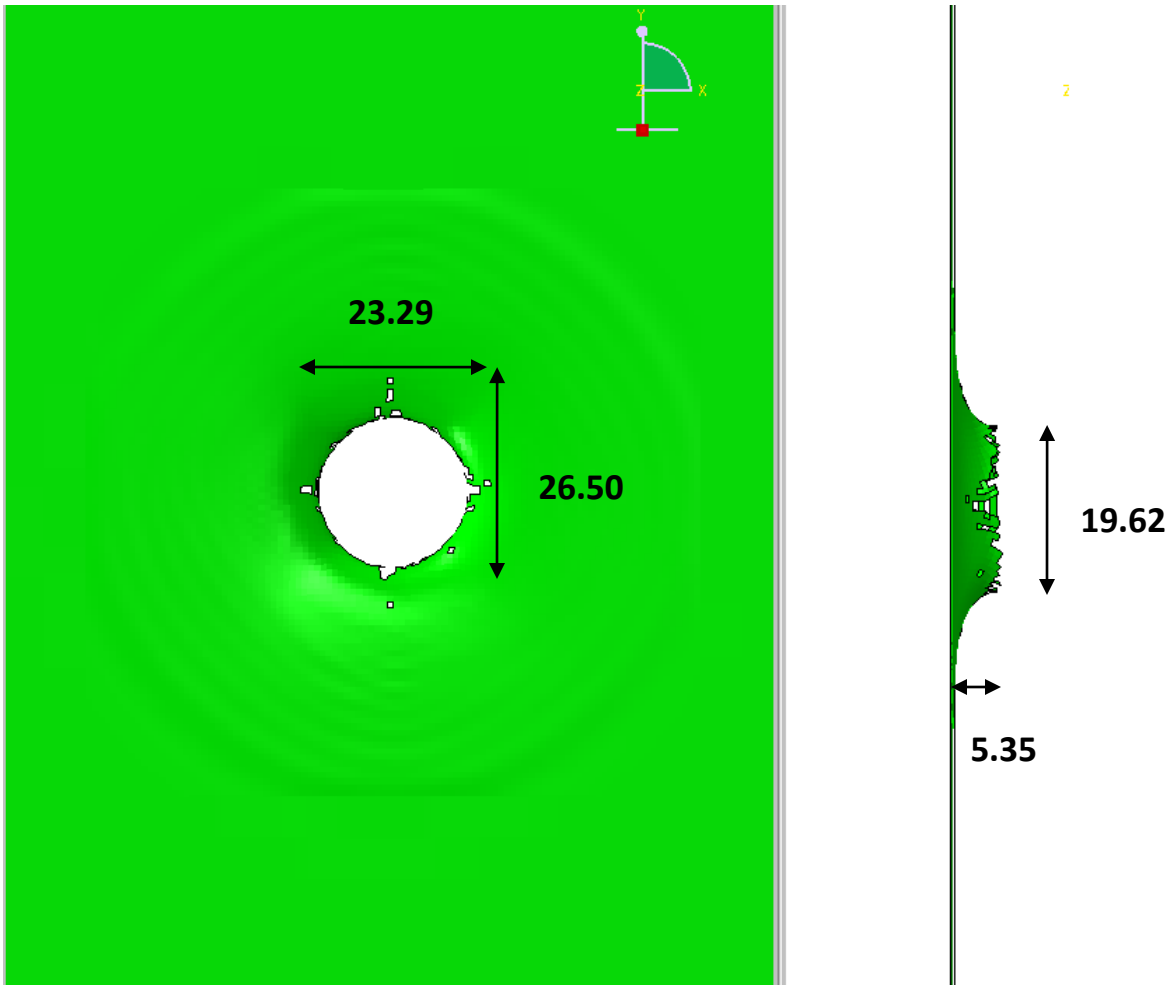

(d)

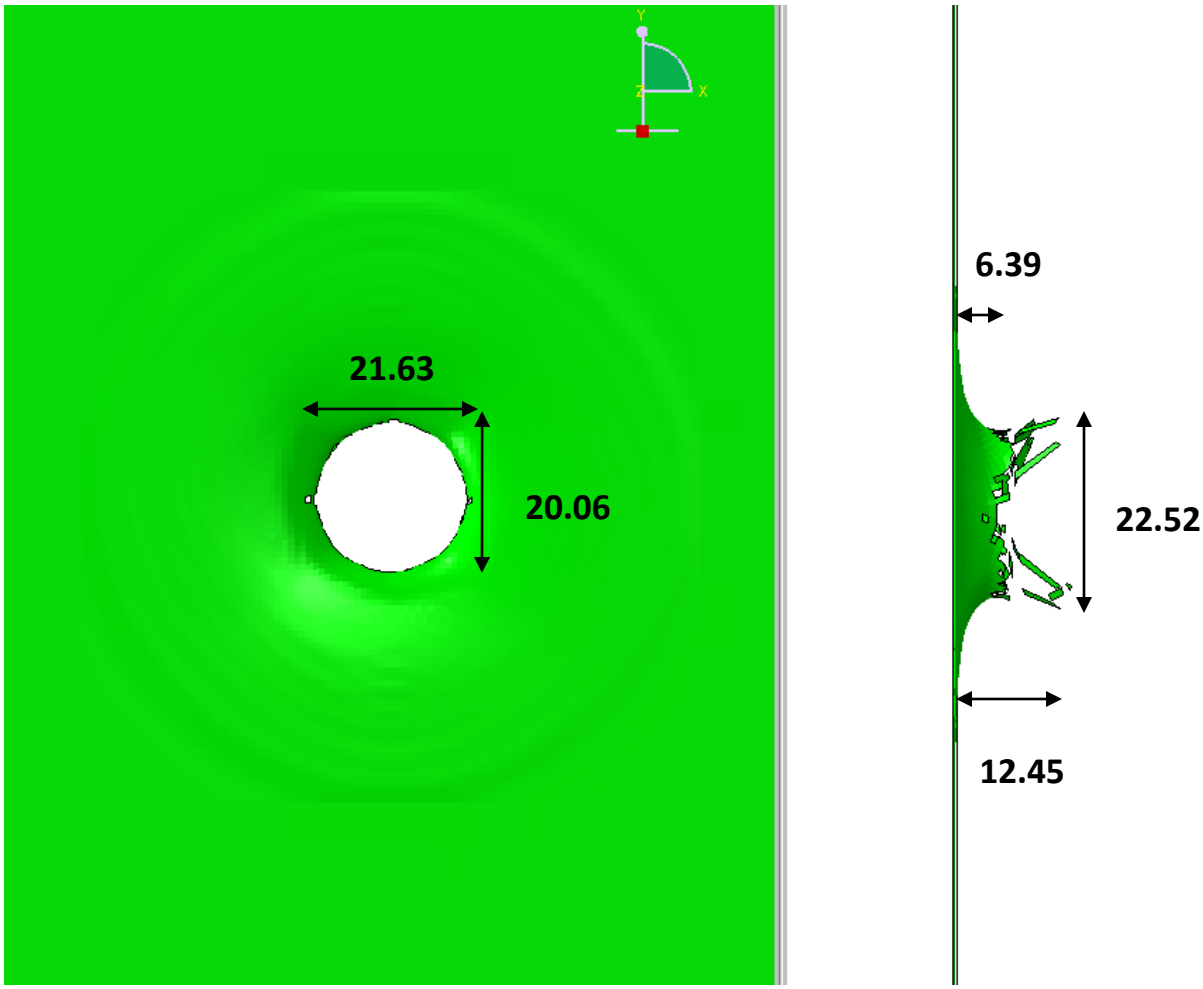

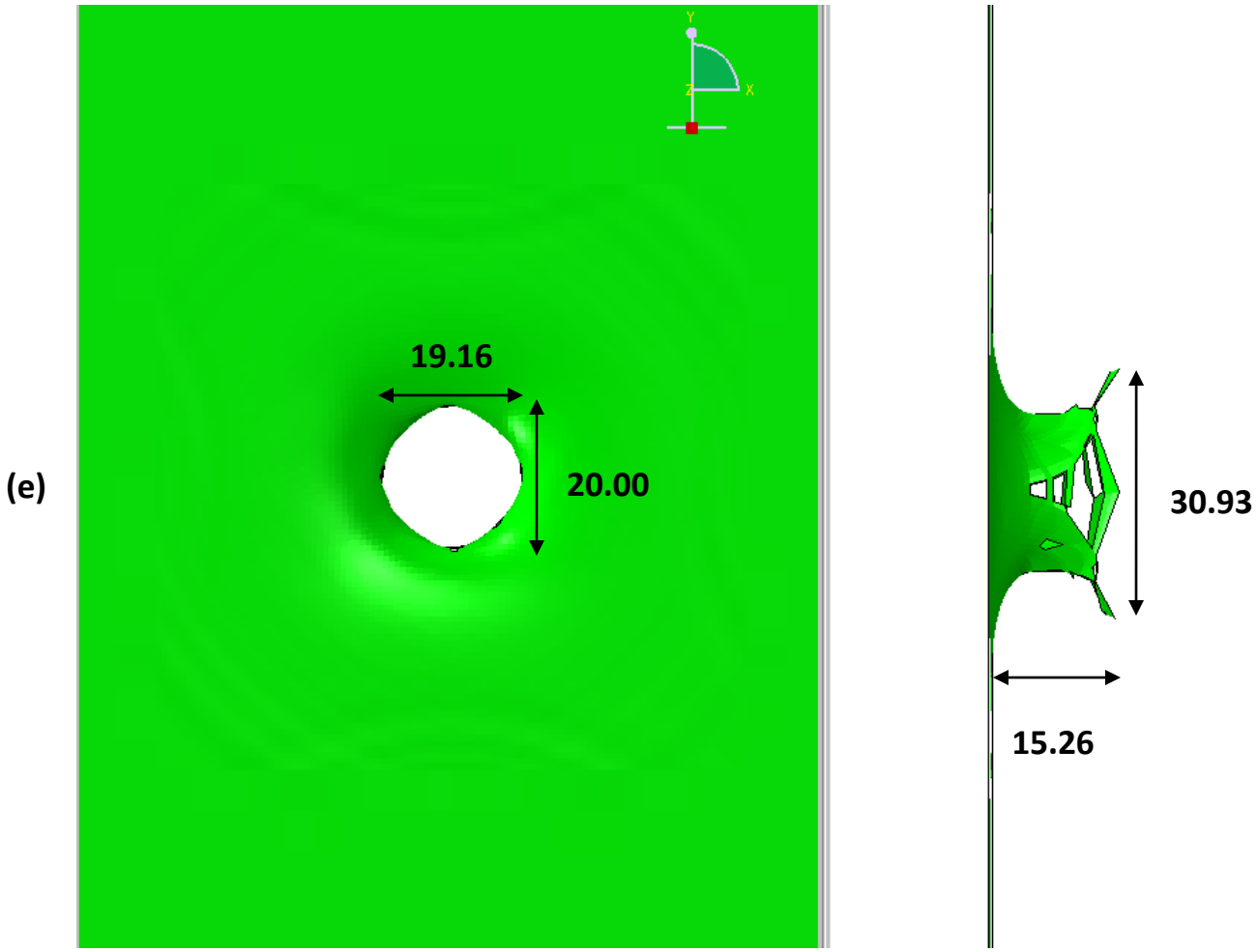

Figure 14. Front and side views of the five composite laminates after penetration by the projectile; AS4/3501-6 (a) , E-glass/117-220 (b), Gevetex/LY556 (c), Silenka/MY750 (d), T300/BSL914C (e) ; all dimensions in mm.

(a)

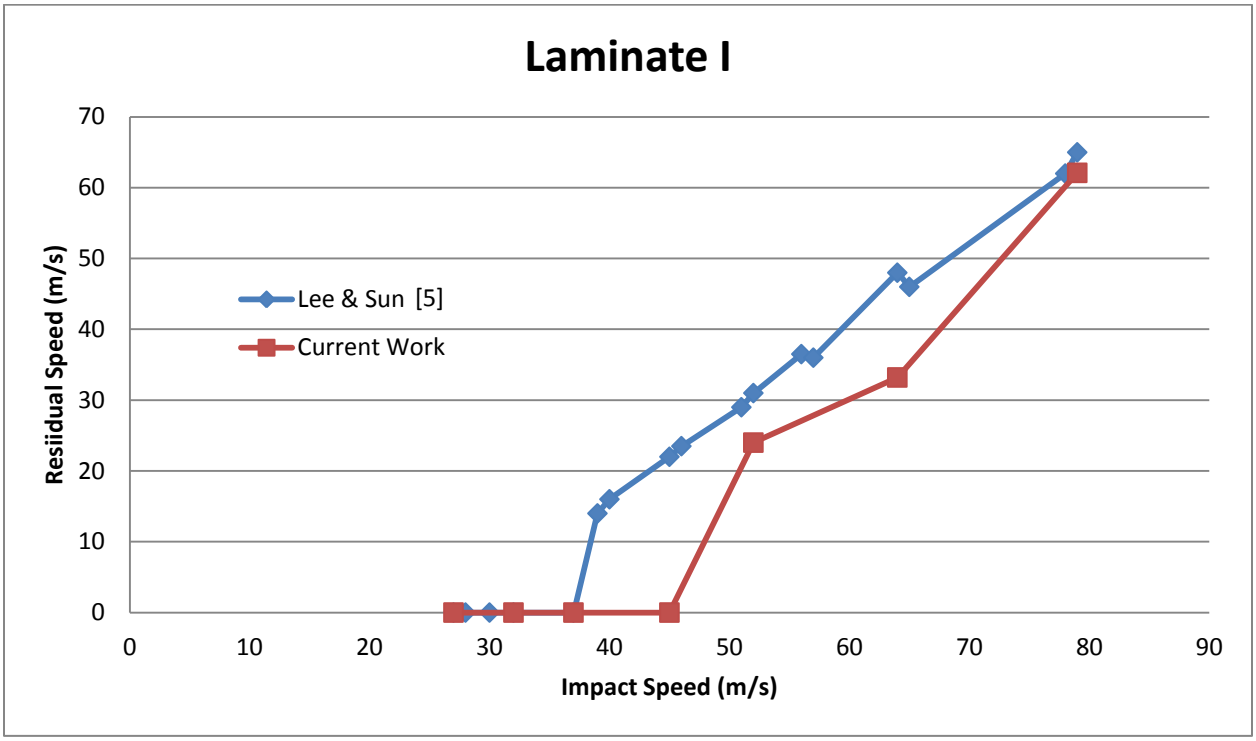
Laminate I
Resiidual Speed (m/s)
Impact Speed (m/s)
Lee & Sun [5]
Current Work
0
10
20
30
40
50
60
70
80
90

(b)

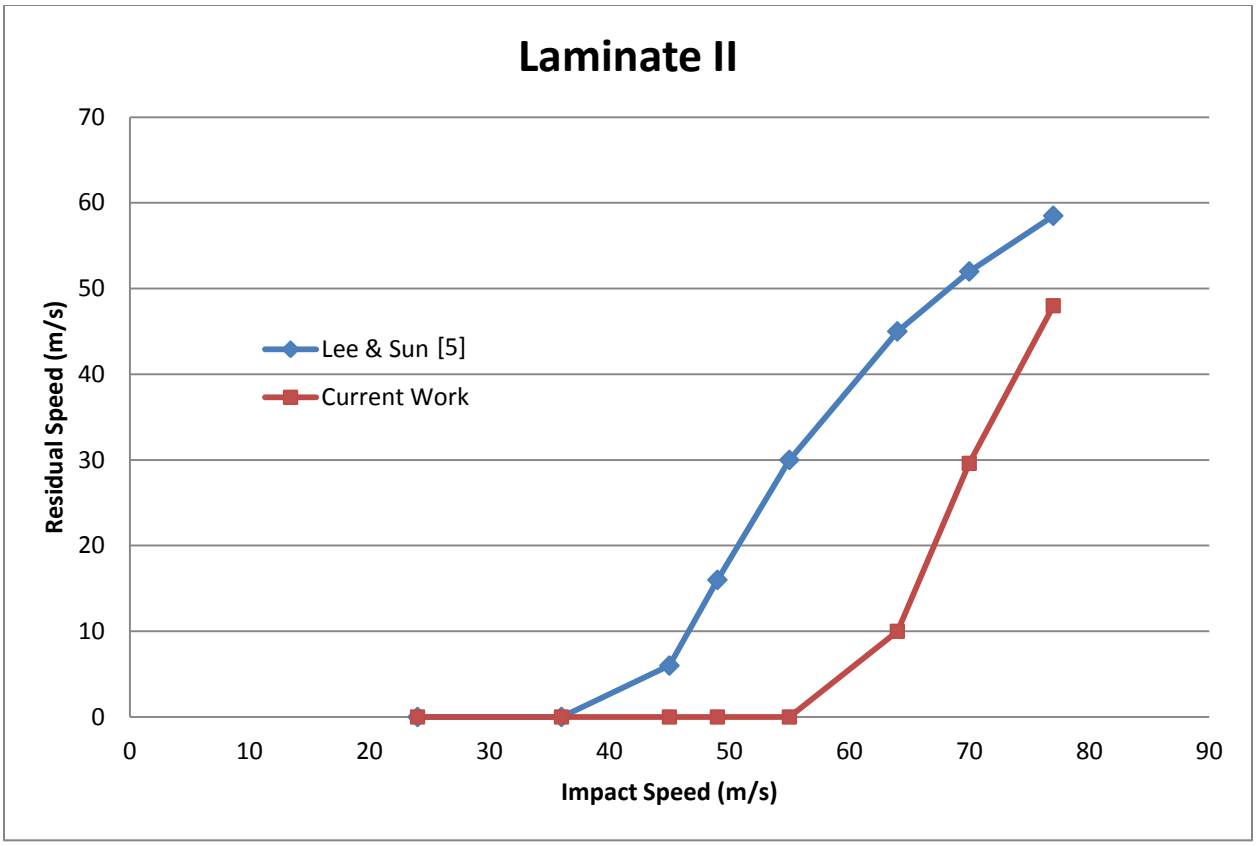
Laminate II
Residual Speed (m/s)
Impact Speed (m/s)
Lee & Sun [5]
Current Work
0
10
20
30
40
50
60
70
80
90

(c)

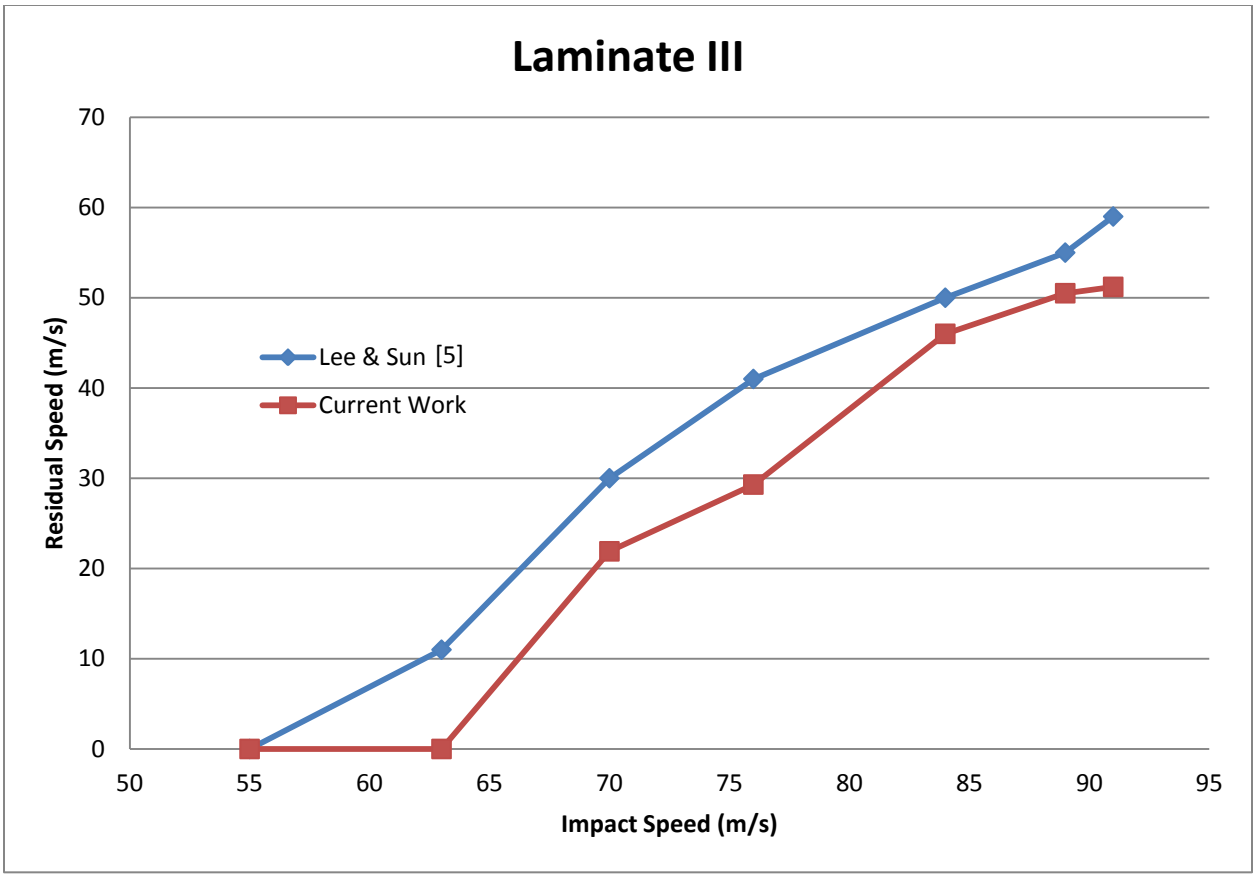

Figure 15. For different impact speeds, comparison of the presently computed residual projectile speed with that found by Lee and Sun for laminates I, II, and III.

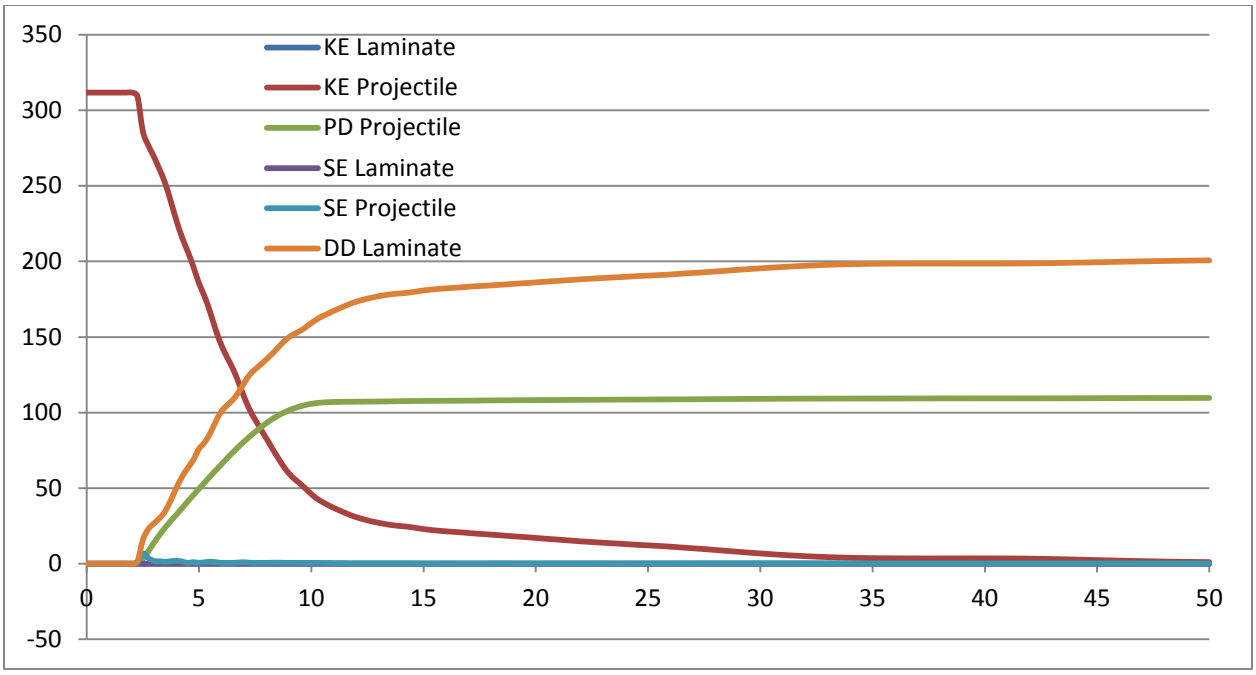

Figure 16. Time histories of projectile and laminate energies for Dyneema laminate C impacted by a FSP with an initial speed of 750 m/s.

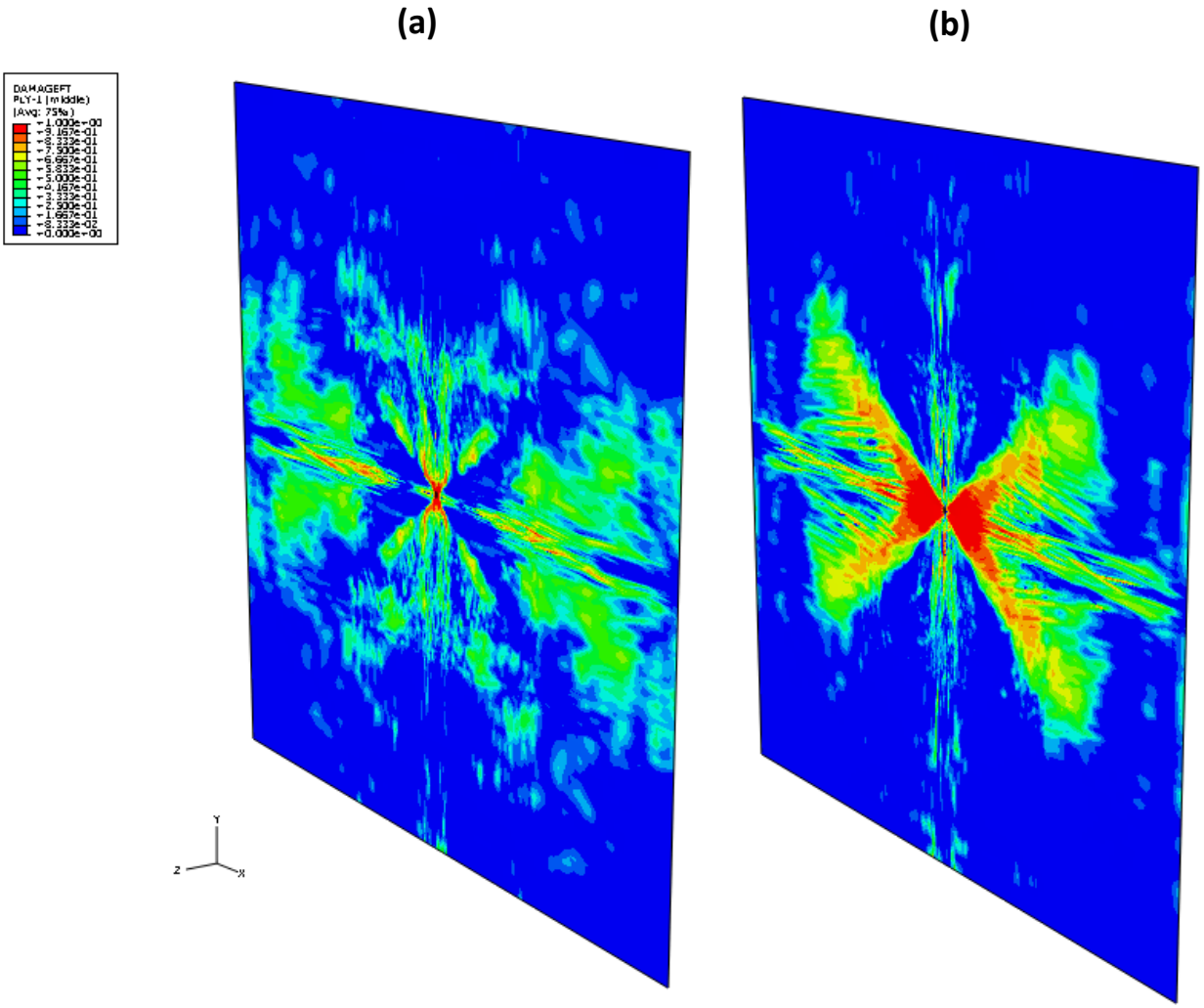

Figure 17. Fiber tension damage in first (a) and last (b) ply of Dyneema laminate C 200 µs after impact by a FSP with an initial speed of 750 m/s.

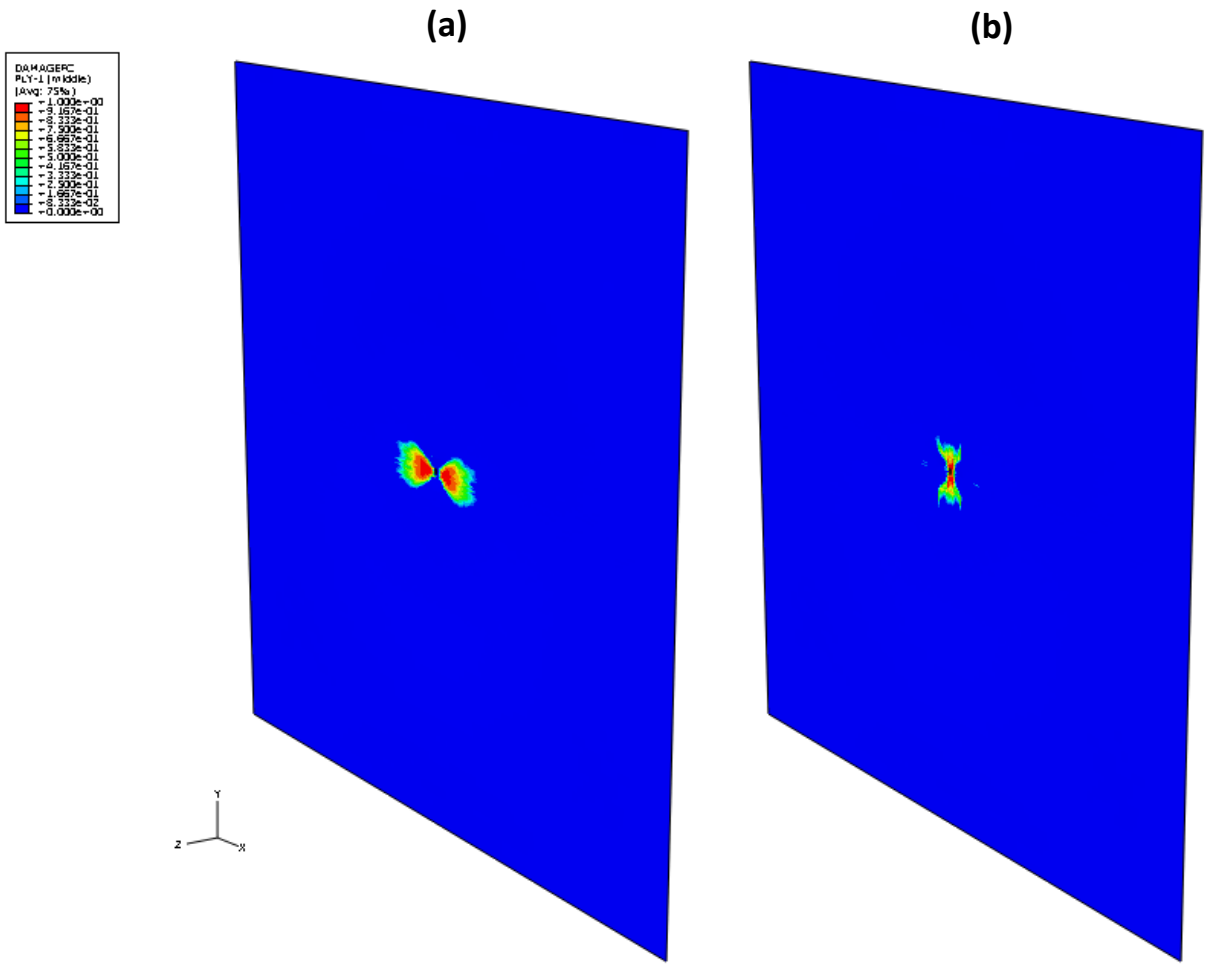

Figure 18. Fiber compression damage in first (a) and last (b) ply of Dyneema laminate C 200 µs after impact by a FSP with an initial speed of 750 m/s.

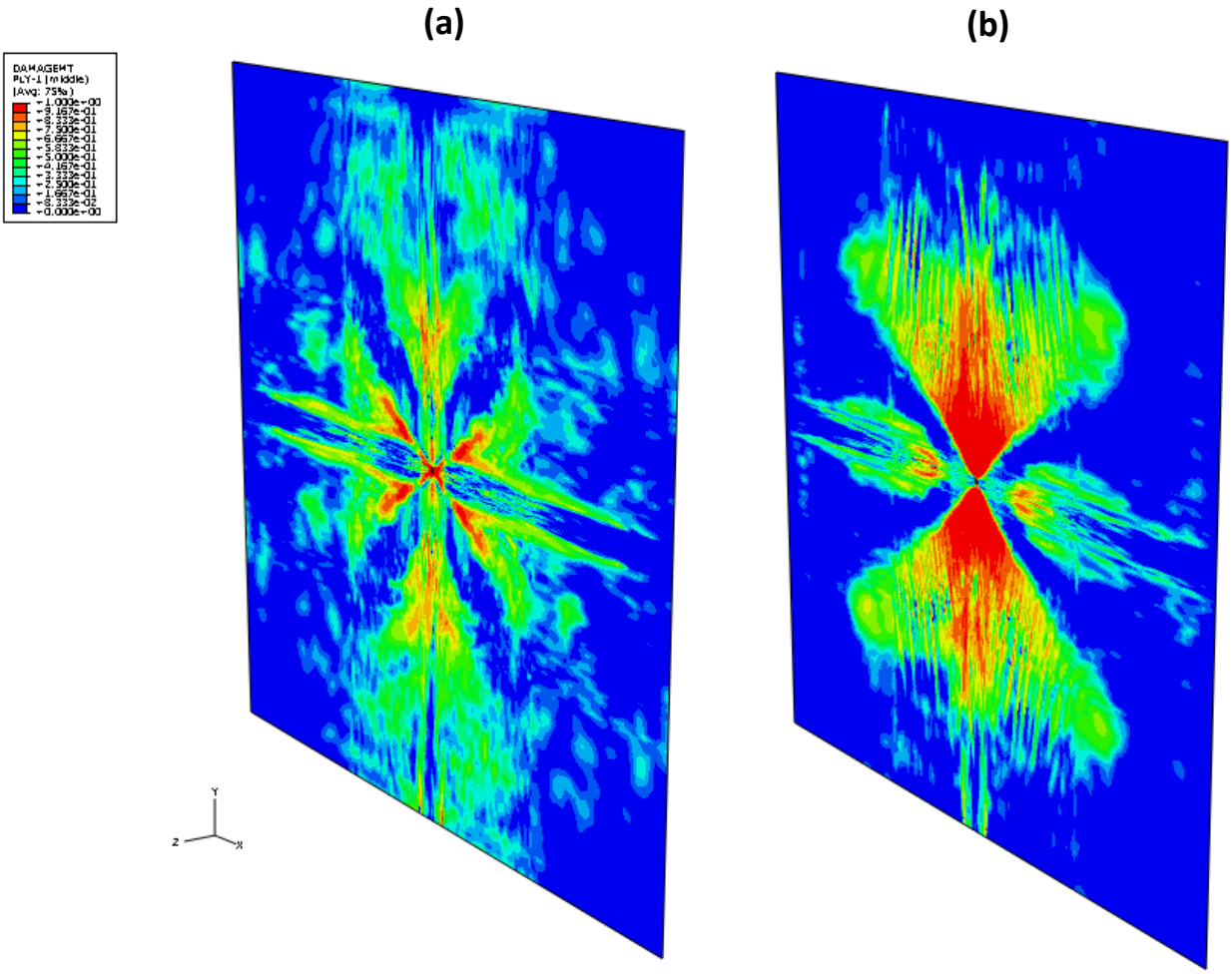

Figure 19. Matrix tension damage in first (a) and last (b) ply of Dyneema laminate C 200 µs after impact by a FSP with an initial speed of 750 m/s.

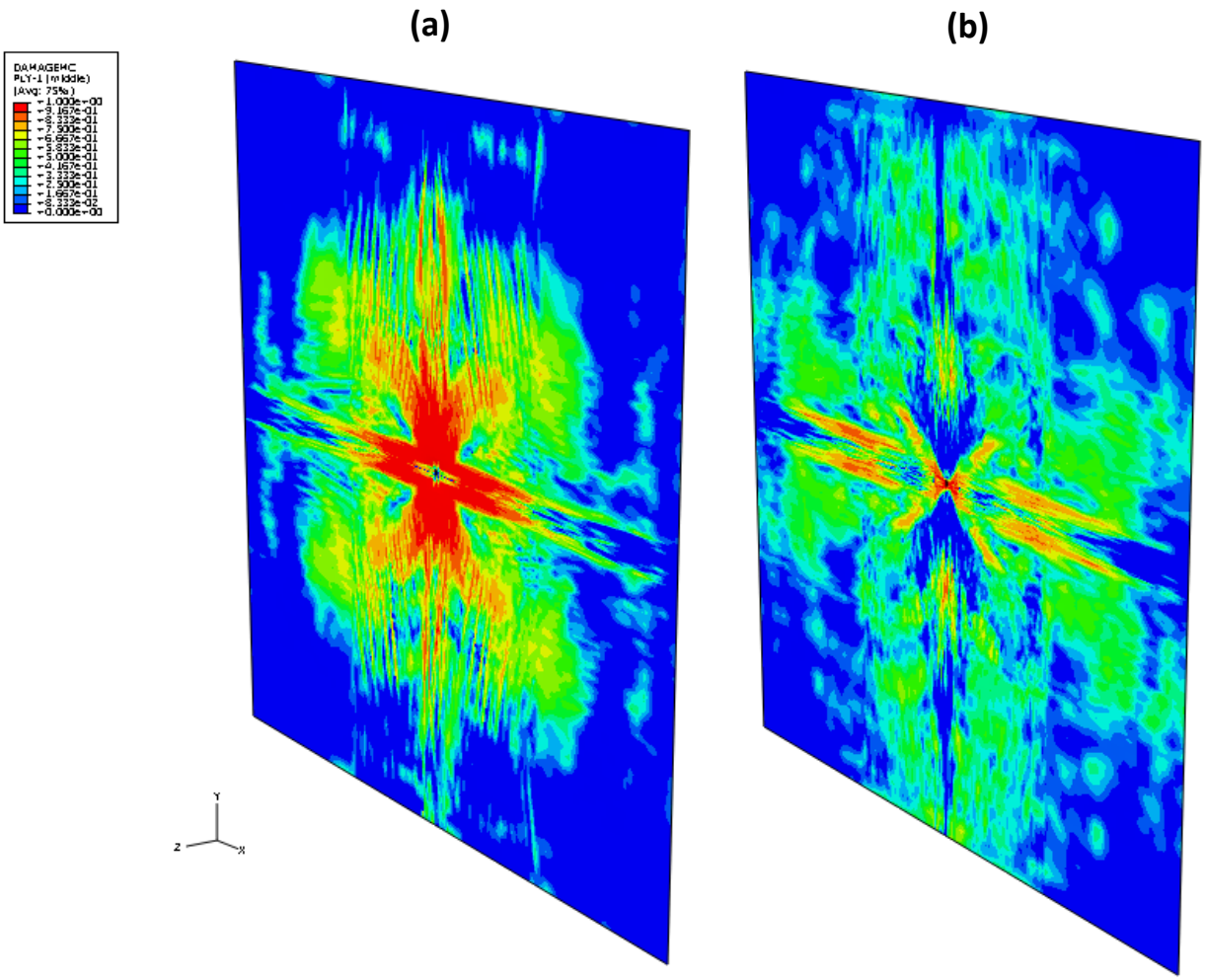

Figure 20. Matrix compression damage in first (a) and last (b) ply of Dyneema laminate C 200 µs after impact by a FSP with an initial speed of 750 m/s.

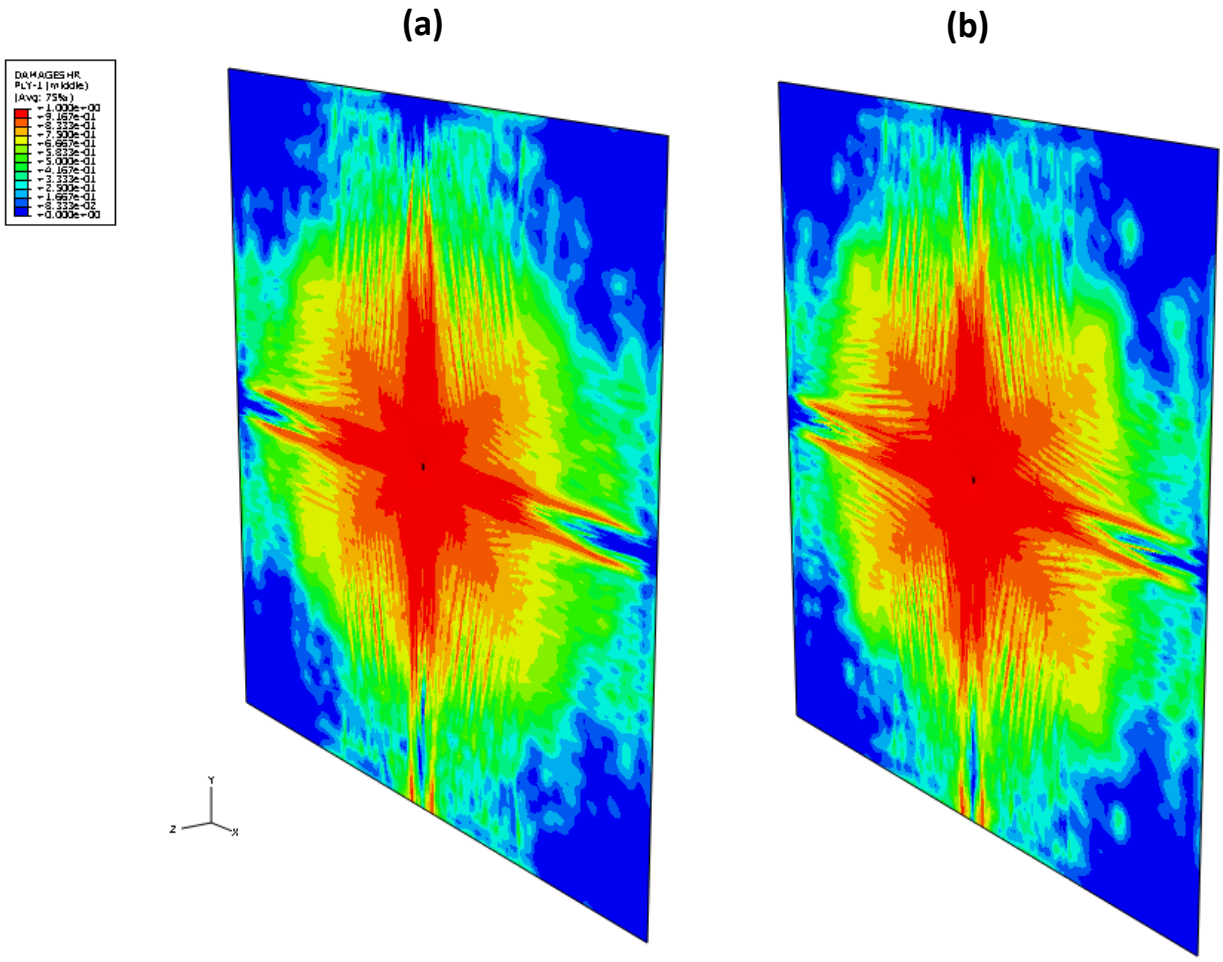

Figure 21. Shear damage in first (a) and last (b) ply of Dyneema laminate C 200 µs after impact by a FSP with an initial speed of 750 m/s.

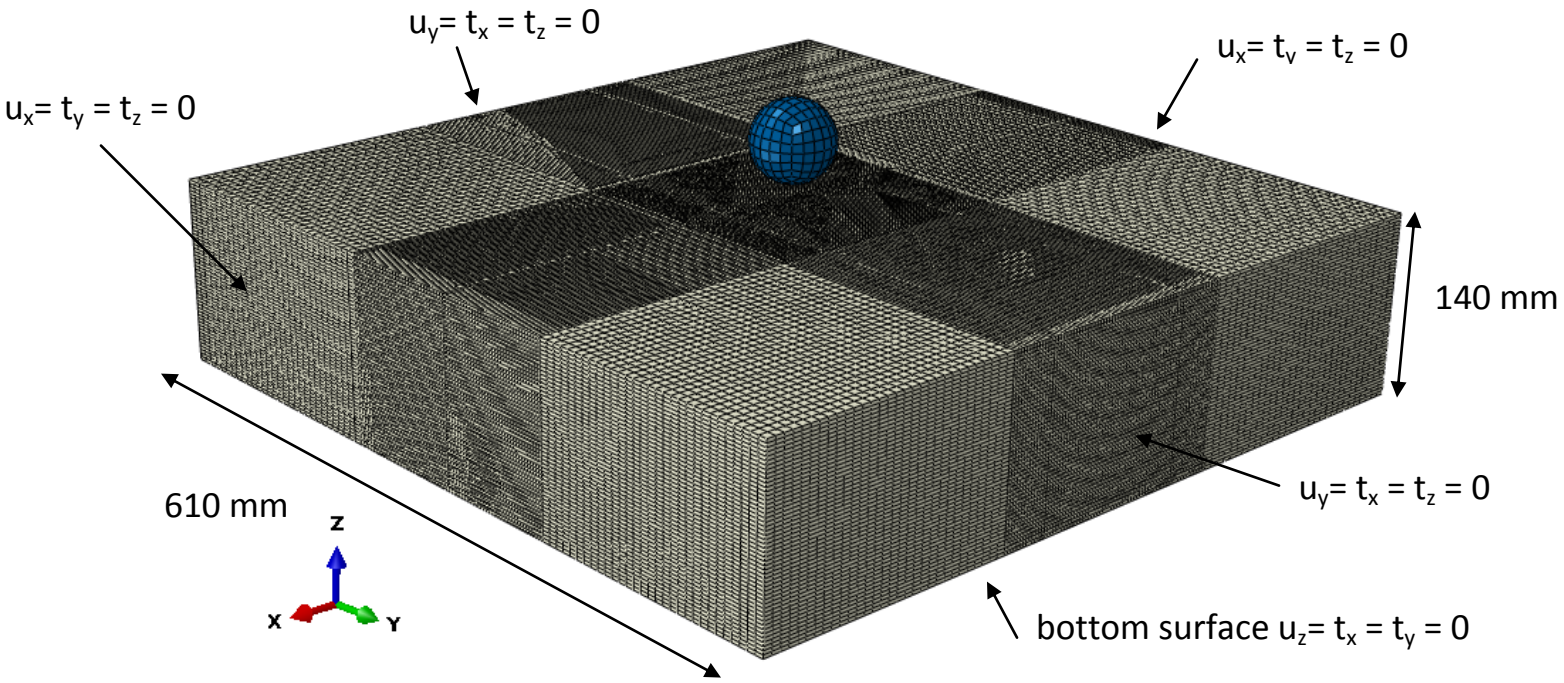

Figure 22. Initial configuration of the clay drop test described in the NIJ standard 101.6. Boundary conditions are shown on the side and bottom surfaces. Points on the top surface except those contacting the projectile are traction free and those contacting the projectile conform to the shape of the projectile; projectile moves in the negative z-direction.

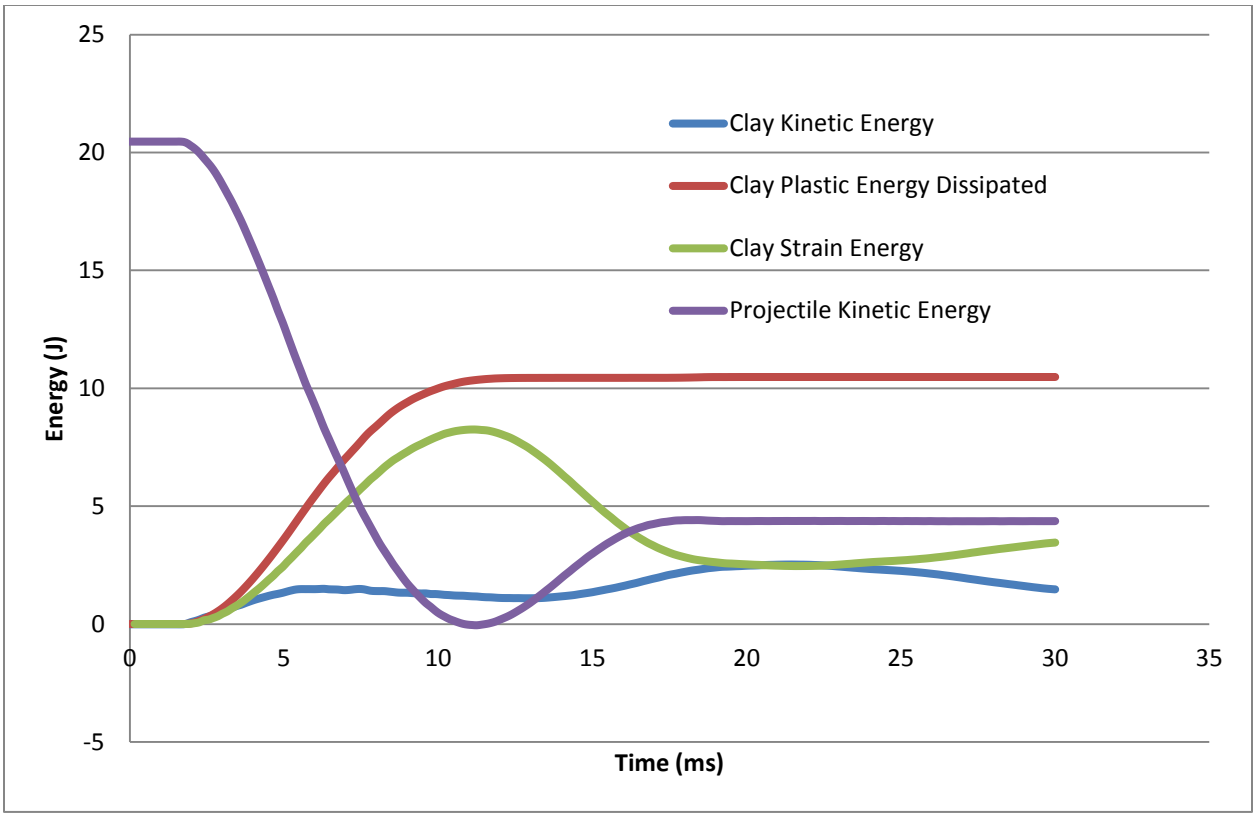

Figure 23. Time histories of energy components in the NIJ clay drop test.

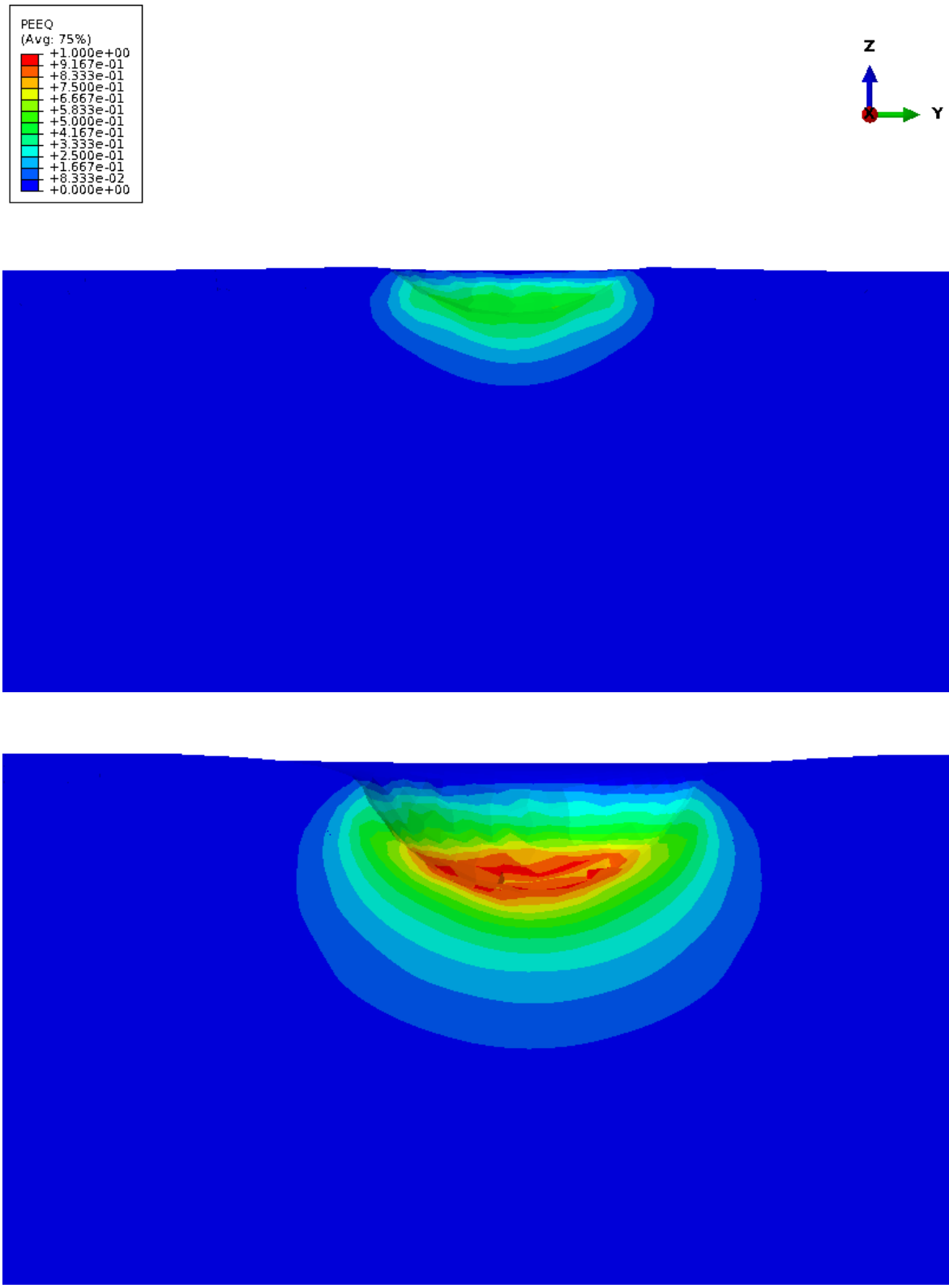
PEEQ
(Avg: 75%)
+1.000e+00
+9.167e-01
+8.333e-01
+7.500e-01
+6.667e-01
+5.833e-01
+5.000e-01
+4.167e-01
+3.333e-01
+2.500e-01
+1.667e-01
+8.333e-02
+0.000e+00
Z
Y
(a)
(b)

(c)

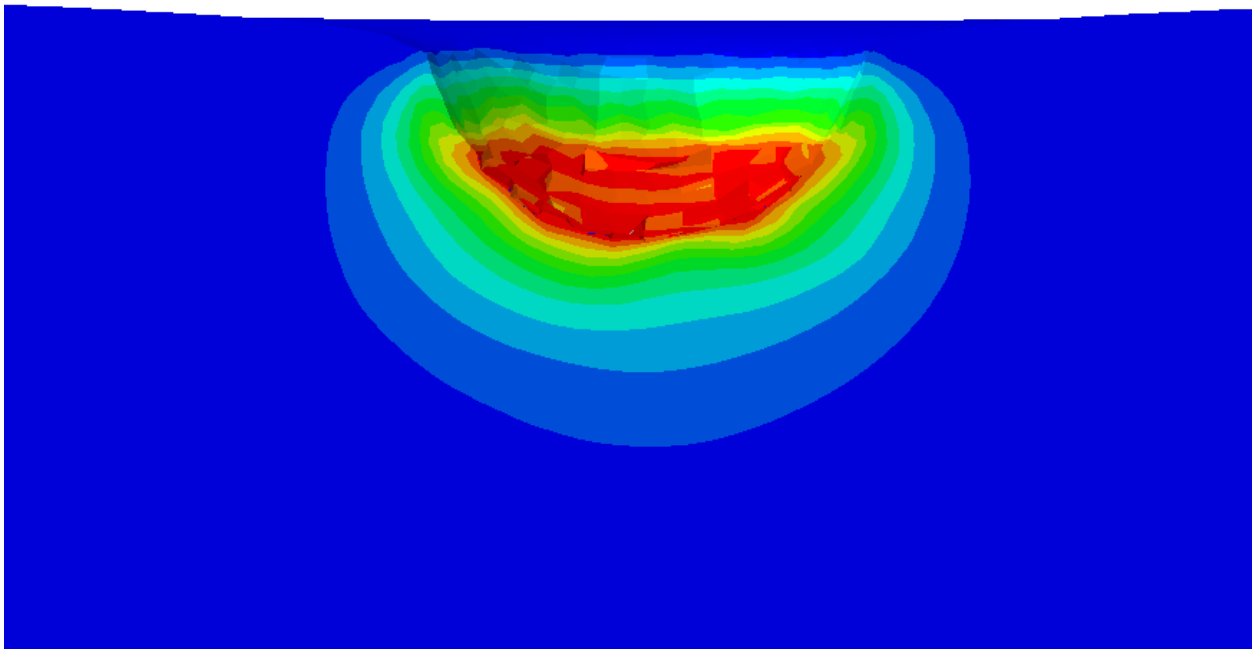

(d)

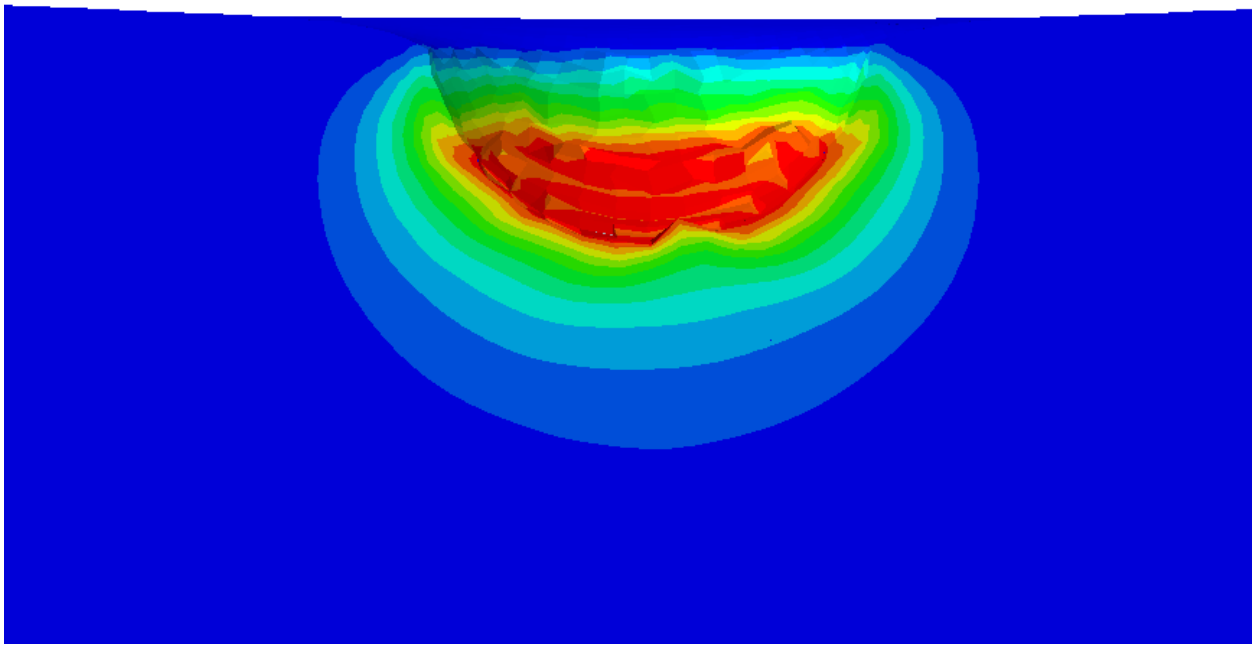

(e)

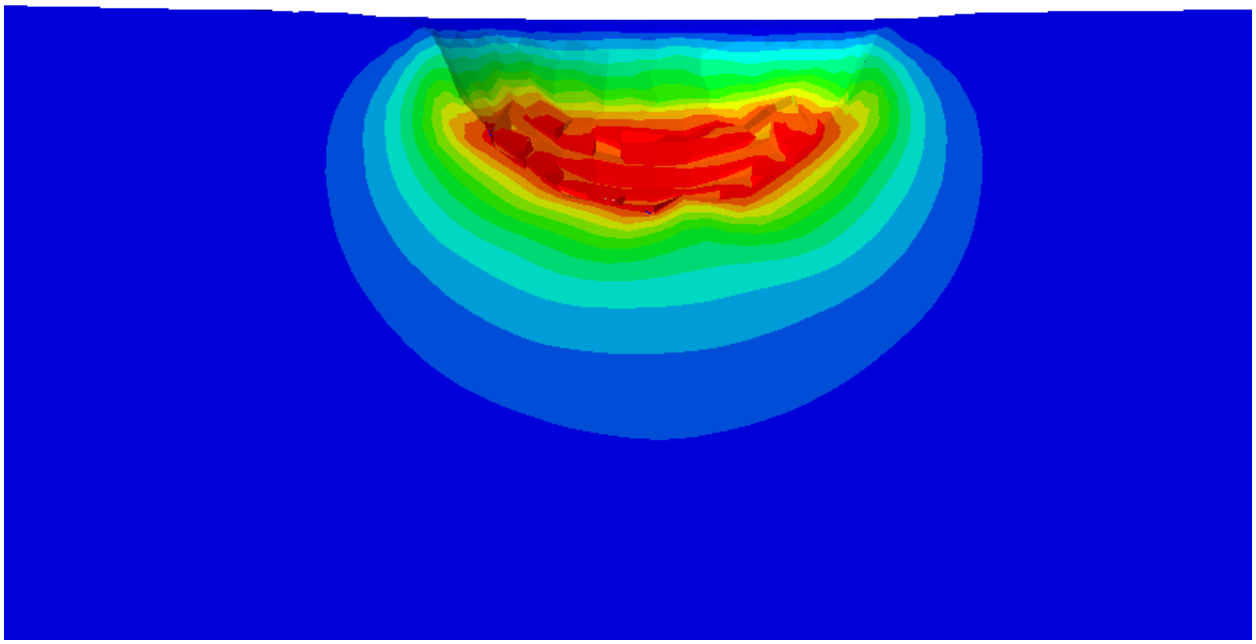

(f)

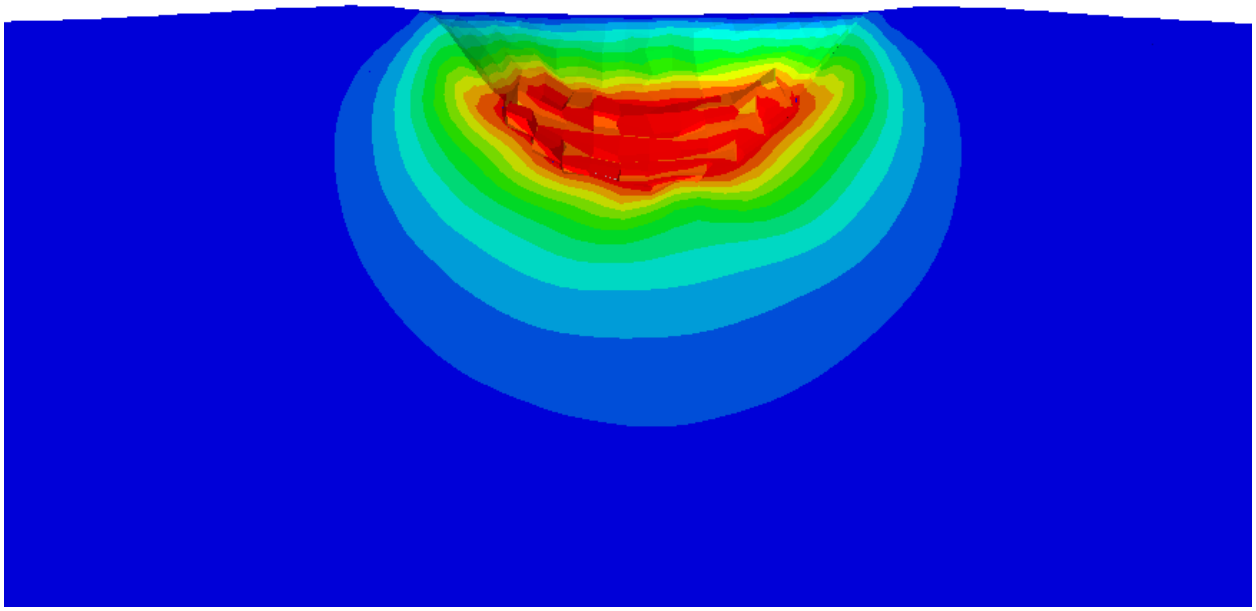

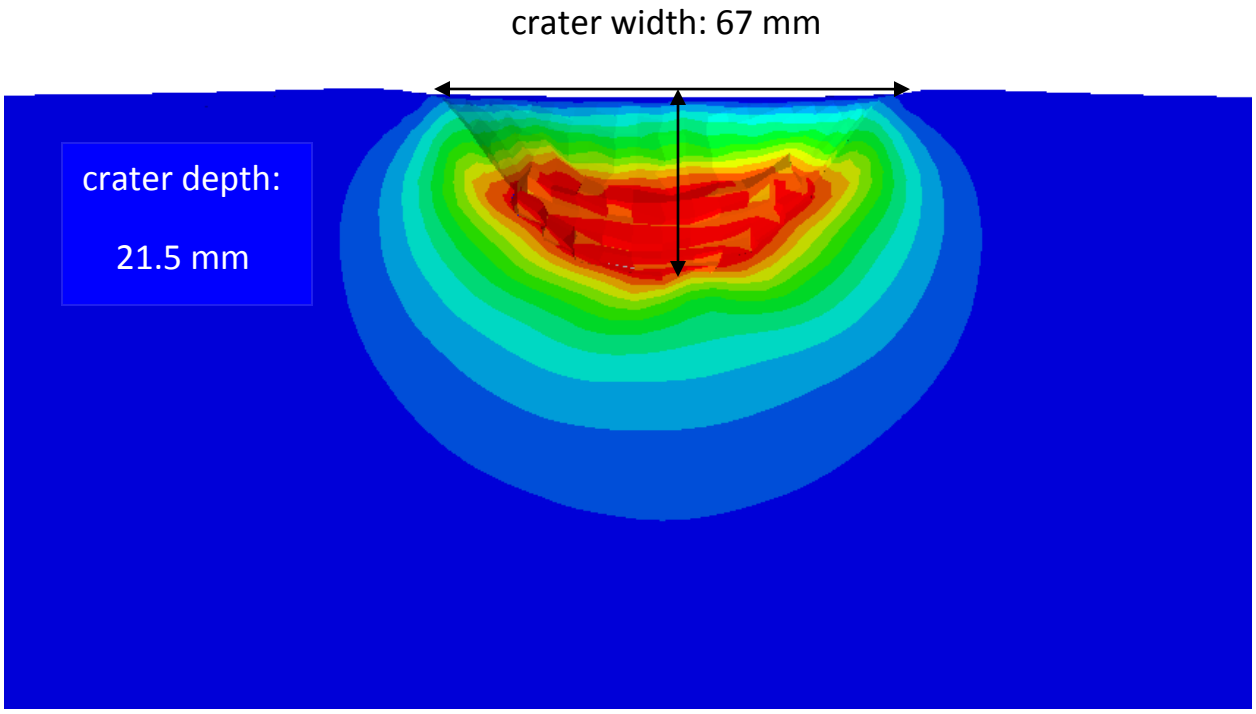

(g)

Figure 24. Contour plot of the equivalent plastic strain in a small region of the clay around the crater at 3 µs (a), 6 µs (b), 9 µs (c), 12 µs (d), 15 µs (e), 21 µs (f), and 27 µs (g).

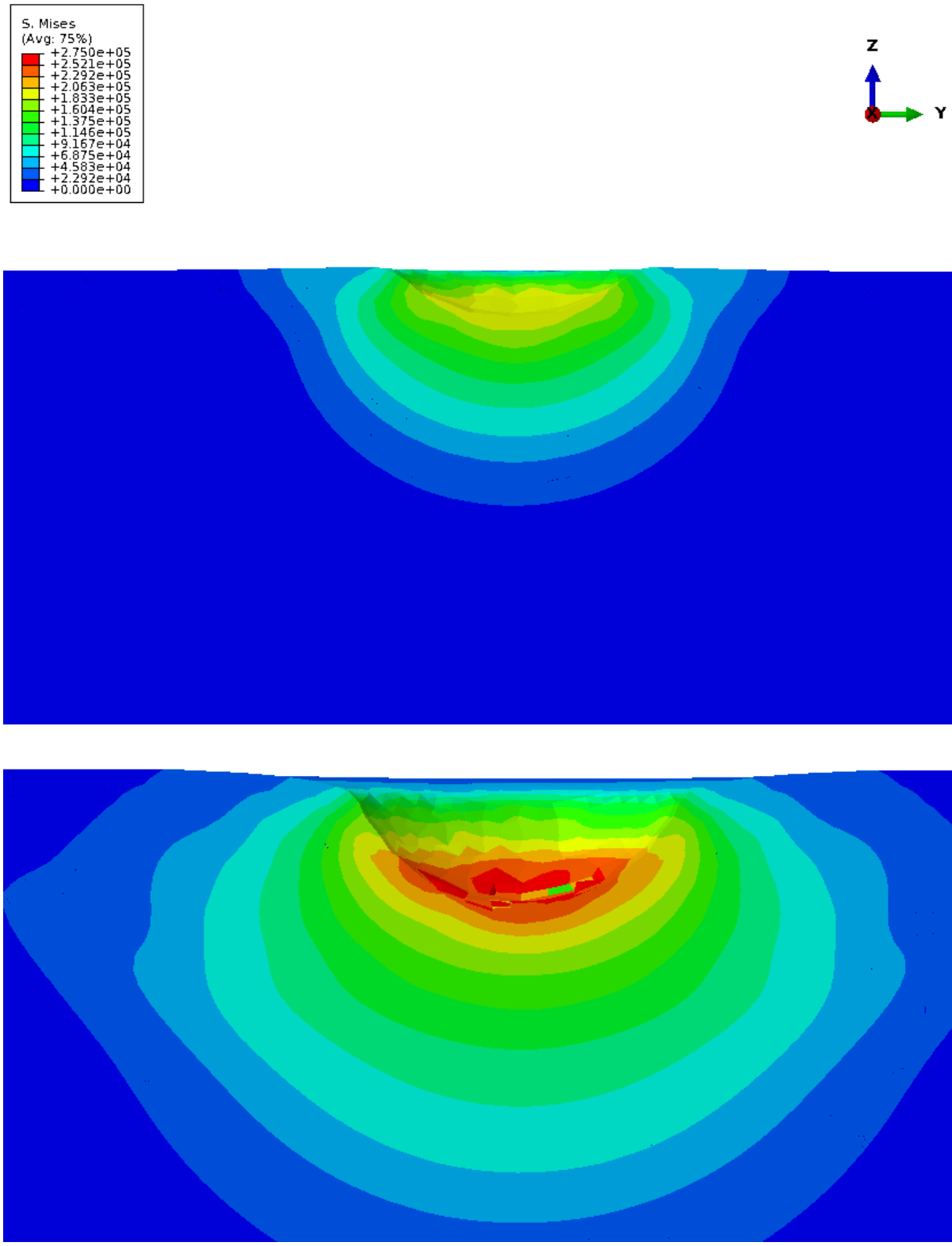
S. Mises
(Avg: 75%)
+2.750e+05
+2.521e+05
+2.292e+05
+2.063e+05
+1.833e+05
+1.604e+05
+1.375e+05
+1.146e+05
+9.167e+04
+6.875e+04
+4.583e+04
+2.292e+04
+0.000e+00
Z
Y
(a)
(b)

(c)

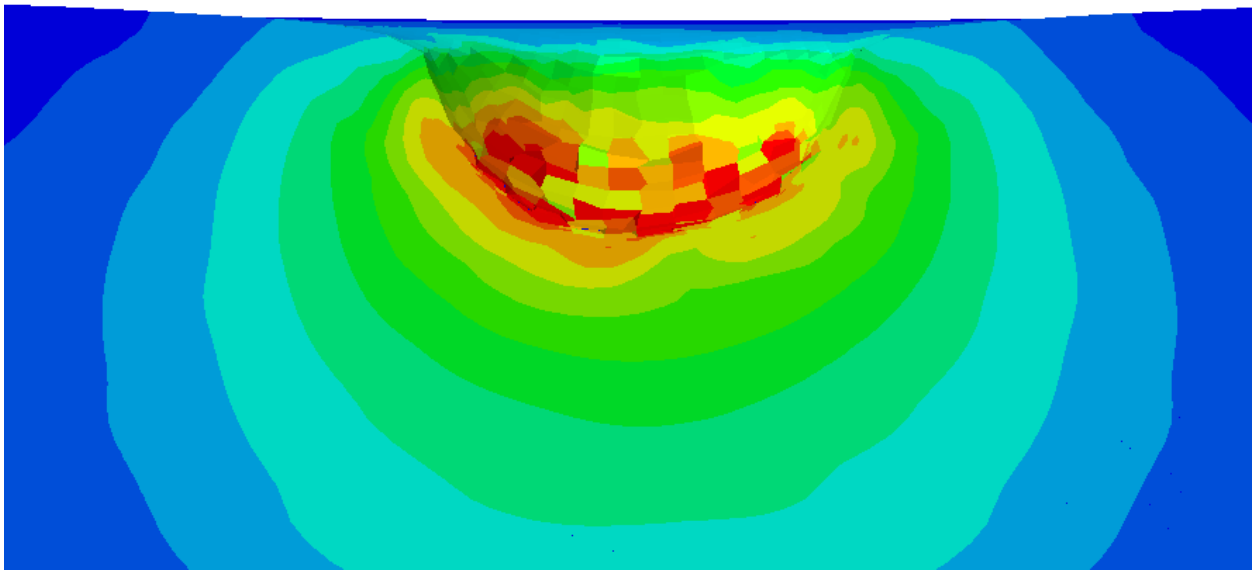

(d)

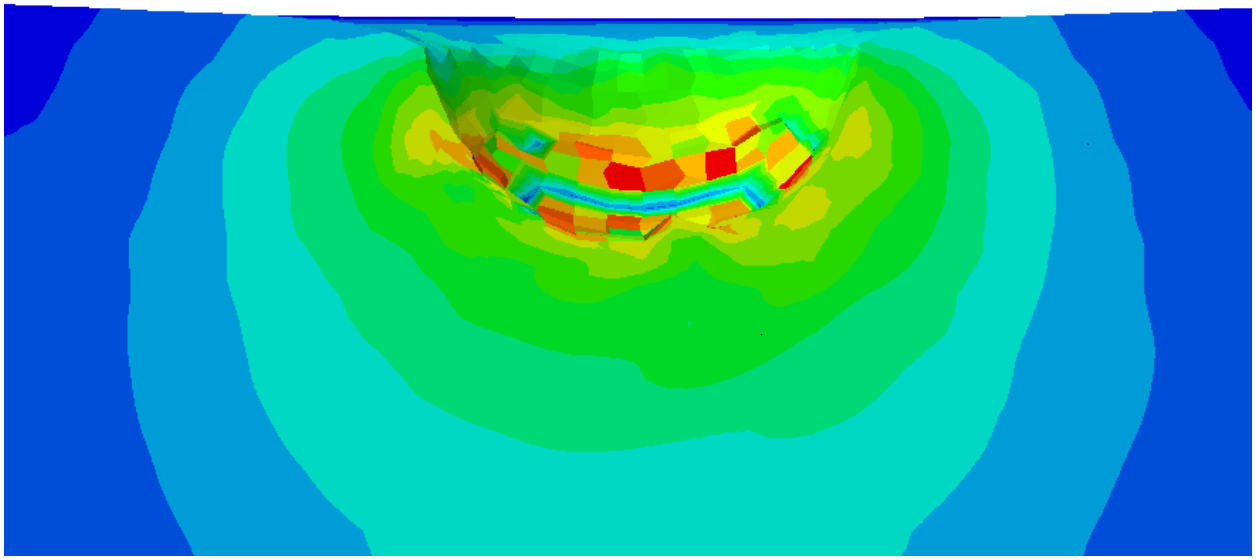

(e)

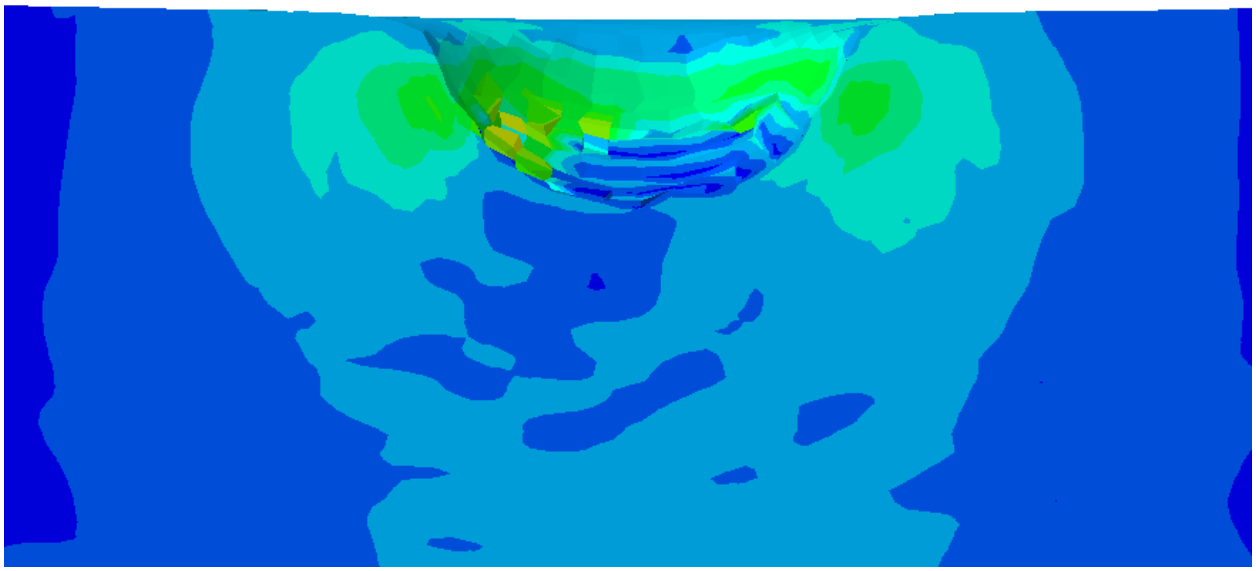

(f)

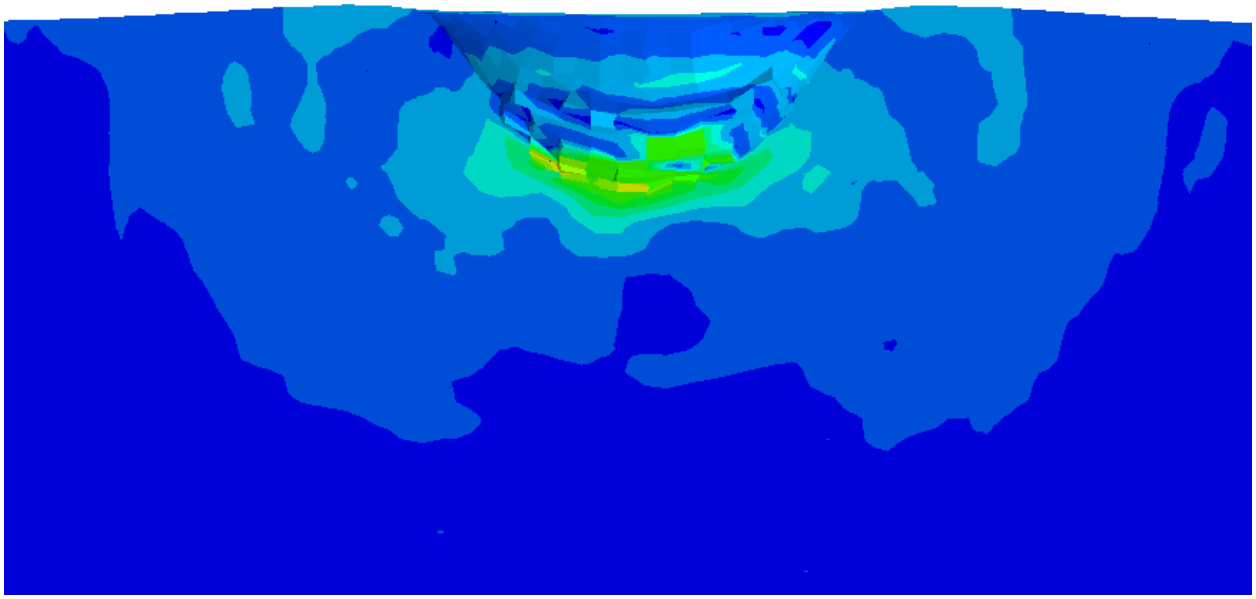

(g)

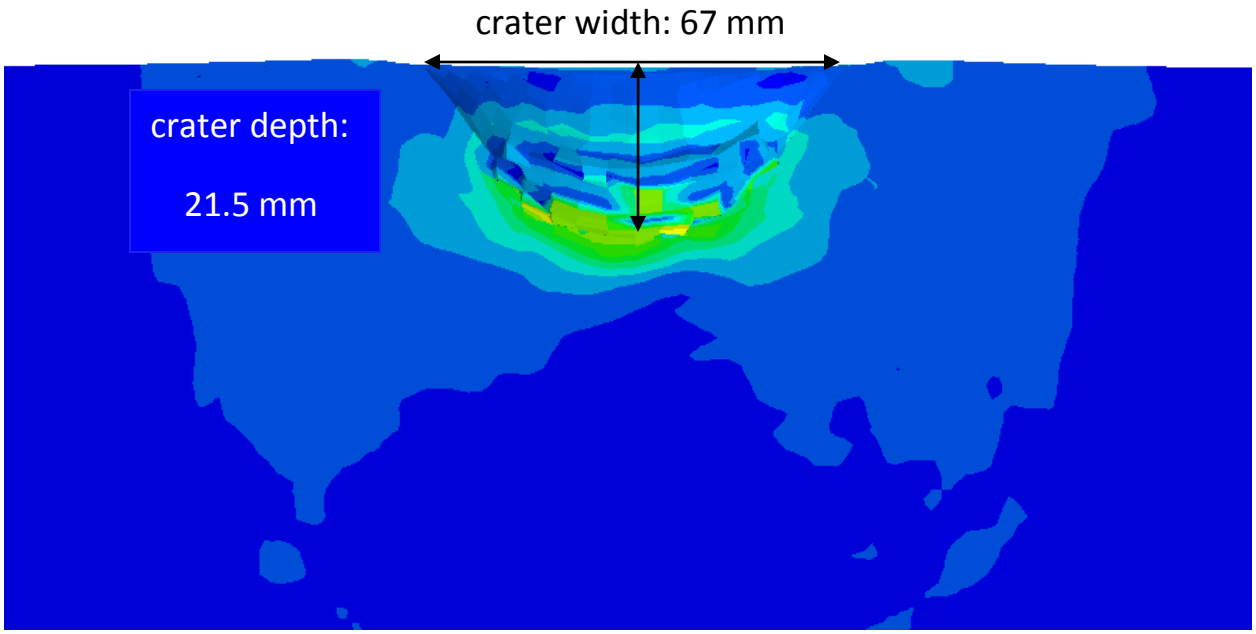

Figure 25. Contour plot of the von Mises stress in a small region of the clay around the crater at 3 μs (a), 6 μs (b), 9 μs (c), 12 μs (d), 15 μs (e), 21 μs (f), and 27 μs (g); volume of crater ~30 cubic cm; **legend units: Pa**

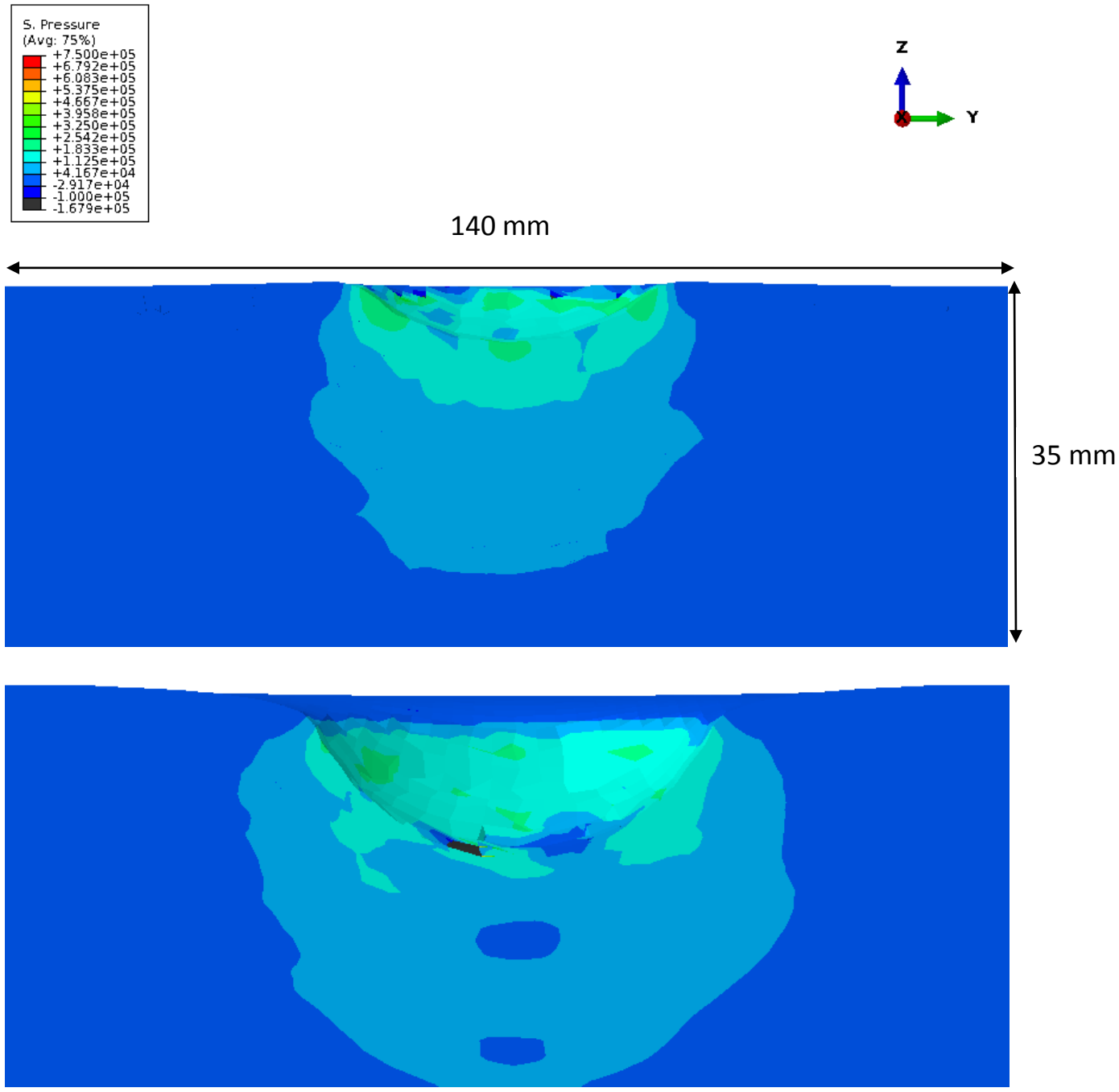
S. Pressure
(Avg: 75%)
+7.500e+05
+6.792e+05
+6.083e+05
+5.375e+05
+4.667e+05
+3.958e+05
+3.250e+05
+2.542e+05
+1.833e+05
+1.125e+05
+4.167e+04
-2.917e+04
-1.000e+05
-1.679e+05
Z
Y
140 mm
35 mm
(a)
(b)

(c)

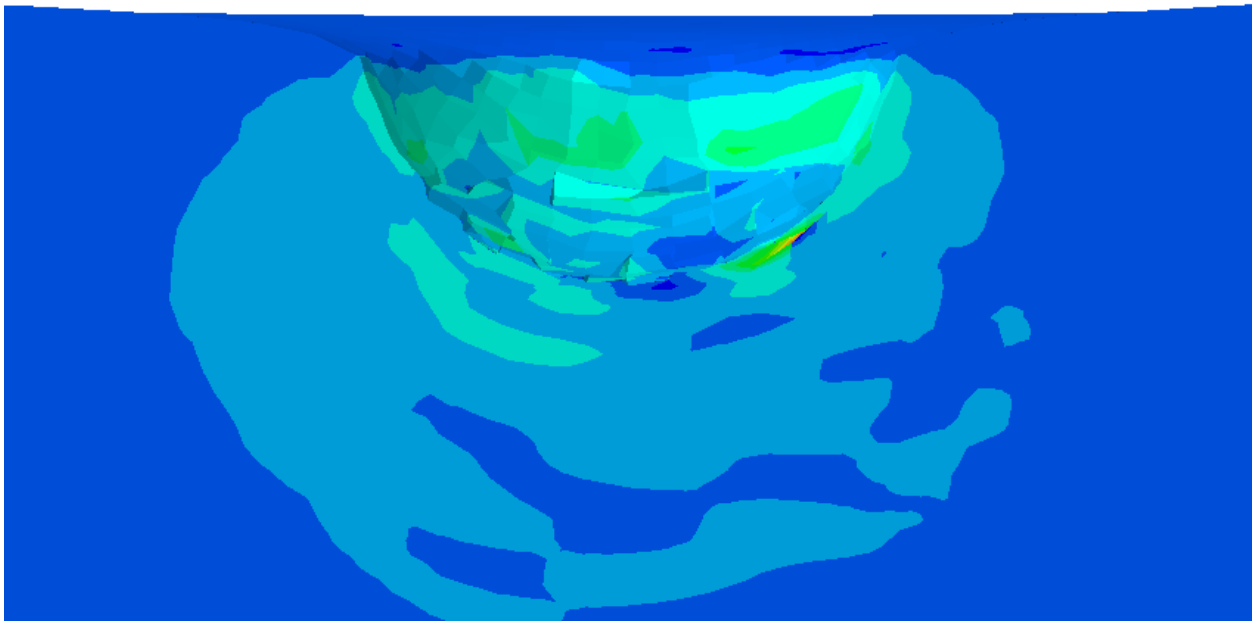

(d)

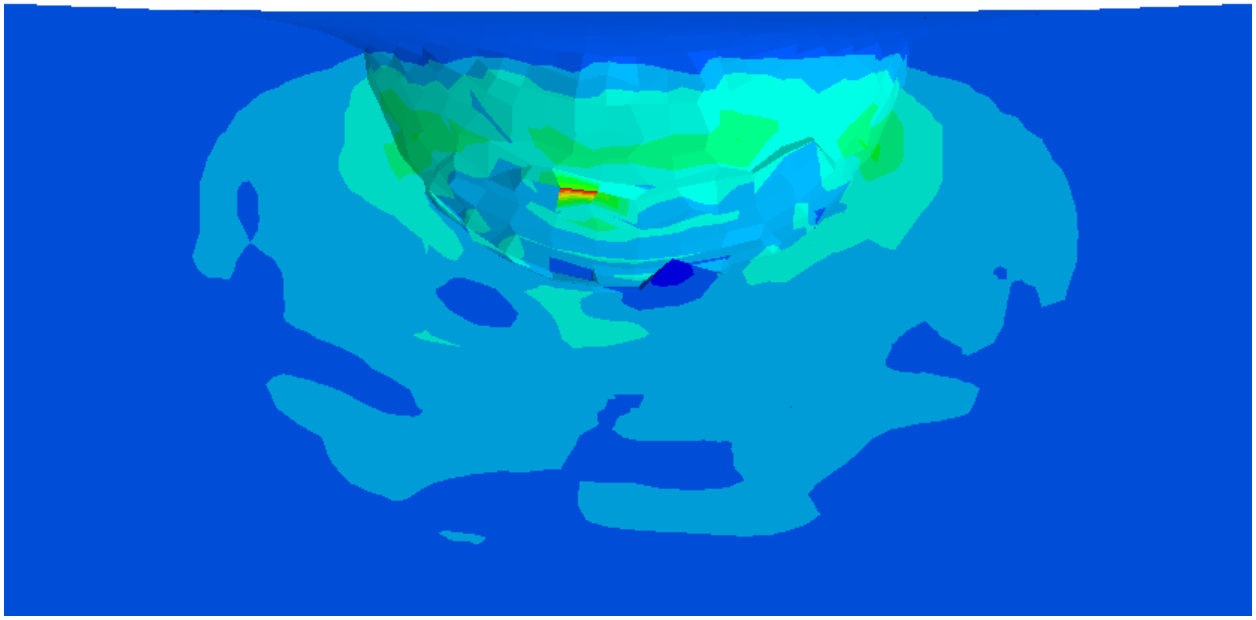

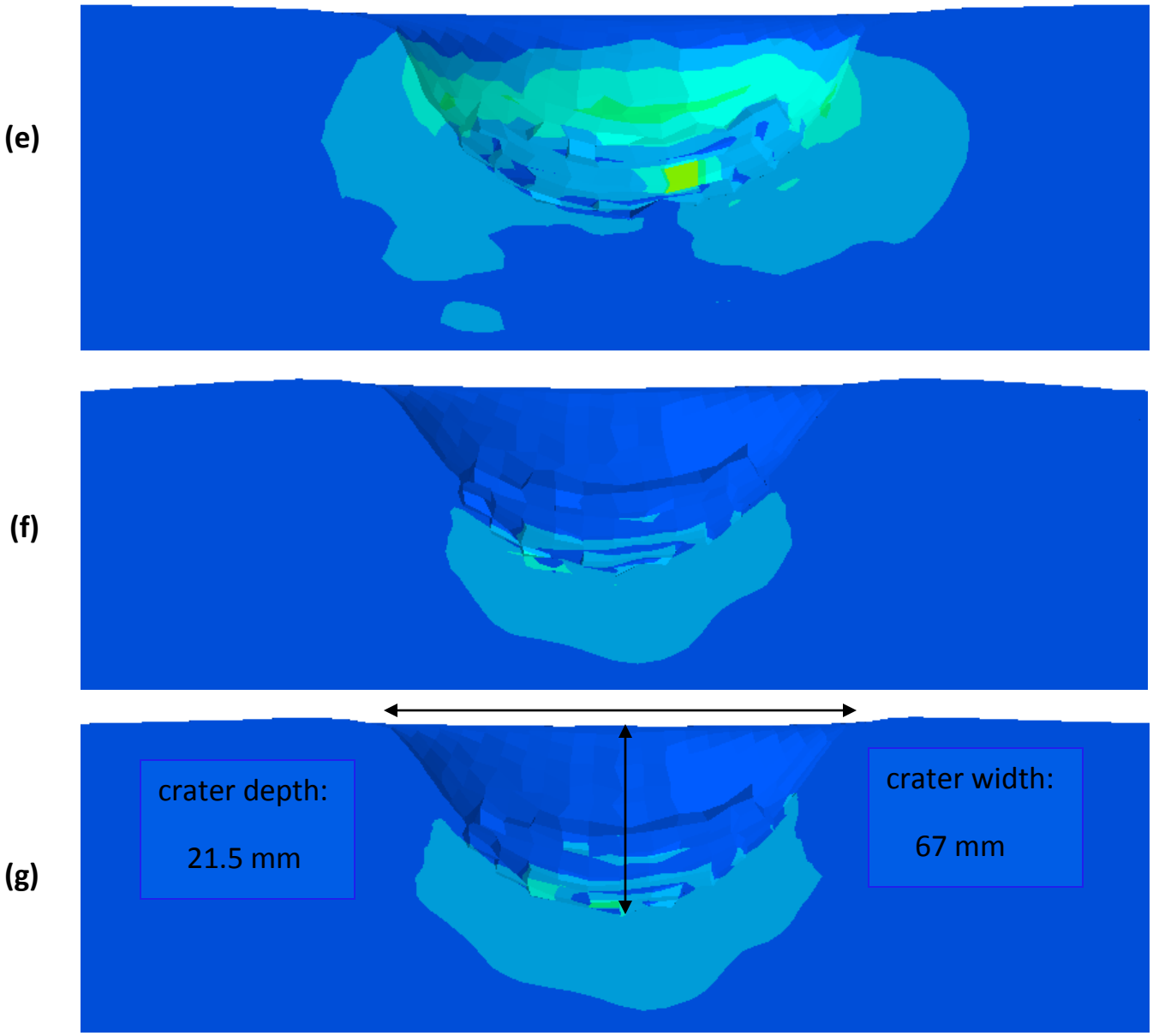

Figure 26. Contour plot of pressure in a small region of the clay around the crater at 3 μs (a), 6 μs (b), 9 μs (c), 12 μs (d), 15 μs (e), 21 μs (f), and 27 μs (g); **legend units: Pa**

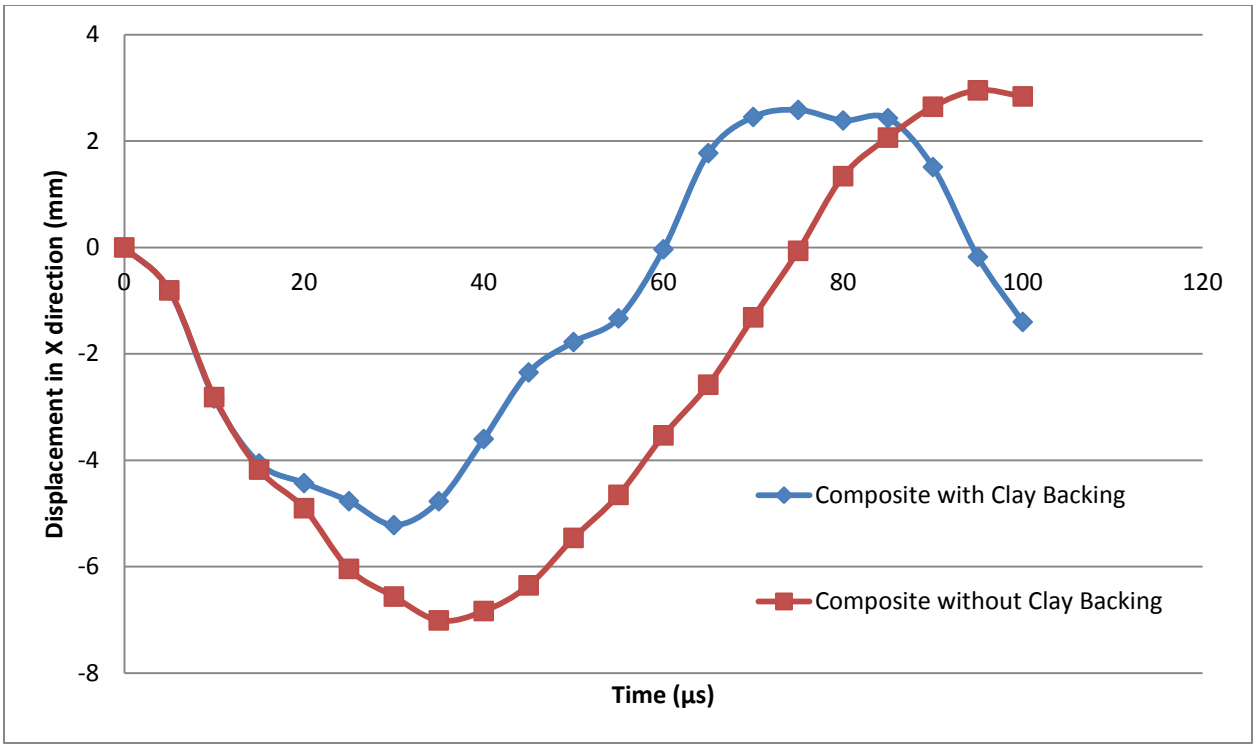

Figure 27. Time histories of the transverse displacement of the center of the impacted face of the laminate with and without the clay backing.

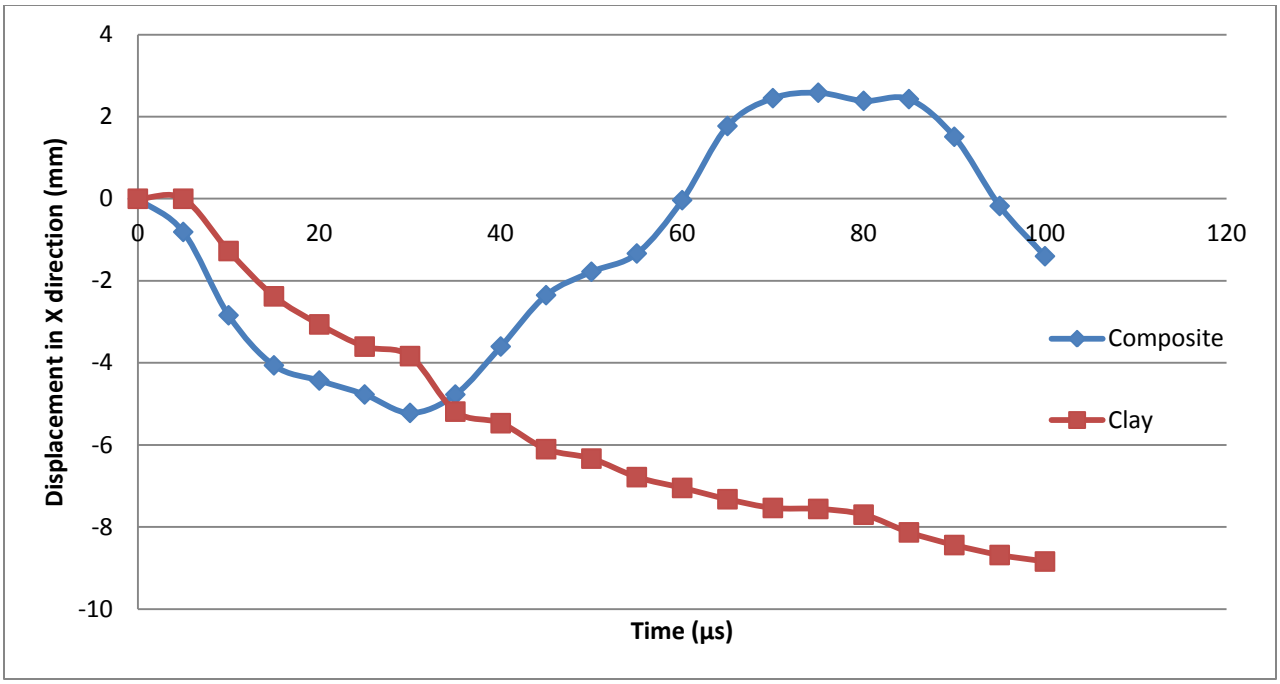

Figure 28. Time histories of the deflection of the center of the bottom surface of the laminate and the corresponding clay particle.

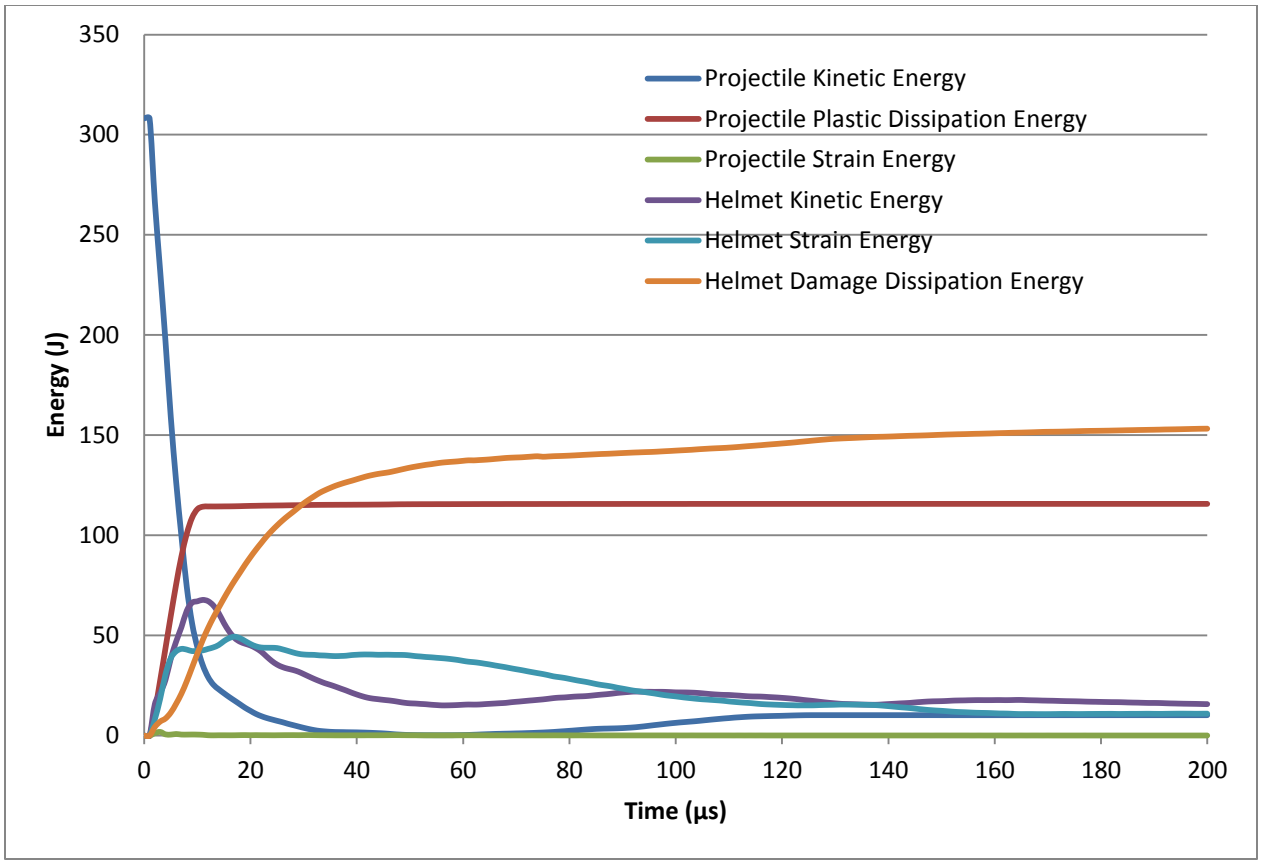

Figure 29. Time history of projectile and helmet energies for front helmet impact by FSP with an initial speed of 750 m/s.

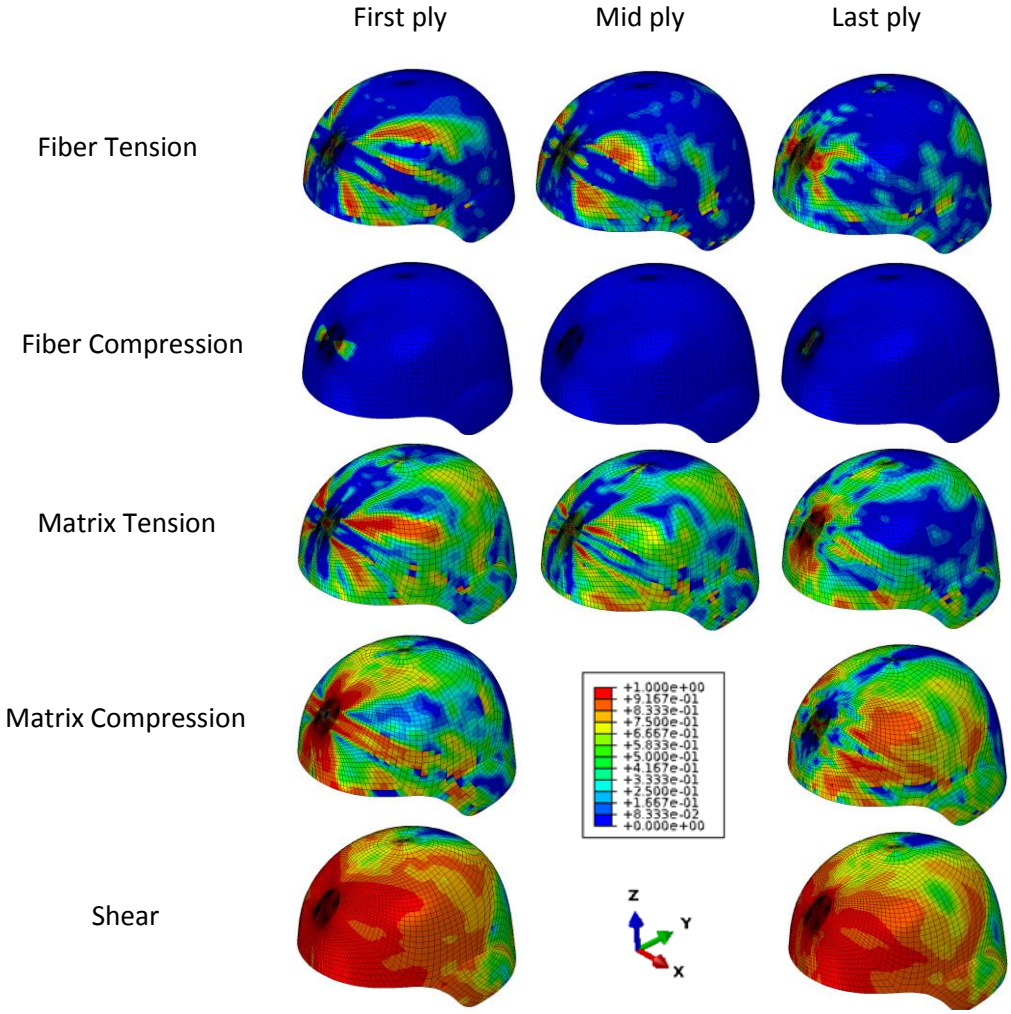

Figure 30. Damage modes in helmet for $v_0 = 0.6\ v_{BL}$ at 200 µs.

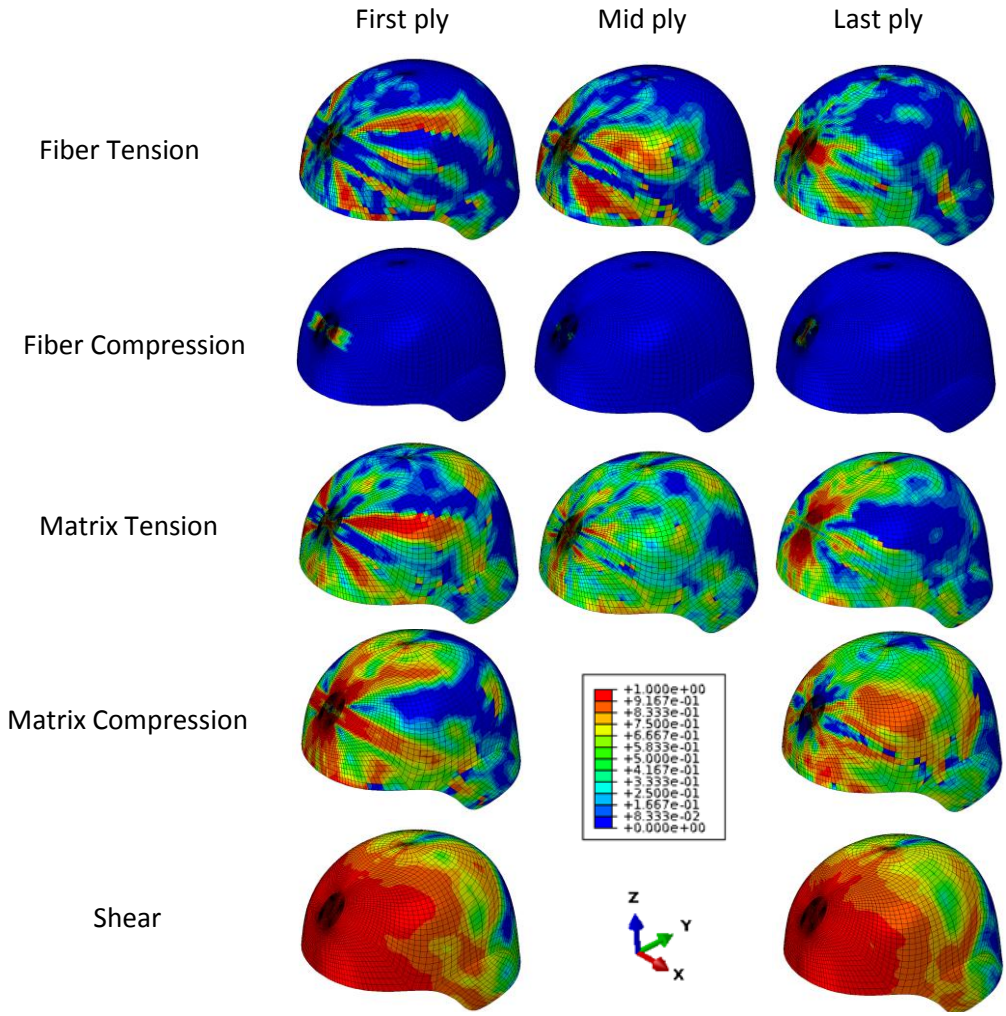

Figure 31. Damage modes in helmet for $v_0 = 0.9\ v_{BL}$ at 200 µs.

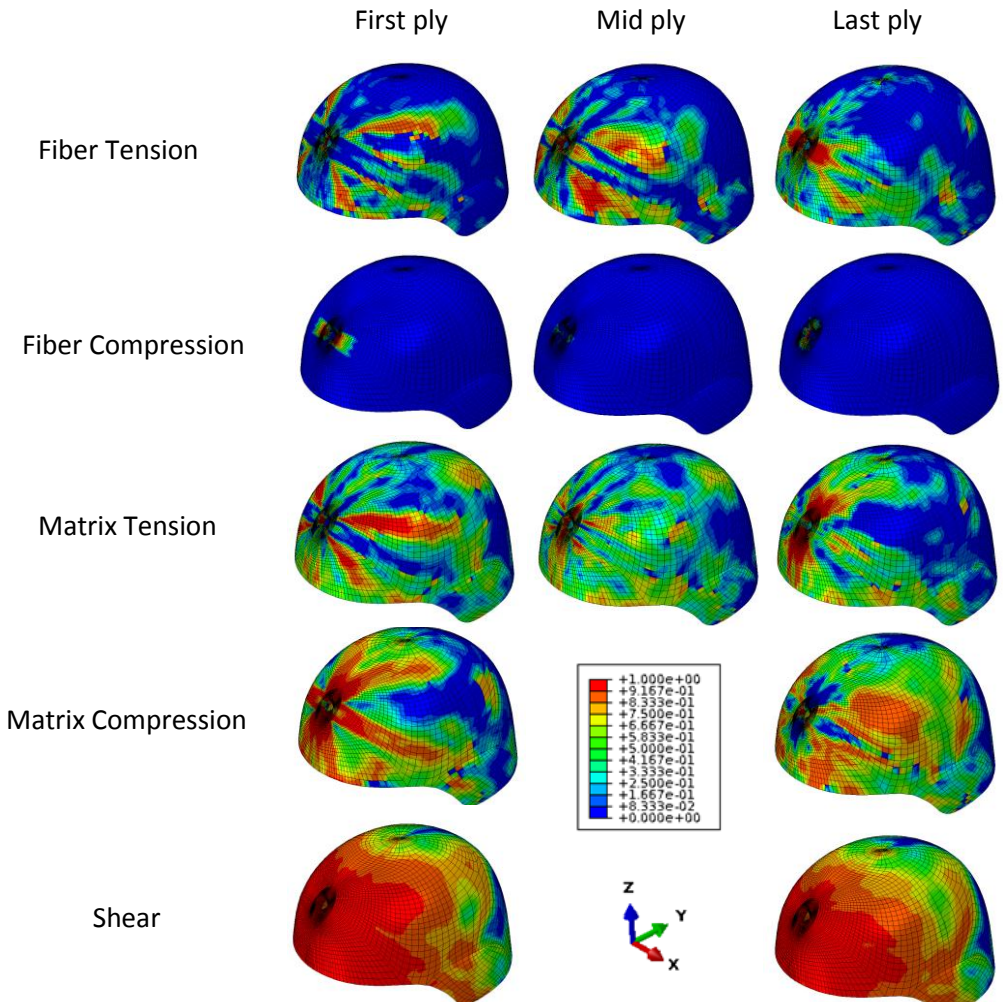

Figure 32. Damage modes in helmet for $v_0 = v_{BL}$ at 200 µs.

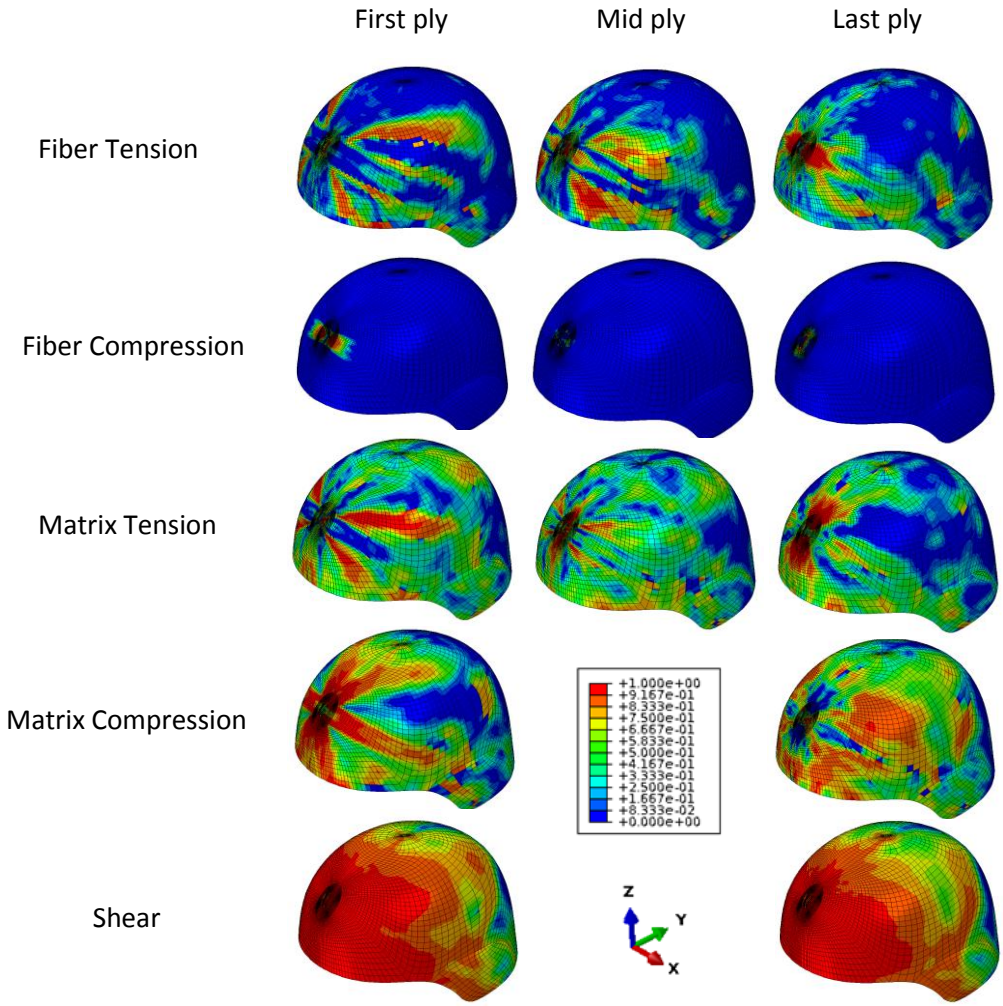

Figure 33. Damage modes in helmet for $v_0 = 1.2\ v_{BL}$ at 200 µs.

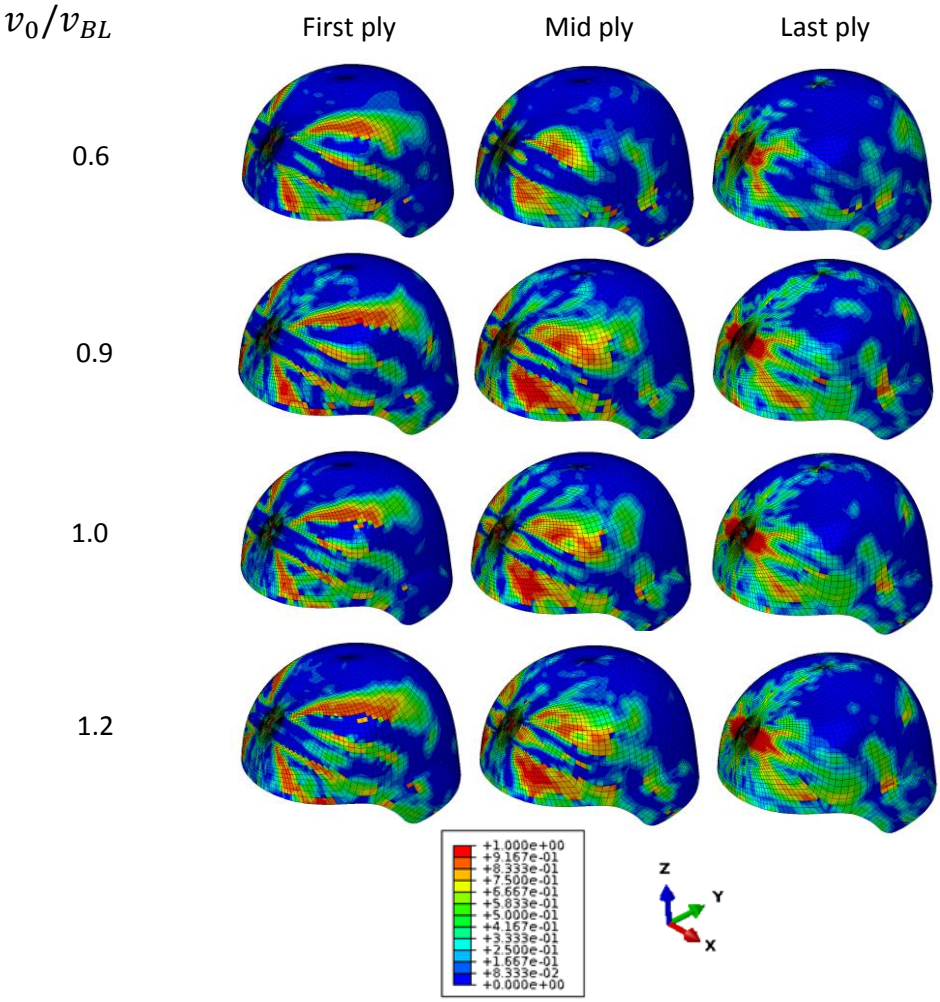

Figure 34. Comparison of helmet fiber tension damage for the impact speeds studied at 200 µs.

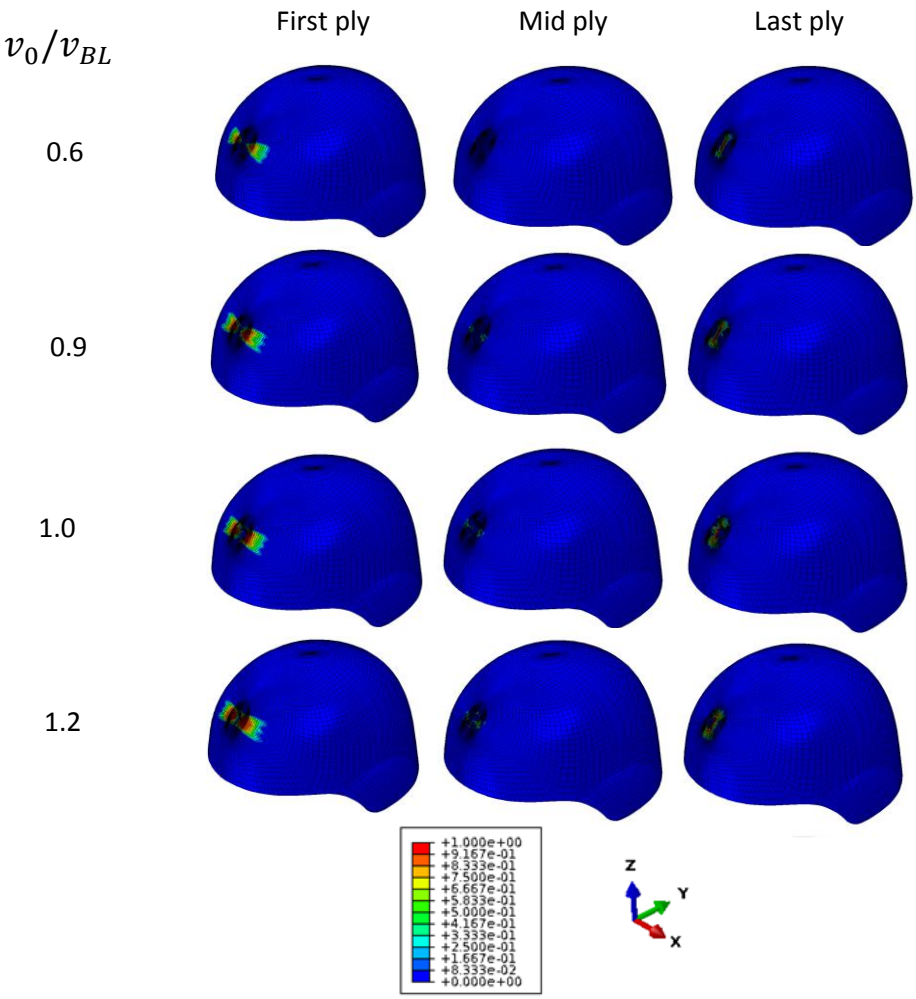

Figure 35. Comparison of helmet fiber compression damage for the impact speeds studied at 200 μs.

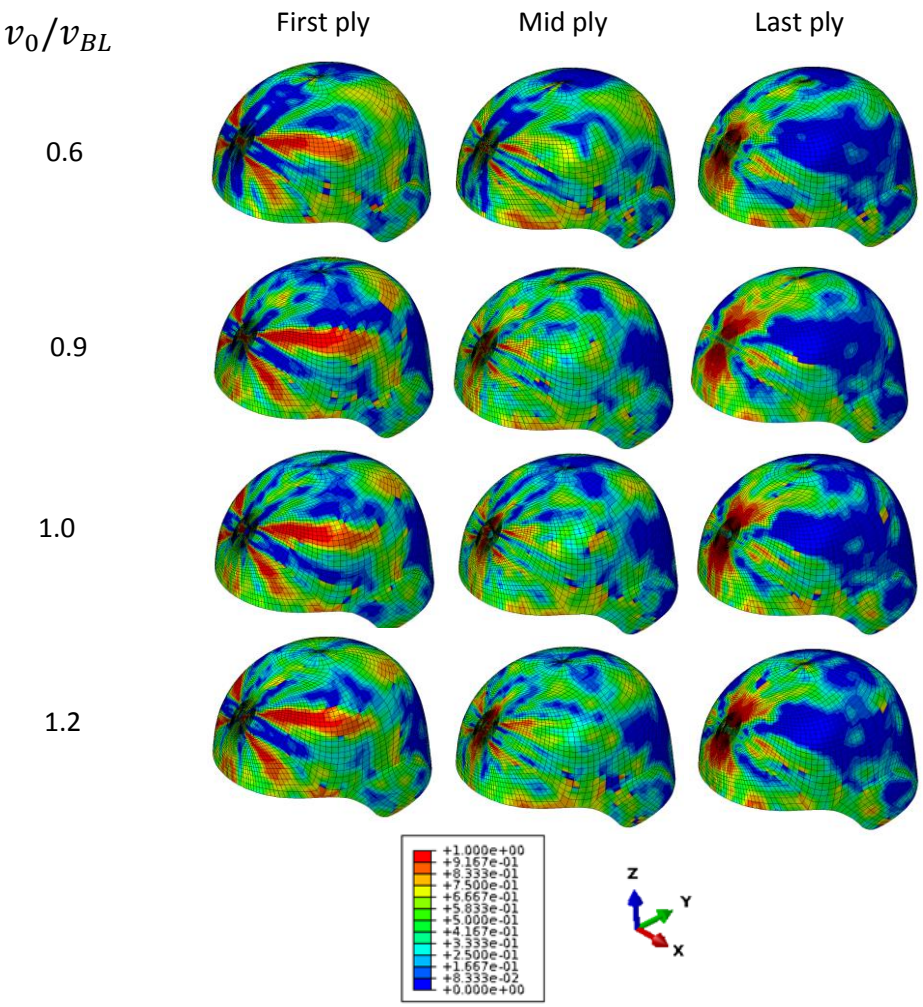

Figure 36. Comparison of helmet matrix tension damage for the impact speeds studied at 200 μs.

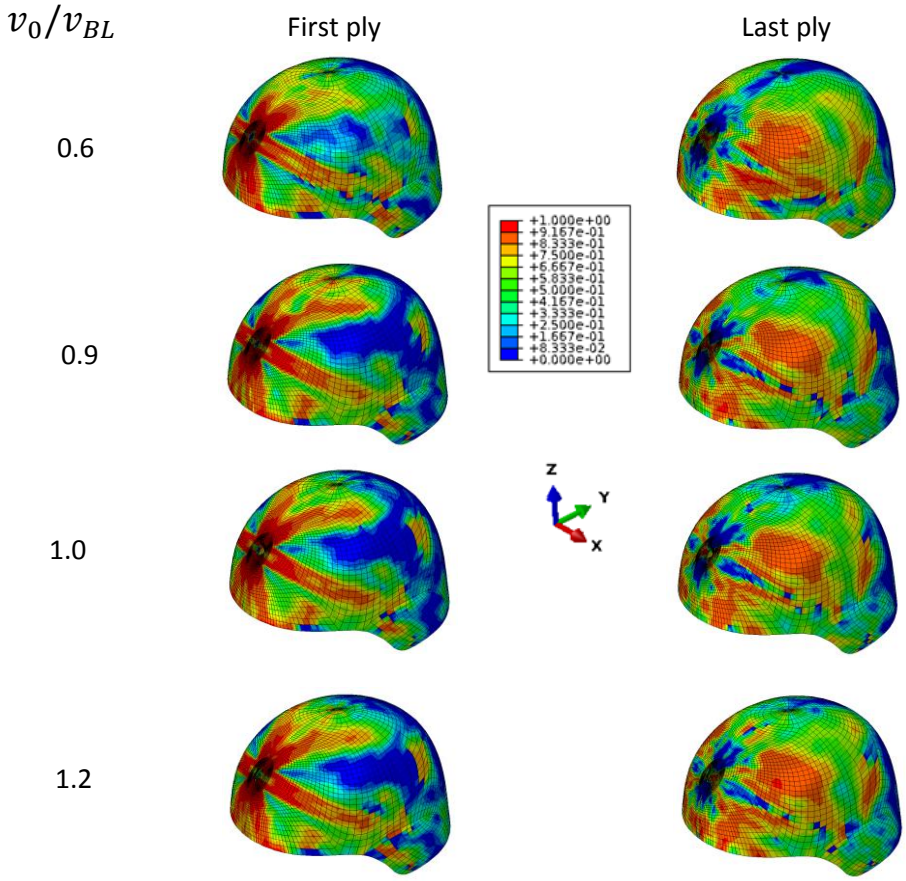

Figure 37. Comparison of helmet matrix compression damage for the impact speeds studied at 200 µs.

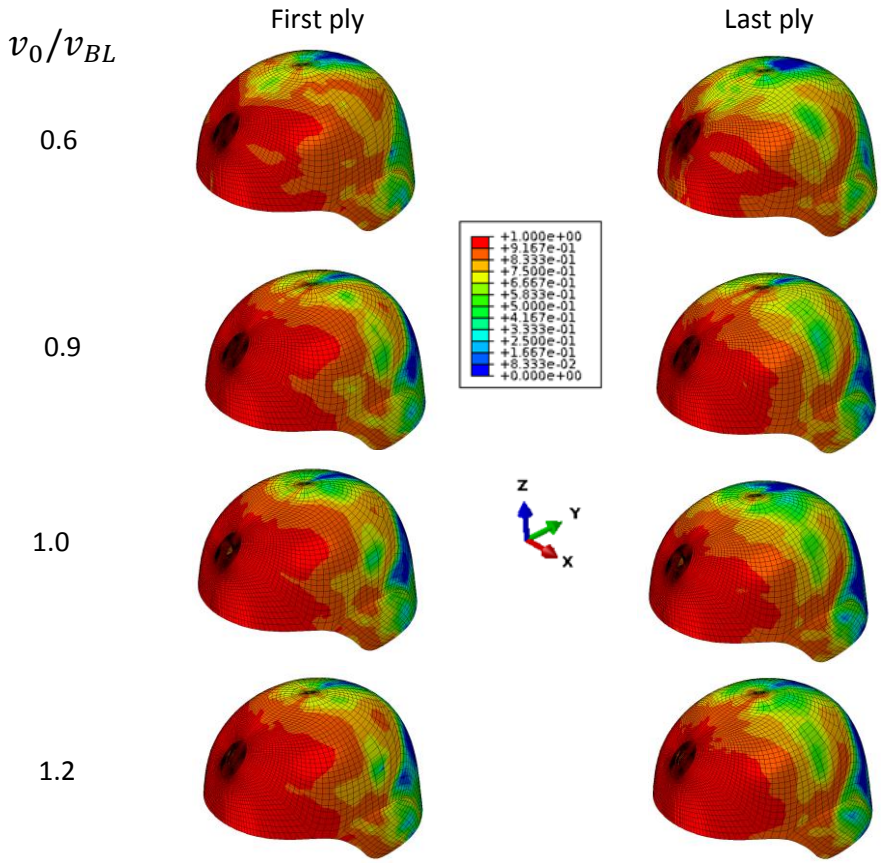

Figure 38. Comparison of helmet shear damage for the impact speeds studied at 200 µs.

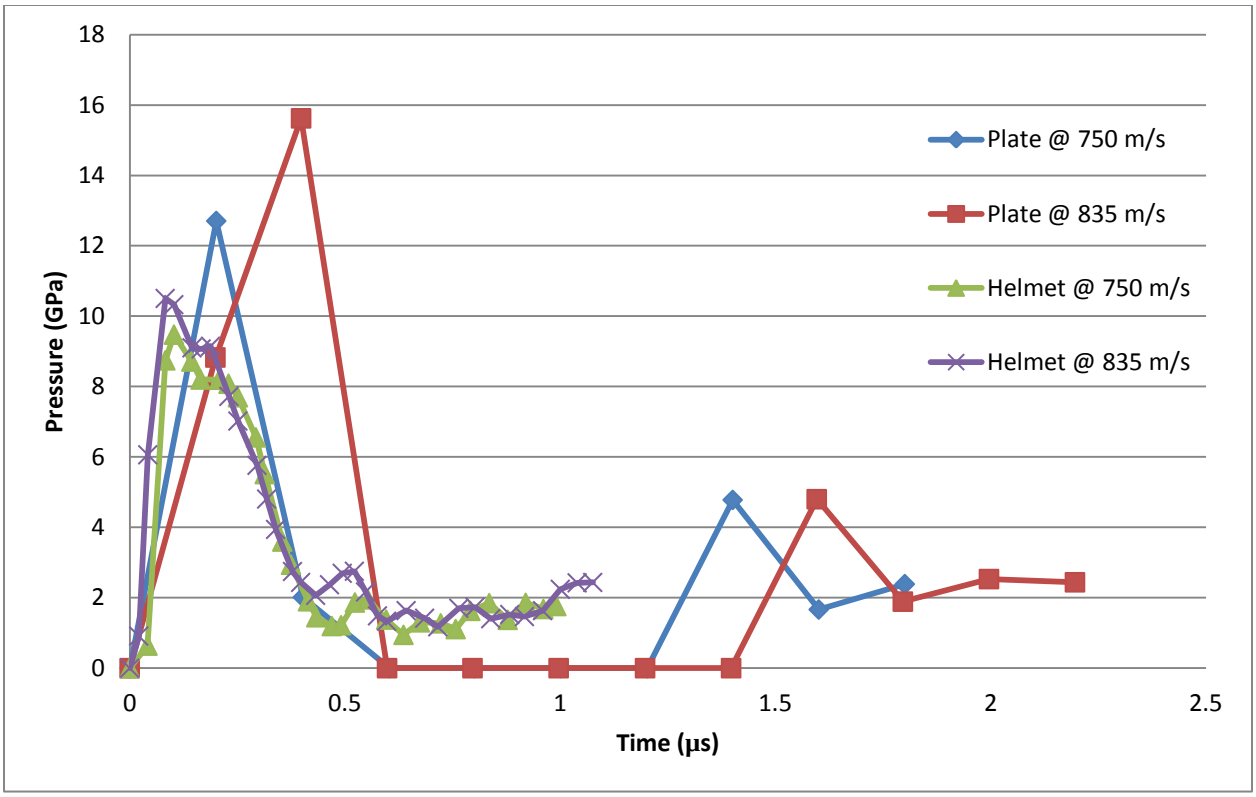

Figure 39. Time histories of the pressure at the initial point of contact for impact speeds of 750 m/s and 835 m/s.

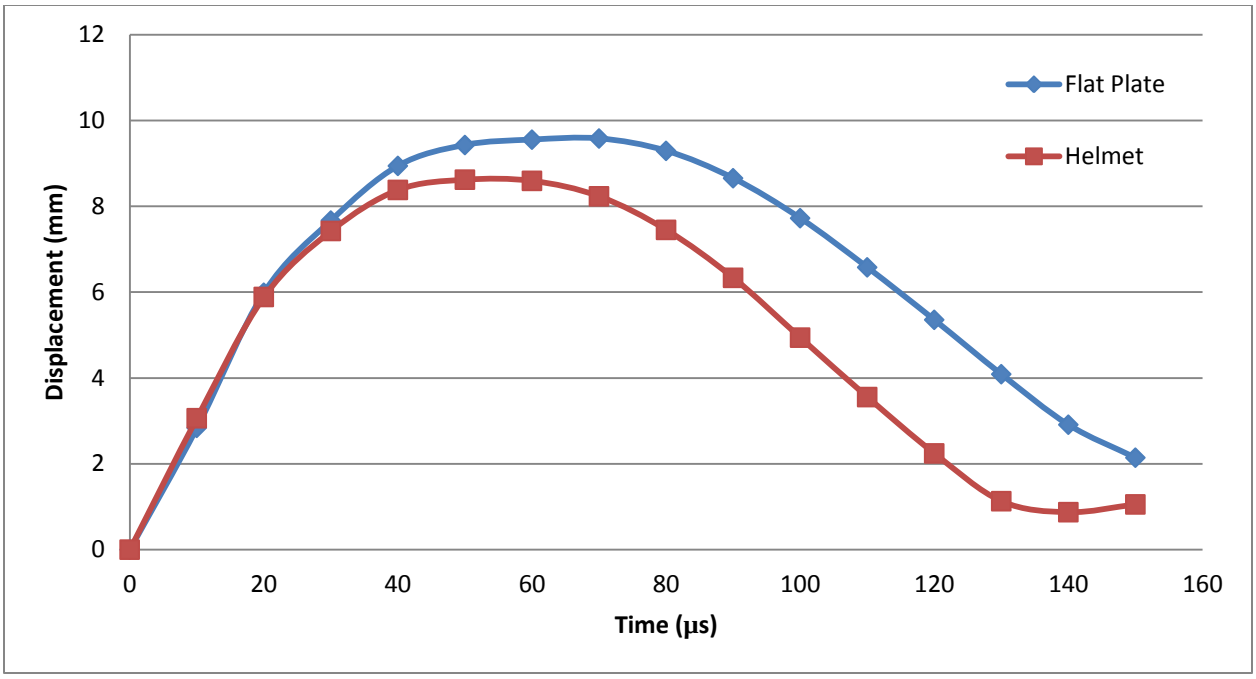

Figure 40. Time histories of the displacement of the initial point of contact for impact speeds of 750 m/s.

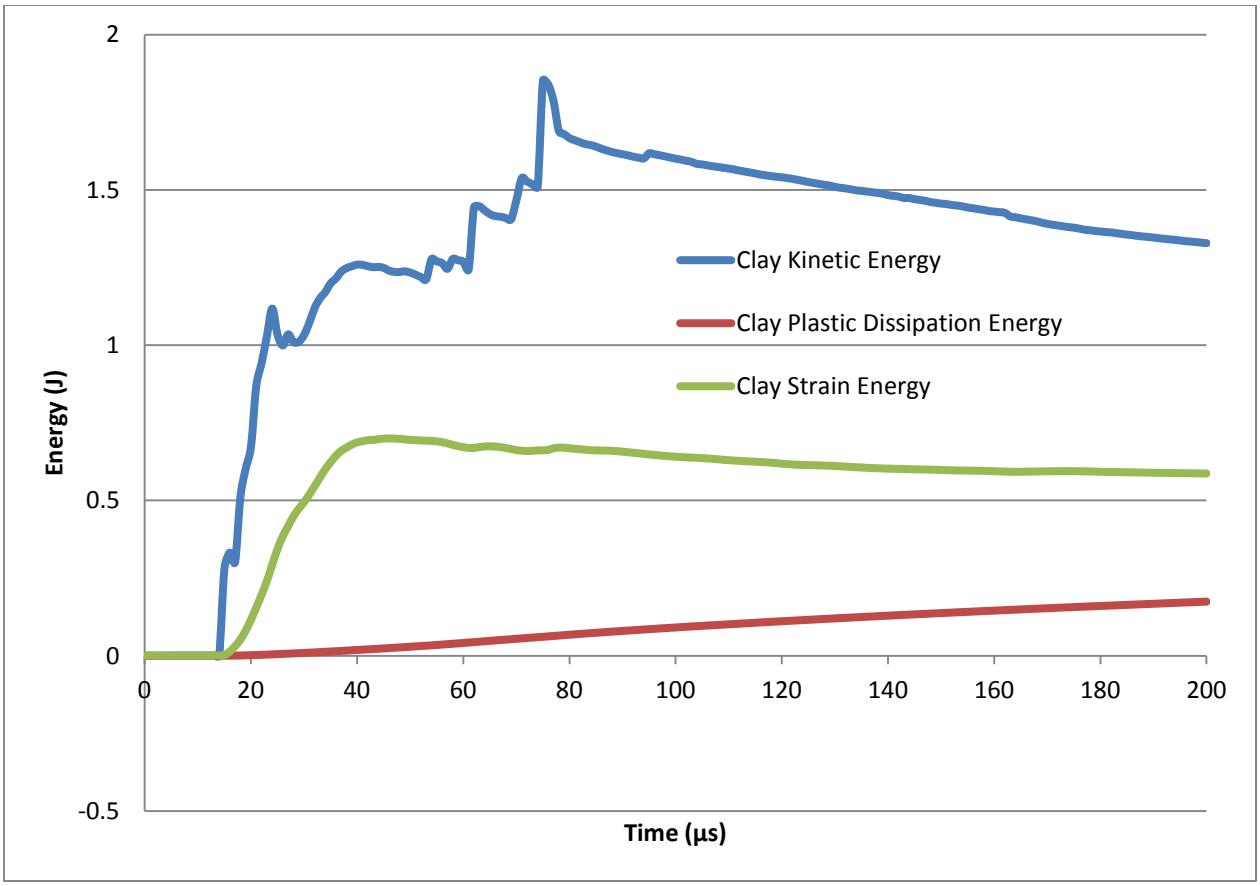

Figure 41. Time history of clay energies for front helmet impact.

(a)

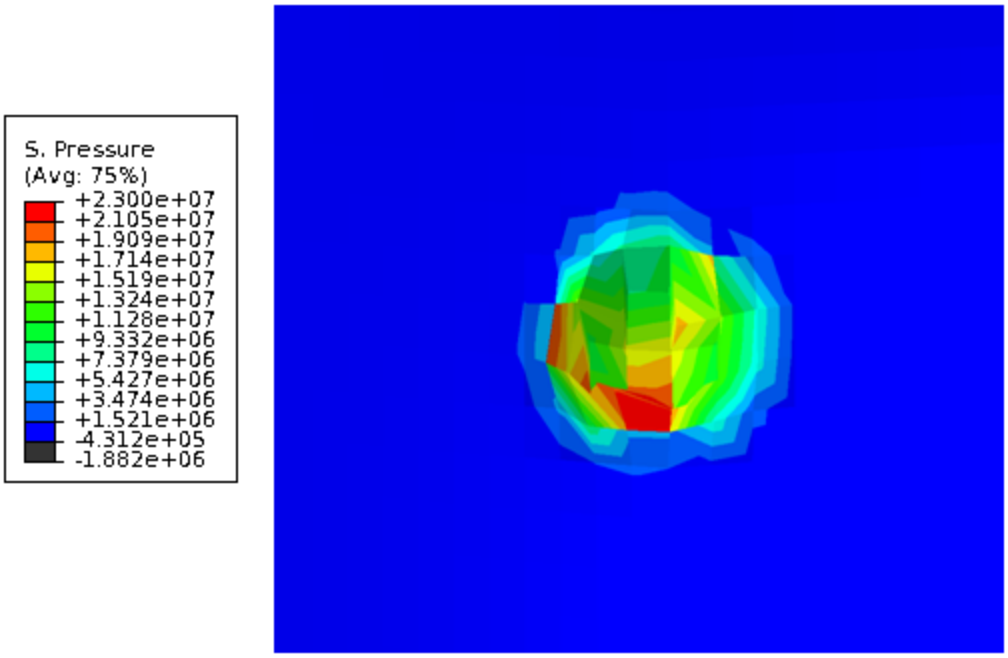
S. Pressure
(Avg: 75%)
+2.300e+07
+2.105e+07
+1.909e+07
+1.714e+07
+1.519e+07
+1.324e+07
+1.128e+07
+9.332e+06
+7.379e+06
+5.427e+06
+3.474e+06
+1.521e+06
-4.312e+05
-1.882e+06

(b)

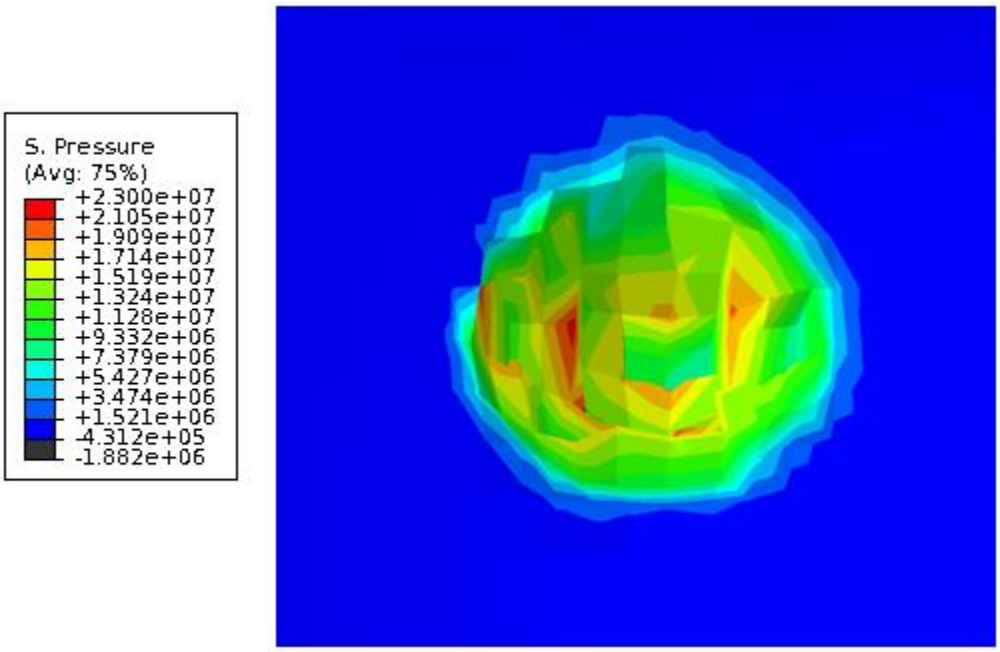
S. Pressure
(Avg: 75%)
+2.300e+07
+2.105e+07
+1.909e+07
+1.714e+07
+1.519e+07
+1.324e+07
+1.128e+07
+9.332e+06
+7.379e+06
+5.427e+06
+3.474e+06
+1.521e+06
-4.312e+05
-1.882e+06

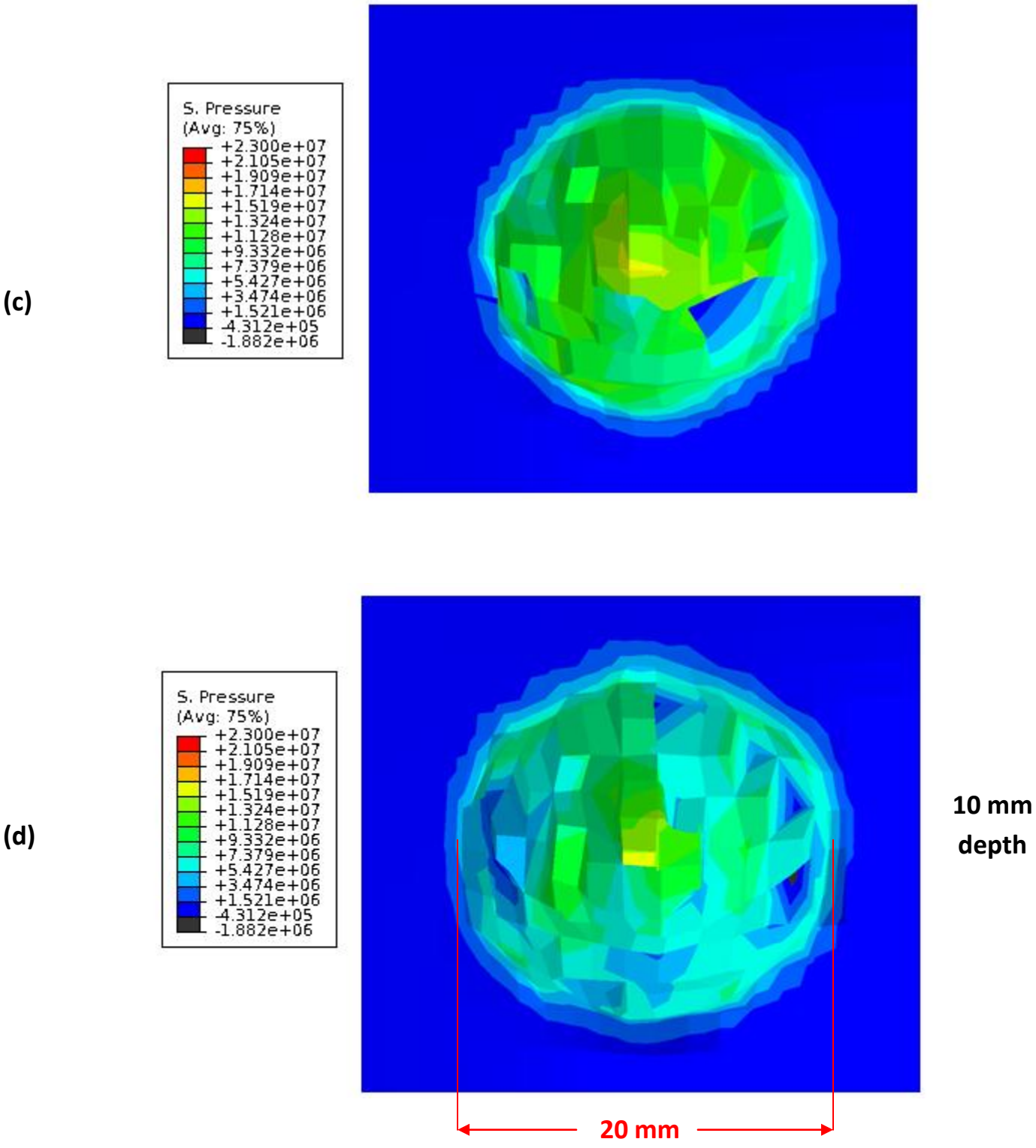

Figure 42. Contour plot of pressure in clay section of headform at 19.5 µs (a), 26 µs (b), 32.5 µs (c), and 39 µs (d) after simulation beginning for $v_0 = 90\%\ v_{BL}$ case; volume of crater ~2100 cubic mm; **legend units: Pa**

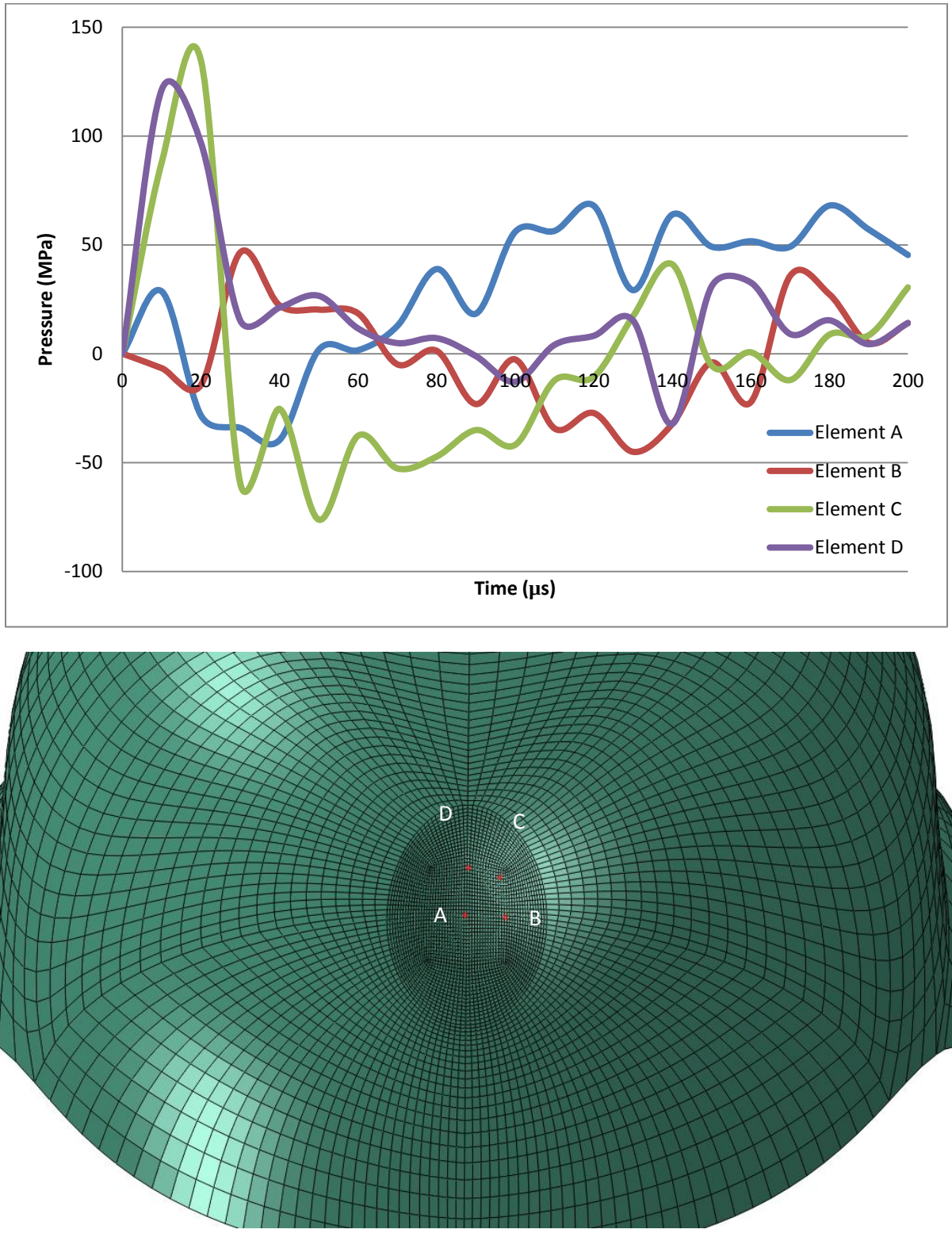

Figure 43. Time history of pressure of four elements on the back of the helmet during front helmet impact by FSP with an initial speed of 750 m/s.

(a)

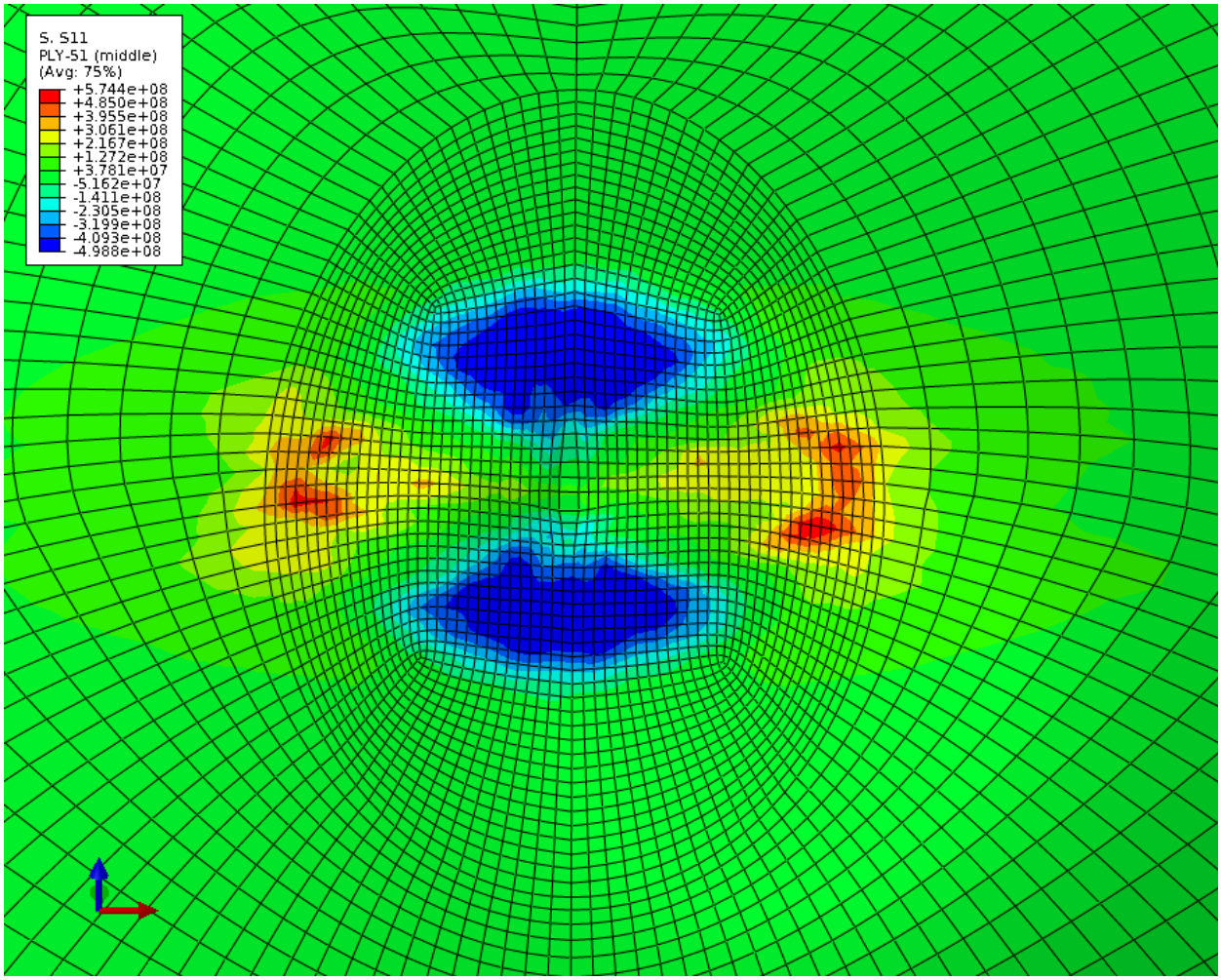
S, S11
PLY-S1 (middle)
(Avg: 75%)
+5.744e+08
+4.850e+08
+3.955e+08
+3.061e+08
+2.167e+08
+1.272e+08
+3.781e+07
-5.162e+07
-1.411e+08
-2.305e+08
-3.199e+08
-4.093e+08
-4.988e+08

(b)

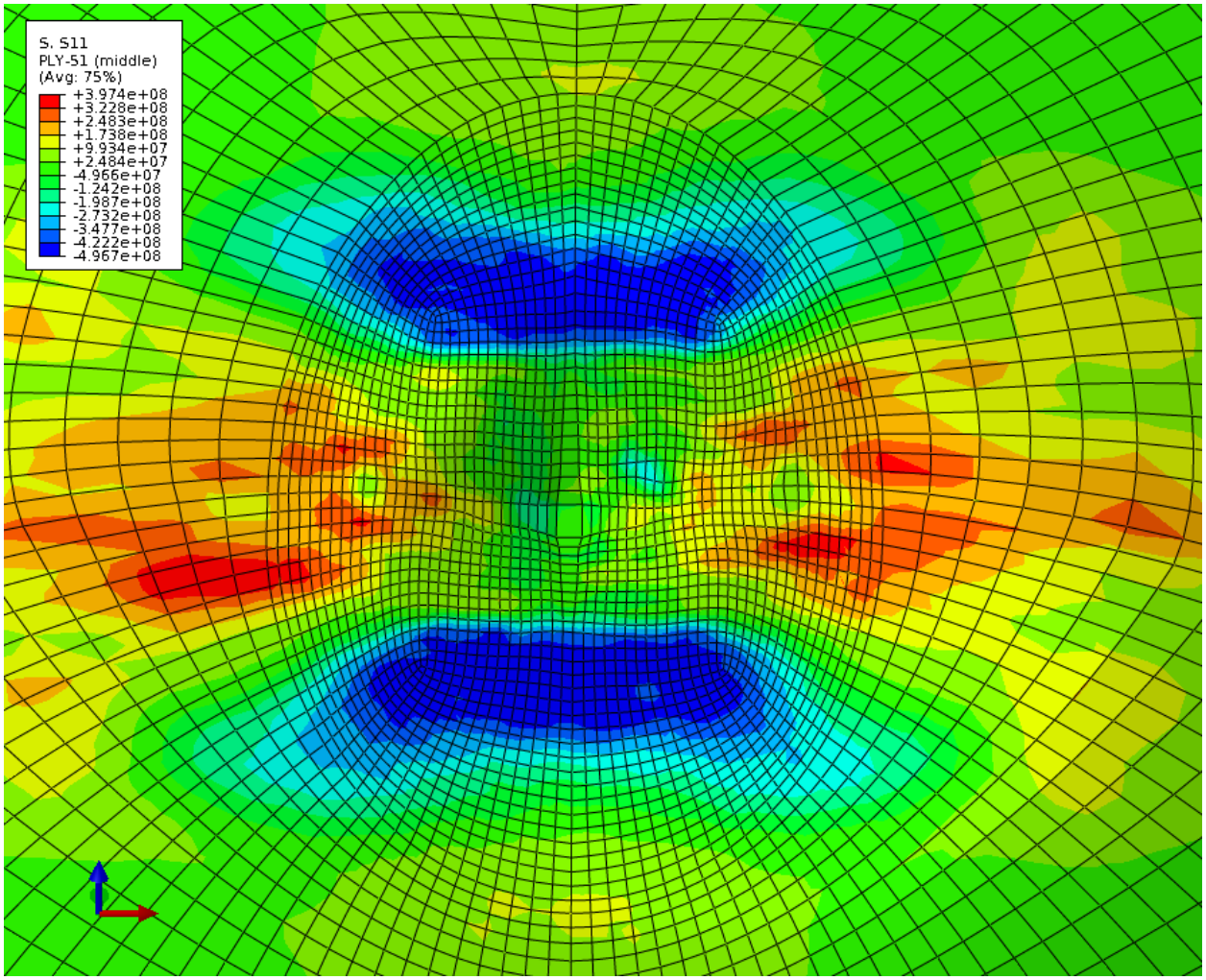
S, S11
PLY-51 (middle)
(Avg: 75%)
+3.974e+08
+3.228e+08
+2.483e+08
+1.738e+08
+9.934e+07
+2.484e+07
-4.966e+07
-1.242e+08
-1.987e+08
-2.732e+08
-3.477e+08
-4.222e+08
-4.967e+08

(c)

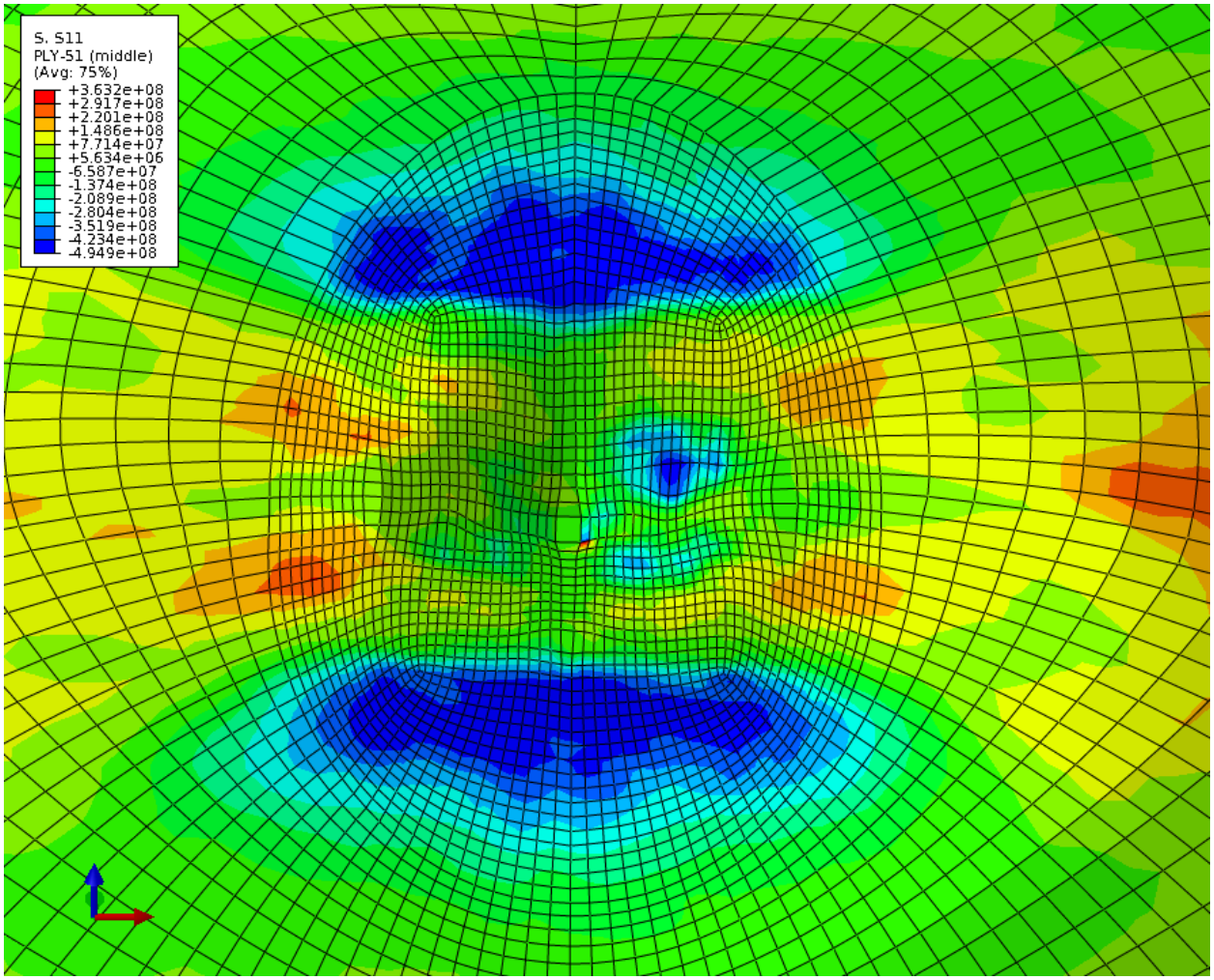
S, S11
PLY-51 (middle)
(Avg: 75%)
+3.632e+08
+2.917e+08
+2.201e+08
+1.486e+08
+7.714e+07
+5.634e+06
-6.587e+07
-1.374e+08
-2.089e+08
-2.804e+08
-3.519e+08
-4.234e+08
-4.949e+08

(d)

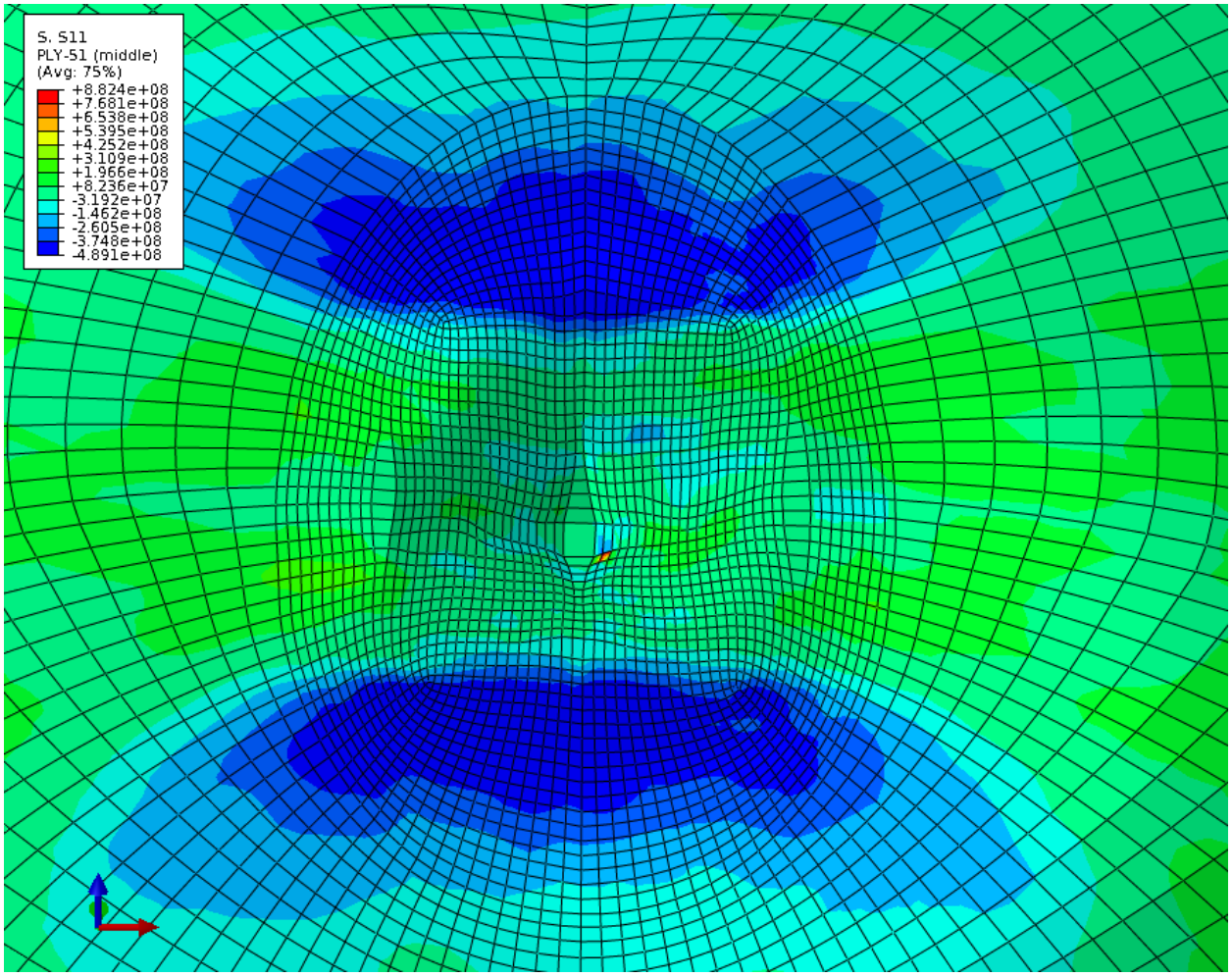
S, S11
PLY-51 (middle)
(Avg: 75%)
+8.824e+08
+7.681e+08
+6.538e+08
+5.395e+08
+4.252e+08
+3.109e+08
+1.966e+08
+8.236e+07
-3.192e+07
-1.462e+08
-2.605e+08
-3.748e+08
-4.891e+08

(e)

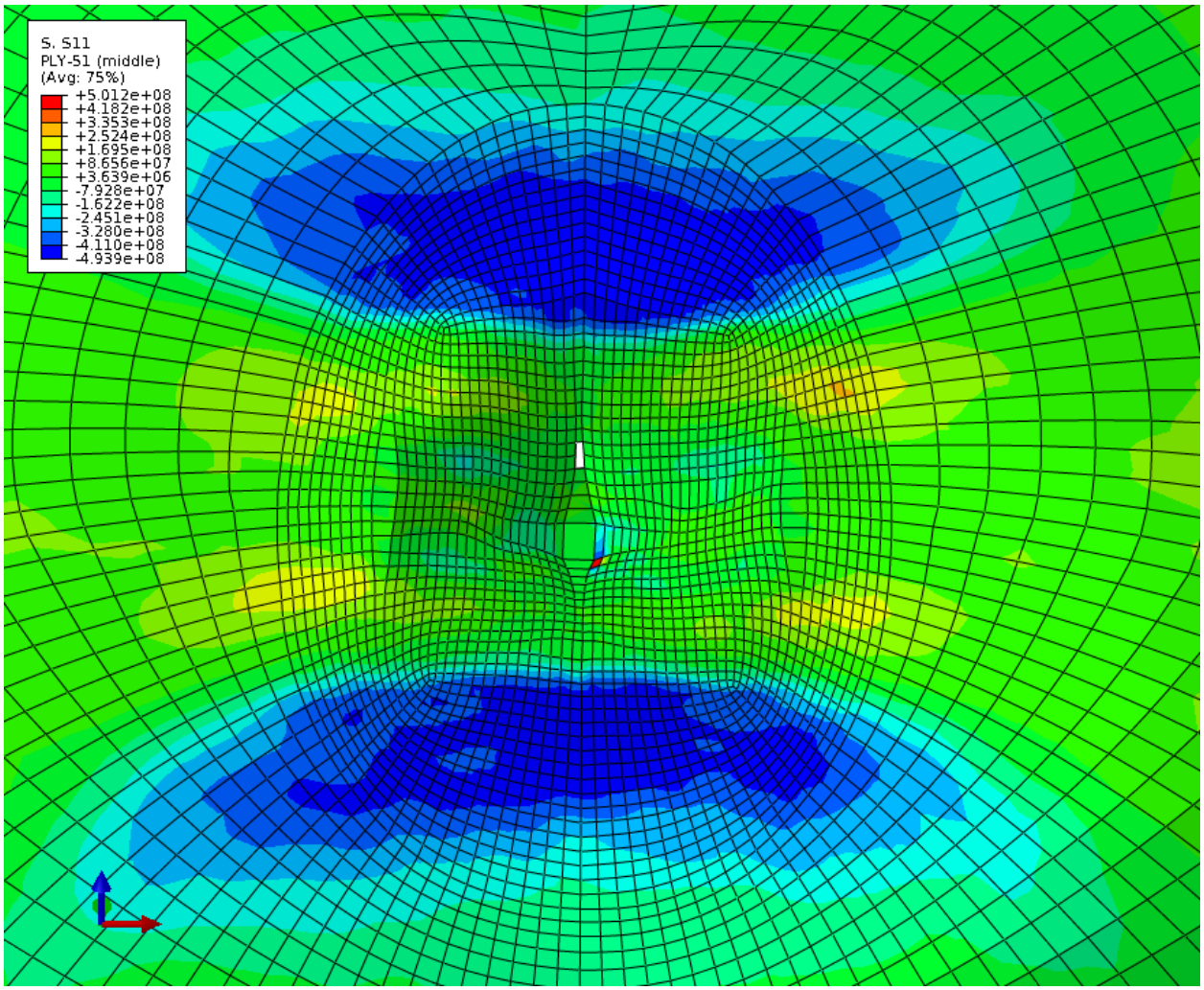
S, S11
PLY-51 (middle)
(Avg: 75%)
+5.012e+08
+4.182e+08
+3.353e+08
+2.524e+08
+1.695e+08
+8.656e+07
+3.639e+06
-7.928e+07
-1.622e+08
-2.451e+08
-3.280e+08
-4.110e+08
-4.939e+08

(f)

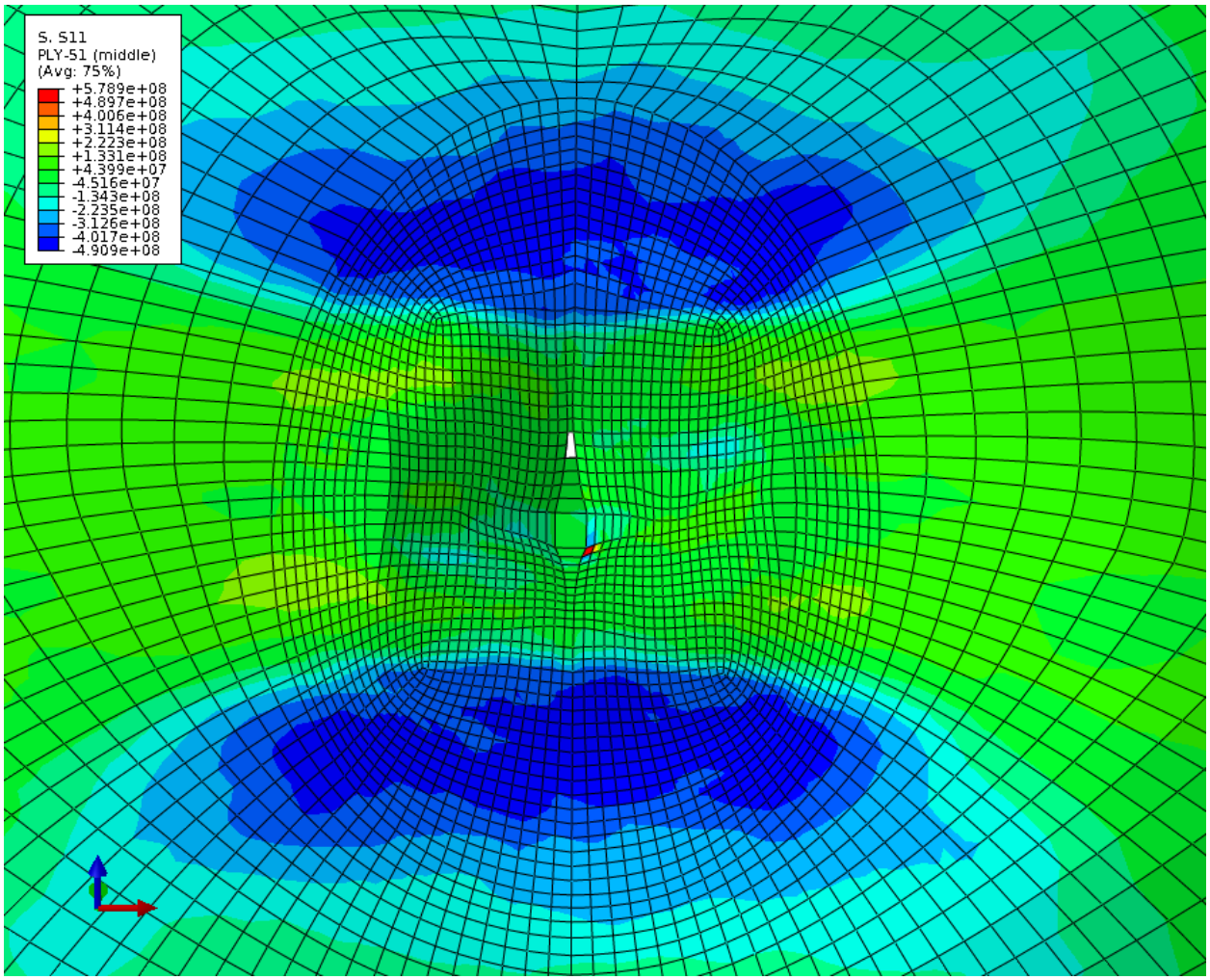
S, S11
PLY-S1 (middle)
(Avg: 75%)
+5.789e+08
+4.897e+08
+4.006e+08
+3.114e+08
+2.223e+08
+1.331e+08
+4.399e+07
-4.516e+07
-1.343e+08
-2.235e+08
-3.126e+08
-4.017e+08
-4.909e+08

(g)

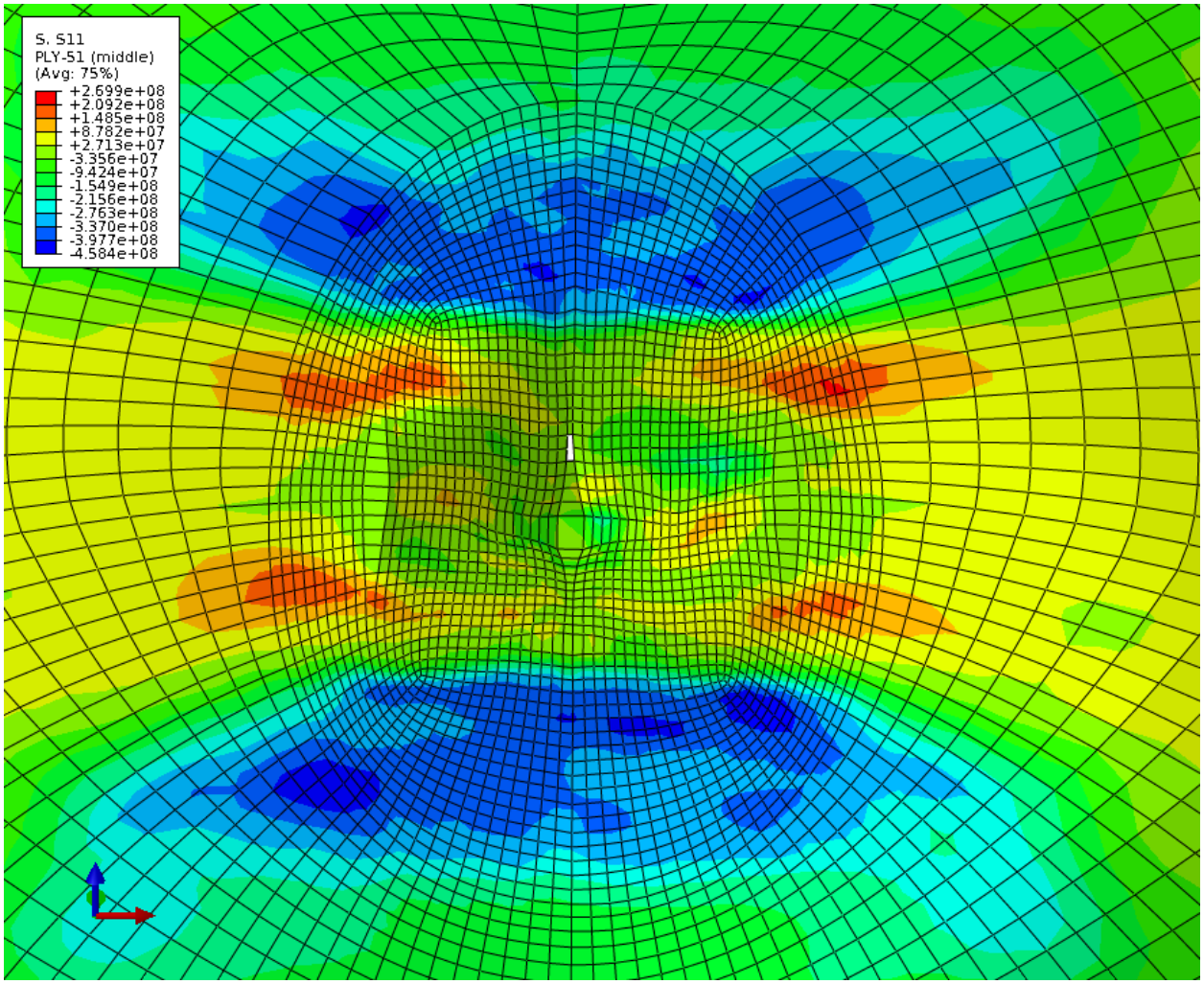
S, S11
PLY-51 (middle)
(Avg: 75%)
+2.699e+08
+2.092e+08
+1.485e+08
+8.782e+07
+2.713e+07
-3.356e+07
-9.424e+07
-1.549e+08
-2.156e+08
-2.763e+08
-3.370e+08
-3.977e+08
-4.584e+08

(h)

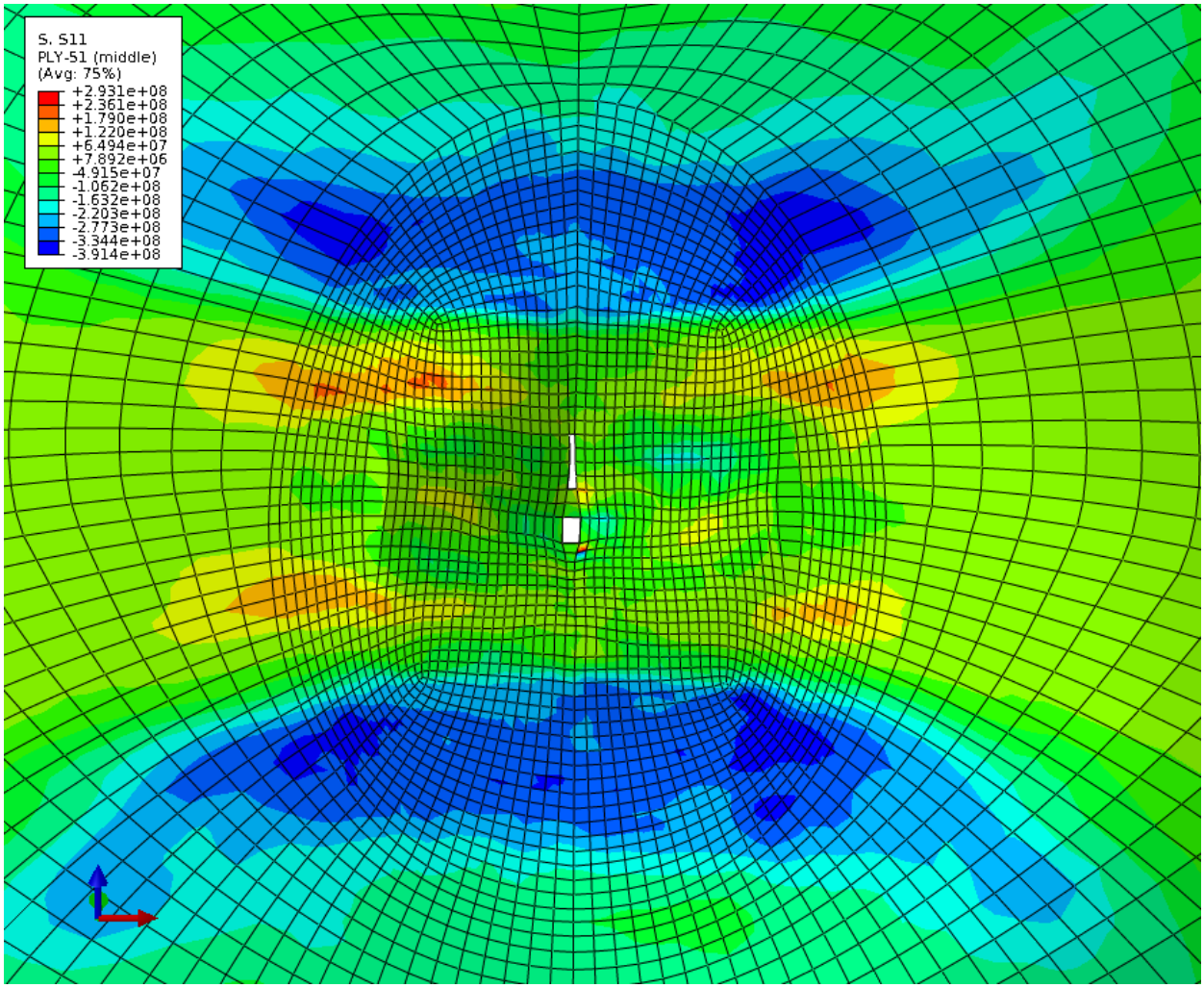
S, S11
PLY-S1 (middle)
(Avg: 75%)
+2.931e+08
+2.361e+08
+1.790e+08
+1.220e+08
+6.494e+07
+7.892e+06
-4.915e+07
-1.062e+08
-1.632e+08
-2.203e+08
-2.773e+08
-3.344e+08
-3.914e+08

(i)

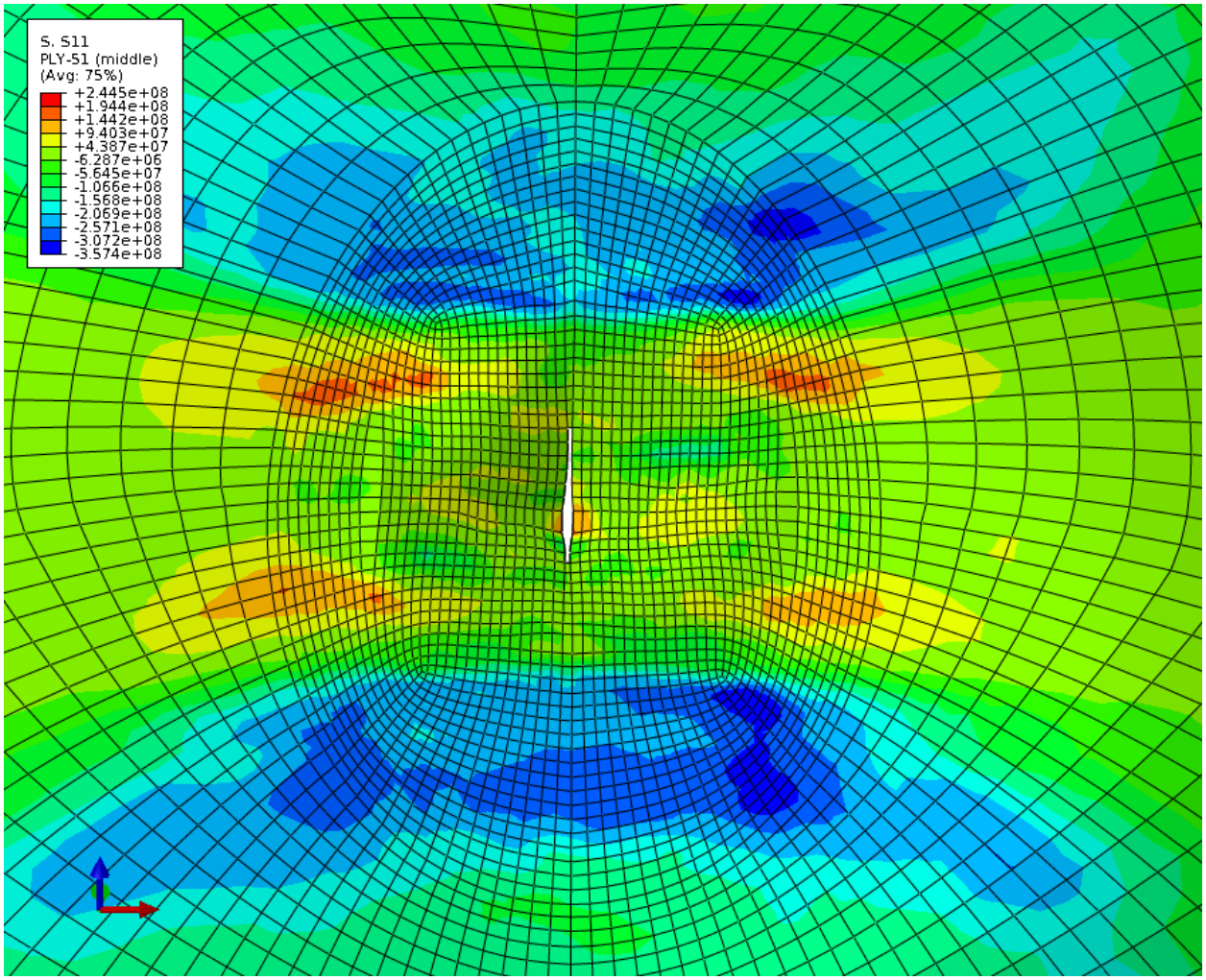
S, S11
PLY-51 (middle)
(Avg: 75%)
+2.445e+08
+1.944e+08
+1.442e+08
+9.403e+07
+4.387e+07
-6.287e+06
-5.645e+07
-1.066e+08
-1.568e+08
-2.069e+08
-2.571e+08
-3.072e+08
-3.574e+08

(j)

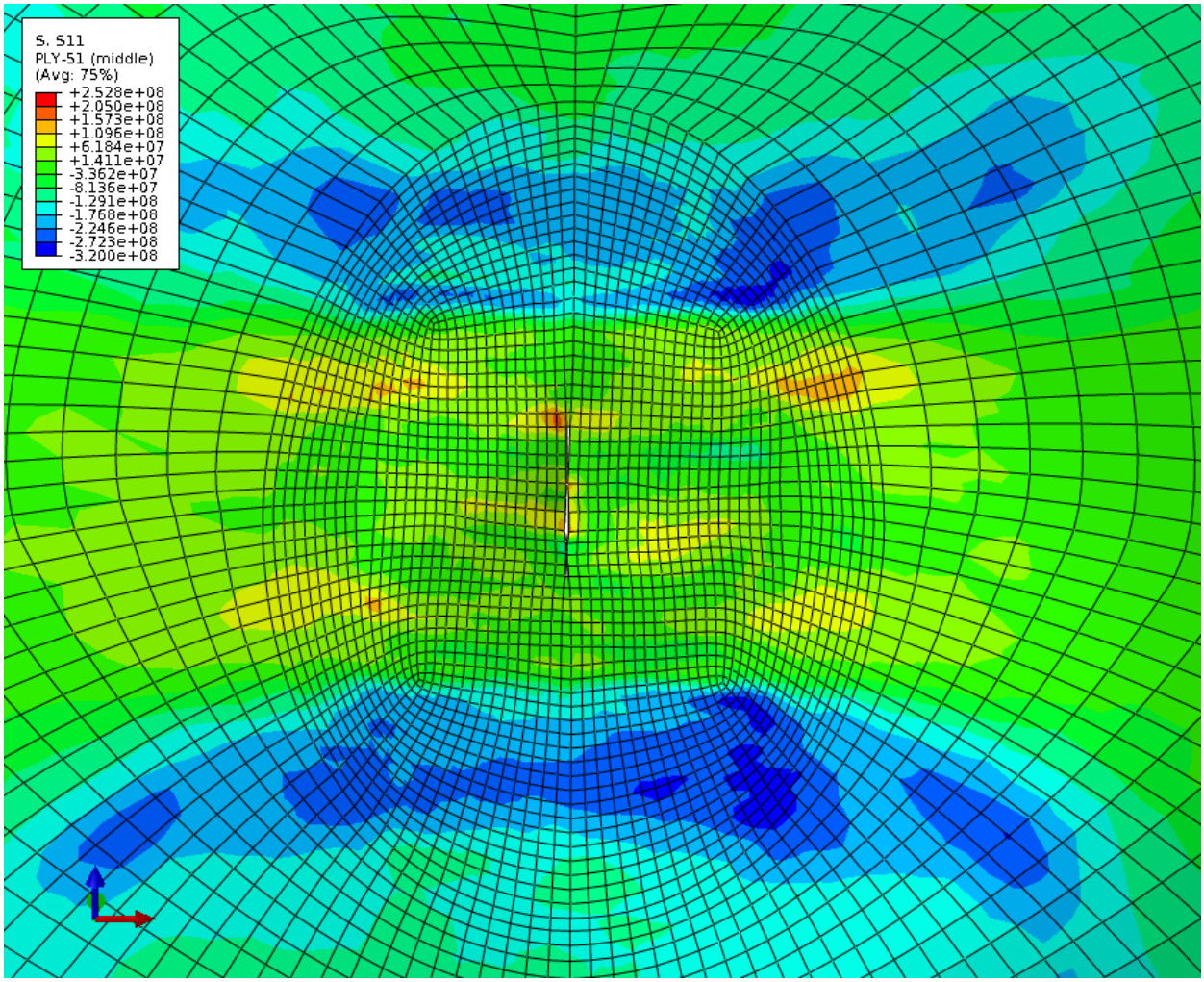

Figure 44. Contour plot of σ_{11}in back ply of helmet at 10 µs (a), 20 µs (b), 30 µs (c), 40 µs (d), 50 µs (e), 60 µs (f), 70 µs (g), 80 µs (h), 90 µs (i), and 100 µs (j) for $v_0 = 0.9\ v_{BL}$; **legend units: Pa**

(a)

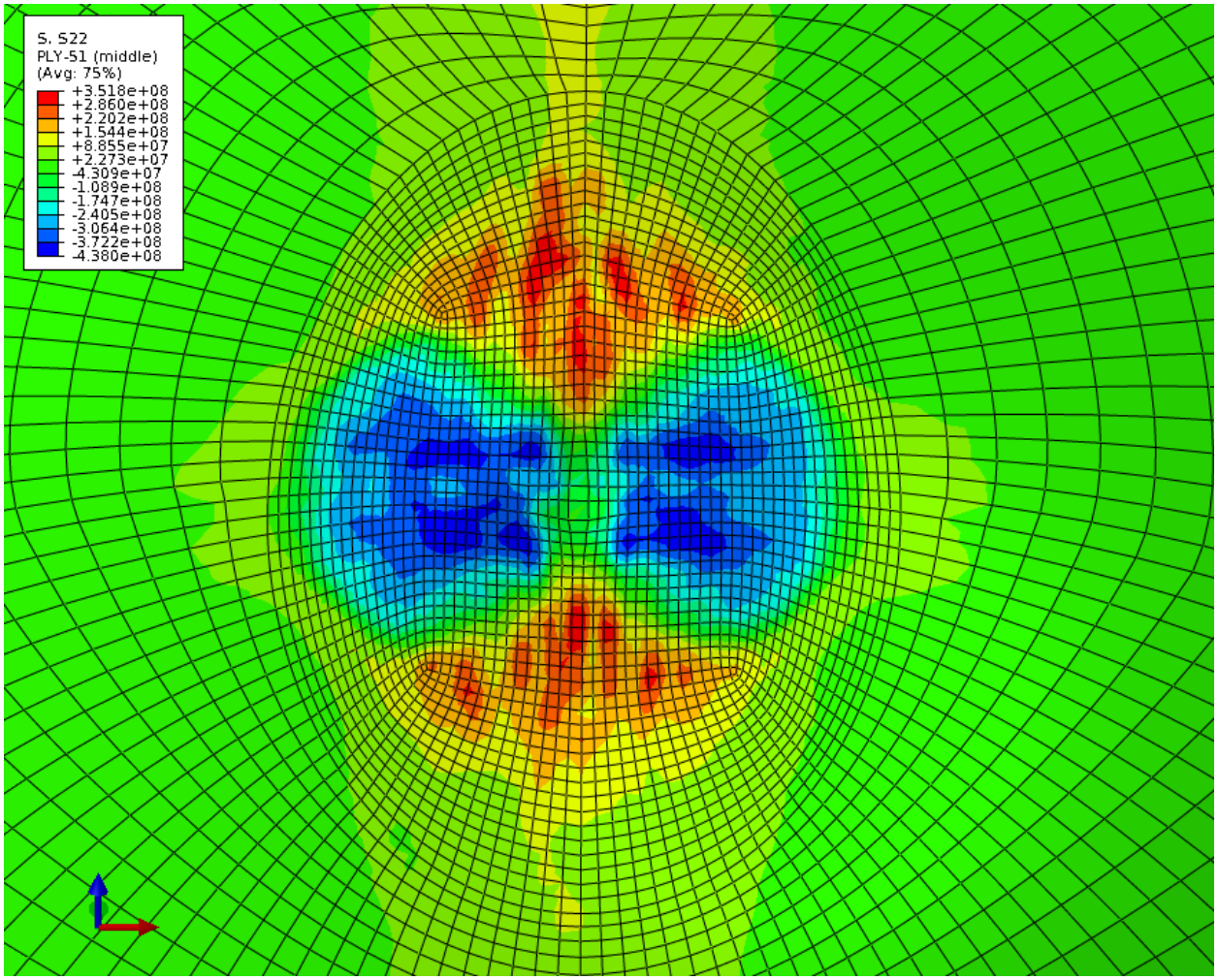
S, S22
PLY-51 (middle)
(Avg: 75%)
+3.518e+08
+2.860e+08
+2.202e+08
+1.544e+08
+8.855e+07
+2.273e+07
-4.309e+07
-1.089e+08
-1.747e+08
-2.405e+08
-3.064e+08
-3.722e+08
-4.380e+08

(b)

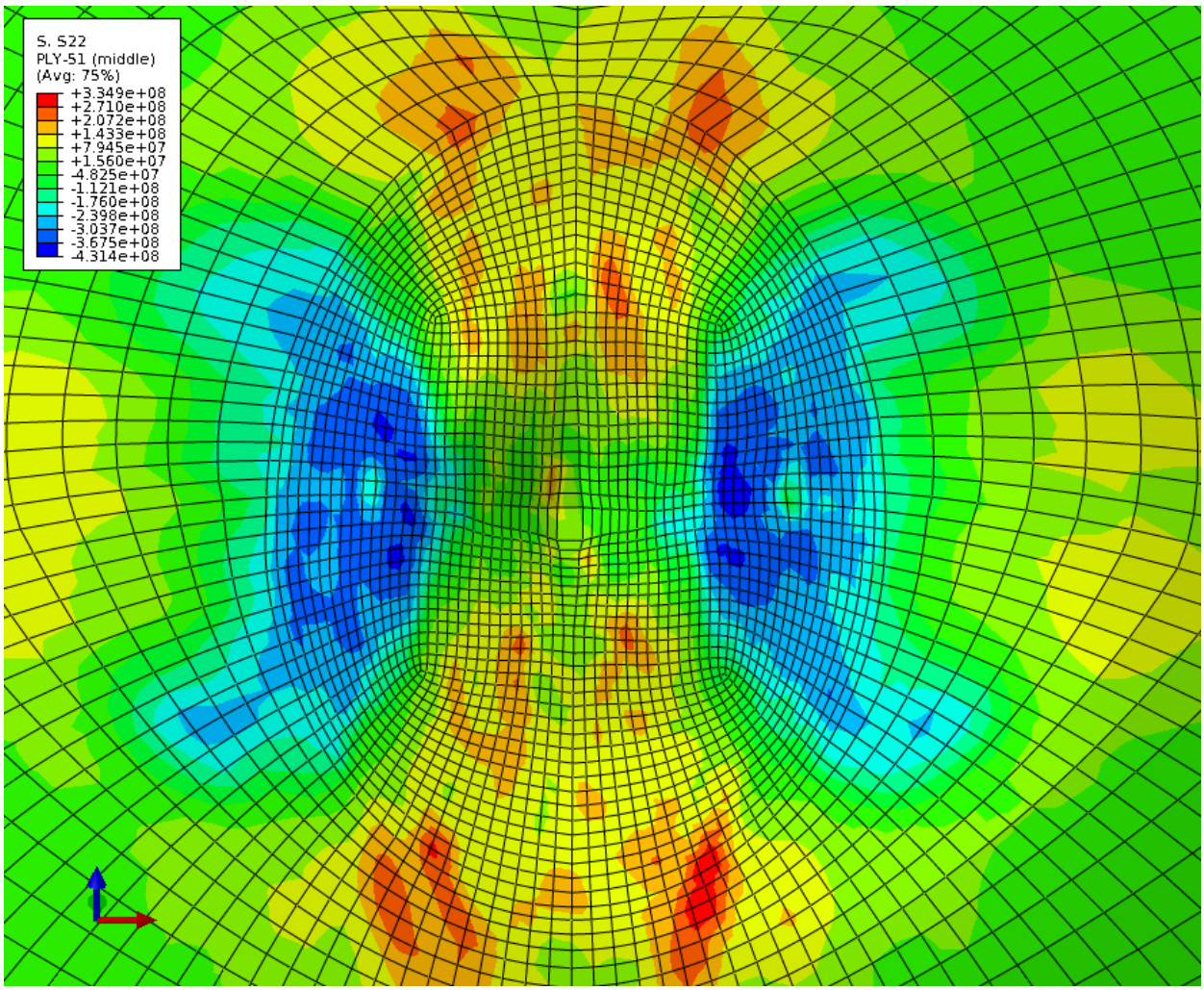
S, S22
PLY-S1 (middle)
(Avg: 75%)
+3.349e+08
+2.710e+08
+2.072e+08
+1.433e+08
+7.945e+07
+1.560e+07
-4.825e+07
-1.121e+08
-1.760e+08
-2.398e+08
-3.037e+08
-3.675e+08
-4.314e+08

(c)

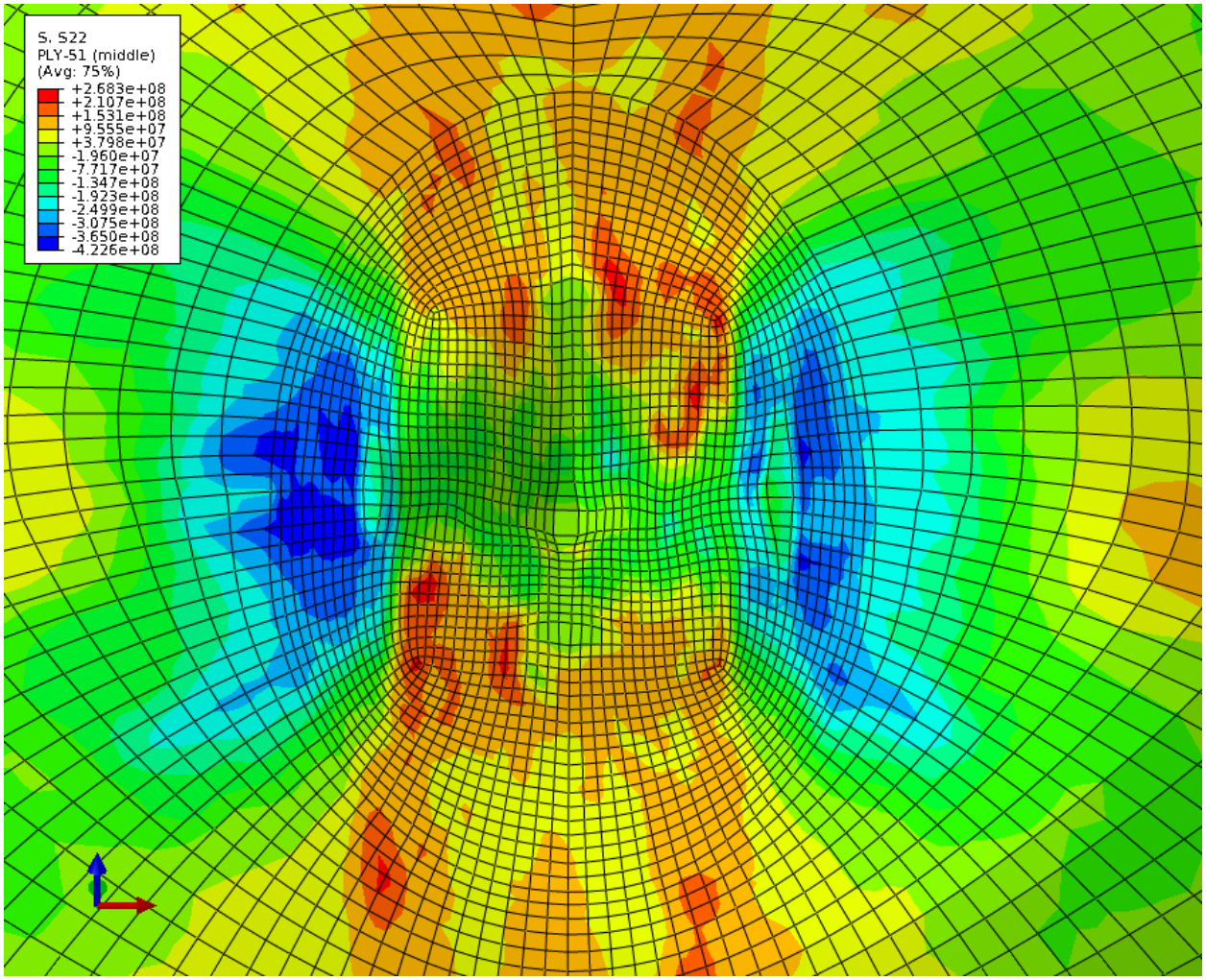
S, S22
PLY-51 (middle)
(Avg: 75%)
+2.683e+08
+2.107e+08
+1.531e+08
+9.555e+07
+3.798e+07
-1.960e+07
-7.717e+07
-1.347e+08
-1.923e+08
-2.499e+08
-3.075e+08
-3.650e+08
-4.226e+08

(d)

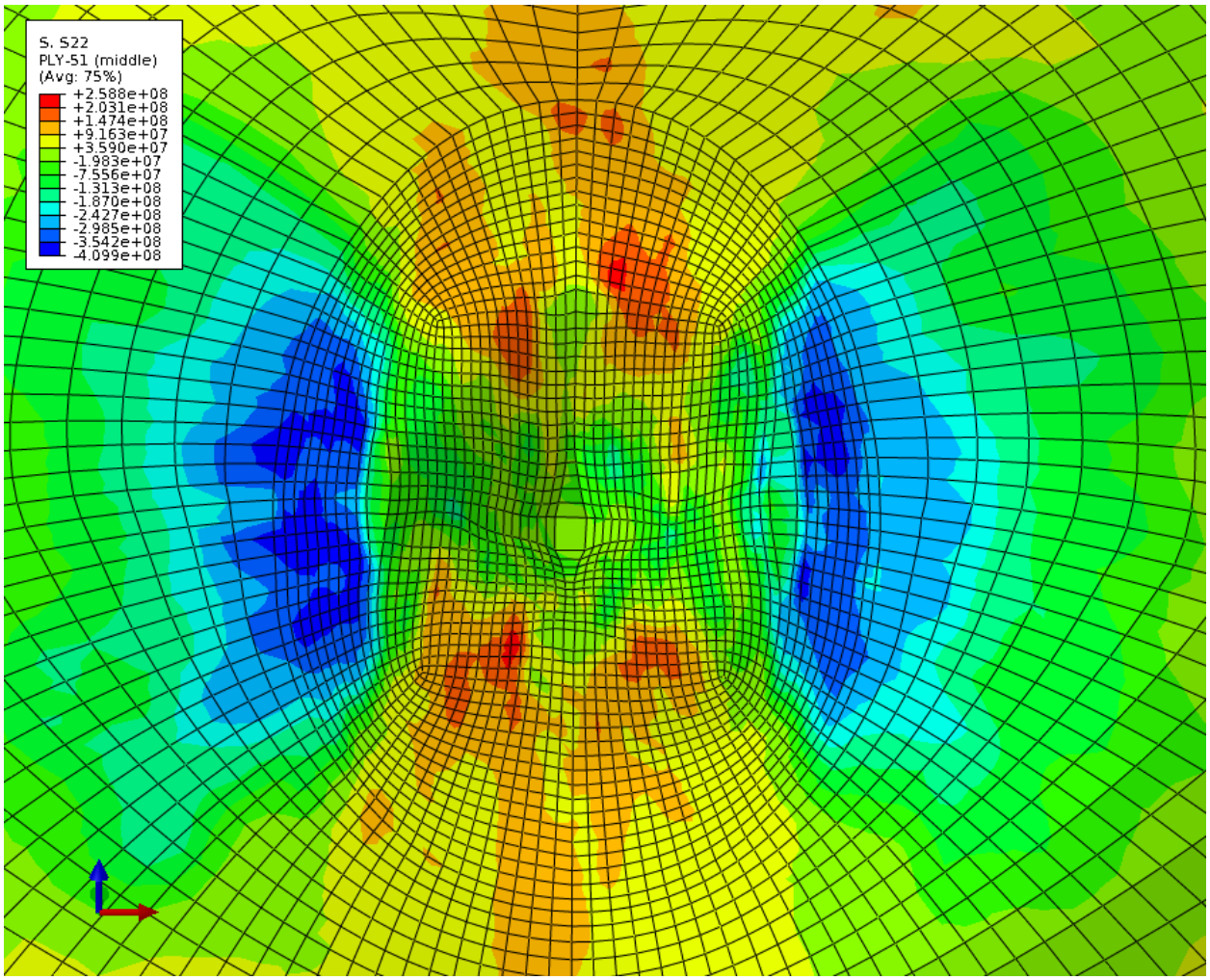
S, S22
PLY-51 (middle)
(Avg: 75%)
+2.588e+08
+2.031e+08
+1.474e+08
+9.163e+07
+3.590e+07
-1.983e+07
-7.556e+07
-1.313e+08
-1.870e+08
-2.427e+08
-2.985e+08
-3.542e+08
-4.099e+08

(e)

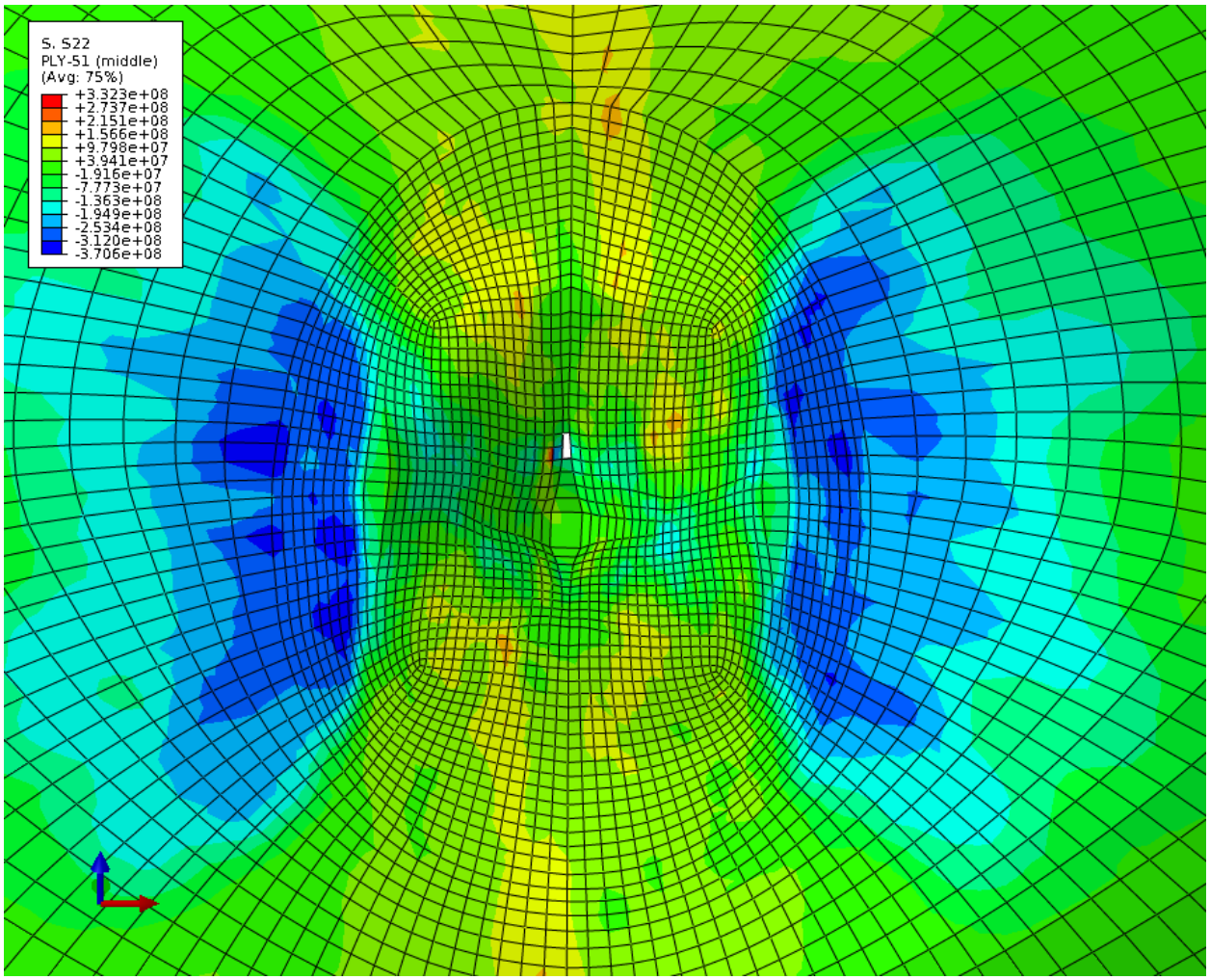
S, S22
PLY-51 (middle)
(Avg: 75%)
+3.323e+08
+2.737e+08
+2.151e+08
+1.566e+08
+9.798e+07
+3.941e+07
-1.916e+07
-7.773e+07
-1.363e+08
-1.949e+08
-2.534e+08
-3.120e+08
-3.706e+08

(f)

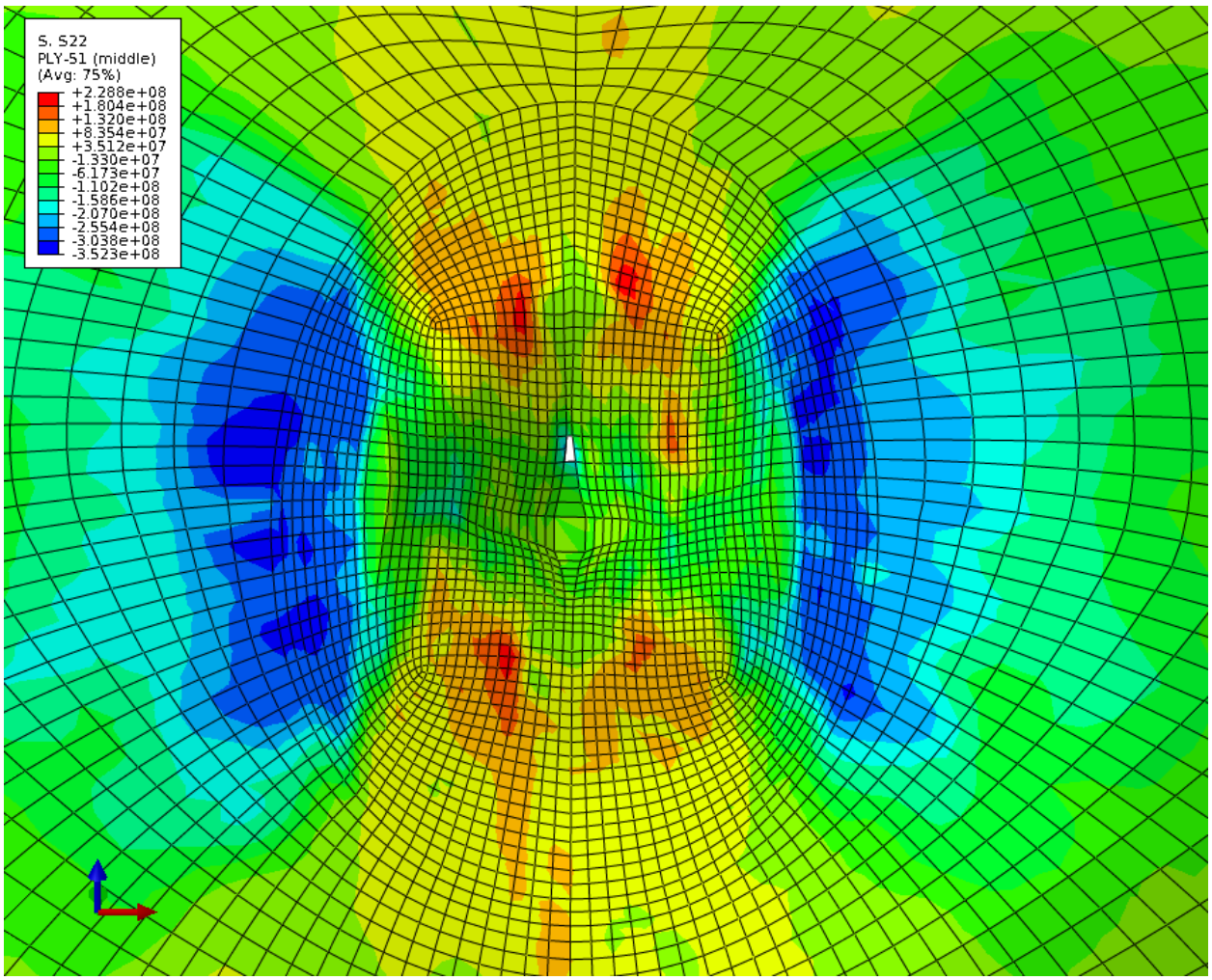
S, S22
PLY-51 (middle)
(Avg: 75%)
+2.288e+08
+1.804e+08
+1.320e+08
+8.354e+07
+3.512e+07
-1.330e+07
-6.173e+07
-1.102e+08
-1.586e+08
-2.070e+08
-2.554e+08
-3.038e+08
-3.523e+08

(g)

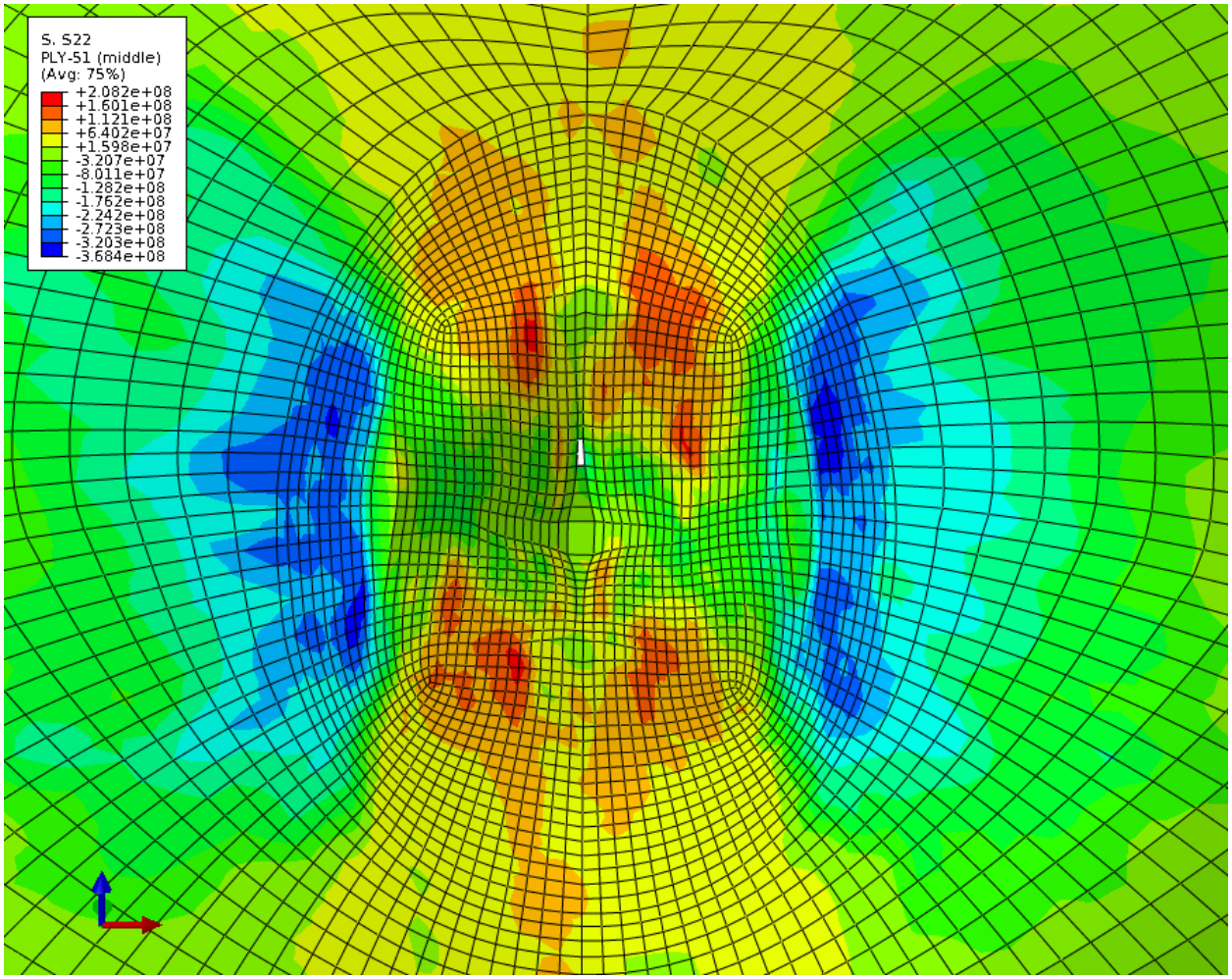
S, S22
PLY-51 (middle)
(Avg: 75%)
+2.082e+08
+1.601e+08
+1.121e+08
+6.402e+07
+1.598e+07
-3.207e+07
-8.011e+07
-1.282e+08
-1.762e+08
-2.242e+08
-2.723e+08
-3.203e+08
-3.684e+08

(h)

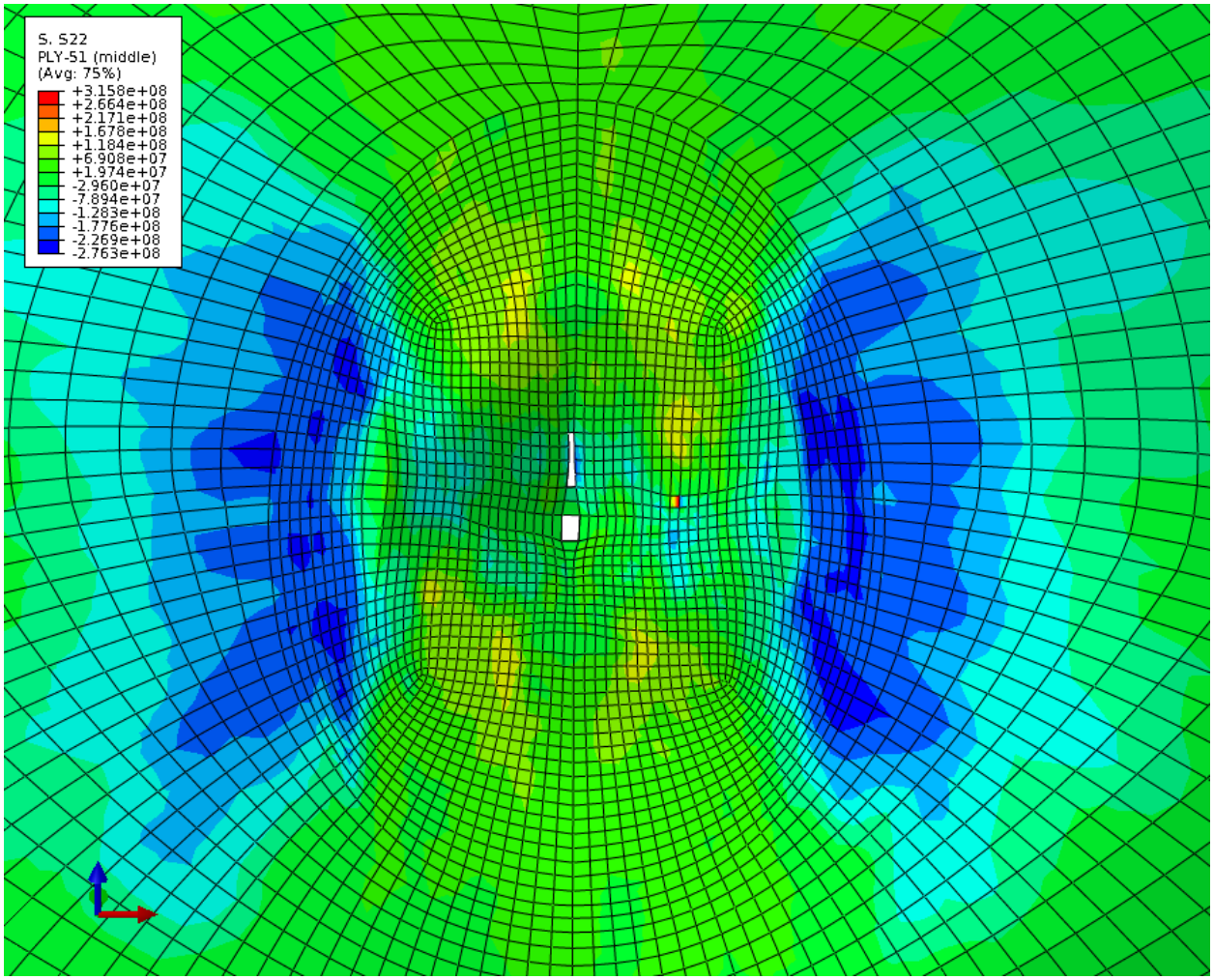
S, S22
PLY-S1 (middle)
(Avg: 75%)
+3.158e+08
+2.664e+08
+2.171e+08
+1.678e+08
+1.184e+08
+6.908e+07
+1.974e+07
-2.960e+07
-7.894e+07
-1.283e+08
-1.776e+08
-2.269e+08
-2.763e+08

(i)

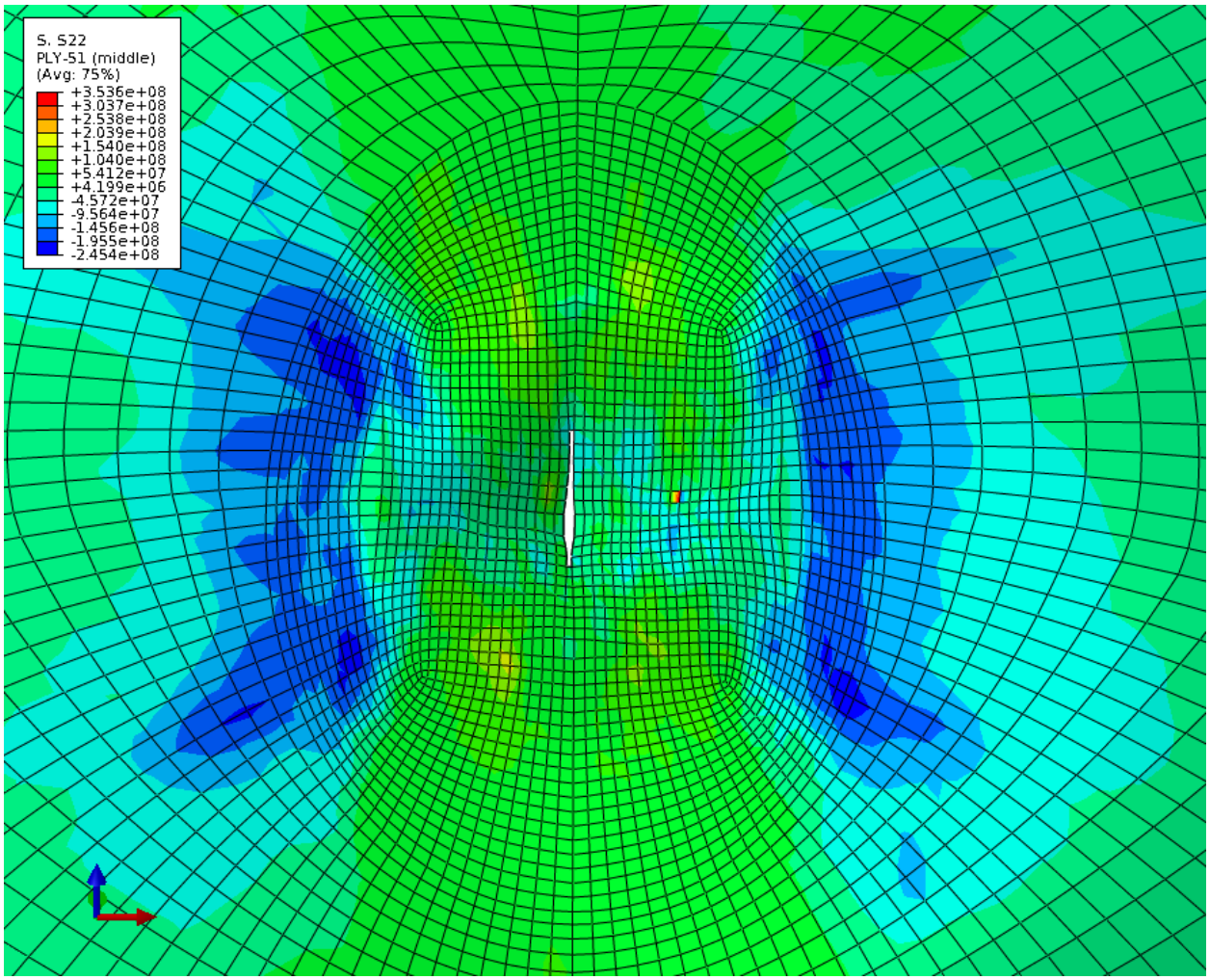
S, S22
PLY-51 (middle)
(Avg: 75%)
+3.536e+08
+3.037e+08
+2.538e+08
+2.039e+08
+1.540e+08
+1.040e+08
+5.412e+07
+4.199e+06
-4.572e+07
-9.564e+07
-1.456e+08
-1.955e+08
-2.454e+08

(j)

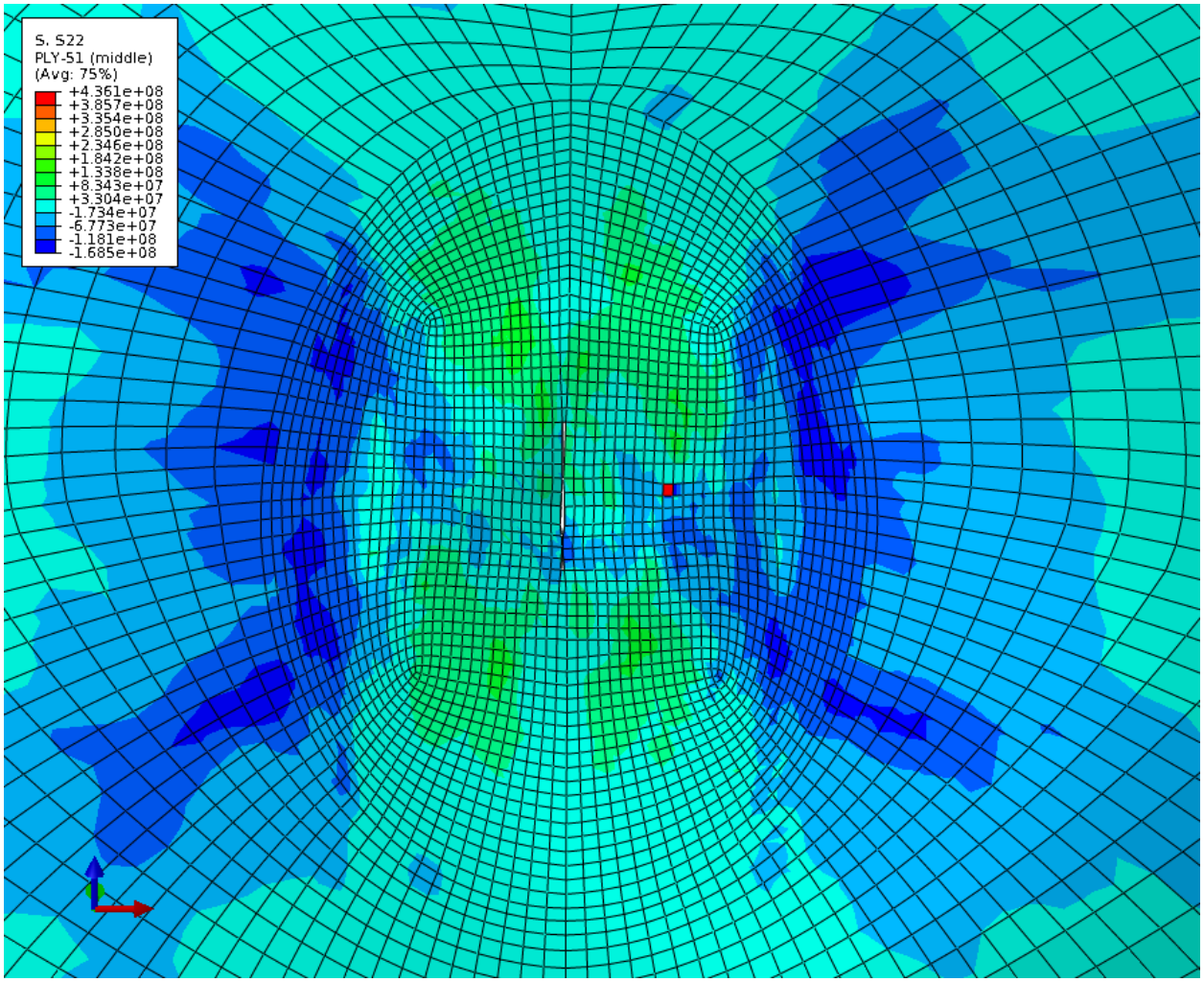

Figure 45. Contour plot of σ_{22}in back ply of helmet at 10 µs (a), 20 µs (b), 30 µs (c), 40 µs (d), 50 µs (e), 60 µs (f), 70 µs (g), 80 µs (h), 90 µs (i), and 100 µs (j) for $v_0 = 0.9\ v_{BL}$; **legend units: Pa**

(a)

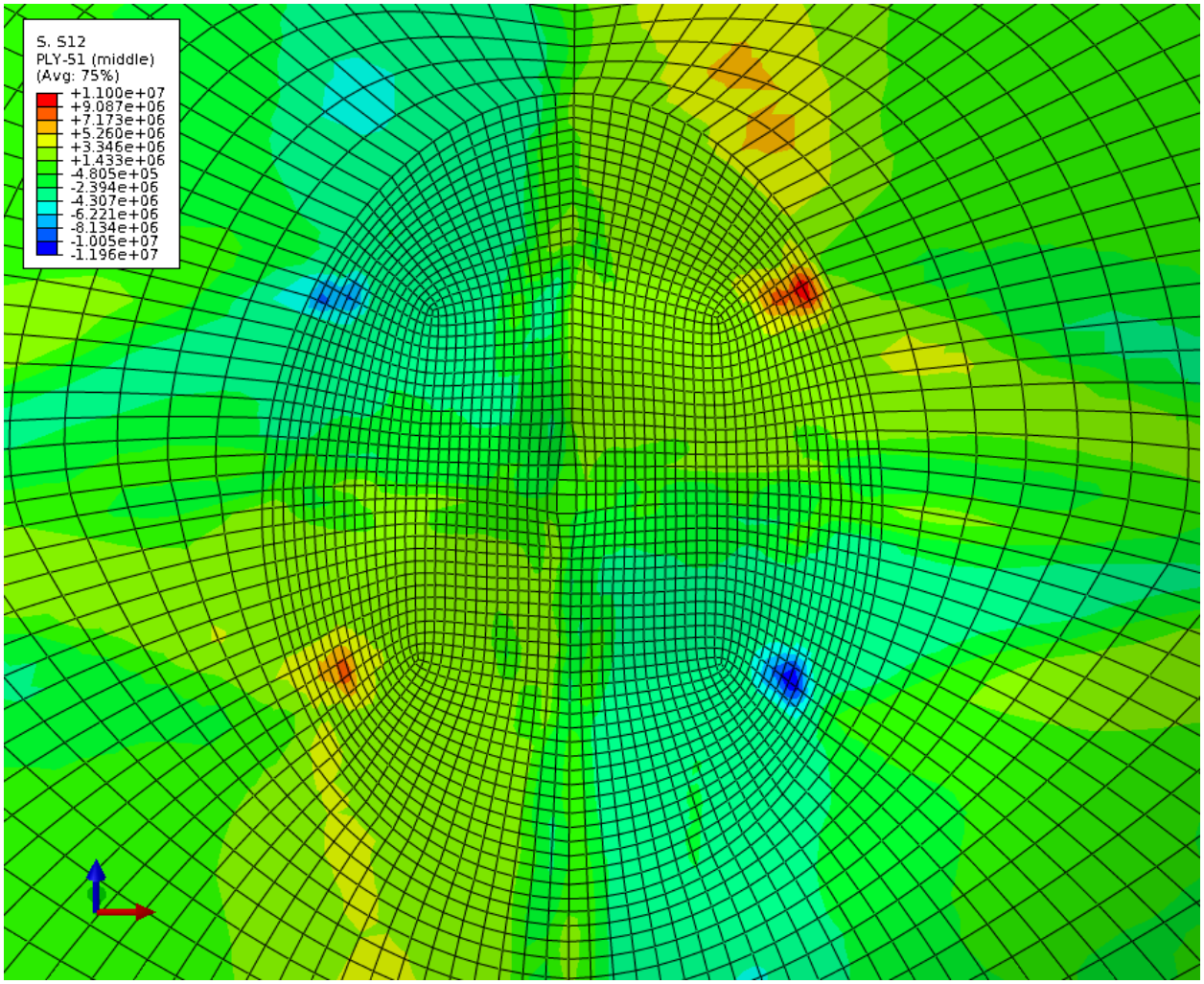
S, S12
PLY-S1 (middle)
(Avg: 75%)
+1.100e+07
+9.087e+06
+7.173e+06
+5.260e+06
+3.346e+06
+1.433e+06
-4.805e+05
-2.394e+06
-4.307e+06
-6.221e+06
-8.134e+06
-1.005e+07
-1.196e+07

(b)

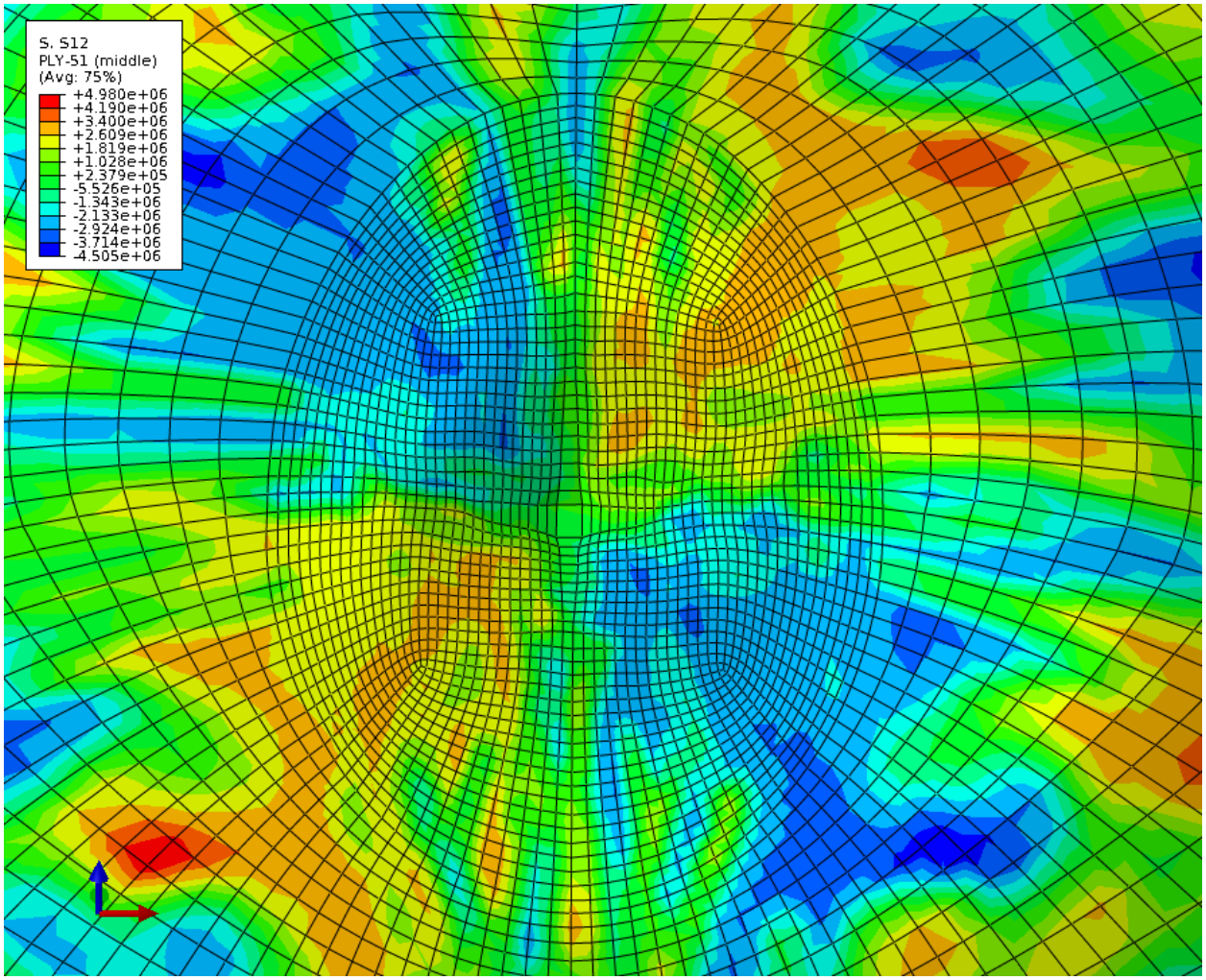
S, S12
PLY-51 (middle)
(Avg: 75%)
+4.980e+06
+4.190e+06
+3.400e+06
+2.609e+06
+1.819e+06
+1.028e+06
+2.379e+05
-5.526e+05
-1.343e+06
-2.133e+06
-2.924e+06
-3.714e+06
-4.505e+06

(c)

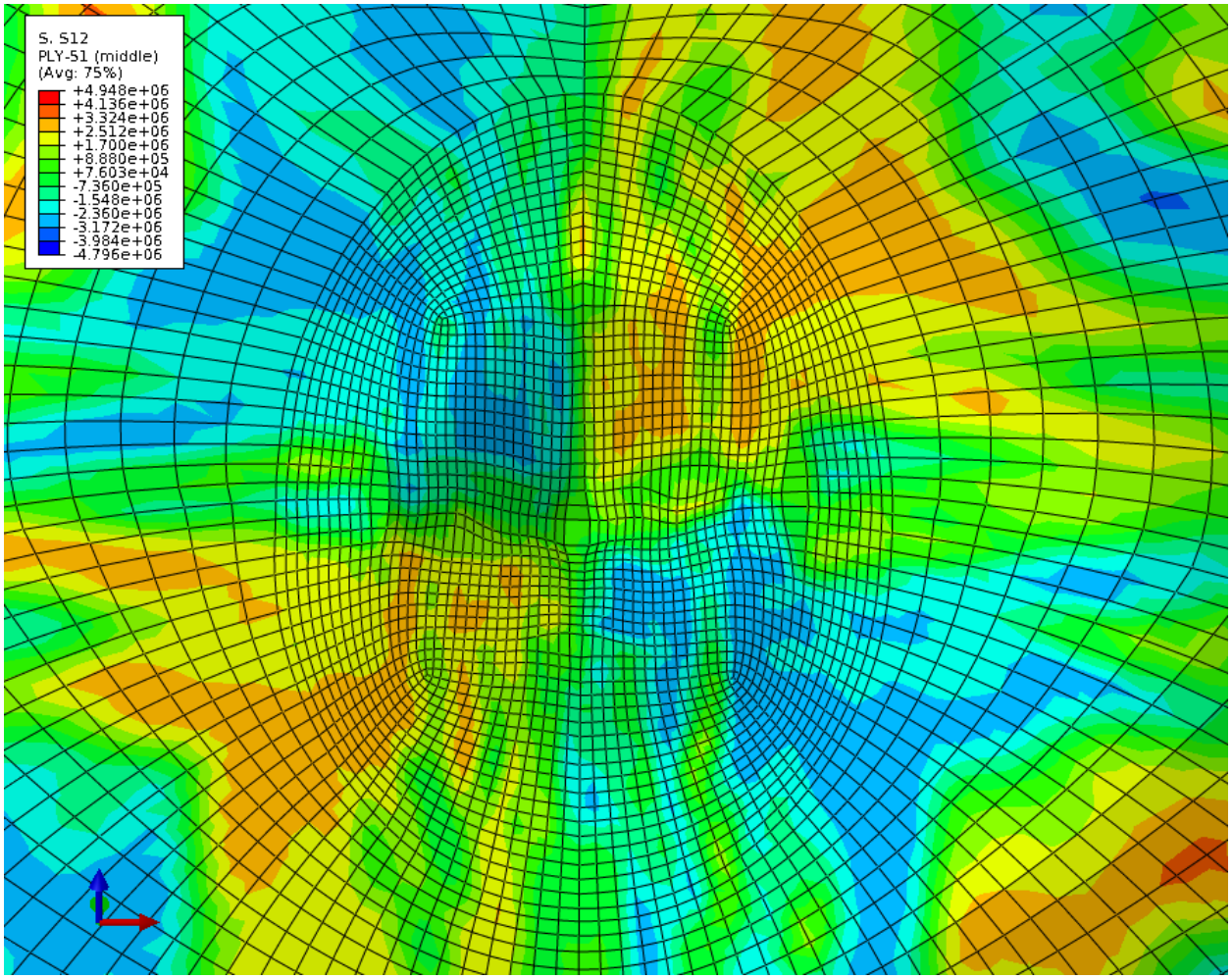
S, S12
PLY-51 (middle)
(Avg: 75%)
+4.948e+06
+4.136e+06
+3.324e+06
+2.512e+06
+1.700e+06
+8.880e+05
+7.603e+04
-7.360e+05
-1.548e+06
-2.360e+06
-3.172e+06
-3.984e+06
-4.796e+06

(d)

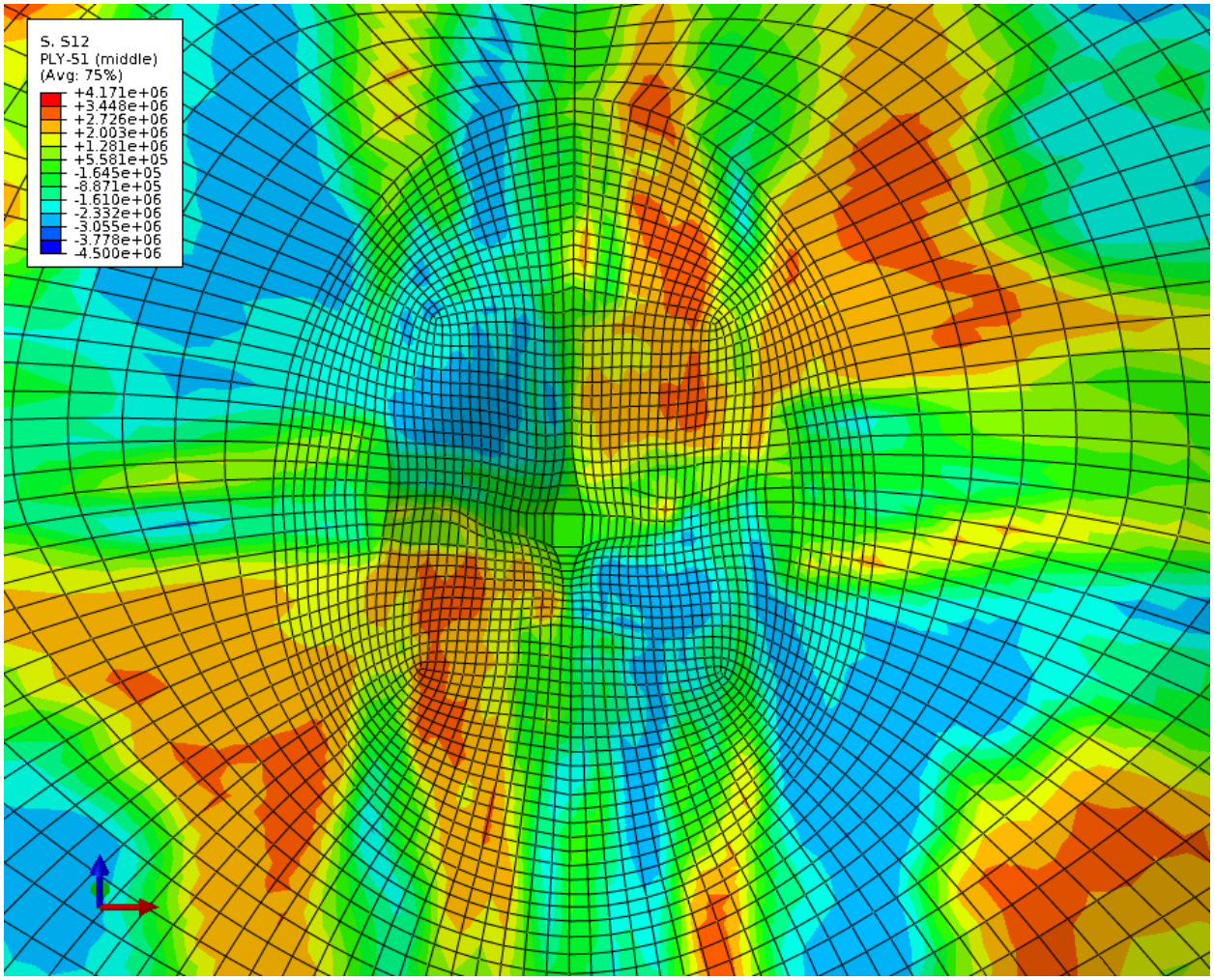
S, S12
PLY-S1 (middle)
(Avg: 75%)
+4.171e+06
+3.448e+06
+2.726e+06
+2.003e+06
+1.281e+06
+5.581e+05
-1.645e+05
-8.871e+05
-1.610e+06
-2.332e+06
-3.055e+06
-3.778e+06
-4.500e+06

(e)

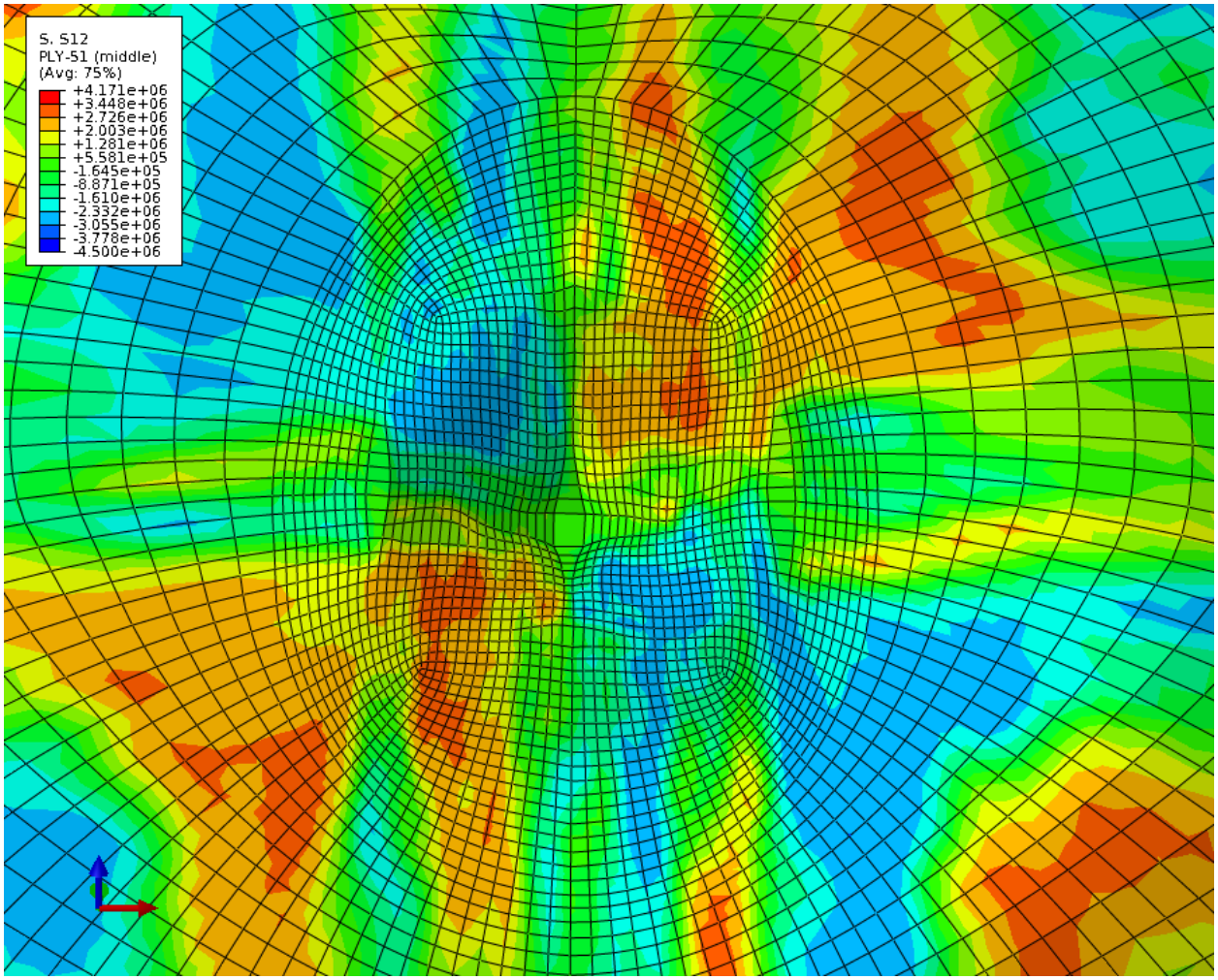
S, S12
PLY-S1 (middle)
(Avg: 75%)
+4.171e+06
+3.448e+06
+2.726e+06
+2.003e+06
+1.281e+06
+5.581e+05
-1.645e+05
-8.871e+05
-1.610e+06
-2.332e+06
-3.055e+06
-3.778e+06
-4.500e+06

(f)

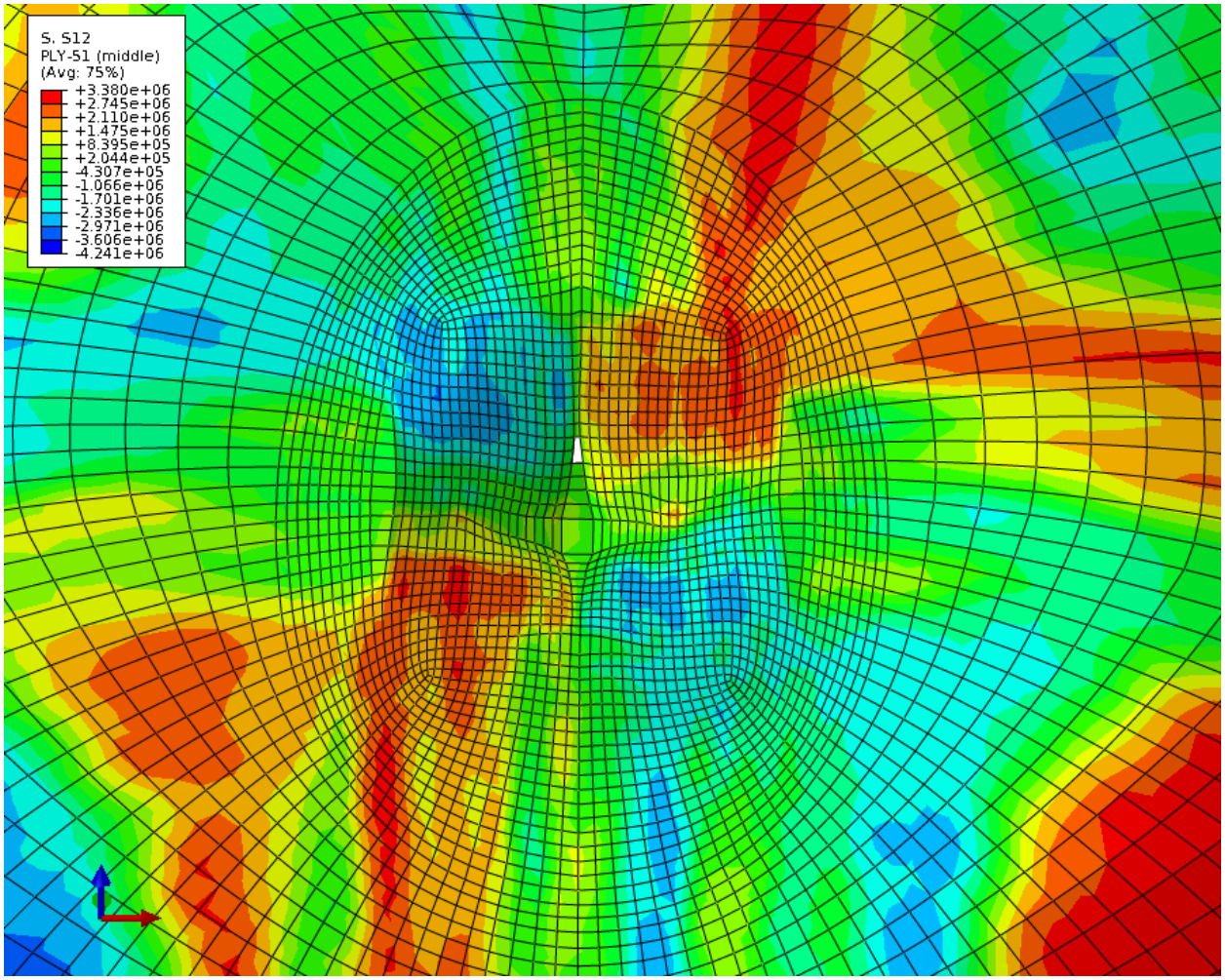
S, S12
PLY-51 (middle)
(Avg: 75%)
+3.380e+06
+2.745e+06
+2.110e+06
+1.475e+06
+8.395e+05
+2.044e+05
-4.307e+05
-1.066e+06
-1.701e+06
-2.336e+06
-2.971e+06
-3.606e+06
-4.241e+06

(g)

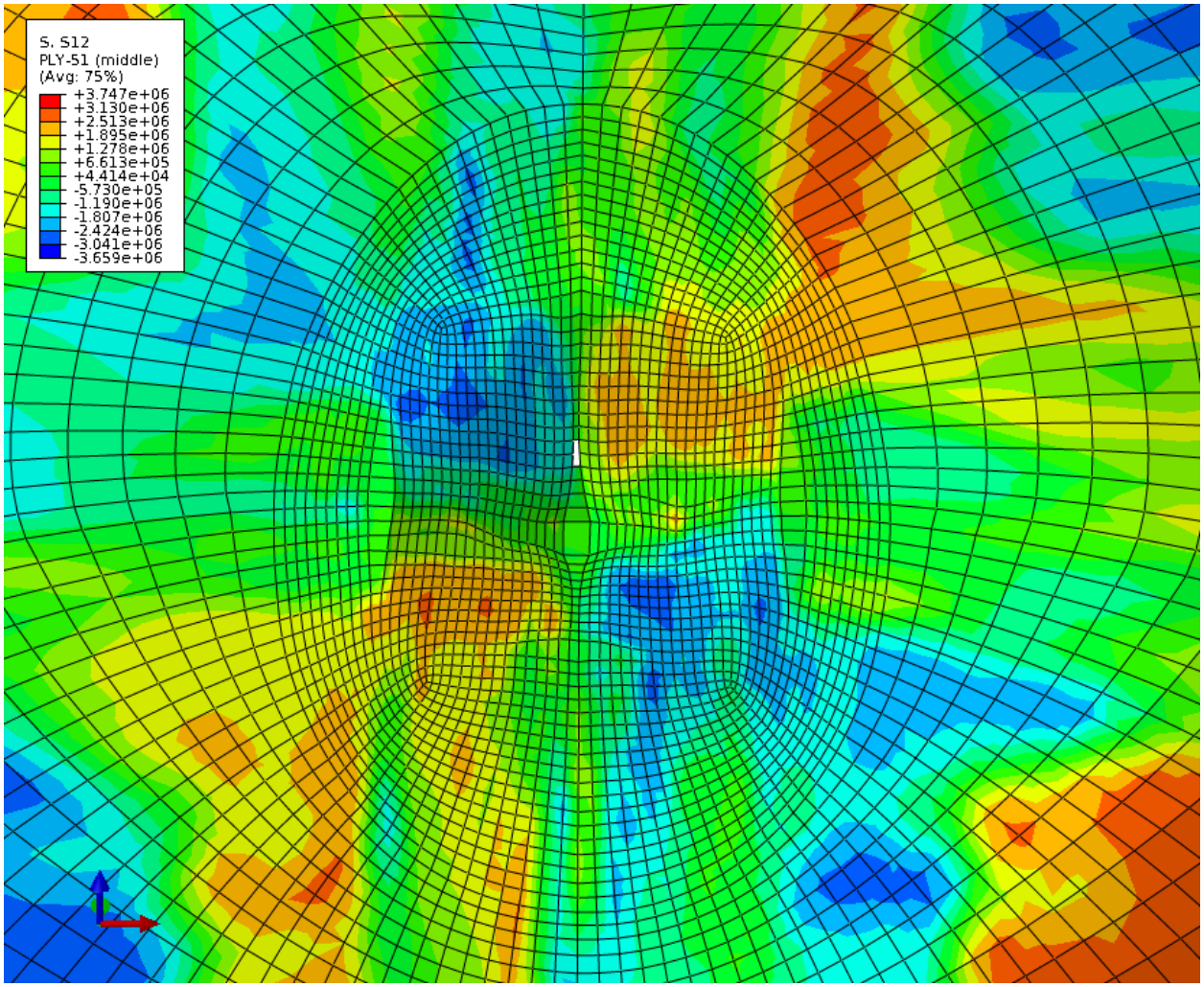
S, S12
PLY-51 (middle)
(Avg: 75%)
+3.747e+06
+3.130e+06
+2.513e+06
+1.895e+06
+1.278e+06
+6.613e+05
+4.414e+04
-5.730e+05
-1.190e+06
-1.807e+06
-2.424e+06
-3.041e+06
-3.659e+06

(h)

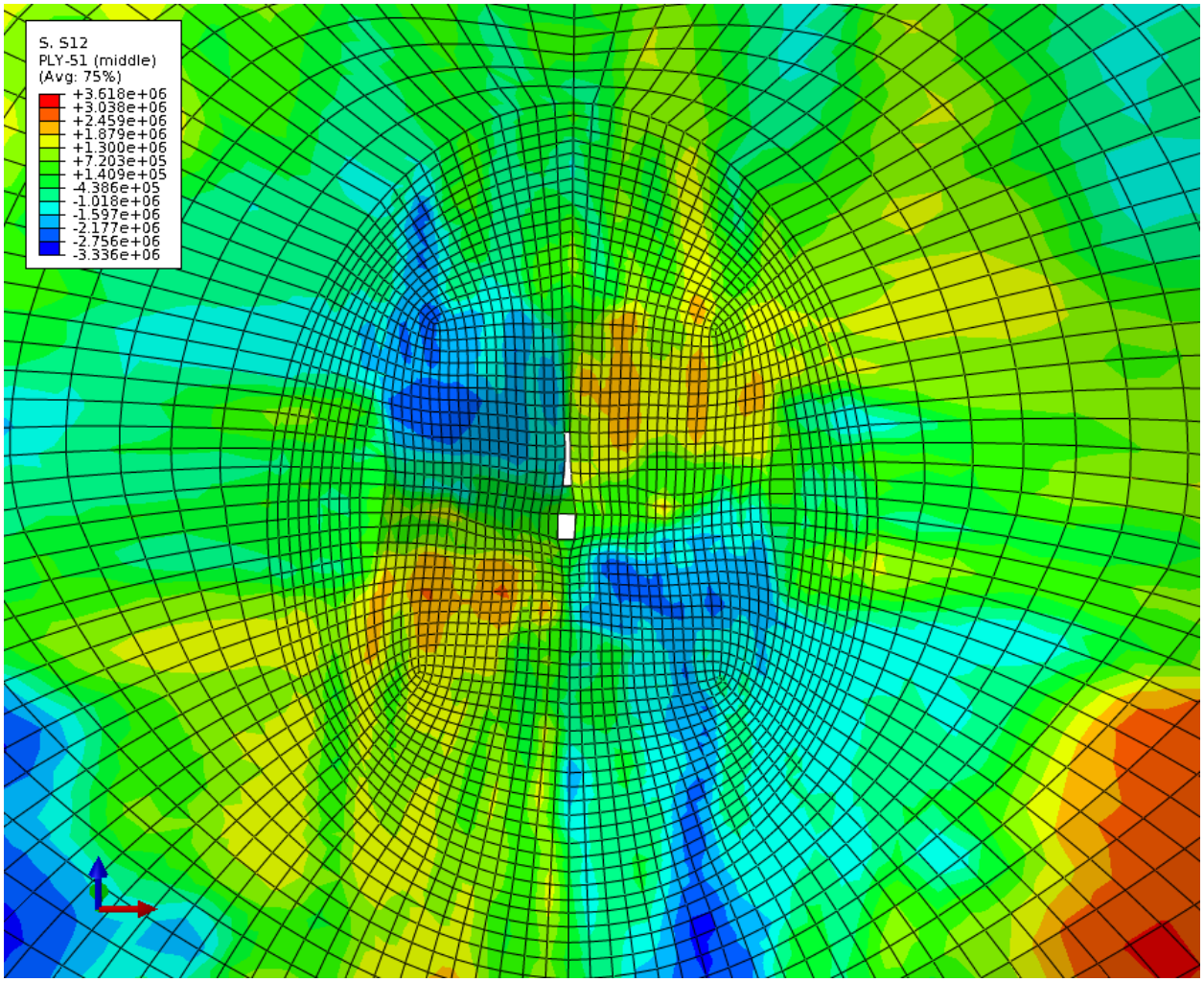
S, S12
PLY-51 (middle)
(Avg: 75%)
+3.618e+06
+3.038e+06
+2.459e+06
+1.879e+06
+1.300e+06
+7.203e+05
+1.409e+05
-4.386e+05
-1.018e+06
-1.597e+06
-2.177e+06
-2.756e+06
-3.336e+06

(i)

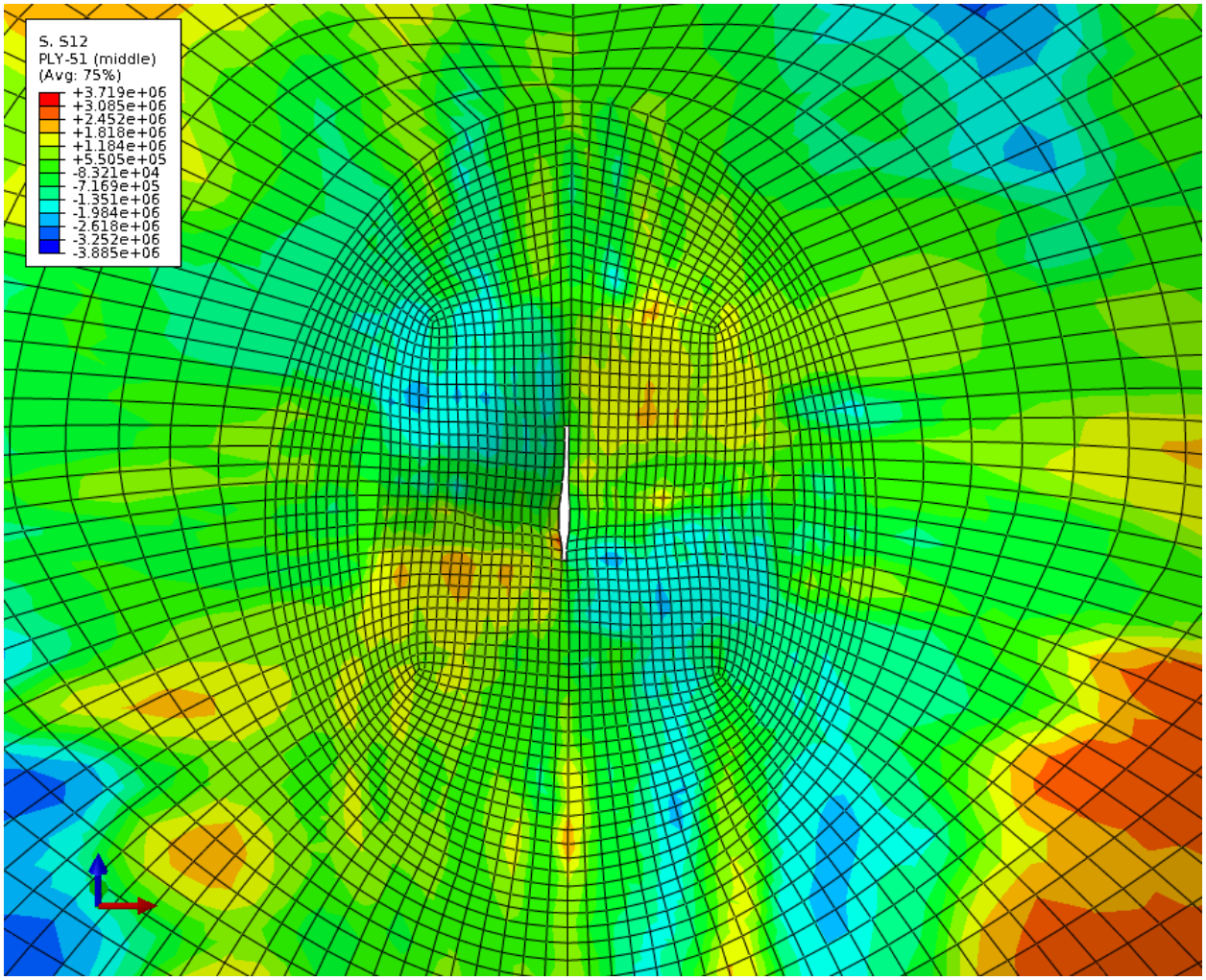
S, S12
PLY-S1 (middle)
(Avg: 75%)
+3.719e+06
+3.085e+06
+2.452e+06
+1.818e+06
+1.184e+06
+5.505e+05
-8.321e+04
-7.169e+05
-1.351e+06
-1.984e+06
-2.618e+06
-3.252e+06
-3.885e+06

(j)

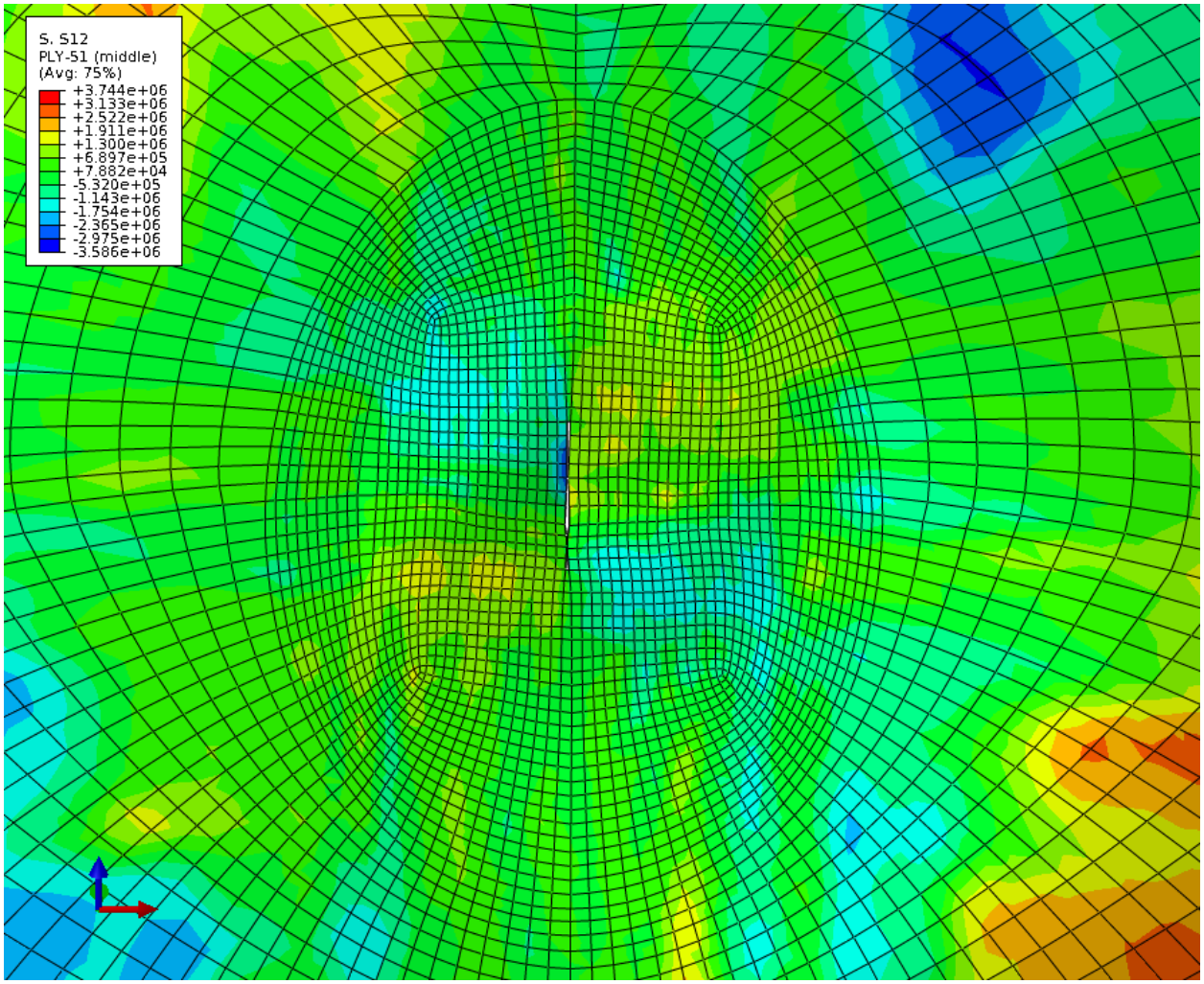

Figure 46. Contour plot of σ_{12}in back ply of helmet at 10 µs (a), 20 µs (b), 30 µs (c), 40 µs (d), 50 µs (e), 60 µs (f), 70 µs (g), 80 µs (h), 90 µs (i), and 100 µs (j) for $v_0 = 0.9\ v_{BL}$; **legend units: Pa**

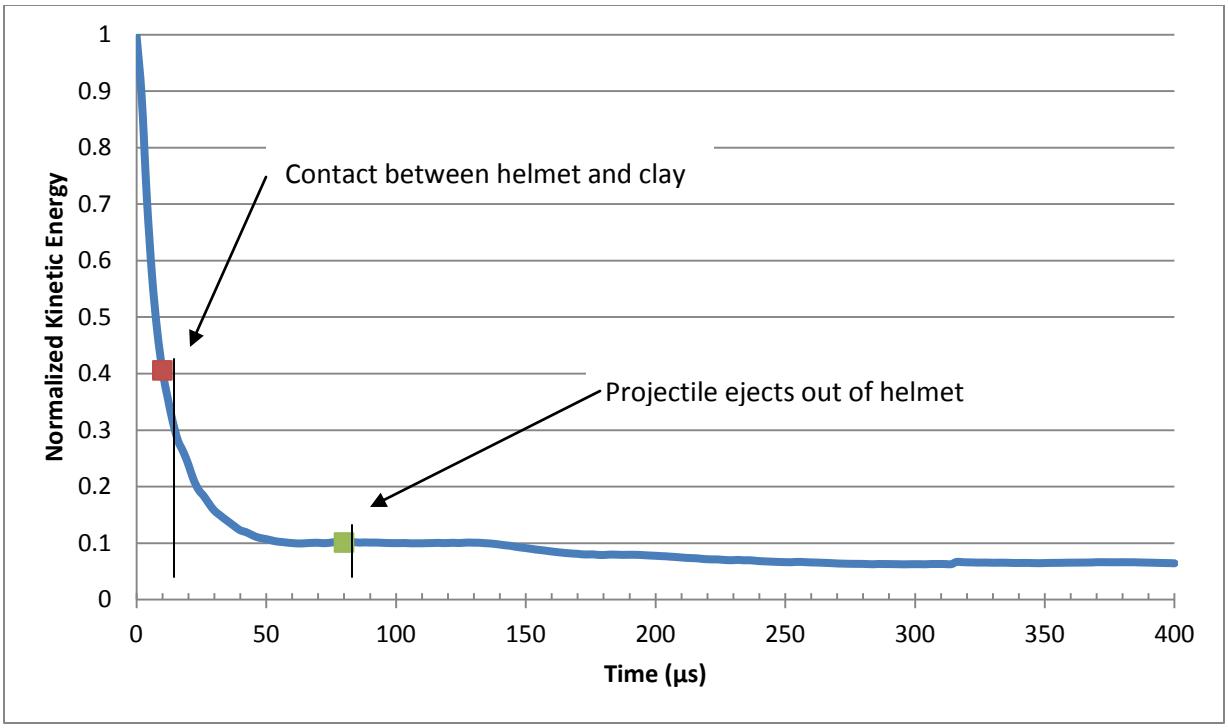

Figure 47. Normalized kinetic energy time history of the system for $v_0 = 1.2\ v_{BL}$ with times highlighted to note changes in contact behavior.

(a)

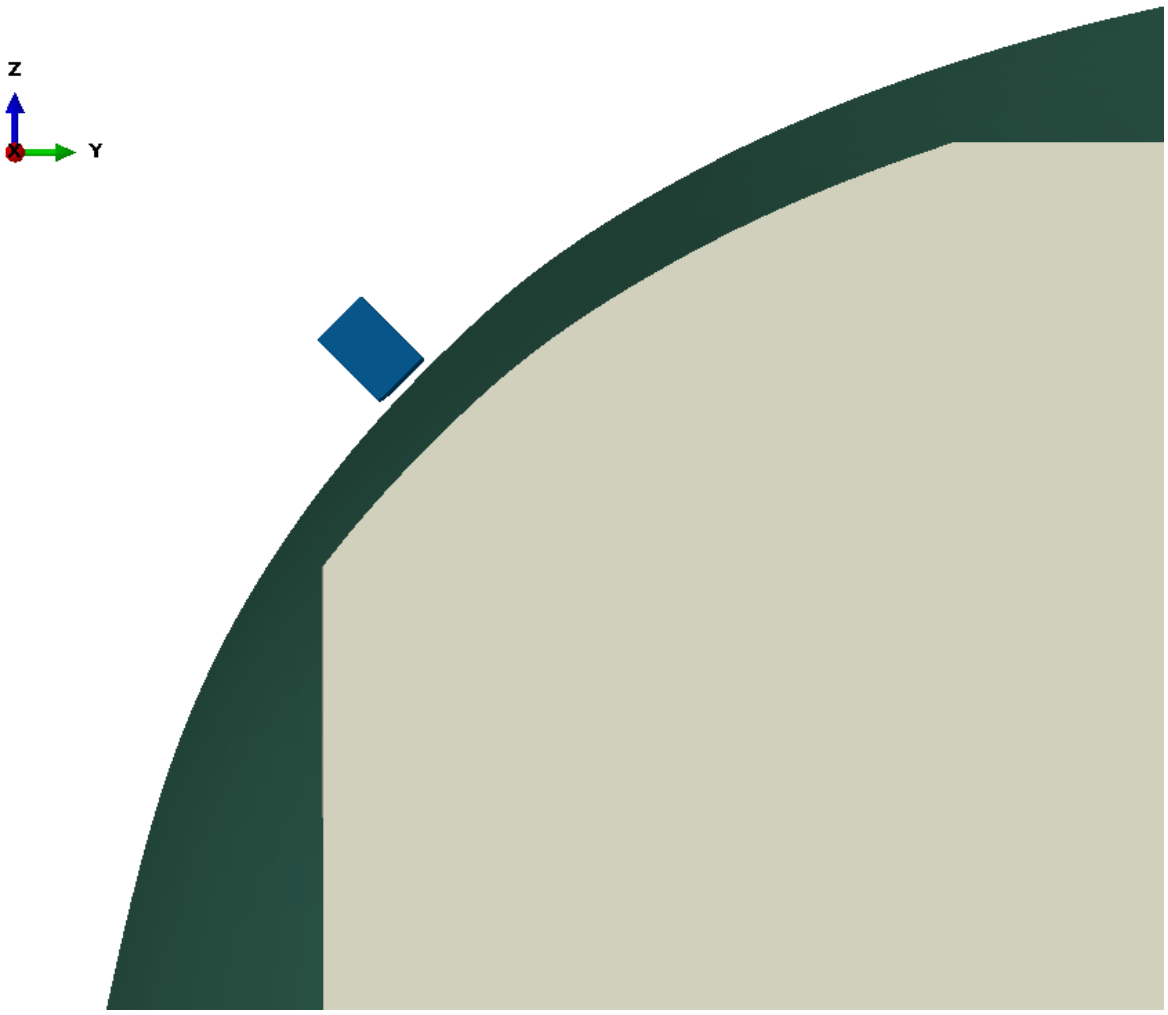

(b)

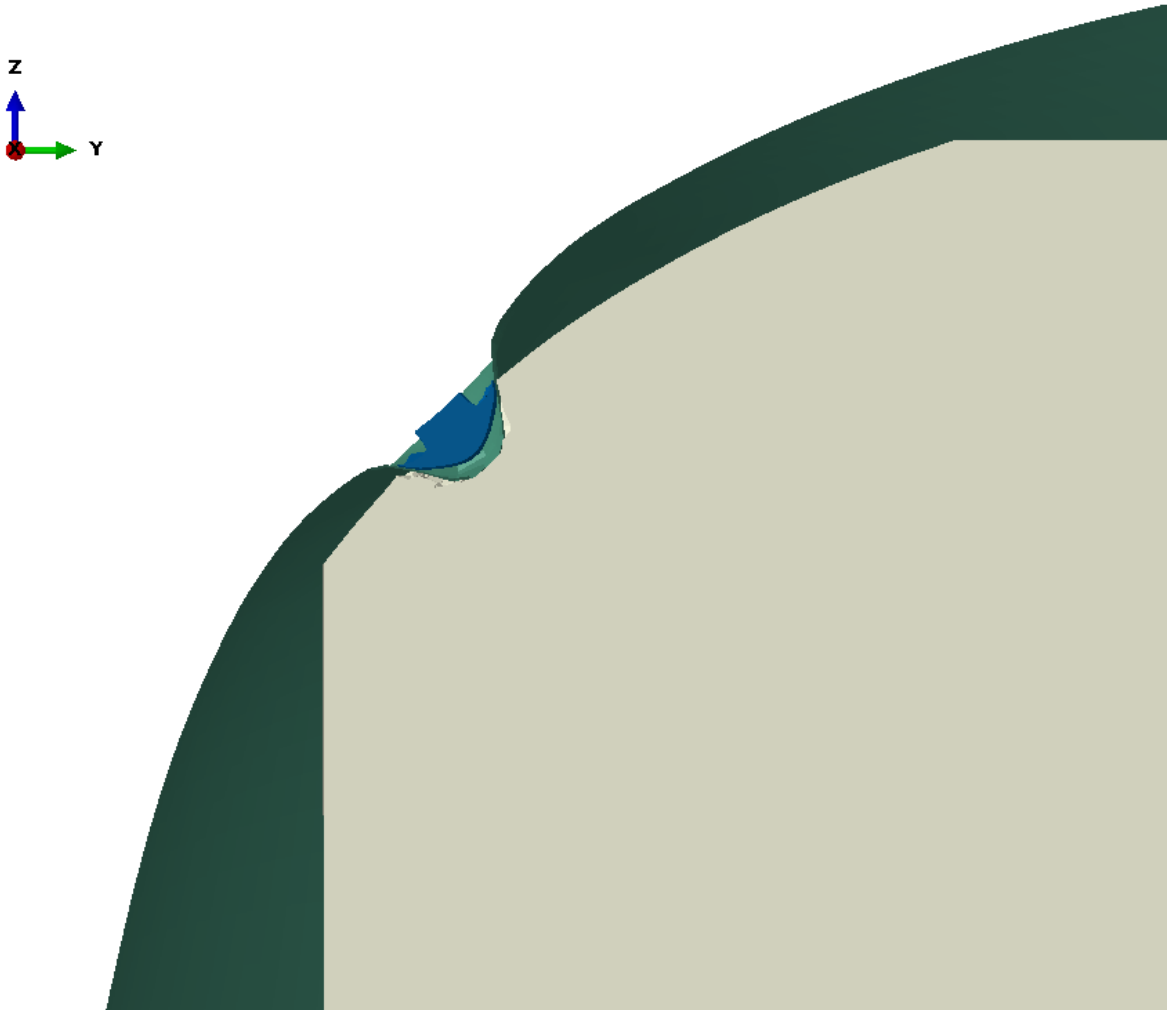

(c)

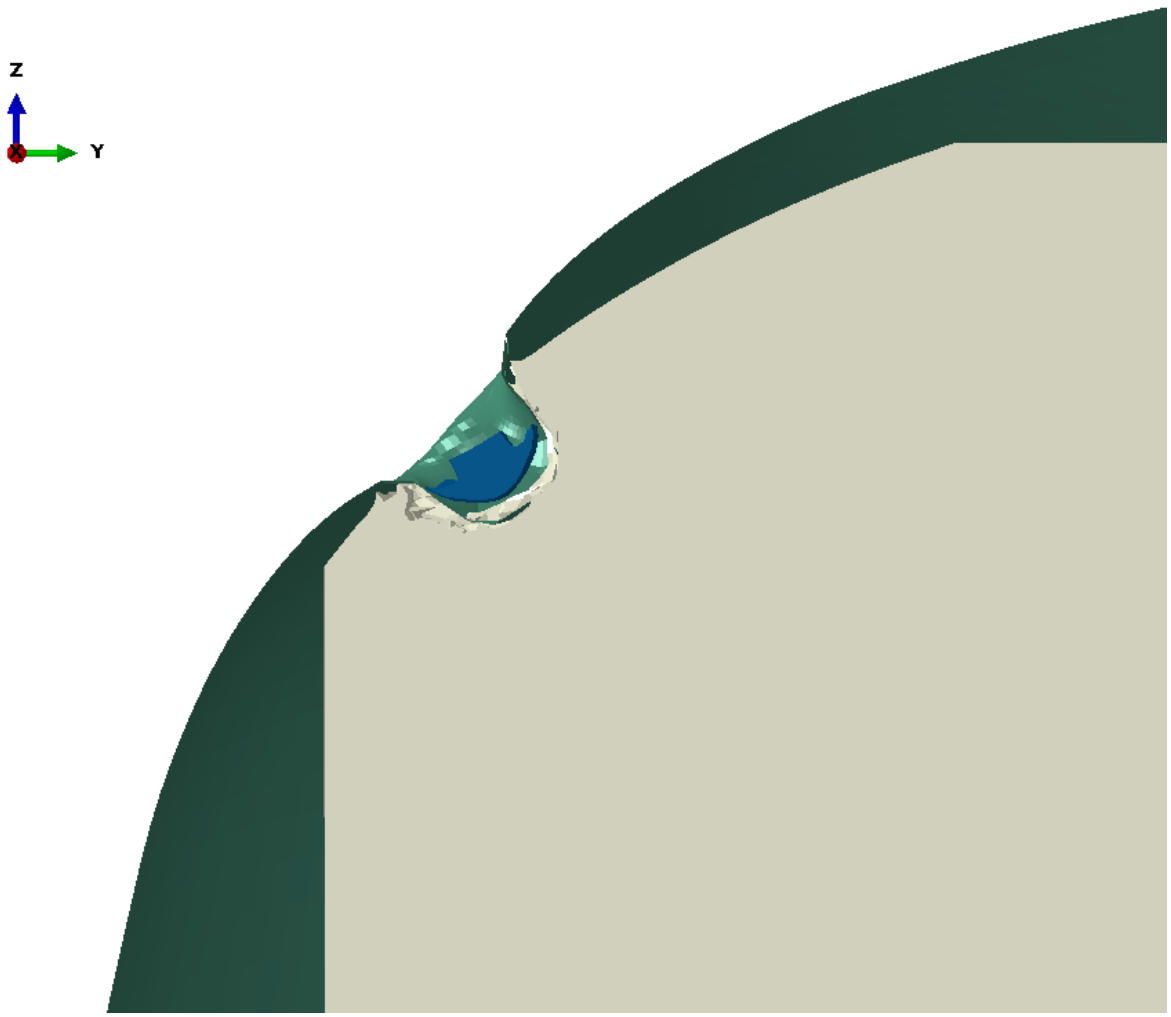

(d)

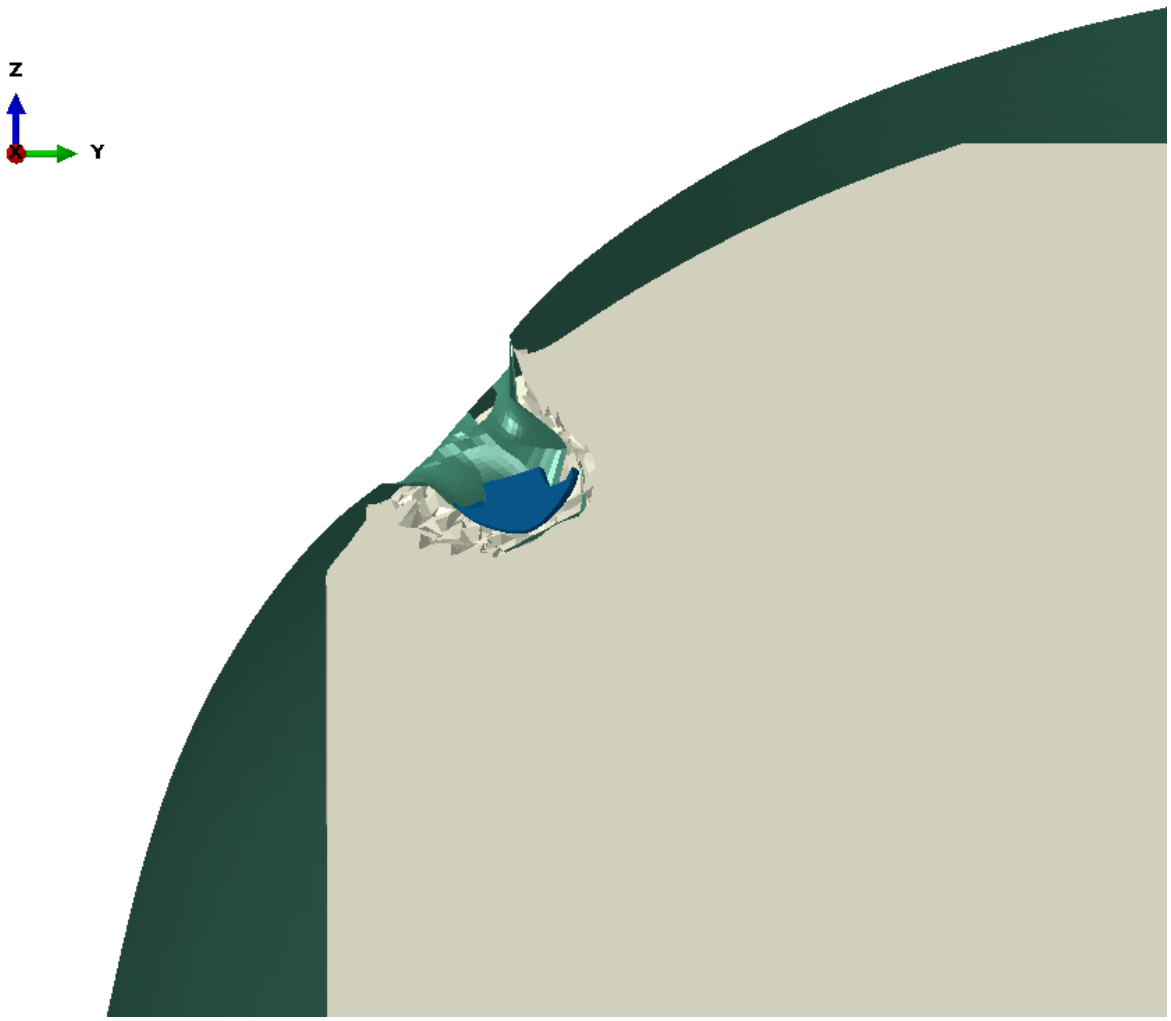

(e)

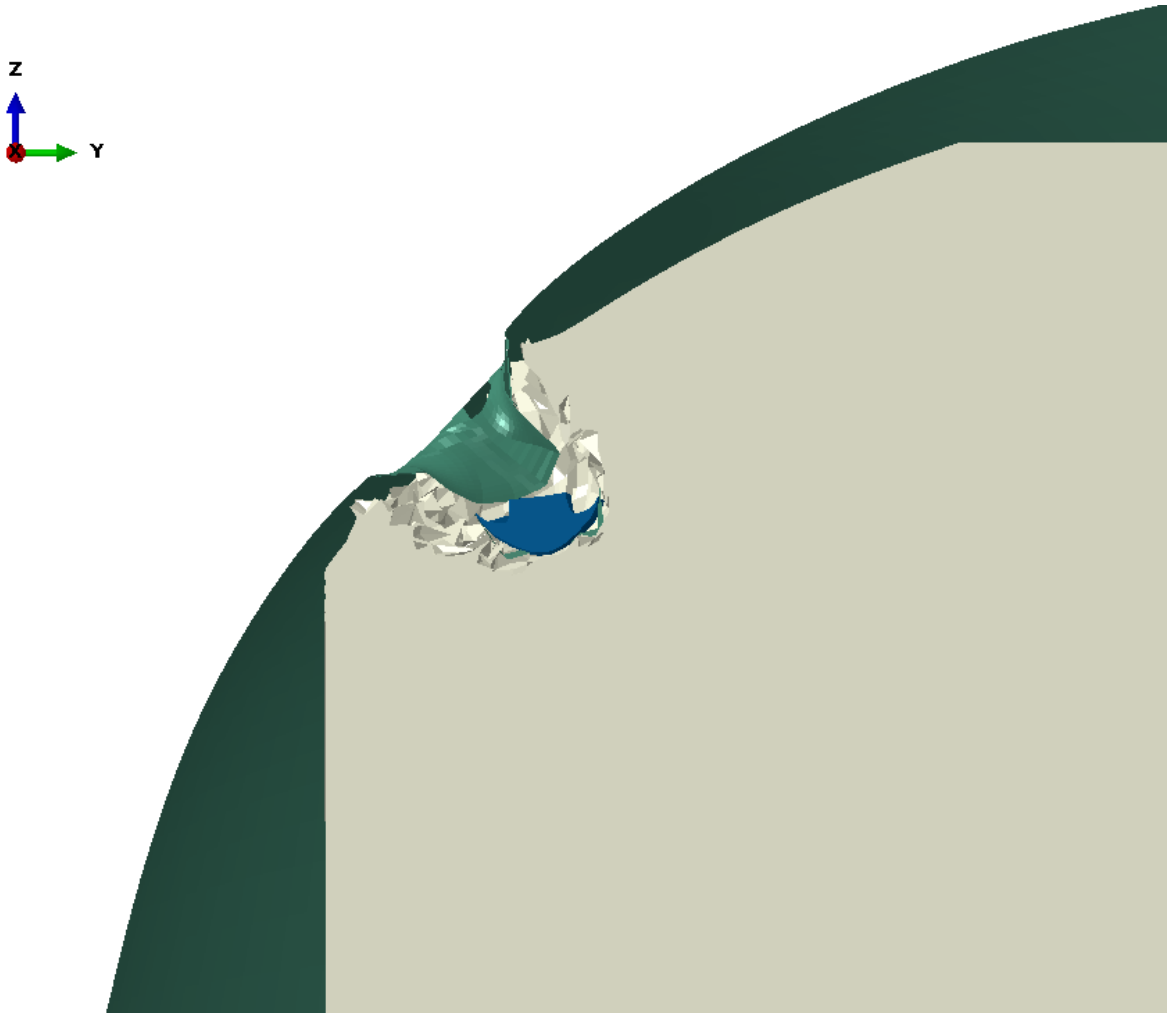

(f)

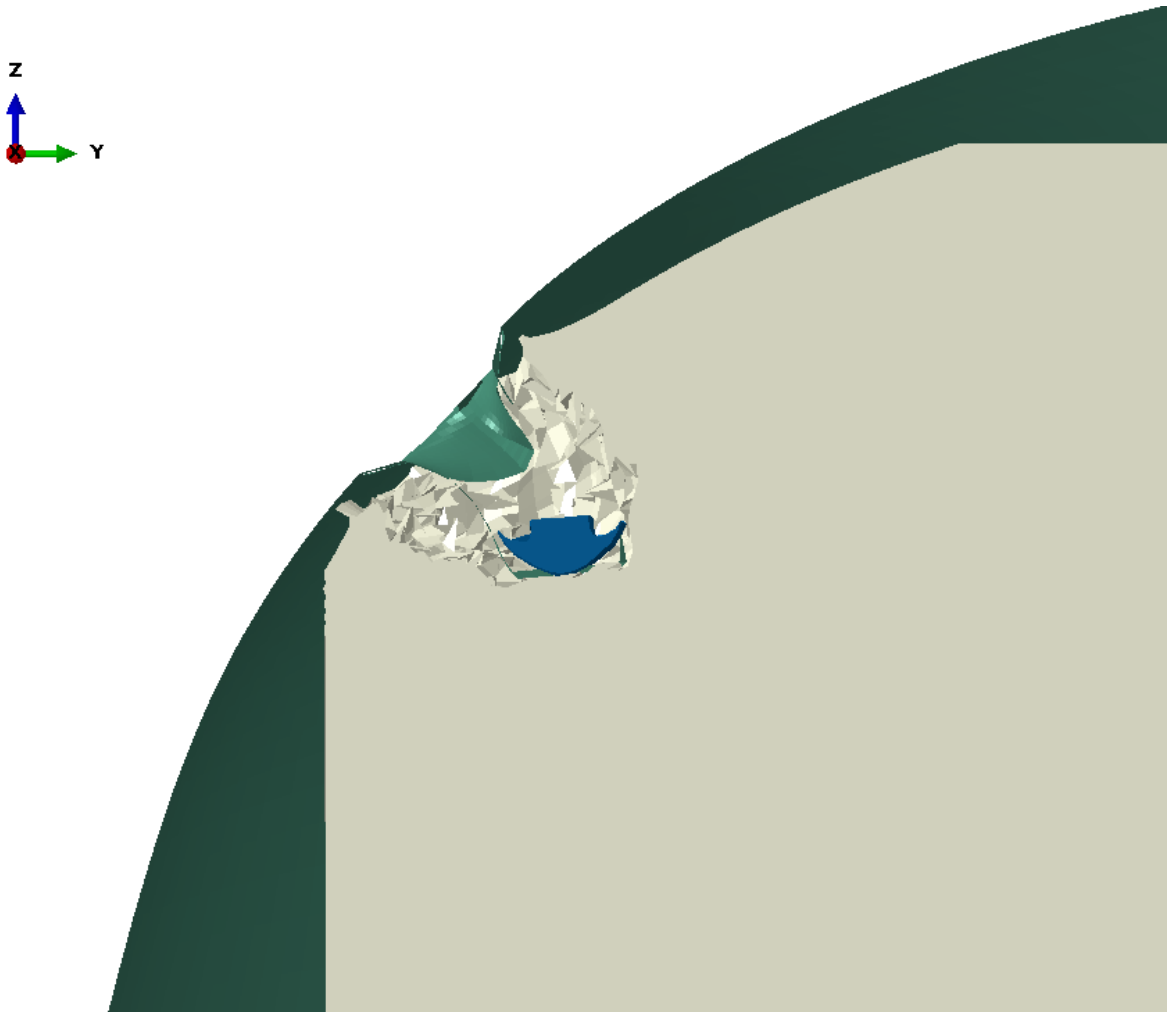

(g)

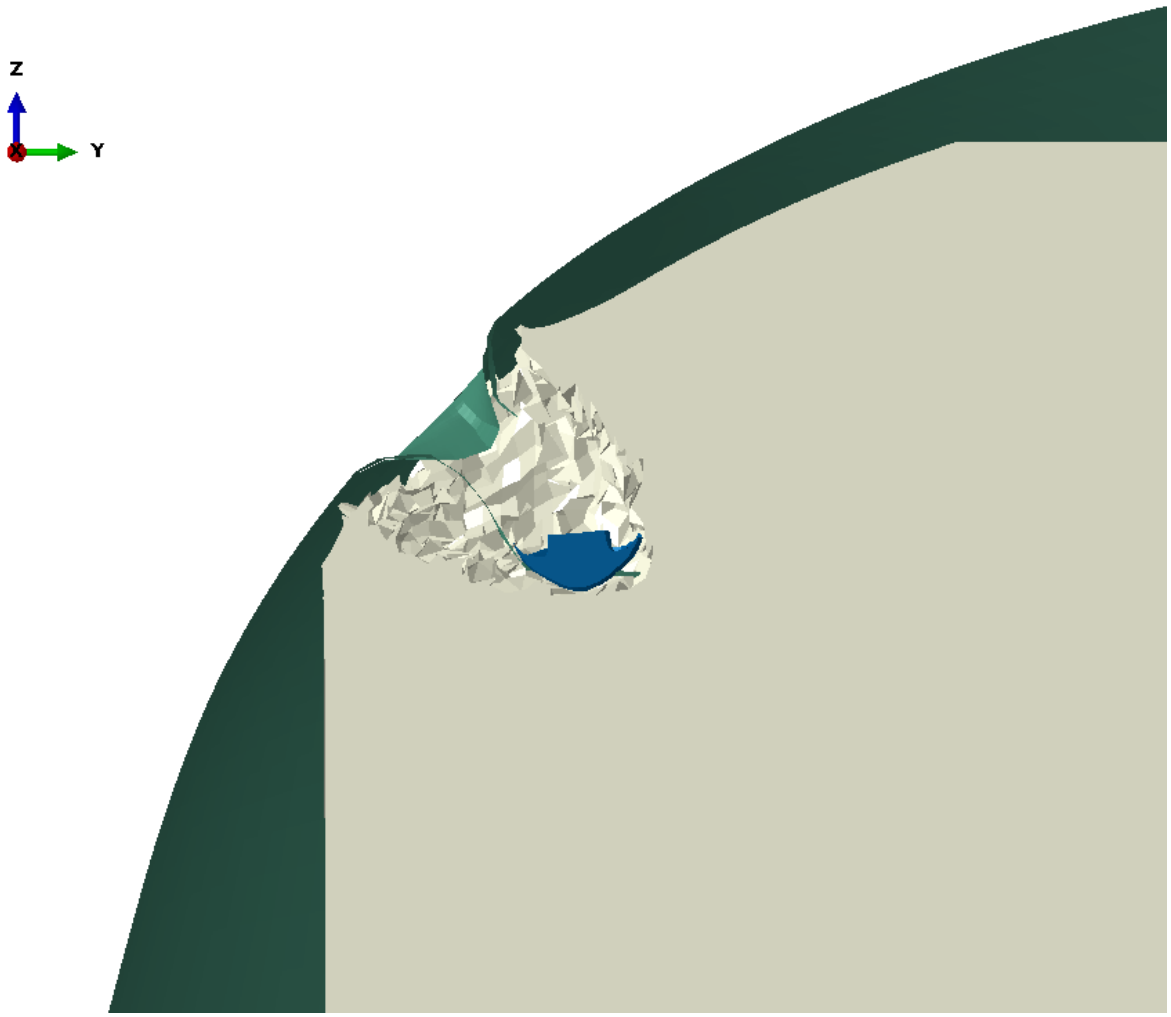

(h)

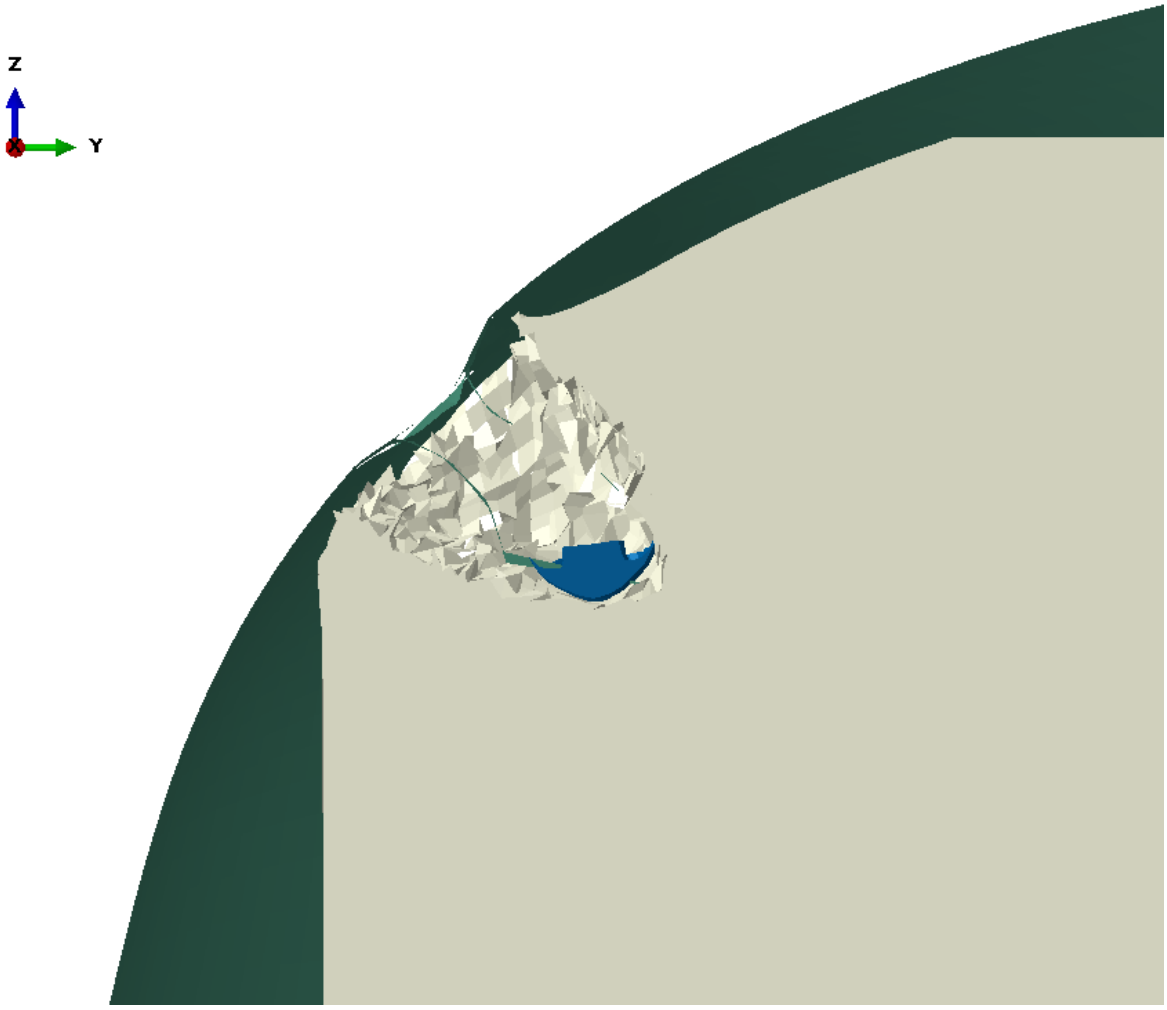

(i)

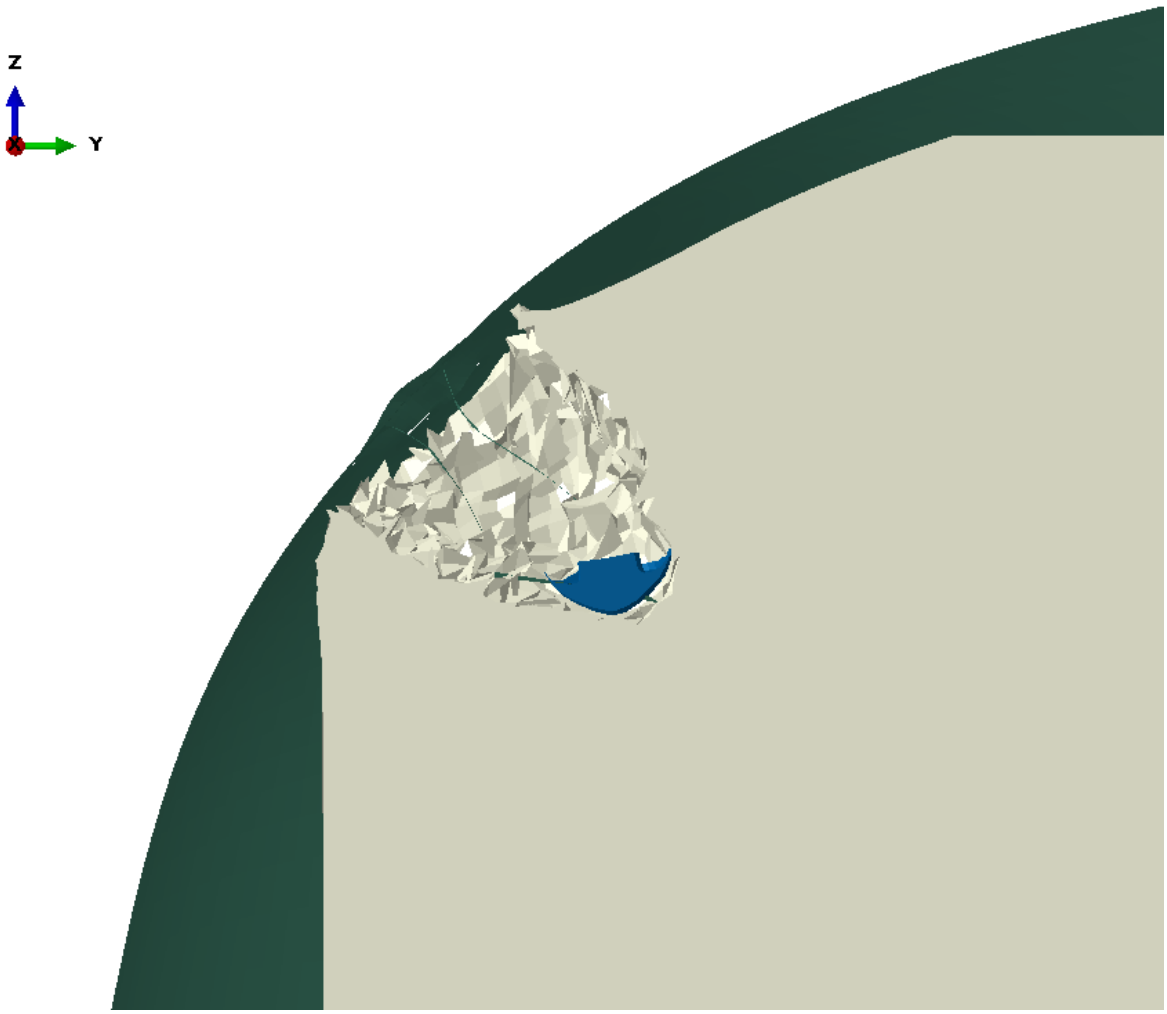

(j)

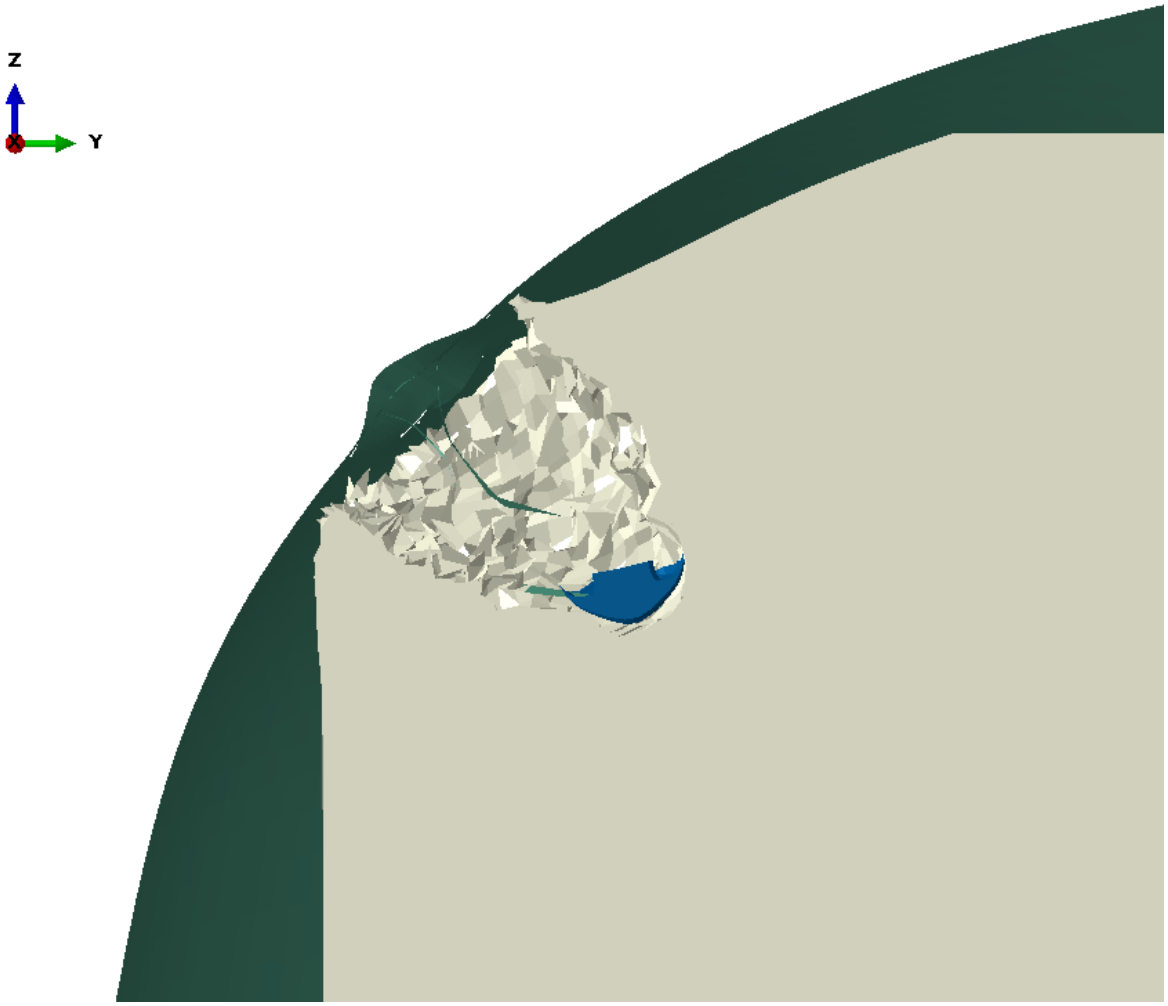

(k)

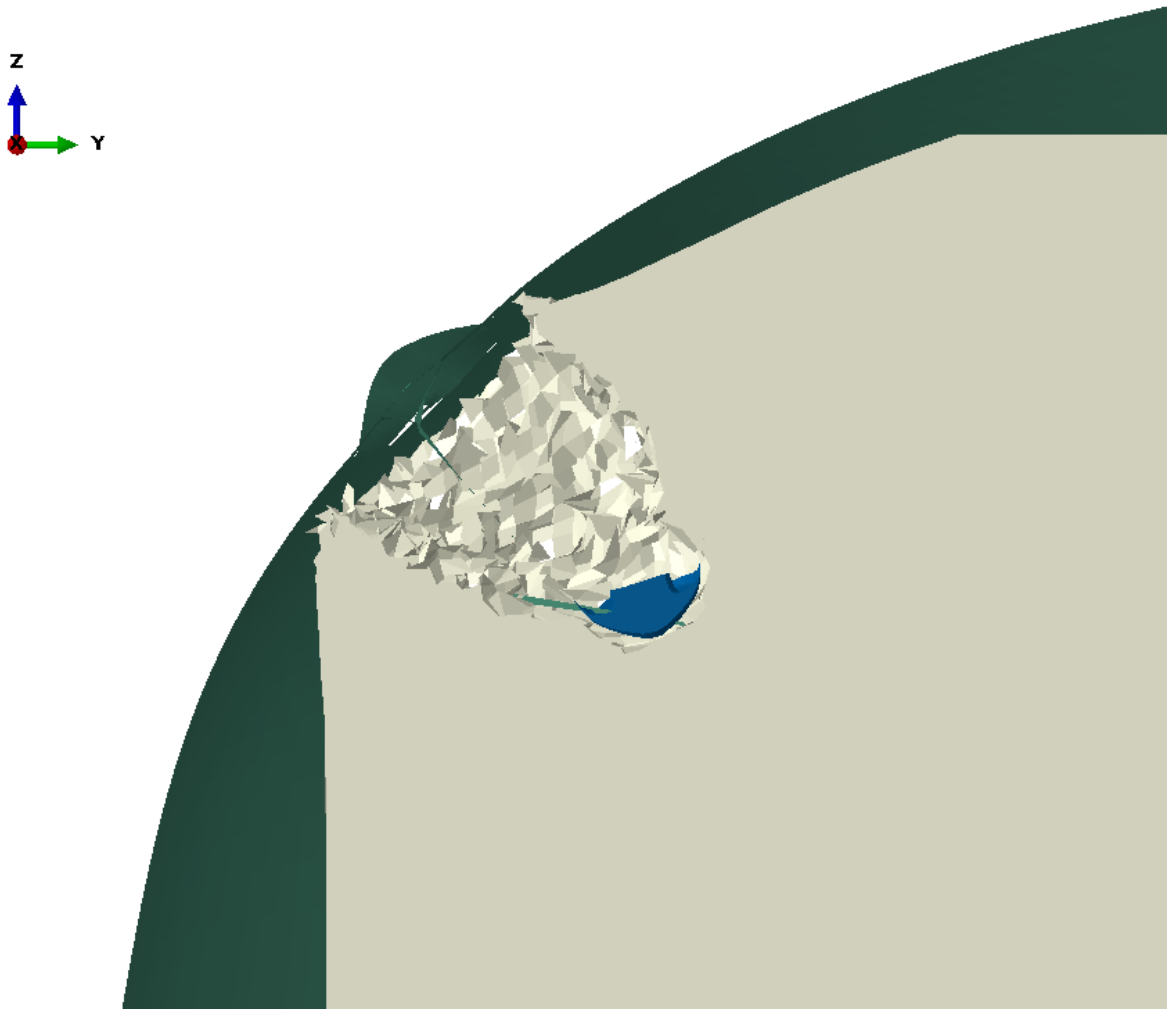

(l)

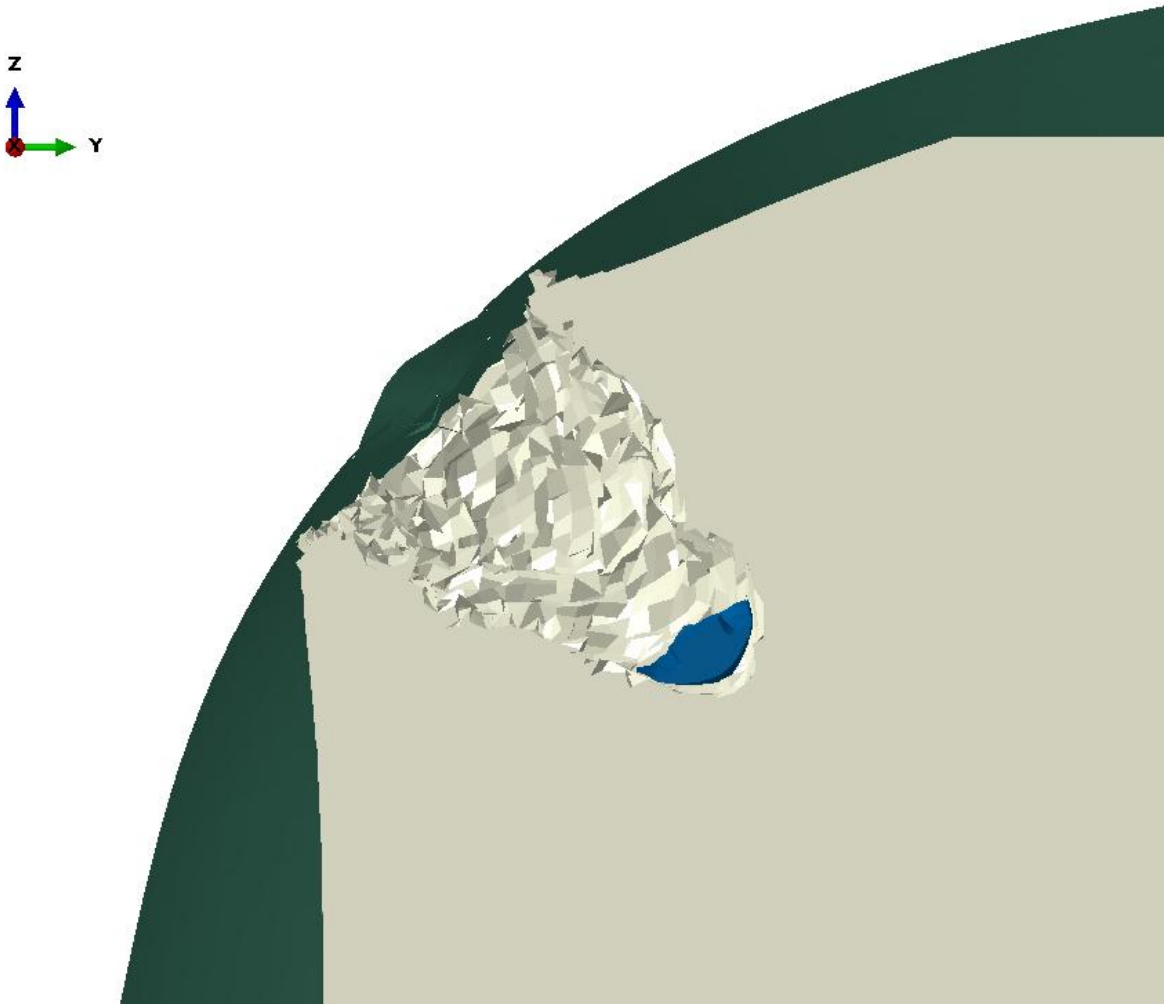

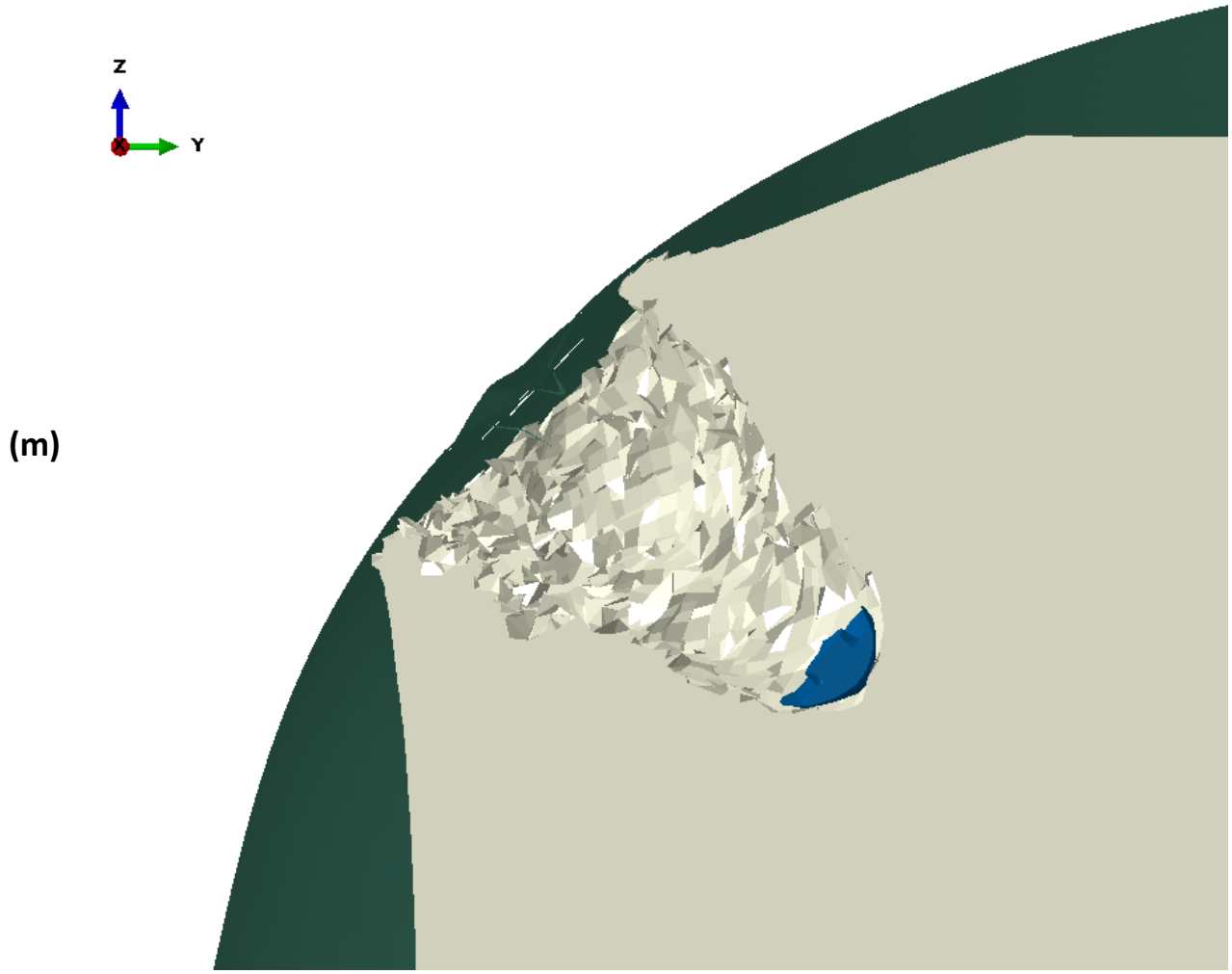

Figure 48. Snapshots of projectile/helmet/clay interaction with a projectile initial speed of 1000 m/s at 0 µs (a), 20 µs (b), 40 µs (c), 60 µs (d), 80 µs (e), 100 µs (f), 120 µs (g), 140 µs (h), 160 µs (i), 180 µs (j), 200 µs (k), 300 µs (l), and 400 µs (m).

Appendix A – Material Properties

Table A1. Values of Metal Material Parameters

Parameter	1100-H12 Aluminum	4340H Steel	Units
ρ	2700	7800	$\frac{kg}{m^3}$
E	65.8	200	GPa
v	0.3	0.29	
A	148	792	MPa
B	346	510	MPa
n	0.183	0.26	
m	0.859	1.03	
C	0.001	0.014	
$\dot{\varepsilon}_0$	1	1	s^{-1}
d1	0.071	0.05	
d2	1.248	3.44	
d3	-1.142	2.12	
d4	0.147	0.002	
u_f^{pl}	0.08	1.6	mm

Table A2. Values of Composite Material Parameters

Parameter	E-glass/117-220	AS4/3501-6 from Soden [3]	T300/BSL914C	Gevetex/LY556	Silenka/MY750	AS4/3501-6 from Lee [5] and Chan [19]	Units
ρ	1850	1580	1750	1585	1585	1550	$\frac{kg}{m^3}$
E_1	38.6	126	138	53.5	45.6	138	GPa
E_2	8.3	11	11	17.7	16.2	9.65	GPa
ν_{12}	0.25	0.28	0.28	0.278	0.278	0.3	
G_{12}	4.2	6.6	5.5	5.83	5.83	5.24	GPa
G_{13}	4.2	6.6	5.5	5.83	5.83	5.24	GPa
G_{23}	61	3.93	39.3	6.32	5.79	3.24	GPa
X^T	1062	1950	1500	1140	1280	2280	MPa
X^C	610	1480	900	570	800	1440	MPa
Y^T	31	48	27	35	40	57	MPa
Y^C	118	200	200	114	145	228	MPa
S^L	72	79	80	72	73	71	MPa
S^T	72	79	80	72	73	100	MPa
G^C	160	220	220	165	165	220	$\frac{J}{m^3}$

Values of material properties of composites with Dyneema fibers are not listed.

Table A3. Material Properties of Fibers

Properties	Dyneema Fiber [33]	AS2C Carbon Fiber [34]	Units
Density	975	1800	$\frac{kg}{m^3}$
Tensile Modulus	116	221	GPa
Tensile Strength	3600	4440	MPa
Strain at Failure	3.5 %	1.9 %	

Table A4. Values of Material Parameters for Roma Plastilina Clay #1

Parameter		Units
ρ	1500	$\frac{kg}{m^3}$
E	1.012	Mpa
ν	0.49	
A	65	kPa
B	210	kPa
n	0.6	
m	1	
ε_f^{pl}	1	

Appendix B – Sample Input File

```
*Heading
** Job name: fronthelmheadtake2test1 Model name: Helmet_Headform_forehead
** Generated by: Abaqus/CAE 6.10-1
*Preprint, echo=NO, model=NO, history=NO, contact=NO
** ----------------------------------------------------------------
**
** PART INSTANCE: Part-4-1
**
*Node
     1, 0.0329999998,  0.109974563, 0.0250000004
...
*Element, type=C3D8R
   1,   171,  3419,   170,     4,  3697, 49269,  3737,   339
...
*Solid Section, elset=Part-4-1__PickedSet241, material=clay
,
** ----------------------------------------------------------------
**
** PART INSTANCE: Part-5-Copy-1
**
*Node
 309555, -0.072668381,  0.141970396,  0.131951168
...
*Element, type=R3D4
295065, 309598, 309599, 310033, 310022
...
*Element, type=R3D3
295148, 310032, 310083, 310082
...
*Node
 312428, 0.0700040087, 0.0689703971, 0.0250000004

** ----------------------------------------------------------------
**
** PART INSTANCE: contourplate-Copy-1
**
*System
      0.0145,       0.084,          0.,       1.0145,       0.084,          0.
*Node
 312429, 0.0599999987, 0.0429703966, 0.0250000004
...
*Element, type=R3D4
297935, 312429, 312430, 312445, 312477
...
*Node
 313017, -0.0144999996, -0.0839999989, 0.0250000004

** ----------------------------------------------------------------
**
** PART INSTANCE: meshedhelmet3_headscale-2
**
*System
     1.8e-05,   -0.003488,   -0.084971,    1.000018,   -0.003488,   -0.084971
```

```
*Node
 313018, 0.0150429169, 0.0108238244,  0.213221565
...
*Element, type=S4R
298521, 313063, 313064, 313805, 313797
...
*Orientation, name=meshedhelmet3_headscale-2-Ori-1
        1.,          0.,          0.,          0.,          1.,          0.
3, 0.
** Region: (CompositeLayup-1-1: Generated From Layup)
*Elset, elset=meshedhelmet3_headscale-2_CompositeLayup-1-1, generate
298521, 305777,     1
** Section: CompositeLayup-1-1
*Shell Section, elset=meshedhelmet3_headscale-2_CompositeLayup-1-1, composite,
orientation=meshedhelmet3_headscale-2-Ori-1,
layup=CompositeLayup-1
0.00015, 3, "Composite", 0., Ply-1
0.00015, 3, "Composite", 0., Ply-2
...
**
** ----------------------------------------------------------------
**
** PART INSTANCE: FSP-1
**
*System
-
0.00057343740992401,0.00632261792847484,0.130505382071525,0.999426562590076,0.00632261792847484,0.1
25975382071525
-0.00057343740992401,0.713429399115022,0.833082163258073
*Node
 320372, -2.64999999e-05,          0., 0.00710000005
...
*Element, type=C3D8R
305778, 320775, 320776, 322185, 322041, 320390, 320391, 320638, 320637
...
** Section: Section-4
*Solid Section, elset=FSP-1__PickedSet11, material="AISI4340 Steel"
,
*System
*Node
**location of body
*Rigid Body, ref node=Part-5-Copy-1-RefPt_, elset=Part-5-Copy-1
*Rigid Body, ref node=contourplate-Copy-1-RefPt_, elset=contourplate-Copy-1
** surface definition for eroding contact
*surface, type=element, name=erodingsurf
,
erode,interior
**
**contact clearance, name=c1, adjust=yes
**
** MATERIALS
**
*Material, name="AISI4340 Steel"
*Damage Initiation, criterion=JOHNSON COOK
 0.05,  3.44,  2.12, 0.002,  0.61, 9000., 8000.,    1.
*Damage Evolution, type=DISPLACEMENT
```

```
 1.6,
*Density
7800.,
*Elastic
 2e+11, 0.29
*Plastic, hardening=JOHNSON COOK
 7.92e+08, 5.1e+08,    0.26,    1.03,   9000.,   8000.
*Rate Dependent, type=JOHNSON COOK
 0.014,1.
**
*Material, name=clay
*Density
 1500.,
*Elastic
 1.012e+06,0.49
*plastic, hardening=JOHNSON COOK
 65000., 210000., 0.6, 1., 9000., 8000.
*SHEAR FAILURE, TYPE=JOHNSON COOK,ELEMENT DELETION=yes
1.0,    0.,    0.,    0. ,    0.
**
*Material, name="Composite"
*Damage Initiation, criterion=HASHIN, alpha=1.
 1.5e+09, 9e+08, 2.7e+07, 2e+08, 8e+07, 8e+07
*Damage Evolution, type=ENERGY
220,220,220,220
*Density
1750.,
*Elastic, type=LAMINA
 1.38e+11, 1.1e+10, 0.28, 5.5e+09, 5.5e+09, 3.93e+10
**
** INTERACTION PROPERTIES
**
*Surface Interaction, name=IntProp-1
*Friction
2.,
**
** BOUNDARY CONDITIONS
**
** Name: BC-1 Type: Symmetry/Antisymmetry/Encastre
*Boundary
_PickedSet105, ENCASTRE
** Name: BC-2 Type: Symmetry/Antisymmetry/Encastre
*Boundary
_PickedSet99, ENCASTRE
** Name: BC-3 Type: Symmetry/Antisymmetry/Encastre
*Boundary
_PickedSet106, ENCASTRE
**
** PREDEFINED FIELDS
**
** Name: Predefined Field-1   Type: Velocity
*Initial Conditions, type=VELOCITY
_PickedSet81, 1, 0.
_PickedSet81, 2, 500.5
_PickedSet81, 3, -500.5
** ----------------------------------------------------------------
```

```
**
** STEP: Step-1
**
*Step, name=Step-1
*Dynamic, Explicit
, 0.0002
*Bulk Viscosity
0.06, 1.2
**
**
** Contact Definition
*contact, op=NEW
*Contact Inclusions
erodingsurf
*contact controls assignment, nodal erosion=no
*contact controls assignment, Contact Thickness Reduction=NOPERIMSELF
**
** OUTPUT REQUESTS
**
*Restart, write, number interval=1, time marks=NO
**
** FIELD OUTPUT: F-Output-1
**
*Output, field
*Node Output
A, RF, RM, RT, U, V
*Element Output, directions=YES
DAMAGEC, DAMAGEFC, DAMAGEFT, DAMAGEMC, DAMAGEMT, DAMAGESHR, DAMAGET,
DMICRT, LE, PE, PEEQ, S, STATUS, TRNOR, TRSHR, TSHR
*Contact Output
CFORCE, CSTRESS
**
**
**Output, field
*Element Output, elset=meshedhelmet3_headscale-2_CompositeLayup-1-1, directions=YES
1, list all section points where you want output data
CTSHR, DAMAGEFC, DAMAGEFT, DAMAGEMT, DAMAGET, MISESMAX, PS, S, SFABRIC, SSAVG,
SVAVG, TRIAX
TSHR, VS
**
**
** HISTORY OUTPUT: H-Output-1
**
*Output, history, variable=PRESELECT
*End Step
```